ASSESSMENT OF GUARDRAIL SYSTEMS WITH A STIFF SURFICIAL LAYER VIA CONTINUUM AND DISCRETE SIMULATIONS

A Dissertation
Presented to
The Academic Faculty

by

Esmaeel Bakhtiary

In Partial Fulfillment
of the Requirements for the Degree
Doctor of Philosophy in the
School of Civil and Environmental Engineering

Georgia Institute of Technology
August 2017

ASSESSMENT OF GUARDRAIL SYSTEMS WITH A STIFF SURFICIAL LAYER VIA CONTINUUM AND DISCRETE SIMULATIONS

Approved by:

Dr. Lauren K. Stewart, Chair
School of Civil Engineering
Georgia Institute of Technology

Dr. Donald W. White, Co-Chair
School of Civil Engineering
Georgia Institute of Technology

Dr. David W. Scott
School of Civil Engineering
Georgia Institute of Technology

Dr. J. David Frost
School of Civil Engineering
Georgia Institute of Technology

Dr. Min Zhou
School of Mechanical Engineering
Georgia Institute of Technology

Date Approved: [07 19, 2017]

[To my beloved wife, Ljilja, and my lovely son, Kai]

ACKNOWLEDGEMENTS

This research was sponsored by the Georgia Department of Transportation (GDOT) under research projects "Evaluating the Performance of Guardrail Systems for Installation in Georgia by Driving through Asphalt Layers – Phase I" and "Dynamic Subcomponent Testing and Finite Element Simulation of Guardrail Systems with Alternative Post Installation Methodologies – Phase II." Any findings, opinions, recommendations, or conclusions expressed herein are those of the author and do not necessarily reflect the views of GDOT.

I would like to thank my advisors, Dr. Lauren Stewart and Dr. Donald White, and my committee members, Dr. David Scott, Dr. David Frost, and Dr. Min Zhou for giving me the opportunity, guidance, and support that I needed to conduct this research.

I greatly appreciate the help of my friends, Joseph (Seo-Hun) Lee, Kami Mohammadi, Mahdy Roozbahani, Mohammad Mehdi Niki Rashidi, Ajinkya Lokhande, Oguzhan Togay, Marc Sanborn, Kathryne Sanborn, Nan Gao, Jiuk Shin, and Javaid Anwar at Georgia Institute of Technology without whom this work would not have been possible.

My sincere love goes to my lovely son, Kai, for his adorable smiles, hugs, and love. Finally, I would be nothing if not for the support of my father, my mother, my wife, and my siblings. Dad, Mom, Ljilja, Mina, Mohsen, Mostafa, and Ebrahim: Thank you all so much for your constant love and support. I hope I made you proud.

TABLE OF CONTENTS

ACKNOWLEDGEMENTS **iv**

LIST OF TABLES **ix**

LIST OF FIGURES **xi**

LIST OF SYMBOLS AND ABBREVIATIONS **xxiii**

SUMMARY **xxvii**

Chapter 1. Introduction **1**
1.1 Problem Statement **1**
1.2 Background **8**
1.2.1 Simulation and Testing of Guardrail Systems Embedded in Soil 8
1.2.2 Simulation and Testing of Guardrail Systems with Mow Strips 11
1.3 Benefits and Significance of This Research **13**
1.4 Organization of the Thesis **14**

Chapter 2. Static Finite Element Modeling of Guardrail Systems with Asphalt Mow Strips **18**
2.1 Overview of Modelling Techniques **18**
2.2 Finite Element Model Description **20**
2.2.1 Model Domain and Boundary Conditions 20
2.2.2 Simulation of Lateral Loading 22
2.2.3 Element Formulations and Mesh Sensitivity Analysis 23
2.2.4 Hourglass Controls and Energy Checks 24
2.2.5 Post and Soil Interface 25
2.2.6 Asphalt Interfaces 27
2.2.7 Mesh Treatments for the Asphalt Layer 28
2.2.8 Importance of Gravity Loading 30
2.2.9 Steel 32
2.2.10 Soil 33
2.2.11 Asphalt 40
2.3 Comparisons between Experiments and FE Simulations **43**

Chapter 3. Static Performance of Guardrail Systems with Asphalt Mow Strips **47**
3.1 Alternative Mow Strip Designs **47**
3.2 Effect of Asphalt Material and Geometric Properties **50**
3.2.1 Effect of the Asphalt Rear Distance 51
3.2.2 Effect of the Asphalt Thickness 53
3.2.3 Effect of the Asphalt Cohesion 53
3.2.4 Effect of the Asphalt Friction Angle 53
3.2.5 Effect of the Asphalt Shear Modulus 54
3.2.6 Effect of the Asphalt Poisson's Ratio 54

3.3 Effect of Asphalt Pre-Cutting 55
3.4 System Assessment using Quantitative Performance Criteria 59
3.4.1 Parametric Studies on Asphalt Mow Strip Geometry 59
3.4.2 Assessment using Peak Force Criterion 60
3.4.3 Assessment using Ground Level Displacement Criterion 60
3.4.4 Assessment using Maximum Strain Criterion 62
3.4.5 Assessment using Combination of the Three Criteria 63

Chapter 4. Dynamic Finite Element Modeling of Guardrail Systems with Asphalt Mow Strips 66
4.1 Design of the Impactor 66
4.2 Mock-up Testing 69
4.3 Dynamic Mock-up Simulations 69
4.3.1 Finite Element Model Description 69
4.3.2 Comparison between Experiments and FE Simulations 76
4.4 Dynamic Subcomponent Simulations 79
4.4.1 Finite Element Model Description 79
4.4.2 Comparisons between Experiments and FE Simulations 84

Chapter 5. Dynamic Performance of Guardrail Systems with Asphalt Mow Strips 92
5.1 System Assessment using Quantitative Performance Criteria 92
5.1.1 Parametric Studies on Asphalt Mow Strip Geometry 92
5.1.2 Assessment using Peak Force Criterion 94
5.1.3 Assessment using Peak Displacement Criterion 94
5.1.4 Assessment using Ground Level Displacement Criterion 96
5.1.5 Assessment using Effective Force Criterion 97
5.1.6 Assessment using Combination of the Four Criteria 98
5.1.7 Effect of Asphalt Pre-Cutting 100
5.1.8 Effect of Asphalt Material Properties 102

Chapter 6. Assessment Using Mash Full-Scale Crash Simulations 106
6.1 Finite Element Model Description 106
6.2 Evaluation Based on MASH Guidelines 109
6.3 Full-Scale Crash Simulation Results 112
6.3.1 Guardrail System without Mow Strip (Soil Only) 112
6.3.2 Guardrail System with Asphalt Mow Strip with 50 mm Thickness and 600 mm Rear Distance (Test T50-R600) 126
6.3.3 Guardrail System with Asphalt Mow Strip with 90 mm Thickness and 300 mm Rear Distance (Test T90-R300) 139
6.3.4 Guardrail System with Asphalt Mow Strip with 90 mm Thickness and 600 mm Rear Distance (Test T90-R600) 152
6.3.5 Guardrail System with Asphalt Mow Strip with 150 mm Thickness and 600 mm Rear Distance (Test T150-R600) 166
6.3.6 Guardrail System with Asphalt Mow Strip with 90 mm Thickness and 600 mm Rear Distance and Asphalt Diagonal Pre-Cuts (Test T90-R600-C) 180
6.3.7 Guardrail System with Asphalt Mow Strip with 90 mm Thickness and 600 mm Rear Distance and a Stiffer Asphalt (Test T90-R600-S) 194

6.4 Quantitative Comparison between Guardrail Systems with Different Mow Strips 207

Chapter 7. Efficient Modeling of Guardrail Posts Embedded in Asphalt Layers via P-Y Curves 212
7.1 Finite Element Model of Constrained Guardrail Posts Embedded in Asphalt Mow Strips 212
7.2 P-Y Curves for the Lateral Strength of Guardrail Posts Embedded in Asphalt Mow Strips Using Simplified Analytical Solutions and Dynamic FE Simulations 214
7.2.1 Rupture 215
7.2.2 Bearing Failure of the Asphalt Perpendicular to Post Flanges 227
7.2.3 Bearing Failure of Asphalt Perpendicular to the Post Web 234
7.2.4 Torsional Failure 239
7.3 Dynamic Simulation of Guardrail Posts Embedded in Asphalt Mow Strips Using P-Y Curves 246
7.4 Full-Scale Crash Simulation of Guardrail Systems with Asphalt Mow Strips Using P-Y Curves (Test T90-R600-Springs) 254

Chapter 8. Concluding Remarks 269
8.1 Conclusions 269
8.2 Future Work 275

REFERENCES 277

LIST OF TABLES

Table 1	– Material constants used in the static finite element models.	35
Table 2	– Comparison of experimental [9] and FEA results.	43
Table 3	– Peak force summary for pre-cutting designs.	58
Table 4	– Comparison between FEA and Experimental results for the mock-up tests.	77
Table 5	– Material constants used in the dynamic finite element subcomponent and full-scale crash simulations.	83
Table 6	– Comparison between measurements using subcomponent dynamic tests [9] and FE simulations.	93
Table 7	– Comparison between measurements predicted by FE simulations and estimated using the equivalent thickness method for a mow strip with the stiffer asphalt and 600 mm rear distance.	
Table 8	– Material constants used in the full-scale crash simulations.	107
Table 9	– Full-Scale Crash Simulations.	108
Table 10	– Comparison between results from FEA in this research and experiment [60] for the setup without an asphalt layer.	125
Table 11	– Summary of full-scale crash simulation results for Test T50-R600.	138
Table 12	– Summary of full-scale crash simulation results for Test T90-R300.	151
Table 13	– Summary of full-scale crash simulation results for Test T90-R600.	165
Table 14	– Summary of full-scale crash simulation results for Test T150-R600.	179
Table 15	– Summary of full-scale crash simulation results for Test T90-R600-C.	193
Table 16	– Summary of full-scale crash simulation results for Test T90-R600-S.	206
Table 17	– Comparison between the simulation results for guardrail systems with different mow strips. Setups are sorted based on decreasing ground restraint from the left side to the right side of the table.	211
Table 18	– Variables and constants for rupture failure.	222

Table 19 – Variables and constants for bearing failure perpendicular to flanges. 230

Table 20 – Variables and constants for bearing failure perpendicular to the web. 236

Table 21 – Variables and constants for torsional failure. 241

Table 22 – Comparison between measurements for different modeling of the asphalt versus experimental results. 252

Table 23 – Comparison between the simulation with continuum asphalt and with asphalt modelled using springs. 268

LIST OF FIGURES

Figure 1 – Schematic of an H-section steel pile embedded in soil [1]. 1

Figure 2 – Typical guardrail post installed in an asphalt mow strip [2]. 2

Figure 3 – (a) Typical guardrail installation in Georgia [8]; (b) Guardrail installation incorporating grout leave-outs as recommended in the Roadside Design Guide. 4

Figure 4 – Analysis of the lateral response of posts embedded in soil using p-y curves and inelastic nonlinear springs. 7

Figure 5 – Finite element model of guardrail post, soil, and asphalt system in LS-DYNA. 22

Figure 6 – Elements used for soil and the steel post. 24

Figure 7 – Shell thickness consideration to avoid initial element penetrations. 27

Figure 8 – Asphalt rupture observed in the experimental program [45]. 30

Figure 9 – Mesh treatments used for the asphalt layer combining hexahedral and tetrahedral elements. 30

Figure 10 – Contact between asphalt and soil. 31

Figure 11 – Comparison of the load-displacement curves with and without dynamic relaxation or gravity loading for a post embedded in soil with 90 mm asphalt layer. 32

Figure 12 – True stress versus true strain curves used in the model for the web and the flanges. 33

Figure 13 – Soil deformation for 300 mm translation at load level. 39

Figure 14 – Comparison between FEA and experiment [37] without an asphalt layer. 40

Figure 15 – System condition after static loading on a post with a 90 mm asphalt layer [45]: (a) experiment; (b) FEA with Mohr-Coulomb asphalt model; (c) FEA with a rigid asphalt model. 44

Figure 16 – Force-displacement comparison between experimental results [9]: FEA with Mohr-Coulomb asphalt model and FEA with rigid asphalt model for a post embedded in a 90 mm asphalt layer. 45

Figure 17 – Comparison between FEA and experimental measurements of the tensile strain in the post for the case with 50 mm thick asphalt and rear distance of 600 mm. 1 inch is equal to 25.4 mm. 46

Figure 18 – Comparison between FEA and experimental measurements of the tensile strain in the post for the case with 90 mm thick asphalt and rear distance of 600 mm. 1 inch is equal to 25.4 mm. 46

Figure 19 – Guardrail post setups with 2 in (50 mm) and 3.5 in (90 mm) thickness. 48

Figure 20 – Guardrail post setups with various rear distances. 49

Figure 21 – Schematic of a guardrail post setup with a pre-cut asphalt layer. 50

Figure 22 – Effect of asphalt geometric and material properties on the peak force in asphalt. 52

Figure 23 – Comparisons between LS-DYNA FEM and experimental results [56]. 56

Figure 24 – Pre-cutting designs for the asphalt mow strip with finite element model simulations. 57

Figure 25 – FEA Contour plots for combinations of thickness and rear distance. Curves are a representation of peak applied force to the post (kN). Experimental results are given in parentheses. 61

Figure 26 – FEA Contour plots for combinations of thickness and rear distance. Curves are a representation of ground level displacement. Experimental results are given in parentheses. 62

Figure 27 – FEA Contour plots for combinations of thickness and rear distance. Curves are a representation of the ratio of measured strains to the yield strain of steel equal to 0.002 mm/mm. Experimental results are given in parentheses. 64

Figure 28 – FEA Contour plots for combinations of thickness and rear distance. Curves are a representation of ground level displacement, peak applied force, and maximum longitudinal strain. 65

Figure 29 – Steel impactor, crushable foam, and rubber. 68

Figure 30 – Representation of the mock-up setup. 70

Figure 31 – Stress-strain curves used for the post flanges. Strain rates are written on each curve. 73

Figure 32 – Stress-strain curves used for the post web. Strain rates are written on each curve. 73

Figure 33 – Stress-strain curve for the foam material. 74

Figure 34 – Nominal yield stress vs. volumetric strain for the foam material. 76

Figure 35 – Plastic deformation of the post at the connection: a. FEA; b. Experiment [9]. 77

Figure 36 – Representation of the system after impact: a. FEA; b. Experiment [9]. 78

Figure 37 – Crushed foam after the impact: a. FEA; b. Experiment [9]. 78

Figure 38 – Finite Element Model used for dynamic subcomponent simulations. 80

Figure 39 – Simulation result for the model with only soil after the impact. 86

Figure 40 – Experimental result for the model with only soil after the impact [9]. 87

Figure 41 – Location of the accelerometers installed on the impactor. 87

Figure 42 – Acceleration-time history obtained from experiments [9] and FEA. 88

Figure 43 – Simulation result for the model with 90 mm thick asphalt and rear distance of 610 mm. 89

Figure 44 – Experimental result for the case with 90 mm thick asphalt and rear distance of 610 mm [9]. 90

Figure 45 – Acceleration-time history obtained from experiments [9] and the **FEA.** 91

Figure 46 – FEA contour plots for combinations of thickness and rear distance. Curves are a representation of peak applied force to the post (kN). Experimental results are given in parentheses [9]. 95

Figure 47 – FEA Contour plots for combinations of thickness and rear distance. Curves are a representation of peak displacement at impact point (mm). Experimental results are given in parentheses [9]. 96

Figure 48 – FEA Contour plots for combinations of thickness and rear distance. Curves are a representation of ground level displacement (mm). Experimental results are given in parentheses **[9]**. 97

Figure 49 – FEA Contour plots for combinations of thickness and rear distance. Curves are a representation of effective applied force to the post (kN). Experimental results are given in parentheses. 98

Figure 50 – FEA contour plots for combinations of thickness and rear distance. Curves are a representation of ground level displacement (mm), peak displacement at the impact point (mm), peak applied force (kN), and effective applied force (kN) for setups with equivalent restraint to the leave-out setup. 99

Figure 51 – Diagonal asphalt pre-cut used in the dynamic tests and simulations. 101

Figure 52 – Parallel asphalt pre-cut used in the dynamic tests and simulations. 102

Figure 53 – Simulation result for 90 mm thick asphalt with 600 mm rear distance and a stiffer asphalt. 103

Figure 54 – FE model with 29 posts. 107

Figure 55 – The suggested coordinate system in MASH. 111

Figure 56 – Simulation result for the guardrail system without mow strip – up to 0.3 sec. 113

Figure 57 – Simulation result for the guardrail system without mow strip–after 0.3 sec. 114

Figure 58 – Simulation result for the guardrail system without mow strip – up to 0.3 sec. 115

Figure 59 – Simulation result for the guardrail system without mow strip–after 0.3 sec. 116

Figure 60 – Simulation result for the guardrail system without mow strip. 117

Figure 61 – Vehicle deformation for the guardrail system with soil only. 117

Figure 62 – 10 m/s average vehicle longitudinal acceleration 119

Figure 63 – Relative longitudinal velocity of the occupant (m/s) – soil only. 120

Figure 64 – Relative longitudinal displacement of the occupant (m) – soil only. 120

Figure 65 – 10 m/s average vehicle lateral acceleration (g) – soil only. 121

Figure 66 – Relative lateral velocity of the occupant (m/s) – soil only. 121

Figure 67 – Relative lateral displacement of the occupant (m) – soil only. 122

Figure 68 – Vehicle roll for the setup with soil only (deg). 123

Figure 69 – Vehicle pitch for the setup with soil only (deg). 123

Figure 70 – Vehicle yaw for the setup with soil only (deg). 124

Figure 71 – Simulation result for Test T50-R600 – up to 0.3 sec. 127

Figure 72 – Simulation result for Test T50-R600 – after 0.3 sec. 128

Figure 73 – Simulation result for Test T50-R600 – up to 0.3 sec. 129

Figure 74 – Simulation result for Test T50-R600 – after 0.3 sec. 131

Figure 75 – Simulation result for Test T50-R600. 131

Figure 76 – Vehicle Deformation for Test T50-R600. 131

Figure 77 – 10 m/s average vehicle longitudinal acceleration (g) - Test T50-R600. 133

Figure 78 – Relative longitudinal velocity of the occupant (m/s) - Test T50-R600. 134

Figure 79 – Relative longitudinal displacement of the occupant (m) – Test T50-R600. 134

Figure 80 – 10 m/s average vehicle lateral acceleration (g) – Test T50-R600. 135

Figure 81 – Relative lateral velocity of the occupant (m/s) - Test T50-R600. 135

Figure 82 – Relative lateral displacement of the occupant (m) - Test T50-R600. 136

Figure 83 – Vehicle roll (deg) - Test T50-R600. 136

Figure 84 – Vehicle pitch (deg) - Test T50-R600. 137

Figure 85 – Vehicle yaw (deg) - Test T50-R600. 137

Figure 86 – Simulation result for Test T90-R300 – up to 0.3 sec. 140

Figure 87 – Simulation result for Test T90-R300 – after 0.3 sec. 141

Figure 88 – Simulation result for Test T90-R300 – up to 0.3 sec. 142

Figure 89 – Simulation result for Test T90-R300 – after 0.3 sec. 143

Figure 90 – Simulation result for Test T90-R300. 144

Figure 91 – Vehicle Deformation for Test T90-R300. 144

Figure 92 – 10 m/s average vehicle longitudinal acceleration (g) - Test T90-R300. 146

Figure 93 – Relative longitudinal velocity of the occupant (m/s) - Test T90-R300. 147

Figure 94 – Relative longitudinal displacement of the occupant (m)–Test T90-R300. 147

Figure 95 – 10 m/s average vehicle lateral acceleration (g) – Test T90-R300. 148

Figure 96 – Relative lateral velocity of the occupant (m/s) - Test T90-R300. 148

Figure 97 – Relative lateral displacement of the occupant (m) - Test T90-R300. 149

Figure 98 – Vehicle roll (deg) - Test T90-R300. 149

Figure 99 – Vehicle pitch (deg) - Test T90-R300. 150

Figure 100 – Vehicle yaw (deg) - Test T90-R300. 150

Figure 101 – Simulation result for Test T90-R600 – up to 0.3 sec. 154

Figure 102 – Simulation result for Test T90-R600 – after 0.3 sec. 155

Figure 103 – Simulation result for Test T90-R600 – up to 0.3 sec. 156

Figure 104 – Simulation result for Test T90-R600 – after 0.3 sec. 157

Figure 105 – Simulation result for Test T90-R600. 158

Figure 106 – Vehicle Deformation for Test T90-R600. 158

Figure 107 – 10 m/s average vehicle longitudinal acceleration (g) - Test T90-R600. 160

Figure 108 – Relative longitudinal velocity of the occupant (m/s) - Test T90-R600. 161

Figure 109 – Relative longitudinal displacement of the occupant (m) – Test T90-R600. 161

Figure 110 – 10 m/s average vehicle lateral acceleration (g) – Test T90-R600. 162

Figure 111 – Relative lateral velocity of the occupant (m/s) - Test T90-R600. 162

Figure 112 – Relative lateral displacement of the occupant (m) - Test T90-R600. 163

Figure 113 – Vehicle roll (deg) - Test T90-R600. 163

Figure 114 – Vehicle pitch (deg) - Test T90-R600. 164

Figure 115 – Vehicle yaw (deg) - Test T90-R600. 164

Figure 116 – Simulation result for Test T150-R600 – up to 0.3 sec. 168

Figure 117 – Simulation result for Test T150-R600 – after 0.3 sec. 169

Figure 118 – Simulation result for Test T150-R600 – up to 0.3 sec. 170

Figure 119 – Simulation result for Test T150-R600 – after 0.3 sec. 171

Figure 120 – Simulation result for Test T150-R600. 172

Figure 121 – Vehicle Deformation for Test T150-R600. 172

Figure 122 – 10 m/s average vehicle longitudinal acceleration (g) - Test T150-R600. 174

Figure 123 – Relative longitudinal velocity of the occupant (m/s) - Test T150-R600. 174

Figure 124 – Relative longitudinal displacement of the occupant(m)–Test T150-R600. 175

Figure 125 – 10 m/s average vehicle lateral acceleration (g) – Test T150-R600. 175

Figure 126 – Relative lateral velocity of the occupant (m/s) - Test T150-R600. 176

Figure 127 – Relative lateral displacement of the occupant (m) - Test T150-R600. 176

Figure 128 – Vehicle roll (deg) - Test T150-R600. 177

Figure 129 – Vehicle pitch (deg) - Test T150-R600. 177

Figure 130 – Vehicle yaw (deg) - Test T150-R600. 178

Figure 131 – Simulation result for Test T90-R600-C – up to 0.3 sec. 182

Figure 132 – Simulation result for Test T90-R600-C – after 0.3 sec. 183

Figure 133 – Simulation result for Test T90-R600-C – up to 0.3 sec. 184

Figure 134 – Simulation result for Test T90-R600-C – after 0.3 sec. 185

Figure 135 – Simulation result for Test T90-R600-C 186

Figure 136 – Vehicle Deformation for Test T90-R600-C. 186

Figure 137 – 10 m/s average vehicle longitudinal acceleration (g) - Test T90-R600-C. 188

Figure 138 – Relative longitudinal velocity of the occupant (m/s) - Test T90-R600-C. 188

Figure 139 – Relative longitudinal displacement of occupant (m) – Test T90-R600-C. 189

Figure 140 – 10 m/s average vehicle lateral acceleration (g) – Test T90-R600-C. 189

Figure 141 – Relative lateral velocity of the occupant (m/s) - Test T90-R600-C. 190

Figure 142 – Relative lateral displacement of the occupant (m) - Test T90-R600-C. 190

Figure 143 – Vehicle roll (deg) - Test T90-R600-C. 191

Figure 144 – Vehicle pitch (deg) - Test T90-R600-C. 191

Figure 145 – Vehicle yaw (deg) - Test T90-R600-C. 192

Figure 146 – Simulation result for Test T90-R600-S – up to 0.3 sec. 195

Figure 147 – Simulation result for Test T90-R600-S – after 0.3 sec. 196

Figure 148 – Simulation result for Test T90-R600-S – up to 0.3 sec. 197

Figure 149 – Simulation result for Test T90-R600-S – after 0.3 sec. 198

Figure 150 – Simulation result for Test T90-R600-S. 199

Figure 151 – Vehicle deformation for Test T90-R600-S. 199

Figure 152 – 10 m/s average vehicle longitudinal acceleration (g) - Test T90-R600-S. 201

Figure 153 – Relative longitudinal velocity of the occupant (m/s) - Test T90-R600-S. 201

Figure 154 – Relative longitudinal displacement of occupant (m) – Test T90-R600-S. 202

Figure 155 – 10 m/s average vehicle lateral acceleration (g) – Test T90-R600-S. 202

Figure 156 – Relative lateral velocity of the occupant (m/s) - Test T90-R600-S. 203

Figure 157 – Relative lateral displacement of the occupant (m) - Test T90-R600-S. 203

Figure 158 – Vehicle roll (deg) - Test T90-R600-S. 204

Figure 159 – Vehicle pitch (deg) - Test T90-R600-S. 204

Figure 160 – Vehicle yaw (deg) - Test T90-R600-S. 205

Figure 161 – Summation of ground level displacement of posts compared for guardrail systems with different mow strips based on simulation results. 210

Figure 162 – The Finite Element Model used for parametric studies in order to develop p-y curves. 213

Figure 163 – Mohr-Coulomb yield criterion with a normal plastic strain rate vector. 215

Figure 164 – Assumed failure mechanism for the shear capacity. 218

Figure 165 – Assumed tensile failure mechanism with zero shear planes. 220

Figure 166 – Rupture capacity predicted by regression model versus FEA results. 223

Figure 167 – Rupture capacity p-y curves for various values of cohesion *c*. 225

Figure 168 – Rupture capacity p-y curves for various values of friction angle Φ. 226

Figure 169 – Rupture capacity p-y curves for various values of rear distance *r*. 226

Figure 170 – Rupture capacity p-y curves for various values of shear modulus *G*. 227

Figure 171 – Bearing capacity failure mechanism perpendicular to the flanges. 228

Figure 172 – Bearing capacity perpendicular to flanges by Eq. 26 versus FEA results. 231

Figure 173 – P-Y curves for the bearing capacity perpendicular to post flanges for various values of cohesion *c*. 233

Figure 174 – P-Y curves for the bearing capacity perpendicular to post flanges for various values of friction angle *Φ*. 233

Figure 175 – P-Y curves for the bearing capacity perpendicular to post flanges for various values of shear modulus *G*. 234

Figure 176 – Bearing capacity failure mechanism when the load is applied perpendicular to the web. 235

Figure 177 – Bearing capacity perpendicular to the web obtained from FEA versus friction angle of asphalt. 236

Figure 178 – P-Y curves for the bearing capacity perpendicular to the post's web for various values of cohesion *c*. 238

Figure 179 – P-Y curves for the bearing capacity perpendicular to the post web for various values of friction angle *Φ*. 238

Figure 180 – P-Y curves for the bearing capacity perpendicular to the post web for various values of shear modulus *G*. 239

Figure 181 – Torsional capacity when a torsional moment is applied to the post. 240

Figure 182 – Asphalt torsional capacity predicted by Eq. 34 versus FEA results. 242

Figure 183 – Comparison between predictions using Eq. 36 and FEA results for *kmt*. 244

Figure 184 – P-Y curves for the torsional capacity for various values of cohesion *c*. 245

Figure 185 – P-Y curves for the torsional capacity for various values of friction angle. 245

Figure 186 – P-Y curves for the torsional capacity for various values of shear modulus *G*. 245

Figure 187 – The model of the guardrail post embedded in soil and asphalt. Asphalt was modeled using one rotational and four translational springs. 247

Figure 188 – The model of the guardrail post embedded in soil and asphalt. Asphalt was modeled using one rotational and four translational springs. 248

Figure 189 – Force-displacement curve for the inelastic spring (Spring #1) behind the post to model asphalt rupture. 248

Figure 190 – Force-displacement curve for the inelastic spring (spring #2) in front of the post to model asphalt bearing capacity when pulled toward the front of the post. 249

Figure 191 – Force-displacement curve for the inelastic springs (spring #1 and #2) on the right and left-hand sides of the post to model asphalt lateral strength. 250

Figure 192 – Torsion-rotation curve for the inelastic spring in the center of the web to model the torsional capacity. 251

Figure 193 – **Acceleration-time history for different methods of modeling of the asphalt versus experimental results.** 253

Figure 194 – FE model used for the full-scale crash simulation with asphalt modeled using springs – top view. 254

Figure 195 – FE model used for the full-scale crash simulation with asphalt modeled using springs. 255

Figure 196 – Illustration of the arrangement of springs in the model. 255

Figure 197 – Simulation for the guardrail system with asphalt modeled via springs. 259

Figure 198 – Simulation for the guardrail system with asphalt modeled via springs. 260

Figure 199 – Simulation for the guardrail system with asphalt modeled via springs. 261

Figure 200 – Simulation for the guardrail system with asphalt modeled via springs. 262

Figure 201 – Vehicle deformation for the system with asphalt modeled via springs. 263

Figure 202 – 10 m/s average vehicle longitudinal acceleration (g) - asphalt modeled via springs versus continuum asphalt. 263

Figure 203 – Relative longitudinal velocity of the occupant (m/s) - asphalt modeled via springs versus continuum asphalt. 264

Figure 204 – Relative longitudinal displacement of the occupant (m) – asphalt modeled via springs versus continuum asphalt. 264

Figure 205 – 10 m/s average vehicle lateral acceleration (g) – asphalt modeled via springs versus continuum asphalt. 265

Figure 206 – Relative lateral velocity of the occupant (m/s) - asphalt modeled via springs versus continuum asphalt. 265

Figure 207 – Relative lateral displacement of the occupant (m) - asphalt modeled via springs versus continuum asphalt. 266

Figure 208 – Vehicle roll (deg) - asphalt modeled via springs versus continuum asphalt. 266

Figure 209 – Vehicle pitch (deg) - asphalt modeled via springs versus continuum asphalt. 267

Figure 210 – Vehicle yaw (deg) - asphalt modeled via springs versus continuum asphalt. 267

LIST OF SYMBOLS AND ABBREVIATIONS

Abbreviations

AASHTO	American Association of State Highway and Transportation Officials
ASTM	American Society for Testing and Materials
CIP	Critical Impact Point
CPU	Central Processing Unit
Exp.	Experiment
FE	Finite Element
FEA	Finite Element Analysis
FHWA	Federal Highway Administration
GDOT	Georgia Department of Transportation
MASH	Manual for Assessing Safety Hardware
MGS	Midwest Guardrail System
NCAC	National Crash Analysis Center
NCHRP	National Cooperative Highway Research Program
OIV	Occupant Impact Velocity
ORA	Occupant Ride-Down Acceleration
P-Y Curve	Force-displacement or Moment Rotation Curve
USCS	Unified Soil Classification System
3D	Three Dimensional

Lower Case Latin Characters

a_{bw}	Dimensionless constant obtained from regression analysis
a_{mt}	Dimensionless constant obtained from regression analysis

a_r Dimensionless constant obtained from regression analysis

b_f Flanges width

b_{kbf} Constant obtained from regression analysis

b_{kmt} Constant obtained from regression analysis

b_{mt} Dimensionless constant obtained from regression analysis

C Cohesion

c' Reference asphalt cohesion equal to 500 kPa

f_{bw} Dimensionless constant obtained from regression analysis

f_{mt} Dimensionless constant obtained from regression analysis

f_r Dimensionless constant obtained from regression analysis

H Post cross section depth

h_{bf} Constant obtained from regression analysis

h_{kbf} Constant obtained from regression analysis

h_{kmt} Constant obtained from regression analysis

h_{mt} Dimensionless constant obtained from regression analysis

k_{bf} Initial slope of the curve for bearing capacity perpendicular to the post flanges

k_{bw} Initial slope of the curve for bearing capacity perpendicular to the post web

k_{ru} Slope of unloading curve for the rupture capacity

l_{yr} Constant with dimension of length obtained from regression analysis

l_{kbw} Constant obtained from regression analysis

m_t Asphalt torsional capacity per unit thickness

m_v Vehicle mass

P Pressure

p_{bf} Bearing capacity perpendicular to the post flanges per unit thickness

p_{bw} Bearing capacity perpendicular to the post web per unit thickness

p_f Failure pressure

p_r Rupture capacity per unit thickness of asphalt

p_s Shear capacity per unit thickness of asphalt

p_t Tensile capacity per unit thickness of asphalt

R Mow strip rear distance

t_e Equivalent thickness

u_r Dimensionless constant obtained from regression analysis

v_t Tangential component of the relative velocity

v_n Normal component of the relative velocity

y_r Lateral displacement at which the peak force occurs

y_u Lateral displacement where one piece of an asphalt layer gets detached and the resistance of the layer goes to zero

Upper Case Latin Characters

D The rate of energy dissipation per unit length of the shear band

$Dvol$ Energy dissipation per unit volume

D_{10} The sieve opening size that 10% of the soil sample mass passes through

D_{30} The sieve opening size that 30% of the soil sample mass passes through

D_{60} The sieve opening size that 60% of the soil sample mass passes through

E Young's modulus

E_d Dissipated energy

G Shear modulus

P_r Full Rupture Capacity

Greek Characters

α	The angle between the assumed zero shear planes and the direction of post's movement
ε_{Max}	Maximum principal strain
$\dot{\varepsilon}_t^p$	Plastic shear strain rate acting tangentially to the slip surface
$\dot{\varepsilon}_n^p$	Plastic extensional strain rate acting normal to the slip surface
ε_1	First principal strain
N	Poisson's ratio
P	Density
σ_b	Bearing stress
σ_{Max}	Maximum principal stress
σ_y	Yield strength
σ_1	First principal stress
σ_2	Second principal stress
σ_3	Third principal stress
T	Shear stress
τ_b	Side shear stress when the bearing capacity is reached
ϕ	Friction angle
ϕ'	Reference friction angle of asphalt equal to 35 deg
ϕ'_{cr}	Critical friction angle
ϕ'_{p}	Peak friction angle

SUMMARY

Mow strips are asphalt or concrete layers which are used in the design of roadside safety structures as vegetation barriers around guardrail posts. Asphalt mow strips have historically been modeled in simulations as a rigid layer. This assumption often results in unrealistic ground level restraint of the guardrail post. Recent experiments conducted in a parallel research effort have shown that asphalt rupture and other material behavior should be considered in the analysis of the response of guardrail posts embedded in mow strips.

This study provides an accurate and efficient approach for simulating the guardrail system and investigates the effect of asphalt material properties and mow strip geometry on the guardrail system performance. In this research, several mow strip designs with various thicknesses, rear distances behind the posts, and asphalt pre-cuts are investigated to provide recommendations for retrofit techniques and new construction. The recommended retrofit and new construction techniques are evaluated with static and dynamic numerical simulations of guardrail posts embedded in asphalt mow strips, and full-scale crash simulations of the guardrail systems are performed. The results are compared with available data from experiments and material tests. The simulation results for guardrail posts are used to evaluate the level of restraint provided by the asphalt mow strips. Thereafter, full-scale crash simulation results are evaluated using guidelines in the Manual for Assessing Safety Hardware (MASH).

Additionally, simplified analytical solutions are constructed to obtain the lateral capacity of posts embedded in asphalt mow strips. These solutions are further enhanced by combining finite element simulations and regression analysis to provide predictive

equations for the lateral strength and stiffness of asphalt mow strips. The predictive equations are utilized to construct force-displacement curves (p-y curves) for asphalt layers with various rear distances and material properties. The p-y curves are then employed to efficiently model asphalt mow strips using nonlinear uncoupled springs.

CHAPTER 1. INTRODUCTION

1.1 Problem Statement

Piles are long, slender foundation members, made of timber, structural steel, or concrete, which are either driven or cast-in-situ. Piles act as structural members that transfer loads coming from the structure above to a required depth in deep foundations. These loads may be lateral, vertical, or combined lateral plus vertical. A schematic of an H-section steel pile embedded in soil is presented in Figure 1. The pile is surrounded by soil, and the structure can be connected to the top of the pile.

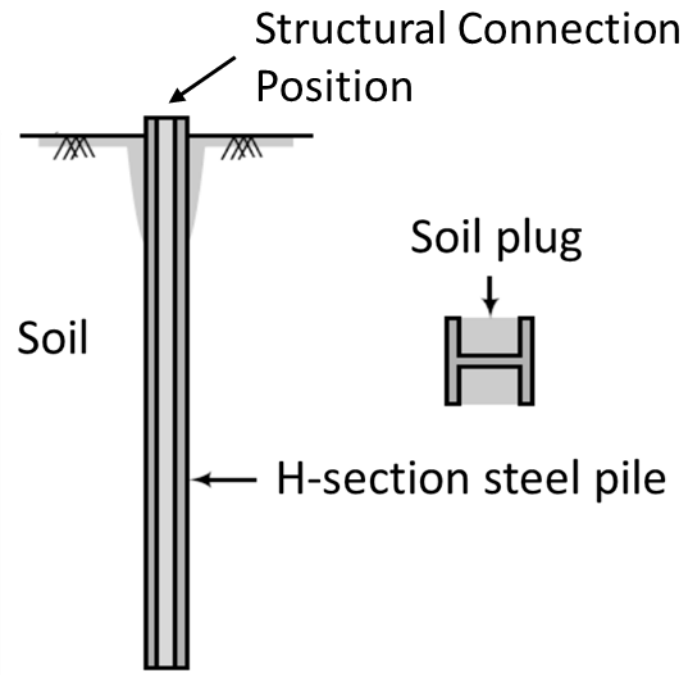

Figure 1. Schematic of an H-section steel pile embedded in soil [1]**.**

In a guardrail system such as the one shown in Figure 2, the pile is a guardrail post, and the structure connecting to the top of it is a guardrail. Guardrail posts are typically embedded in the soil, and in some cases, asphalt mow strips are used on top of the soil. Asphalt mow strips are layers of pavement that are installed around guardrail posts to serve as vegetation barriers. The word "asphalt," as it is used here, refers to asphalt concrete pavement. For steel guardrail installation, a hydraulic machine typically drives the posts through a layer of asphalt mow strip. A guardrail post driven into an asphalt mow strip and definitions of key mow strip geometric parameters, rear distance and thickness, are shown in Figure 2. The mow strip rear distance is defined as the distance from the back of the guardrail post to the back edge of the asphalt mow strip.

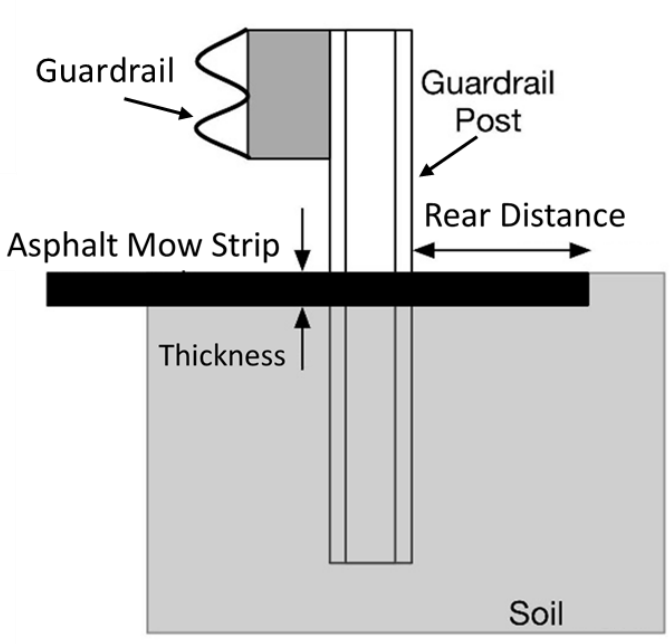

Figure 2. Typical guardrail post installed in an asphalt mow strip [2]**.**

Bligh et al. [3] conducted the first research project on the effect of asphalt mow strips on the performance of guardrail systems. They modeled the asphalt mow strip as a rigid material and concluded that asphalt mow strips significantly increase the ground-level restraint of guardrail posts. Based on their assumption, the results showed that steel guardrail posts confined in asphalt exhibit a plastic hinge during a vehicle impact, causing the vehicle to pass over the guardrail instead of being redirected back to the road, which is not a desirable performance in guardrail systems. Therefore, the American Association of State Highway and Transportation Officials (AASHTO) Roadside Design Guide (AASHTO, 2011) classifies mow strips as rigid foundations and states that guardrail posts in mow strips must not be able to rotate in the soil.

However, other researchers have reported that asphalt strength and other material properties of the mow strip are sensitive to temperature ([4],[5]) and age ([6],[7]), which contradicts the assumption that asphalt is a rigid material. Other issues also exist in these models that can potentially affect the results. For example, in some cases, gravity was applied without dynamic relaxation, and in others, a small domain was used to model the soil. Therefore, a more appropriate modeling technique, which includes a material model for the asphalt, proper simulation of asphalt rupture, and proper handling of gravity, domain, and boundaries is needed.

Rigid mow strips can significantly affect the energy dissipation mechanism of guardrail systems. Without an asphalt mow strip, when a post is loaded laterally, it shifts

horizontally in the direction of the applied load, causing bending, rotation, and translation of the post. The post applies a force on the soil and asphalt, generating compressive and shear stresses and strains in the materials, which offer resistance to the post movement. This is the primary mechanism of load transfer for guardrail posts. However, a thick asphalt layer can potentially prohibit the movement of the post and interrupt the energy dissipation provided by the soil. As a solution to the increased ground level restraint provided by asphalt mow strips, the Roadside Design Guide recommends using a leave-out, where the portion of the mow strip around the post is removed and replaced with a relatively weak material such as low-strength cementitious grout (Figure 3a).

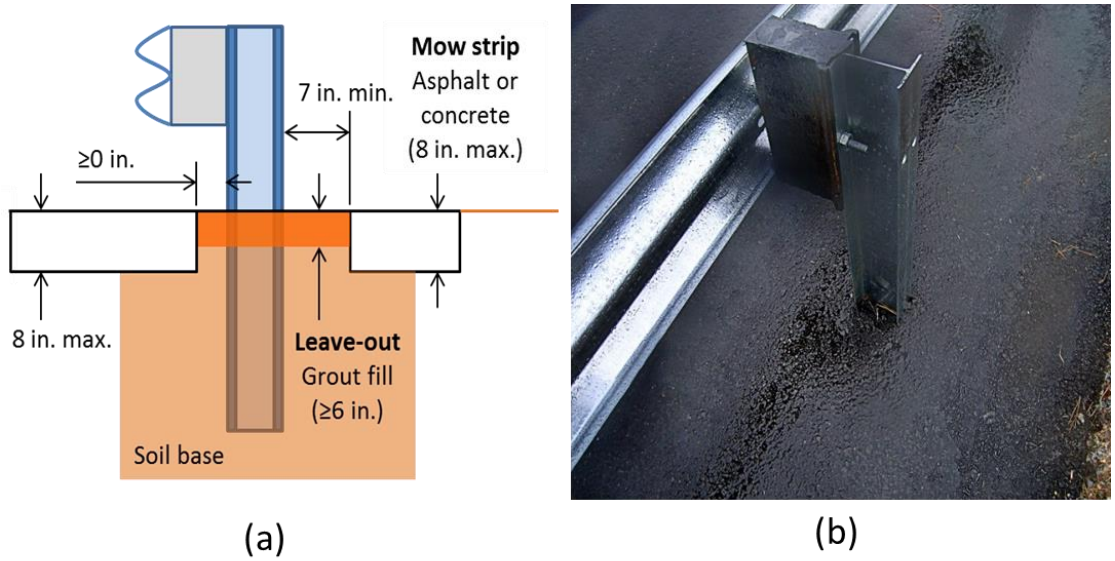

Figure 3. (a) Typical guardrail installation in Georgia [8]**; (b) Guardrail installation incorporating grout leave-outs as recommended in the Roadside Design Guide.**

While generally effective, installing a leave-out requires more time and cost compared to typical post-driven mow strips, which are installed by a machine (Figure 3b). This can be attributed to additional construction processes such as the removal of mow strips around the posts and the preparation/placement of leave-out materials. Additional research, discussed in this document, is needed to identify better alternatives to using a leave-out. In order to determine that, the effects of mow strip geometric and material properties on guardrail systems performance must be considered.

This dissertation is part of a project sponsored by the Georgia Department of Transportation to investigate the effect of asphalt mow strips on guardrail systems performance. Two phases of the project are included in this dissertation. The first phase is static testing and simulation of guardrail posts encased in asphalt mow strips. The second phase is dynamic testing and simulation of guardrail posts encased in asphalt mow strips plus finite element crash simulations and assessment of guardrail systems in asphalt mow strips. The experimental testing part of the project was conducted in research parallel to this effort, and the results and discussions related to the experimental tests are provided in [9]. The aspects of the project that focused on the simulation results and analysis of guardrail systems in asphalt mow strips are discussed here in this dissertation.

Guardrail systems are investigated in this dissertation using numerical simulations. Nonlinear explicit finite element analysis is one of the most accurate methods for predicting the response of guardrail systems. As will be discussed in the following chapters, asphalt

mow strips can be simulated accurately using a Mohr-Coulomb material model and the element erosion method available in the LS-DYNA [10] software. Although finite element simulations can be computationally intensive, they are often applied because there have been no simple equations available in the existing literature that can be used in lieu of simulations to determine the strength and stiffness of asphalt layers around guardrail posts. As will be discussed in Chapter 7, these types of simplified equations offer insights as to how each geometric and material property of the asphalt layer directly affects its strength and stiffness. Dynamic finite element simulation results, along with simplified analytical solutions, are shown here to be able to provide predictive equations for the mow strip strength and stiffness as a function of friction angle, cohesion, modulus of elasticity, and the rear distance of mow strips.

In the simplified analytical approach, preliminary investigation of the effect of asphalt material properties and geometry on a guardrail system can be performed by modeling soil and asphalt using springs. By using force-displacement (p-y) curves, a common fast method for analysis and design of piles under lateral loading, this method replaces the soil with an array of uncoupled nonlinear springs. Each spring is then governed by a given p-y curve. P-Y curves have been used by many researchers to model guardrail posts embedded in soil ([11],[12],[13],[14]), such as the example shown in Figure 4. However, prior to this research, there were no p-y curves available to apply to asphalt layers.

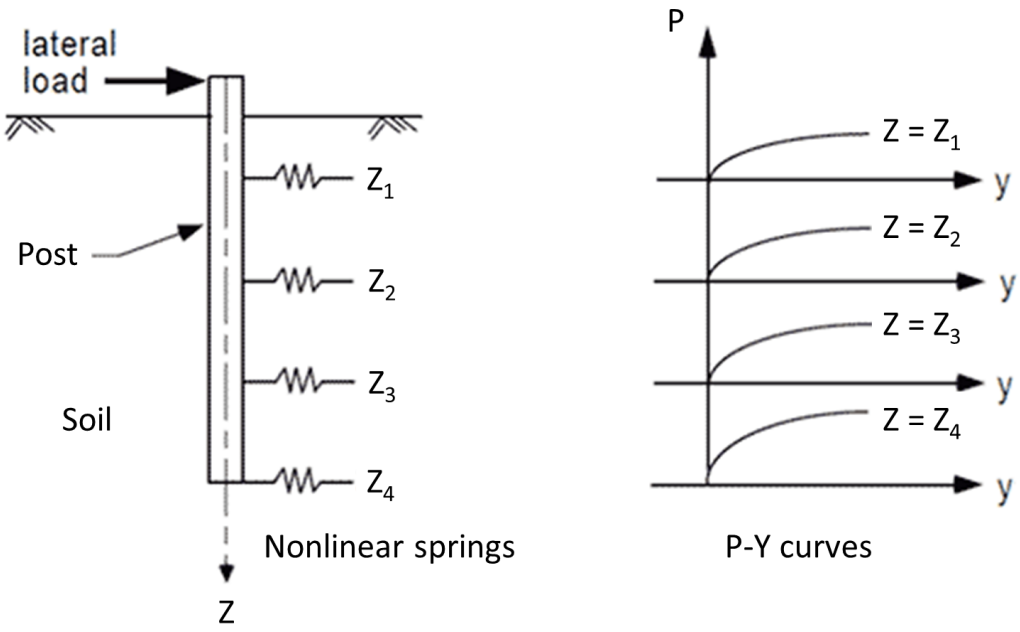

Figure 4. Analysis of the lateral response of posts embedded in soil using p-y curves and inelastic nonlinear springs.

Using p-y curves significantly reduces the simulation time. For the modeling of only one guardrail post using the finite element method, including the asphalt layer as a continuum makes the simulation two to three times longer. The full-scale finite element crash simulations discussed in this research include guardrails, an impacting vehicle, and 29 guardrail posts. Therefore, each simulation takes approximately one week to complete using a computer with six 3.5 GHz Intel CPUs. Adding the asphalt mow strip with two rows of elements through its thickness adds 300,000 elements to the model, which increases the total number of elements from 1 million to 1.3 million, which, in turn, increases the simulation time by approximately 30%. If more than two layers of elements are needed, then the increase in the simulation time will be even more dramatic. The

proposed p-y curves can be employed to efficiently model asphalt mow strips in full-scale crash simulations and simulations of guardrail posts using nonlinear uncoupled springs.

1.2 Background

1.2.1 Simulation and Testing of Guardrail Systems Embedded in Soil

A large volume of work exists regarding the testing and assessment of guardrail posts and systems embedded in soil. Summaries of representative work are presented below.

A synthesis report by Ray and McGinnis [15] provides a broad summary of crash testing for various barrier types. Articles by Reid [16] and Atahan [17] provide detailed reviews of finite element simulations of vehicle barrier impacts. Atahan [13] conducted an explicit nonlinear finite element simulation of a strong post W-beam guardrail system. The results of a previously conducted full-scale crash test of a failed guardrail system were used in the study. Before the next full-scale crash test, numerical simulations of the failed system were used to identify the cause of the failure and to propose possible improvements to the system. Borovinšek et al. [12] and Ren et al. [18] used computational crash simulations in early efforts to evaluate various guardrail setups and determine the best barrier design for high and low containment levels. In the study completed by Hampton and Gabler [19], the effects of missing posts on guardrail crash performance were quantitatively evaluated.

Mohan et al. [20] developed a detailed finite element model of a three-strand cable barrier, which was validated against a previously conducted full-scale crash test. Sicking et al. [21] used numerical and experimental full-scale crash testing for the development of the Midwest Guardrail System. Mak et al. [22] reported the results of eight full-scale crash tests on typical guardrail systems including W-beam, cable, box-beam, and Thrie-beam configurations. All crash tests were performed in accordance with NCHRP Report 350 [23]; three of the test configurations did not satisfy the NCHRP criteria. Plaxico et al. [24] performed a full-scale crash test on a W-beam guardrail system and also performed a non-linear finite element analysis using LS-DYNA; here, the guardrails were found to meet the requirements of NCHRP 350. Gabauer et al. [25] investigated the crash performance of longitudinal barriers with minor damage using pendulum tests. The authors tested systems with five different types of typical damage seen in existing guardrail systems, and found that vertical tears in the guardrail posed a significant threat to the structural performance of the system. Bligh et al. [26] performed a full-scale crash test on a 31-inch W-beam guardrail with standard offset blocks. The AASHTO Manual for Assessing Safety Hardware (MASH) criteria [27] was used to perform the crash test; the elevated post design met all safety criteria. Abu-Odeh et al. [28] reviewed full-scale crash test reports performed at a number of accredited testing facilities; fifty-three different guardrail configurations and corresponding test results were examined and tabulated. Schrum et al. [29] performed two full-scale crash tests on the non-blocked Midwest Guardrail System (MGS) in accordance with MASH criteria; the system was shown to meet MASH requirements.

Some studies have focused more on soil behavior and its interaction with the guardrail post. Dewey et al. [30] studied the soil-structure interaction behavior of highway guardrail posts. Although the models used in this study were much simpler than the sophisticated continuum models utilized in the current research, this work emphasized the importance of soil modeling for the guardrail system.

Ferdous et al. [31] identified performance limits of commonly used barriers in terms of acceptable vehicle impact using non-linear finite element methodology. In this study, the soil was modeled with a Joint-Rock material [32] model. This model cannot capture the soil behavior because it was designed for rocks with joints. The LS-DYNA user's manual [32] recommends using the Mohr-Coulomb material model instead to model soils.

Rohde et al. [33] discussed the instrumentation required to determine guardrail-soil interaction in bogie vehicle testing. Plaxico et al. [14] performed finite element modeling of guardrail timber posts and the post soil interaction. In this study, the post-soil interaction was modeled using the subgrade reaction approach, which involved an array of nonlinear springs attached along the length of the post below grade.

Wu et al. [34] studied the interaction between a guardrail post and soil during quasi-static and dynamic bogie vehicle testing. This study used static testing to inform dynamic testing. According to the measurement data, the dynamic resistance of the soil in the bogie vehicle testing was approximately twice the quasi-static resistance. Tabiei and Wu [31,32] performed finite element simulation of a strong W-beam guardrail post to be used in full-

scale crash test simulations using a Eulerian formulation to model the soil media as part of the overall system [35].

1.2.2 Simulation and Testing of Guardrail Systems with Mow Strips

Research performed by the Texas Transportation Institute (TTI) investigating the impact of mow strips on the performance of guardrail systems [3] was the basis for the Roadside Design Guide's adoption of the guardrail post installation detail incorporating grout leave-outs. The researchers examined the performance of guardrail/mow strip systems using experimental testing and numerical simulation. Mow strip dimensions, materials, and depths were considered, in addition to the presence of leave-out sections around posts. Seventeen configurations of wood and steel guardrail posts embedded in various mow strip systems, providing various confinement conditions, were subjected to dynamic impact testing with a bogie vehicle. The dynamic impact tests were numerically simulated, and complete mow strip and guardrail system models were assembled using the subcomponent models. Based on predictive numerical simulations, a concrete mow strip with a grout-filled leave-out was selected for full-scale crash testing in accordance with NCHRP 350 criteria. Crash tests of a steel post guardrail system and wood post guardrail system encased in the chosen mow strip configuration were deemed successful. Of primary interest to this project were the subcomponent dynamic tests involving post installations which included an asphalt mow strip.

Further research on the performance of guardrail systems with concrete mow strips was presented in 2009 by Dusty et al. [36]. This work focused primarily on alternative materials used in the post leave-outs: two-part urethane foam, two types of molded rubber mat, and a precast concrete wedge. The alternative configurations were evaluated using the bogie vehicle employed in the previous study. The authors asserted that three of the four alternative leave-out materials demonstrated satisfactory performance when compared to a post with no mow strip installed.

One important facet of this previous body of work [3] is the lack of distinct objective criteria in the assessment process for each guardrail installation method. Post rotation and translation versus deformation were observed, but not measured or recorded. Further, some installation methods were deemed unsatisfactory because they did not prevent the bogie vehicle from "…sliding up and over the posts…" [3]. However, no specific criteria were presented for what constituted a post failure in this manner. In both studies, peak accelerations were recorded and submitted for each test, but no threshold value was offered except for the baseline response without a mow strip. Tests performed relating to direct encasement of the posts used asphalt thicknesses of four and eight inches, the latter of which is significantly higher than what is typically used in Georgia.

In addition, in the finite element models developed in these studies:

- Soil plowing and strain softening were not modeled, which precludes the prediction of large deformation regimes on the post after the peak of the load-displacement curve.
- The gravity load was not applied to the soil using dynamic relaxation. This is necessary to accurately simulate the behavior of the soil media under dynamic loads. When gravity load is applied, dynamic relaxation should be used at the beginning of the simulation to avoid oscillations in the results due to the gravity loading.
- Rupture of the asphalt layer was not modeled. The behavior of guardrail posts embedded in an asphalt layer generally involves a rupture of the asphalt.
- The dependency of the asphalt strength on the pressure component of the stresses $p = (\sigma_1 + \sigma_2 + \sigma_3) / 3$ was not considered.

1.3 Benefits and Significance of This Research

The first aim of this research is to identify cost-effective installation methodologies for steel guardrail systems with asphalt mow strips. This effort addresses a specific concern regarding current guardrail installation procedures' compliance with guidelines found in the Roadside Design Guide. The preferred installation method is considered to be one that is more economical and allows for better quality control during the construction process; in contrast, using a leave-out for posts in vegetation barriers is seen as less desirable because of significantly higher expected costs for new construction and repairs, variability

in the placement and spacing of posts, and the need for multi-phase construction scheduling.

The FE modeling and simulation approach developed in this research can be used by other researchers to accurately simulate a guardrail system's response embedded in soil only or with asphalt mow strips. Moreover, the FE simulation method used to capture the interaction between the guardrail posts and the soil and asphalt can be applied to piles embedded in soil and a stiff ground layer.

The failure mechanism that is studied here for asphalt can be adopted for rock or other pressure-dependent materials surrounding guardrail posts or piles. The developed predictive equations can be used to obtain an estimate of asphalt mow strip strength and rigidity. The constructed p-y curves in this research can be used to estimate the system performance using simple software such as Excel; it can also be applied to sophisticated simulations of full-scale crash testing. The methodology employed herein to develop the predictive equations or the p-y curves can be adopted for other pressure-dependent materials.

1.4 Organization of the Thesis

Chapter 2 provides a detailed explanation of static finite element modeling of guardrail systems with mow strips. The details required to make an accurate finite element model are given, including: the model domain; the boundary conditions; the element formulations; the mesh sensitivity analysis; the hourglass controls; the correct application

of gravity loading with dynamic relaxation; the proper material models used for the asphalt, soil, and steel; the capturing of asphalt rupture using element erosion in LS-DYNA; the appropriate contact definitions between different parts; the appropriate domain size to model the soil and asphalt; and the necessity of modeling the pseudo-static loading with an explicit integration. The process used to calibrate, verify, and validate the finite element models are also presented.

Chapter 3 presents parametric studies that use the validated finite element models to vary the asphalt mow strip material and geometric properties in order to investigate their effects on the system performance. A set of alternatives for guardrail post installation is identified; then, a series of static finite element simulations are performed to evaluate the structural performance of posts installed using these alternatives. The results of these simulations are presented, and the system behavior is compared with the behavior of a guardrail post with leave-out in order to identify more promising setups with acceptable ground restraint. Three particular representative parameters are checked to compare the behavior of the systems: the maximum longitudinal strain in the post; the ground displacement of the posts associated with a reference amount of work done on the system [37]; and the peak force applied to the post. The response of the guardrail posts using these criteria is plotted in contours to check which setups show less ground restraint than the setups with leave-out.

Chapter 4 provides a detailed explanation of dynamic finite element modeling of guardrail systems with mow strips. Details required to make an accurate finite element

model of the guardrail post system are provided, including: element formulations and mesh sensitivity analysis; hourglass controls; proper material models used for the asphalt, soil, a foam programmer, and steel; and appropriate contact definitions between different parts in the system. The material properties of the foam programmer and steel are incorporated to account for strain rate effects. The process used to calibrate, verify, and validate the finite element models are presented. Comparisons are made between the finite element simulation results and experimental results [9]. The verified and calibrated numbers used in different materials and parts of the model are provided.

Chapter 5 includes dynamic subcomponent simulation of guardrail post systems. Parametric studies are performed using the validated finite element models by varying the asphalt mow strip material and geometric properties to investigate their effects on the system performance. A set of alternatives for guardrail post installation is identified; then, a series of dynamic finite element simulations are performed in order to evaluate the structural performance of posts installed using these alternatives. The results of these simulations are presented, and the system behavior is compared with the behavior of a guardrail post with leave-out to identify more promising setups with acceptable ground restraint. The peak force applied to the post, the maximum displacement of the post at the impact point, the ground displacement of the post, and the effective applied force to the post are all recorded and compared against a leave-out system. This procedure allows for determining which setups have a lower ground restraint than the leave-out system.

Chapter 6 includes full-scale crash simulation and analysis of guardrail systems with various mow strip designs. Each design is simulated based on the MASH guidelines. The occupant risk measurements and structural adequacy of the system are evaluated for each case based on MASH criteria. The results are compared for different mow strip geometries and mow strips with various material properties.

Simplified analytical solutions are presented in Chapter 7 to estimate the strength of asphalt mow strips using Mohr-Coulomb parameters, including cohesion and friction angle. To enhance the analytical solutions, numerical simulations are performed and correlated with results from experiments. The simulation results, along with simplified analytical solutions, are used to provide predictive equations for the mow strip strength and stiffness as a function of friction angle, cohesion, modulus of elasticity, and the rear distance of mow strips. These predictive equations are utilized to construct p-y curves for the unit thickness of asphalt layers with various rear distances and material properties. The p-y curves are employed to efficiently model asphalt mow strips using nonlinear uncoupled springs.

Concluding remarks are presented in Chapter 8.

CHAPTER 2. STATIC FINITE ELEMENT MODELING OF GUARDRAIL SYSTEMS WITH ASPHALT MOW STRIPS

Experimental static tests are often considerably cheaper than dynamic tests. Therefore, predicting the dynamic response using static tests can considerably decrease the testing costs. Static tests were initially employed in this research on a more comprehensive set of mow strip parameters in order to focus the dynamic tests. A description of the static finite element model is presented in this chapter.

2.1 Overview of Modelling Techniques

The interactions between the soil, asphalt, and post play a vital role in the response of the system during loading. These interactions can be investigated by first considering the post to be a specialized form of a laterally loaded pile. There are various techniques for solving laterally loaded pile problems. These approaches include: (1) the finite element approach, in which the post is embedded in a soil continuum of solid finite elements, and (2) the subgrade reaction approach, in which the post is supported by a series of uncoupled springs, which are defined using nonlinear p-y curves. The subgrade reaction method is used widely because of the high computational costs associated with 3D finite element modeling of the soil around the guardrail post. With recent advances in computing speeds, researchers have attempted to model the post-soil interaction using the finite element method. With this approach, models of the post are constructed, with the post embedded in a continuum of soil modeled using three-dimensional solid elements. Simulations of

physical responses using 3D finite element analysis (FEA) can be readily produced, and the availability of sophisticated FEA tools provides substantial promise for detailed numerical studies to address outstanding questions of the post-soil behavior. However, the quality of the results from simulations depends on several factors including:

- accurate representation of geometric details, initial condition, and boundary conditions;
- constitutive relationships for the various materials such as loss of strength in the soil and asphalt under large strains, asphalt material properties, and the rupture of asphalt; and
- the contact conditions between various components, such as the contact between the soil and the post and the contact between the asphalt layer and the soil.

This approach does not consider the granular matter of soil and crushing of soil grains under dynamic loading, which can only be captured accurately using other methods such as discrete element approach [[38]–[40]].

Three-dimensional FEA was utilized in this research to calculate the response of a guardrail post subjected to static loading. The model presented in this dissertation was developed by selecting material constants based on commonly accepted values, testing materials, and calibrating based on the system testing. Once the model was calibrated at the system level, the material properties and other model parameters (e.g., loading rate, contacts, etc.) were kept constant. The performance and accuracy of the model were

evaluated by comparing results from the model with further experimental tests before independently using it to conduct parametric studies.

2.2 Finite Element Model Description

2.2.1 Model Domain and Boundary Conditions

LS-DYNA V971 R9.1.0 [41] was used in this research. The model developed in this chapter was updated to incorporate effects associated with dynamic impact loading, as discussed in Chapter 4. This model was also utilized to perform the full-scale crash simulations discussed in Chapter 6. The quasi-static problem was solved by using an explicit algorithm, rather than an implicit one, as optimizing the model for implicit integration was not useful. Moreover, the Mohr-Coulomb material model in LS-DYNA, which is used to model soil and asphalt, does not support an implicit solution algorithm for analysis at large strains, and the contact algorithms are less robust with implicit time integration.

The soil domain considered in the model is a rectangular prism. The bottom boundary of the prism was fixed at depth (z-direction) of 2 m, which is approximately twice the embedment depth. For the lateral boundaries, there were three options to use: free, rigid, or non-reflecting boundary conditions. The lateral boundaries were placed far enough from the post that the displacements and change in stresses at the boundaries were negligible. Therefore, the response was insensitive to the lateral boundary assumptions. For the

pseudo-static loading employed in this chapter, the non-reflecting boundary conditions were effectively the same as the free boundary conditions. Therefore, using any of these three boundary conditions gave similar results. However, because explicit integration was employed, using a non-reflecting boundary decreased noise in the system response, and so the lateral soil boundary was modeled using non-reflecting boundary conditions.

Three different criteria were used to determine the size of the prism within the plan of the problem in order to avoid boundary effects:

1. The size of the prism in the plan was increased, and the force-displacement curve for the post was monitored. The results showed that the boundary effects on the post's response vanished when the planar size of the soil was larger than 4 m, and the force-displacement curve was effectively unchanged when using greater than this size.
2. The nodes on the lateral boundary were initially set free. The size of the prism in the plan was increased until the displacements of the nodes at the boundaries were less than one percent of the ground level displacement of the steel post. Using this approach, the dimension of the prism in the plan was determined to be 5 m. Then, the lateral boundaries were modeled using non-reflecting boundary conditions.
3. The width of the model (perpendicular to the post's lateral movement) had to be large enough to capture asphalt rupture. The width was increased until the boundaries were far from the end of asphalt rupture and shear stress at the

boundaries was less than 1 percent of the shear stress close to the post. The size of the model in this direction was determined to equal to 10 m.

Therefore, the dimensions of the prism were set as 5 m in the y-direction (parallel to the post's lateral movement) and 10 m in the x-direction (perpendicular to the post's lateral movement). The steel post was a W150x13 member with a total length of 1.83 m and an embedded depth of 1 m [42]. The FE model was comprised of approximately 250,000 solid elements for the soil and asphalt and 1,000 shell elements for the steel post. A representation of the model is shown in Figure 5**.**

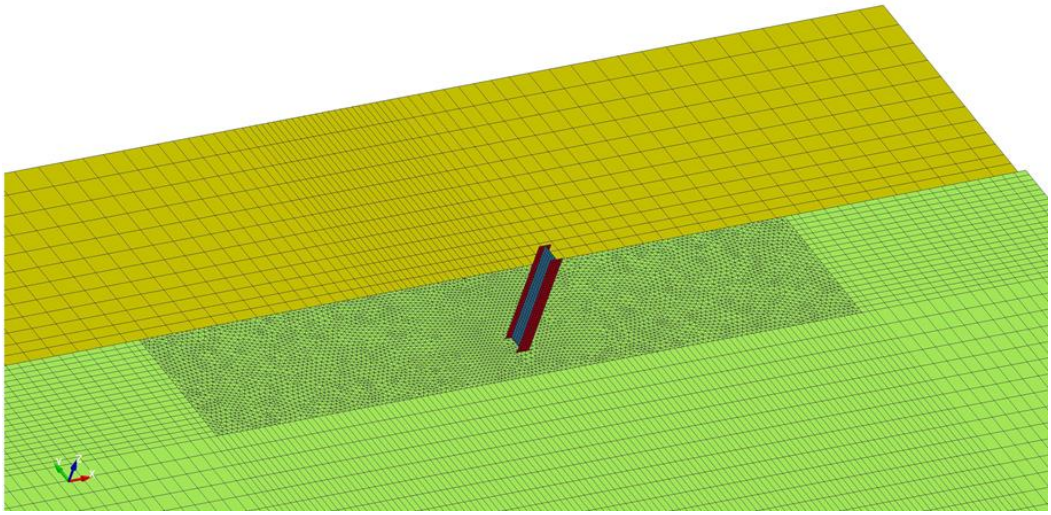

Figure 5. Finite element model of guardrail post, soil, and asphalt system in LS-DYNA.

Other attributes of the finite element mesh and model are discussed below.

2.2.2 Simulation of Lateral Loading

Lateral loading in the static test program was simulated as follows. A transverse displacement was applied to the post at 625 mm above the ground level. Mass scaling was not used, and the rate of displacement of the post was varied between 5,000 mm/s and 25 mm/s. Analysis of the results showed that rates slower than 50 mm/s gave results within 1 percent for all the primary response quantities. Therefore, 50 mm/s was used as the displacement rate of the post to represent quasi-static loading. The kinetic energy of the system was checked and determined to be less than 0.5 percent of the total energy. The simulation time using 6 CPUs at 3.5 GHz was approximately 24 hours; this duration will change if the asphalt geometric parameters such as thickness and rear distance are changed.

2.2.3 Element Formulations and Mesh Sensitivity Analysis

Fully integrated shell elements with nine integration points through the thickness and a uniformly structured mesh with a size of 25 mm were used for the steel post, as shown in Figure 6. Using an element size of 12 mm within the steel post increased the peak force applied to the post by approximately 5% and decreased the ground level displacement by approximately 7%. These changes occurred because using a finer mesh provided greater resolution in capturing local deformation of the post. However, using the finer mesh increased the simulation time by approximately 100%. Thus, the 25 mm element size was considered sufficient. The soil was modeled using structured hexahedral constant stress solid elements. The final mesh size for soil changes, from 25 mm close to the post to 200

mm at locations far from the post (Figure 6). Using a mesh in the soil that was finer than approximately 25 mm caused instability in the model.

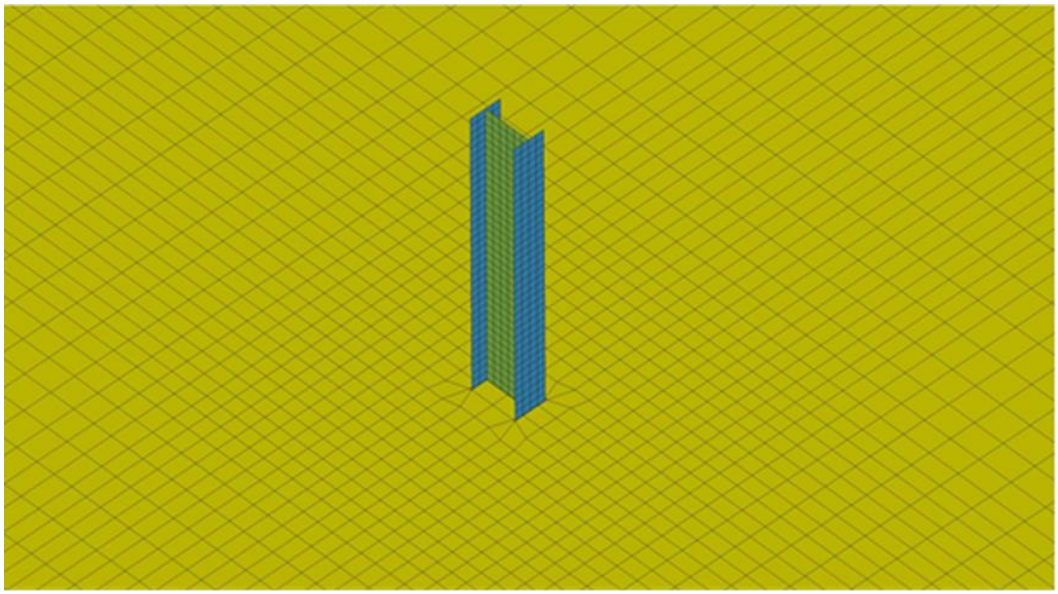

Figure 6. Elements used for soil and the steel post.

2.2.4 Hourglass Controls and Energy Checks

The enhanced assumed strain stiffness form for 3D hexahedral elements hourglass control (number 9) was utilized for the soil elements and the hexahedral mesh part of the asphalt to prevent high hourglass energy during simulations. Hourglass coefficients equal to 0.004 and 0.1 were used for the soil elements and the hexahedral mesh part of the asphalt, respectively. Because of the element type utilized for the steel post and tetrahedral mesh part of the asphalt, these two parts did not have any hourglass energy and did not need an hourglass control. Hourglass energy was monitored and compared with the internal energy.

The hourglass energy in the soil and the hexahedral mesh part of the asphalt were less than 3% of the internal energy, which is acceptable [43].

2.2.5 Post and Soil Interface

Various approaches exist for modeling the interface between the soil and post using a Lagrangian mesh:

1. Nodes from the soil elements are tied to the nodes of the post elements. No contact definition between the post and the soil is necessary when this approach is used. This method assumes infinite friction between the soil and the post, which is not a correct physical representation. This method yields a stiffer behavior than reality and is not recommended.
2. Nodes from the soil elements are not tied to the nodes of the post elements, and eroding contact is used to simulate the soil failure. When elements are eroded based on specific failure criteria, they are removed from calculations in the model and do not have resistance. This model demands a very dense mesh and can yield incorrect results. The failed elements are removed from the analysis, and a gap is created between the soil and the post. Therefore, application of a relatively small force in the axial direction can pull out the post. This behavior is observed even using a friction coefficient larger than one [11].
3. Nodes from the soil elements are not tied to the nodes of the post elements. Automatic surface-to-surface contact, which is explained in more detail below, is

defined between the post and the soil. In this method, the friction between the post and soil has an influence on the behavior [11].

The contact search algorithms utilized by automatic contacts in LS-DYNA make them better suited than older contact types. Moreover, subroutines that check the slave nodes for penetration are used a second time to check the master nodes for penetration through the slave segments in this approach. The definition of the slave surface and the master surface is arbitrary. Therefore, in this study, the contacts between soil and the steel post are modeled using the automatic surface-to-surface contact model. Static and dynamic friction coefficients are set equal to 0.6, which is typical for an interface between the soil (a mixture of gravel, sand, and clay) and a driven smooth steel pile [44]. The segment-based penalty formulation contact algorithm (SOFT 2) in LS-DYNA checks for segments-versus-segments penetration instead of nodes-versus-segments, which are used in default penalty contact formulation. Therefore, it is unlikely for nodes to penetrate undetected as can happen with the standard penalty contact when nodes slip between segments at corners. Because the stiffness of steel is significantly greater than the stiffness of the soil, and because of the edges of the steel post, the segment-based contact is used to avoid contact related problems and element penetration. The thickness of the shell elements used for modeling the steel post is considered with the contact formulation used with the soil around the post (Figure 7) to avoid initial element penetrations.

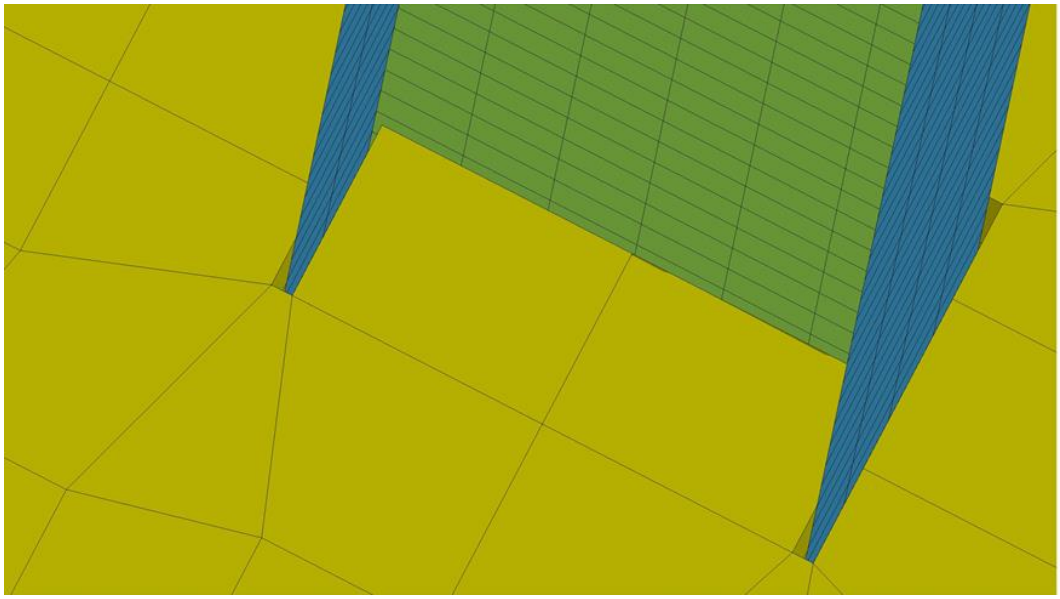

Figure 7. Shell thickness consideration to avoid initial element penetrations.

FRCENG (frictional contact energy), the LS-DYNA parameter for frictional energy, is set to one to enable sliding energy calculations. The frictional energy is important because a portion of the energy during steel post movement in the soil is dissipated by friction. This energy is verified as a positive value; negative sliding energy is an indication of an erroneous sliding condition between two contact surfaces.

2.2.6 Asphalt Interfaces

The interface between the asphalt layer and the soil cannot be modeled as continuous because asphalt is composed of a material with significantly different mechanical properties than soil. In this case, a contact definition needs to be defined between the layers. Automatic surface-to-surface contact was used between the asphalt

layer and the soil. Moreover, the contact between the post and the asphalt was also modeled using the automatic surface-to-surface contact model. The static coefficient of friction for these surfaces was set to a relatively high value of 1.0 to account for the bitumen in the asphalt that is bonded to the soil and steel surface.

However, after this connection breaks and the asphalt layer starts to slip, friction substantially decreases. The kinetic coefficient of friction was assumed negligible and was set equal to zero to avoid large forces at the free edge of the asphalt behind the post. This allowed the asphalt to move easily on the soil as observed in the experiments, and avoided mesh distortions at the edge of the asphalt layer where there was no confining pressure. Segment based (SOFT 2) contact was used on these contact surfaces.

2.2.7 Mesh Treatments for the Asphalt Layer

When the rupture failure pattern propagates in the asphalt, the tip of the rupture moves from the edges of the post toward the sides of the asphalt layer (Figure 9). Therefore, it is not sufficient to refine the mesh only in the local region around the post. The mesh must be refined for the whole area covering the rupture. Therefore, the mesh around the post was composed of small tetrahedral elements, and larger hexahedral elements were used at further distances from the post where rupture was not occurring. Using these larger hexahedral elements reduced computational time significantly and more accurately modeled the rupture conditions via the use of tetrahedral elements.

A tied surface-to-surface contact model was employed in LS-DYNA to tie the surfaces of the different regions to each other in the model. In tied contact types, the slave nodes are constrained to move with the master surface, which enables mesh transition between two different kinds of elements. The nearest master segment for each slave node was located based on an orthogonal projection of the slave node to the master segment. The two meshes for the asphalt were connected to make a continuum of asphalt using the tied surface-to-surface contact model. Figure 9 shows the mesh transition used for the asphalt layer.

Figure 8. Asphalt rupture observed in the experimental program [45]**.**

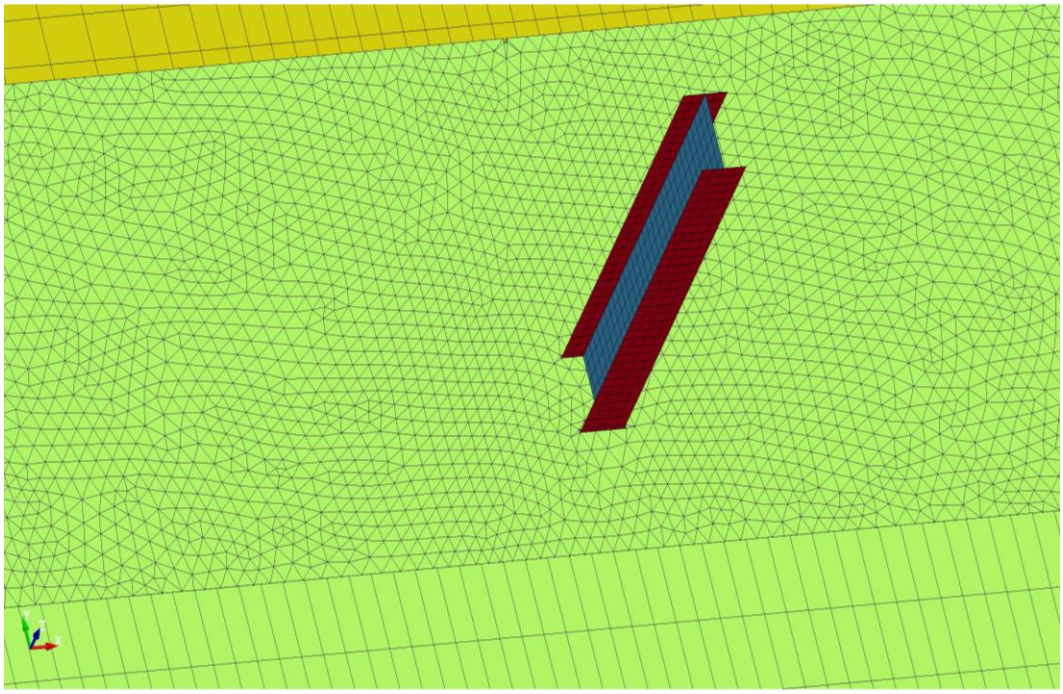

Figure 9. Mesh treatments used for the asphalt layer combining hexahedral and tetrahedral elements.

2.2.8 Importance of Gravity Loading

Soil is a pressure dependent material. Therefore, the soil behavior changes at different depths as the pressure changes with increasing depth. To capture this important aspect, gravity loading must be applied, and stresses must be initialized before the start of the main simulation. This is accomplished by applying a "load body" in the z-direction to all parts of the model. Because applying gravity loading during real-time simulation causes dynamic waves that can contaminate the results, the gravity load was applied in the pseudo-time before the main simulation, using a ramped load to minimize dynamic waves;

dynamic relaxation was utilized in the pseudo-time to dampen the waves caused by applying gravity. After the waves were damped and the material reached a static equilibrium, the main simulation was conducted in real-time. Applying the gravity load also ensured the proper representation of friction forces on the surfaces that are in contact with each other, such as asphalt and soil, which is shown in Figure 10.

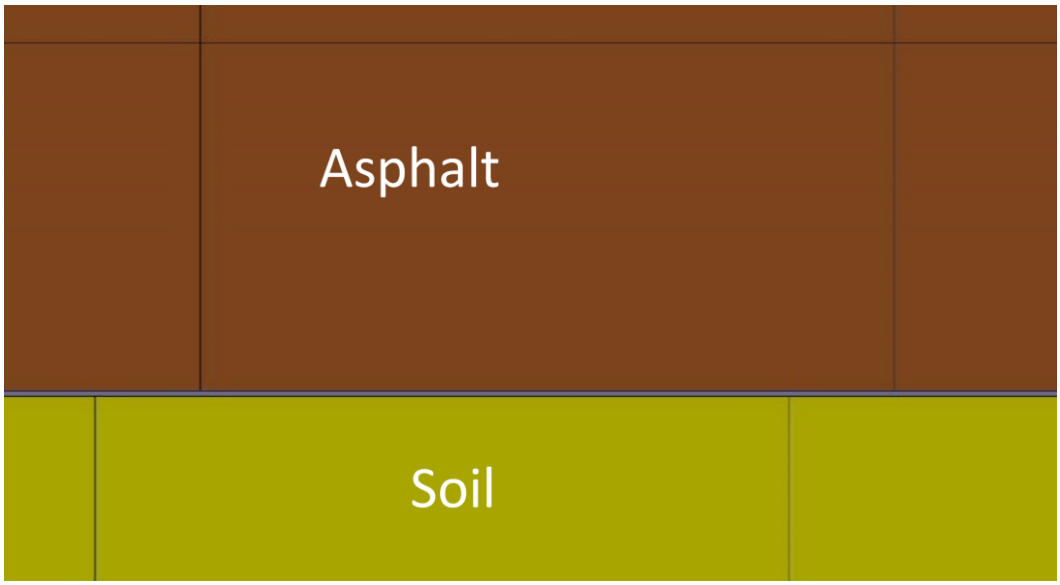

Figure 10. Contact between asphalt and soil.

As can be seen in Figure 11, applying gravity and using dynamic relaxation is critical to modeling the guardrail post system accurately. The figure shows comparisons between experimental results and three variations of simulations: cases with applied gravity and dynamic relaxation; cases with applied gravity without dynamic relaxation; and cases without gravity loading. If the gravity load is applied without a dynamic relaxation phase, large dynamic waves contaminate the result. Moreover, if the gravity loading is not applied

in the model, the soil material shows significantly lower strength and the contact between the soil, the asphalt, and the post does not perform correctly.

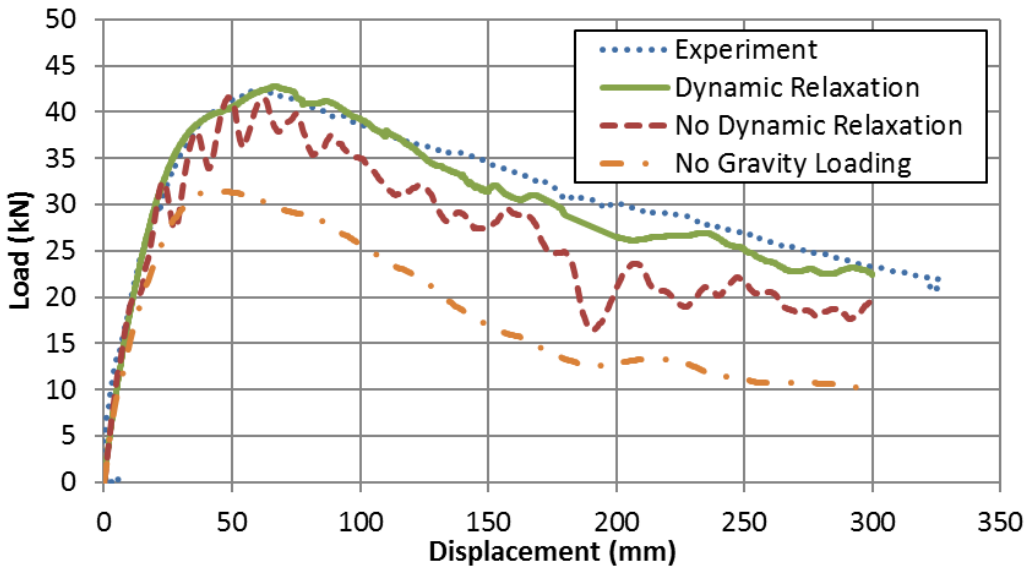

Figure 11. Comparison of the load-displacement curves with and without dynamic relaxation or gravity loading for a post embedded in soil with 90 mm asphalt layer.

2.2.9 Steel

A piecewise linear metal plasticity model was used for the steel post. The yield strength of the steel, modulus of elasticity, and Poisson's ratio were given as inputs using a representative steel stress-strain curve. The common steel parameters presented in Table 1 are employed in this model. Lee [9] obtained experimental stress-strain curves using tension tests on samples from the guardrail posts web and flange in accordance with ASTM E8/E8M [46]. The stress-strain curves utilized in the model for the web and flange are

given in Figure 12. These curves show significant strain hardening in the flanges and the web. Shell element formulation number 16 was selected; this element does not exhibit hourglass modes.

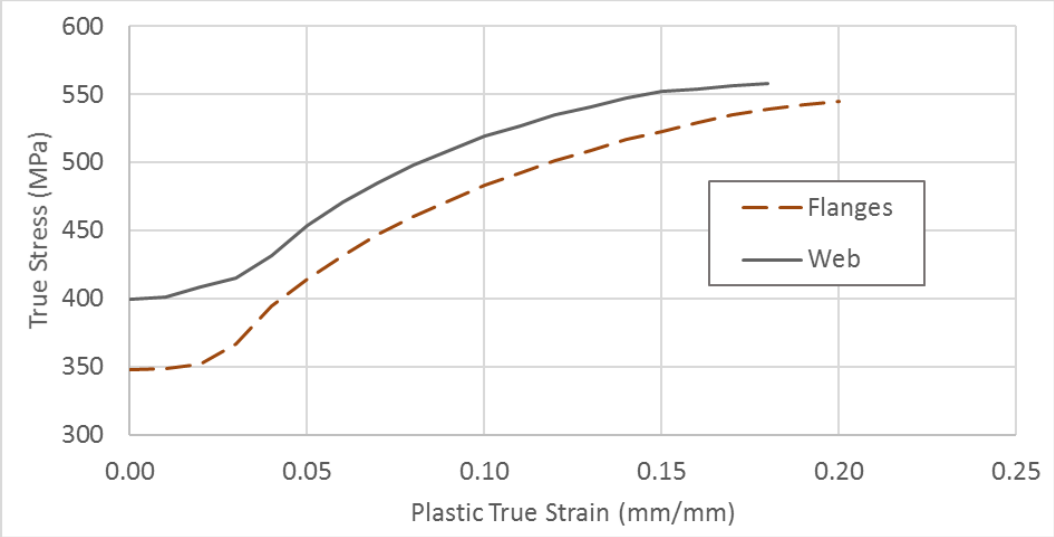

Figure 12. True stress versus true strain curves used in the model for the web and the flanges.

2.2.10 Soil

2.2.10.1 Soil Classification

2.2.10.1.1 Unified Soil Classification System

The Unified Soil Classification System (USCS) uses symbols for the particle size groups. These symbols and their representations are G for gravel, S for sand, M for silt, and C for clay. These are combined with other symbols that express gradation

characteristics: W for well graded and P for poorly graded. USCS is used to classify the compacted soil that is deposited around the guardrail post.

Grain size distribution was obtained using a laboratory sieve test. Forty-seven percent of the grains passed through sieve #4; therefore, the soil was gravel. Next, it was necessary to understand if the soil is poorly graded or well graded. From the grain size distribution, the sieve opening size that 10% of the soil sample mass passed through was defined as D_{10}; the sieve opening size that 30% of the soil sample mass passed through was defined as D_{30}; the sieve opening size that 60% of the soil sample mass passed through was defined as D_{60}. These were equal to 0.093 mm, 0.81 mm, and 9.5 mm respectively. Using these values, the coefficient of uniformity and coefficient of curvature were computed as 102.15 and 0.75, respectively [44]. The soil was considered poorly graded because the coefficient of curvature is less than one. There were 8% fine grains (that is, grains that pass through sieve #200) in the soil sample. The fine grains were assumed to be silt (M), so the soil was graded as GP-GM. Moreover, 40% of the soil mass was sand and, therefore, the soil was classified as "poorly graded gravel with silt and sand".

2.2.10.1.2 AASHTO Soil Classification System

The AASHTO soil classification system is used to determine the suitability of soils for earthworks, embankments, and roadbed materials (subgrade: natural material below a constructed pavement; subbase: a layer of soil above the subgrade; and base: a layer of soil above the subbase). According to the grain size distribution, 37% of the soil mass passed through sieve #10, 25% passed through sieve #40, and 8% passed through sieve #200. The

AASHTO soil classification system graded the soil as A-1-a, which is the best rating for soils being used as a subgrade. The soil name is “Stone Fragments, Gravel, and Sand.”

Table 1. Material constants used in the static finite element models.

Material	Constitutive Parameter	Value	Determined from
Steel	Density, ρ	7930 kg/m3	Material test
	Young modulus, E	200 GPa	[3]
	Poisson's ratio, ν	0.3	[3]
	Yield Strength for flanges, σ_{yf}	348 MPa	Material test
	Yield Strength for the web, σ_{yw}	400 MPa	Material test
Soil	Density, ρ	2300 kg/m3	Material test
	Cohesion, c	13 kPa	Material test and via system test calibration[a]
	Peak friction angle, ϕ'_p	45^o	Material test and via system test calibration[a]
	Critical friction angle, ϕ'_{cr}	15^o	[1] and via system test calibration[a]
	Shear modulus, G	50 MPa	[47] and via system test calibration[a]
	Poisson’s ratio, ν	0.25	[48]
Asphalt	Density, ρ	2300 kg/m3	Material test
	Cohesion, c	500 kPa	Material test
	Friction angle, ϕ'	35°	[49]
	Shear modulus, G	50 MPa	Via system test calibration[a]
	Poisson's ratio, ν	0.35	[50]
	Maximum principal stress, σ_{Max}	680 kPa	$\sigma_{Max} = 0.95c/\tan(\phi')$
	Maximum principal strain, ε_{Max}	0.07	Via system test calibration[a]

a. The term “system test calibration” refers to the selection of particular material constants based on one selected system test as described above.

After determining the soil type based on grain size distribution, the typical range of mechanical properties of soil can be obtained in order to verify the numbers obtained from FEA calibration.

2.2.10.2 Yield Surface

Different material models are available in LS-DYNA for modeling soil; these were examined to find the most appropriate for modeling soil in this research. Lewis [51] provides a discussion of available materials in LS-DYNA that are suitable for soil. From these materials, soil and foam (material number 5), soil and foam with failure (material number 14), Mohr-Coulomb (material number 173), Drucker-Prager (material number 193), and FHWA (material number 147) soil material models were selected to be evaluated in this research. The FHWA material model manual [51] and the verification of the model with experimental results [52] were reviewed. The FHWA soil model captures damage evolution, strain softening, pore water pressure effects, strain rate effects, and moisture content effects. The model has numerous parameters, some of which cannot be determined from experiments. Additionally, this study is not focused on the influences of soil parameters such as pore water pressure and moisture content effect. Therefore, the research team selected a simpler material model.

After performing the simulations with the various relevant material models, the soil and foam model and Mohr-Coulomb model both proved to be stable under the desired displacement for the current problem. An extensive investigation was conducted to determine the more appropriate of these two for this application. In general, the soil and foam material model is easier to work with; it only has three constitutive parameters for the yield surface and one parameter for pressure cut off. It is also possible to give a volumetric strain versus stress curve as an input. This model is stable for large displacements and low confining pressures; however, the yield surface is smooth, and the material model does not capture the difference in the soil behavior under extension and compression. Many experiments in the past have proven that soil behaves differently under extension and compression [53]. Therefore, the Mohr-Coulomb model is employed to capture this behavior. The Mohr-Coulomb failure criterion represents a linear envelope that is obtained from a relation between the shear strength of a material and the applied normal stress. The failure criterion is written as

$$\tau = \sigma tan(\phi) + c \quad (1)$$

where τ is the shear strength, σ is the normal stress, c is cohesion or the intercept of the failure envelope with the axis, and ϕ is the angle of the internal friction or the slope of the failure envelope.

2.2.10.3 Soil Calibration

A model without an asphalt mow strip was created to calibrate the soil material properties based on a system-level static experiment [37] without an asphalt layer. The contact forces between the post and the soil in the y-direction were calculated to determine the applied force versus displacement curve for the post. The density of the soil was determined to be 2,300 kg/m^3 by conducting a laboratory test on a soil sample. This value was used as the soil density in the model. Lee [9] conducted experimental direct shear tests in accordance with ASTM D3080 [54] on soil samples. Cohesion and peak friction angle were estimated equal to 32 kPa and 51 degrees, respectively. These values were initially used in the model, which was subsequently calibrated to capture the peak applied force and the displacement at which the peak force occurs in the load-displacement response of the system. Values of 13 kPa and 45 degrees were found for the cohesion and peak friction angle, respectively, which are within the range of recommended values for gravel with silt and sand used as subbase material ([30], [1], [55]). The small value of *C* was expected for a coarse grain soil since *C* represents the apparent soil cohesion that is typically associated with strength due to suction in fine grain soils. The peak friction angle in dense soils with coarse grains is usually higher than the critical friction angle, due to dilation. To account for dilation and the change of friction angle, a trilinear curve was specified to define the friction angle of the Mohr-Coulomb material model as a function of the effective plastic strain. The friction angle equaled 45 degrees for plastic strain values less than 0.4 and linearly decreased to 0.15 between the plastic strains of 0.4 and 0.5. For plastic strains greater than 0.5, the friction angle equaled 15 degrees. A standard value of 0.25 that is

typical for the mixture of gravel, coarse sand, and silt was used for the Poisson's ratio [48]. The initial linear elastic portion of the load-displacement curve was used to estimate the shear modulus as 50 MPa, which is within the common range of values for the soil type used in this research [47]. The soil material constants and the determination procedures are summarized in Table 1. An example of the soil deformation using the model for a 300 mm translation at the load level is shown in Figure 13. A force-displacement comparison between the calibrated finite element model and the experiment done by Lee [37] is given in Figure 14.

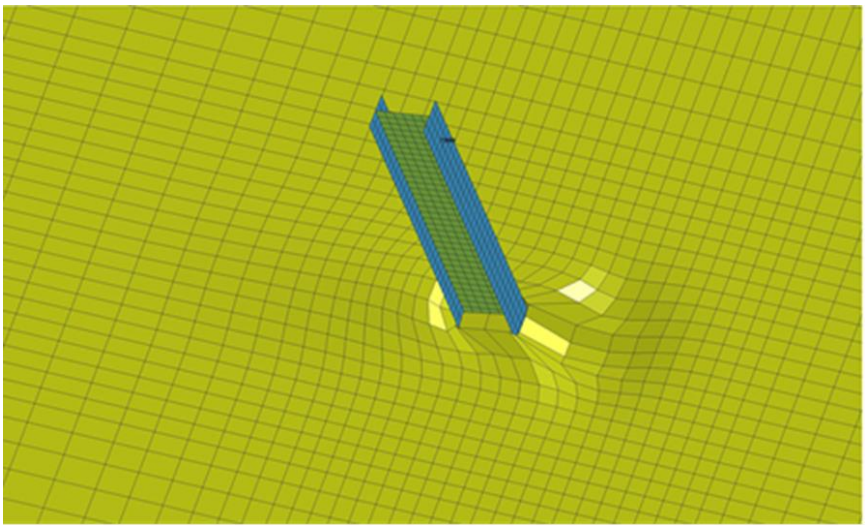

Figure 13. Soil deformation for 300 mm translation at load level.

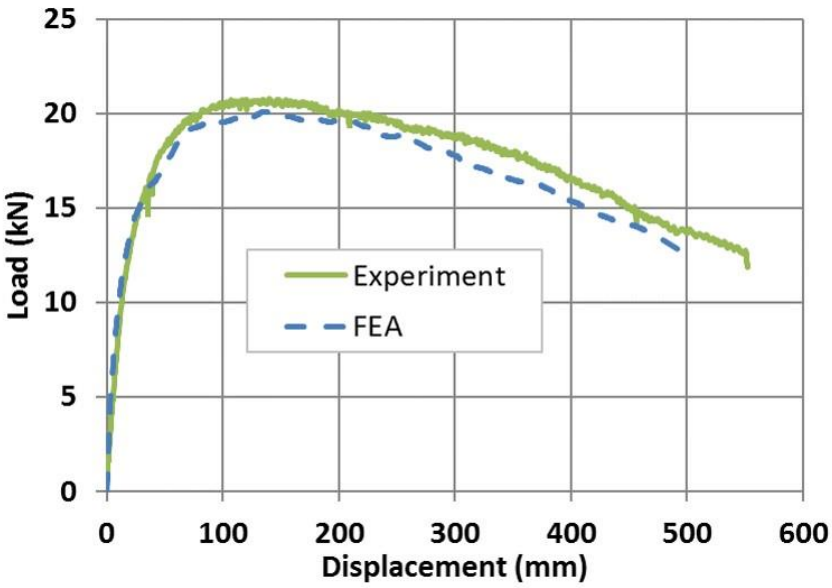

Figure 14. Comparison between FEA and experiment [37] **without an asphalt layer.**

2.2.11 Asphalt

2.2.11.1 Asphalt Calibration

The same type of hot-mixed asphalt (HMA), classified as PG 76-22 binder and 19 mm aggregate size, was installed as a mow strip for each test. Georgia Department of Transportation (GDOT) recommended this type of HMA for use in the testing program because it is one of the more commonly used paving materials in the state of Georgia. When the asphalt is loaded, part of its deformation comes from viscous behavior. To account for this, the shear modulus of the material was lowered to consider the viscous deformation effects under quasi-static loading. The Mohr-Coulomb material model is widely used to model asphalt, and this material model was chosen to model the shear

strength of the asphalt. In this study, the density of the asphalt was estimated to be equal 2,300 kg/m^3 from laboratory tests. The Poisson's ratio and friction angle of the asphalt were specified as 0.35 and 35 degrees, respectively, which are typical values for asphalt ([49], [50]). Lee [9] estimated the cohesion of the 118-day old asphalt at a temperature of 20^o C, using experimental unconfined compression tests on asphalt specimens to be equal to 0.5 MPa, which is used in the model.

The tensile rupture in the asphalt was modeled using element erosion. Element erosion was implemented in this research using the general erosion criteria for solid elements in LS-DYNA. Each criterion was applied independently, and satisfaction of one or more criteria caused deletion of an element from the calculation. The erosion criteria for element removal can be user-specified. The maximum principal stress criterion was initially used in this research to eliminate the elements when the tensile failure criterion was met. However, the rupture in the asphalt was abrupt when this sole criterion was used, and the strength decreased dramatically, similar to what is commonly observed in very brittle materials. To account for the fact that asphalt can accommodate larger strains before failing under tensile stress, a maximum principal strain failure criterion was added to the material model. Therefore, an element was removed when both the maximum principal stress criterion and the principal strain criteria were satisfied as follows:

1. $\sigma_1 \geq \sigma_{Max}$, where σ_{Max} is the failure principal stress and σ_1 is the current maximum principal stress.

2. $\varepsilon_1 \geq \varepsilon_{Max}$, where ε_{Max} is the failure principal strain and ε_1 is the current maximum principal strain.

The maximum principal stress at failure can be obtained using Mohr-Coulomb yield criterion as $0.95C/\tan(\phi') = 680$ kPa. A reduction factor of 0.95 was chosen to facilitate proper element erosion. Without the reduction factor, the maximum principal stress may not reach the failure value because the stress state is limited in the Mohr-Coulomb yield criterion. By calibrating the post-peak response of the system, the maximum principal strain at failure was obtained as 0.07.

For the asphalt, the mesh around the post was composed of unstructured tetrahedral elements with one-point integration to better capture asphalt rupture propagation and element erosion. The average size of the mesh was approximately 25 mm. The principal strain at failure, which is used for asphalt element erosion, is mesh-size dependent. The rupture propagates faster with a finer mesh and slower with a coarser mesh. Using a much coarser or much finer mesh (as large as two times coarser or finer) for this part of the asphalt requires a different value for the principal strain at failure, which requires additional calibration. The cohesion value for soil was increased to 13 kPa to account for the additional compaction and moisture of the soil when an asphalt layer is present. A comparison between the results obtained from the FEA simulation and the experiment done by Lee [9] is given in Section 2.3. The model calibration was conducted for one experiment (90 mm asphalt), and these parameters were kept constant for all parametric studies on

mow strip geometry. The asphalt's material constants and determination method are summarized in Table 1. In the table, the term "system test calibration" refers to the selection of particular material constants based on one selected system test as described above.

2.3 Comparisons between Experiments and FE Simulations

Lee [9] conducted five experiments with an asphalt layer. The results of these experiments were compared with finite element simulations. System behavior after loading from one static experiment (90 mm asphalt layer) FEA with asphalt modeled as discussed above, and FEA with asphalt modeled as rigid are shown in Figure 15. The corresponding force-displacement plots are provided in Figure 16. These results indicate that the material model chosen for the asphalt has a significant effect on the prediction of the system performance, and the utilization of a rigid model significantly overestimates the ground level restraint. Numerical results from the remaining experiments and finite element simulations with the calibrated Mohr-Coulomb asphalt model are summarized in Table 2. The model is capable of predicting the peak force and maximum ground displacement within 15 percent, with most predictions within 10% compared to experimental results.

Table 2. Comparison of experimental [9] **and FEA results.**

Test	Thickness	Rear Distance	Peak Force	Max Ground Displacement

No.	(mm)	(mm)	Exp. (kN)	FEA (kN)	Var. %	Exp. (mm)	FEA (mm)	Var. %
1	50	600	38.6	37.5	2.8	110	117	6.4
2	90	600	42.5	41.7	1.9	97	90	7.2
3	50	150	28.9	26.3	8.9	150	155	3.3
4	50	300	33.1	29.9	9.6	129	149	15.5
5	90	300	40.7	34.5	15.2	-[a]	146	-[a]

a. Not available due to gauge malfunction.

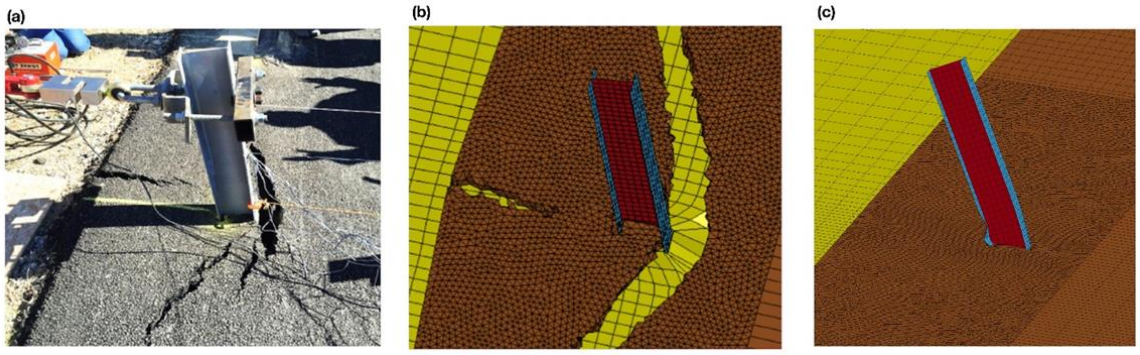

Figure 15. System condition after static loading on a post with a 90 mm asphalt layer [45]**: (a) experiment; (b) FEA with Mohr-Coulomb asphalt model; (c) FEA with a rigid asphalt model.**

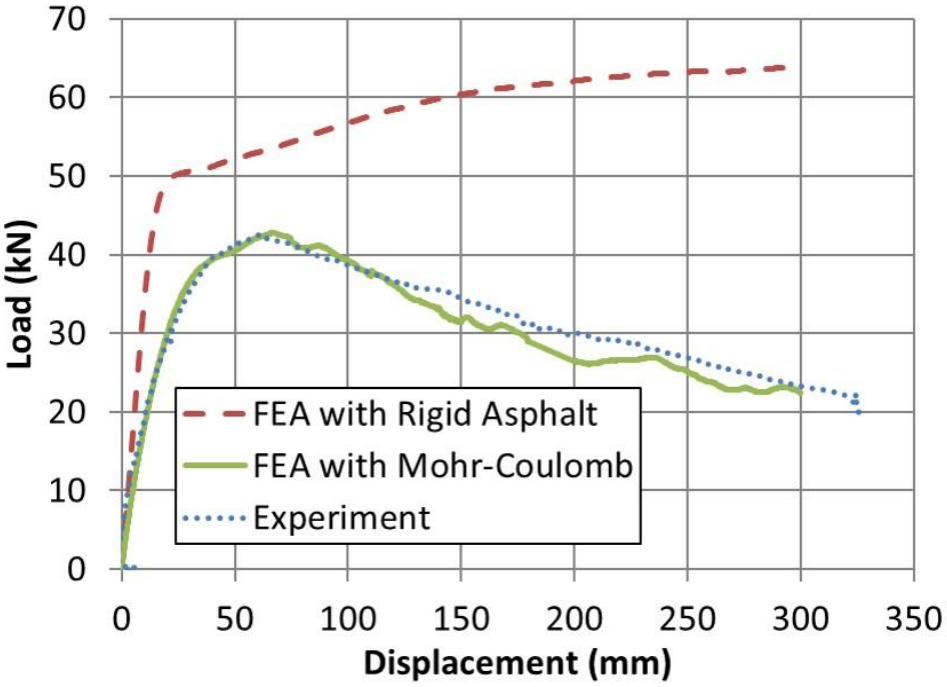

Figure 16. Force-displacement comparison between experimental results [9]**: FEA with Mohr-Coulomb asphalt model and FEA with rigid asphalt model for a post embedded in a 90 mm asphalt layer.**

Strain gauges were used to record strain values along the post in the experiments. Similarly, the strains were obtained by reading strain values of elements along the post in the FE simulations. The results for 50 mm thick asphalt and 90 mm thick asphalt setups are compared in Figure 17 andFigure 18. The strain values in these two figures were measured at the time of the peak force in the system. As can be seen in these figures, the FEA closely predicts the strain values for the case with 90 mm thick asphalt and underestimates strains for the case with 50 mm thick asphalt.

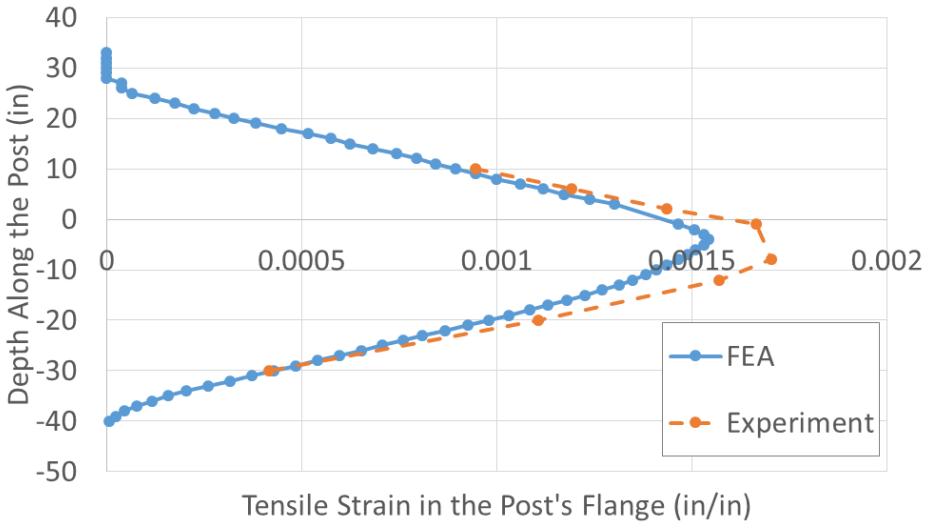

Figure 17. Comparison between FEA and experimental measurements of the tensile strain in the post for the case with 50 mm thick asphalt and rear distance of 600 mm. 1 inch is equal to 25.4 mm.

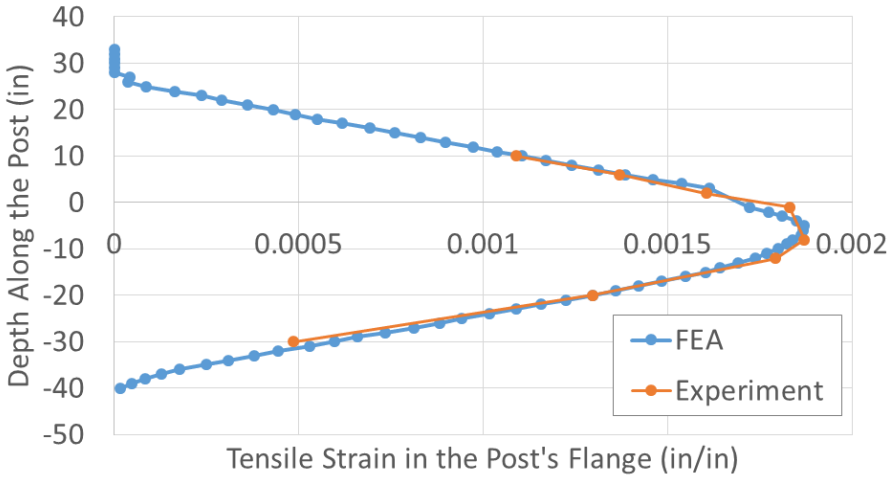

Figure 18. Comparison between FEA and experimental measurements of the tensile strain in the post for the case with 90 mm thick asphalt and rear distance of 600 mm. 1 inch is equal to 25.4 mm.

CHAPTER 3. STATIC PERFORMANCE OF GUARDRAIL SYSTEMS WITH ASPHALT MOW STRIPS

3.1 Alternative Mow Strip Designs

A workshop with Georgia Department of Transportation personnel was held to discuss alternative design and installation strategies for guardrail systems with asphalt mow strips. Five alternative design strategies were identified and prioritized to decrease the ground level stiffness of guardrail posts installed in asphalt mow strips:

1. limit the maximum rear distance and thickness of the asphalt layer;
2. pre-cut the asphalt mow strip behind the post;
3. use a tapered mow strip;
4. make a cutout portion in the mow strip behind the post; and
5. replace the asphalt with gravel to prevent vegetation growth.

After consideration of constructability and potential maintenance issues, options (1) and (2) were selected for further investigation; they are explained in this section.

The common asphalt thickness used for mow strips in the state of Georgia is 3.5” (90 mm); the minimum feasible asphalt thickness considering the constructability is 2” (50 mm), as shown in Figure 19. This minimum thickness is based on the aggregate size, construction equipment, and the goal that the asphalt mow strip will avoid vegetation growth (an asphalt layer that is too thin cannot avoid vegetation growth).

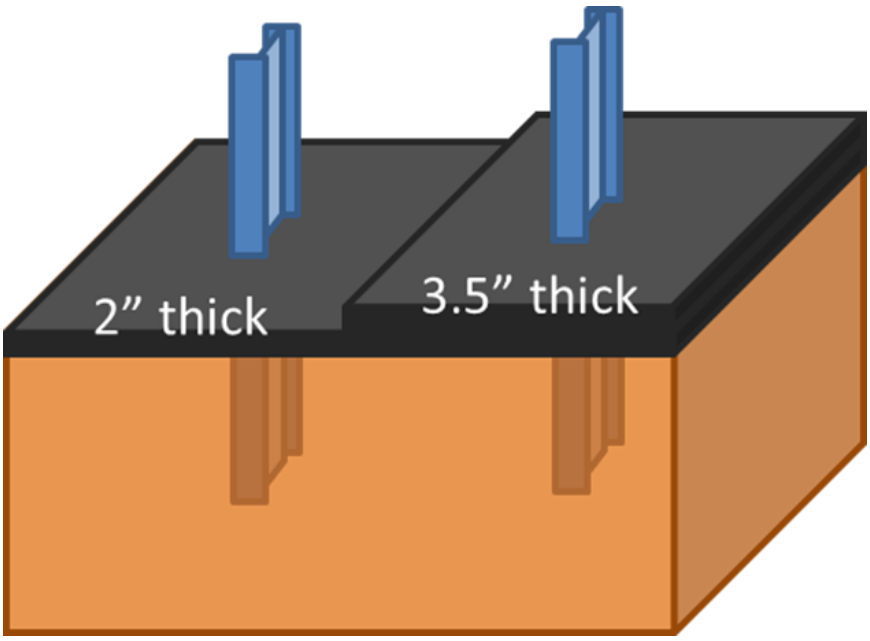

Figure 19. Guardrail post setups with 2 in (50 mm) and 3.5 in (90 mm) thickness.

Three rear distance values equal to 0.5 ft (150 mm), 1 ft (300 mm), and 2 ft (600 mm) are shown in Figure 20. These values range from the minimum value (based on avoiding vegetation growth) and the maximum value (based on the fact that the width of the asphalt behind the post should be limited to minimize the construction cost). A combination of different thicknesses and rear distances was used to study the effect of each of these parameters on the system performance.

Based on the experimental results, rupture is the primary form of the asphalt failure. As the rupture extends in the asphalt, the strength of the asphalt layer decreases up to the point that one part of the asphalt detaches from the rest of the mow strip. After this point,

asphalt has little to no impact on the system, and the soil becomes the only source of ground strength.

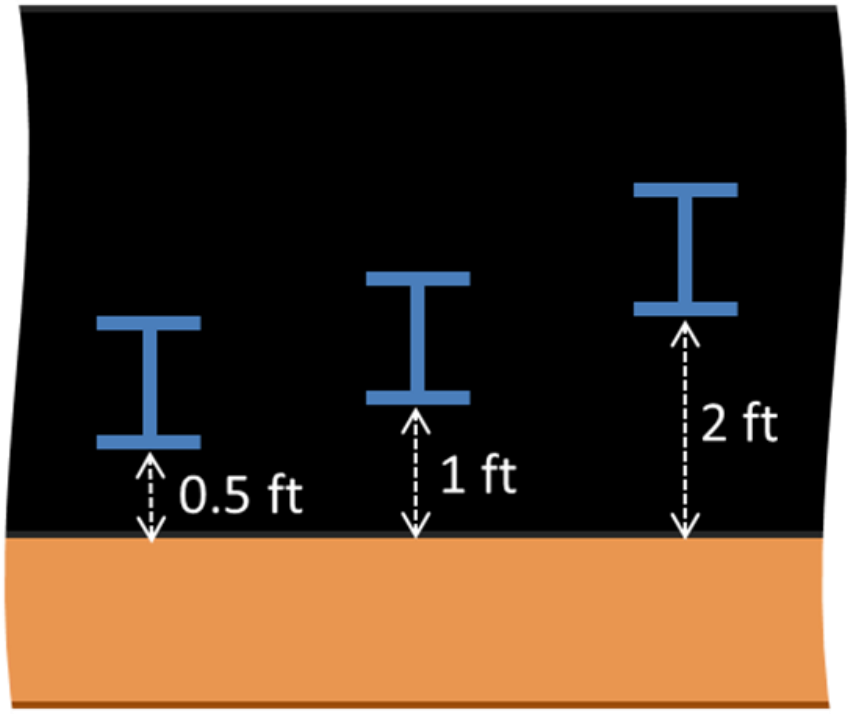

Figure 20. Guardrail post setups with various rear distances.

One effective way to decrease the asphalt ground restraint is to introduce predetermined cuts in the asphalt. When these are utilized, the asphalt breaks into two or more parts during a rupture. This type of design has the potential to significantly decrease the ground restraint while also controlling the direction of rupture. A controlled rupture in the asphalt avoids crack propagation in a large area and reduces maintenance costs. Pre-cuts should be designed based on an investigation of rupture patterns of the asphalt layer. An example of a pre-cut mow strip is shown in Figure 21. This pre-cut pattern was tested

experimentally [56], and more design patterns are investigated in this Chapter using finite element simulations to determine the most effective crack pattern.

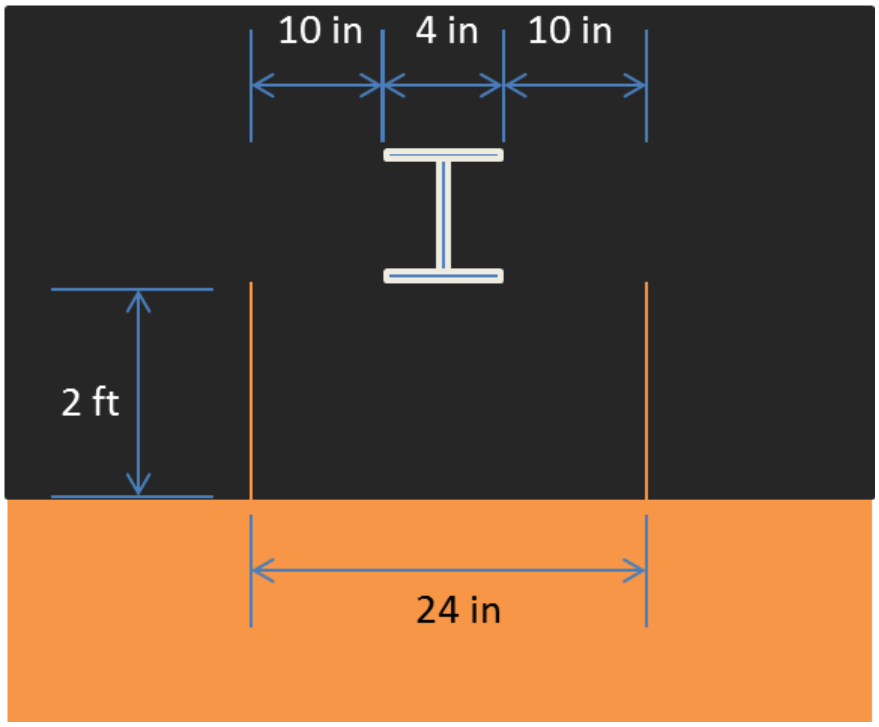

Figure 21. Schematic of a guardrail post setup with a pre-cut asphalt layer.

3.2 Effect of Asphalt Material and Geometric Properties

It is often not cost-effective to perform full-scale experimental tests on an entirely comprehensive set of parameters. Simulation of guardrail posts using nonlinear FEA is an effective way to assess these systems. The FE model was used to evaluate the relative performance of guardrail posts with various designs, including pre-cutting of the asphalt layer. The following sections discuss the effects of the asphalt material and geometric

properties on the overall performance. The effects of asphalt material constants on the system response were studied because these constants change with temperature changes and the aging of the asphalt layer. Therefore, it is important to investigate the relationship between the system response and these constants.

3.2.1 Effect of the Asphalt Rear Distance

The numerical simulations indicate that the rear distance of the mow strip behind the post significantly affects the post/mow strip system performance. The rear distance was varied using discrete values equal to 0, 150, 300, 600, 1,200, 2,500 mm, and infinity (i.e., infinite medium) with all other system parameters held constant (G = 50MPa, ν = 0.35, C = 0.5 MPa, ϕ' = 35°, asphalt thickness = 50 mm, ε_{Max} = 0.09, σ_{Max} = 0.7 MPa). The peak force applied to the post from the asphalt layer was measured, and the results are presented in Figure 22a. The results show a proportional relationship between peak force and rear distances, up to a certain point; there appears to be a cap on this proportionality. After the rear distance reaches approximately 1,200 mm, a further increase does not significantly change the response. This occurs because the zone of influence behind the guardrail post is close to 1,200 mm. As the rear distance passes 1,200 mm, the asphalt behind the guardrail post gets near the bearing capacity, which is not a function of the rear distance.

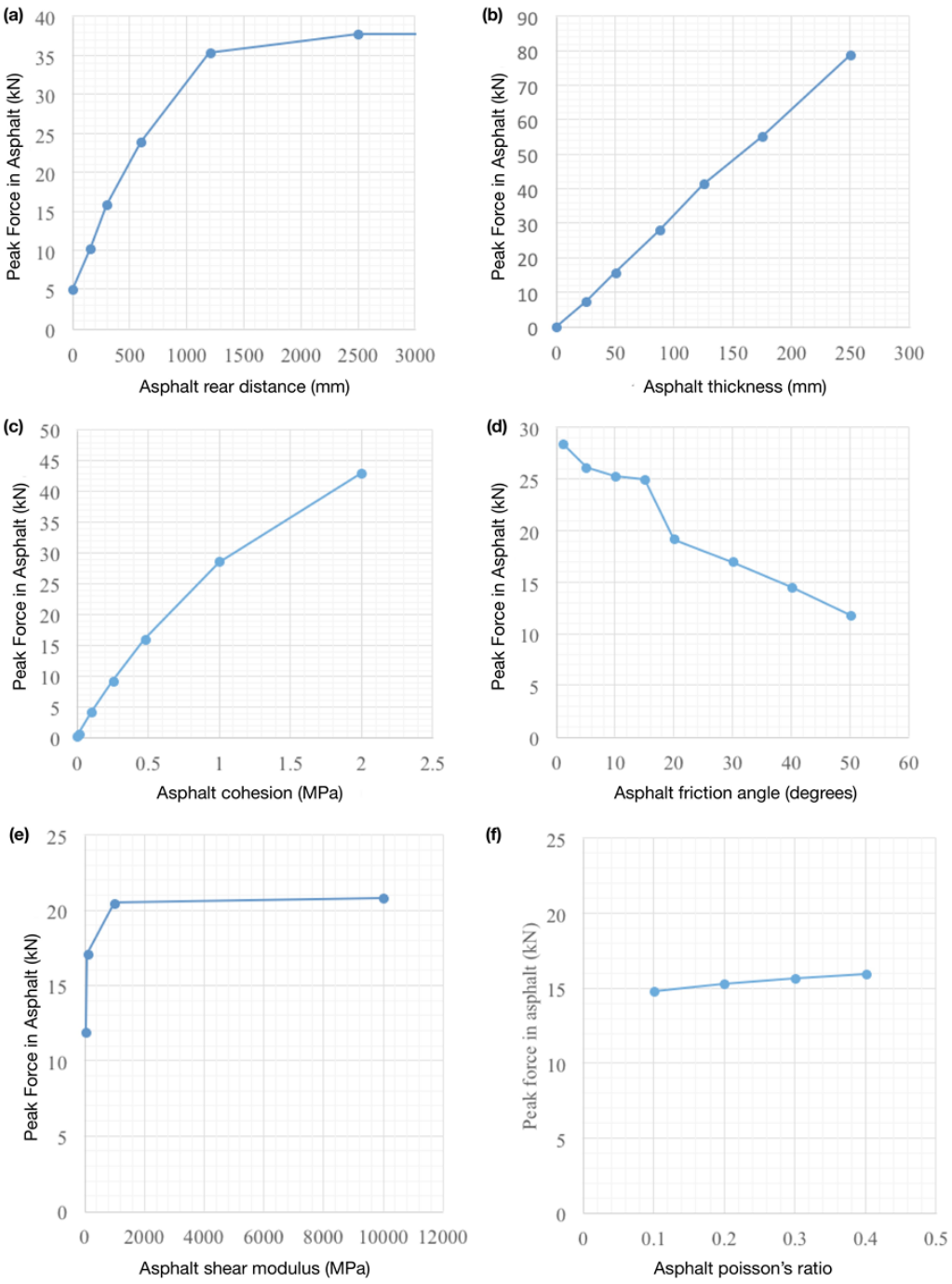

Figure 22. Effect of asphalt geometric and material properties on the peak force in asphalt.

3.2.2 Effect of the Asphalt Thickness

The asphalt thickness was varied using discrete values equal to 0, 25, 50, 90, 125, 175, and 250 mm. The remaining parameters were held constant as in Section 3.2.1, with the asphalt rear distance equal to 300 mm. The peak force from the asphalt layer applied to the post was measured, and the results are presented in Figure 22b. The peak force appears to be proportional to the asphalt thickness throughout the range of values investigated.

3.2.3 Effect of the Asphalt Cohesion

The asphalt's cohesion value was varied using discrete values equal to 0.01, 0.1, 0.25, 0.5, 1, and 2 MPa. The principal stress was varied as a function of cohesion using the relation $\sigma_{Max} = 0.95c/\tan(\phi')$. The peak force from the asphalt layer applied to the post was measured, and the results are presented in Figure 22c. As shown in the figure, the peak force is roughly linearly proportional to the asphalt cohesion for values less than 1 MPa. For values larger than 1 MPa, the asphalt becomes very stiff, and it causes high bending stresses in the steel post.

3.2.4 Effect of the Asphalt Friction Angle

The asphalt friction angle was varied using discrete values equal to 1, 5, 10, 15, 20, 30, 40, and 50 degrees. The peak force applied to the post was measured, and the results are presented in Figure 22d. As can be seen, the peak force is linearly related to the asphalt friction angle when the angle is greater than 20 degrees. For values less than 20 degrees,

the asphalt's strength in tension increases substantially, and shear failure occurs instead of principal stress failure. This results in higher peak forces.

3.2.5 Effect of the Asphalt Shear Modulus

The asphalt's shear modulus was varied using discrete values equal to 50, 100, 1,000, and 10,000 MPa. The peak force from the asphalt layer applied to the post was measured, and the results are presented in Figure 22e. The peak force increases nonlinearly as the shear modulus increases. For values of the shear modulus less than 1,000 MPa, the effect of the shear modulus is substantially higher. This can be explained by the nonlinearity in the system. For very low values of shear modulus, large displacements are required to reach the asphalt strength, which causes highly nonlinear secondary effects. However, after the shear modulus passes a threshold value, the nonlinear effects become negligible; increasing the shear modulus beyond that value does not have a noticeable effect on the system.

3.2.6 Effect of the Asphalt Poisson's Ratio

The asphalt's Poisson's ratio was varied using discrete values equal to 0.1, 0.2, 0.3, and 0.4. The peak force applied to the post was measured, and the results are presented in Figure 22f. From the plot, the peak force changes from 15 kN to 16 kN when the Poisson's ratio changes from 0.1 to 0.4, which is 7% higher. Therefore, changing the Poisson's ratio does not have a significant effect on the system response. This occurs because the top side

of the asphalt layer is free, and the asphalt can deform without any resistance in that direction. The free side of the asphalt layer decreases the Poisson's ratio effect on the stresses in the loading direction. The asphalt strength parameters such as friction angle and cohesion, which affect the Mohr-Coulomb yield surface, have more direct effect on the peak force than the Poisson's ratio.

3.3 Effect of Asphalt Pre-Cutting

If the asphalt is modeled as a rigid material, the asphalt rupture cannot be captured, and the system performance changes significantly. Based on the experimental results, rupture is the primary mechanism of the asphalt failure around the guardrail post. As the rupture propagates, the strength of the asphalt layer decreases until one portion of the asphalt detaches from the rest of the mow strip. After this occurs, the asphalt has a negligible impact on the system and the soil is the only source of ground restraint. Therefore, one potentially effective way to decrease mow strip restraint is to introduce predetermined fracture planes (referred to here as "pre-cuts") in the asphalt layer. A controlled rupture along a predetermined fracture plane in the asphalt avoids uncontrolled crack propagation in a large area and potentially reduces expected maintenance costs. The cuts would be designed based on the experimental and numerical investigation of rupture patterns of the asphalt layer. Two cut patterns which were tested experimentally (Figure 23) by Lee [56] were used to verify the FEA with pre-cuts. Additional design patterns were investigated using finite element simulations to find the most effective pattern. Different

possible pre-cutting alternatives that were considered are numbered and presented along with FEA results in Figure 24.

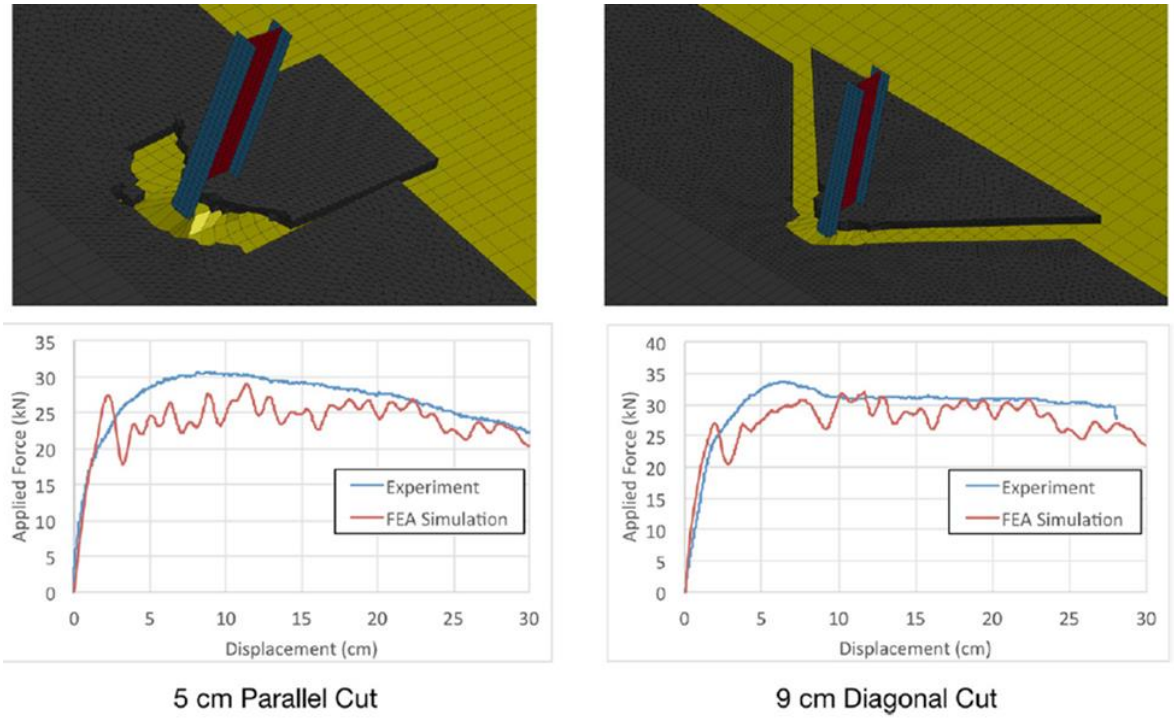

Figure 23. Comparisons between LS-DYNA FEM and experimental results [56]**.**

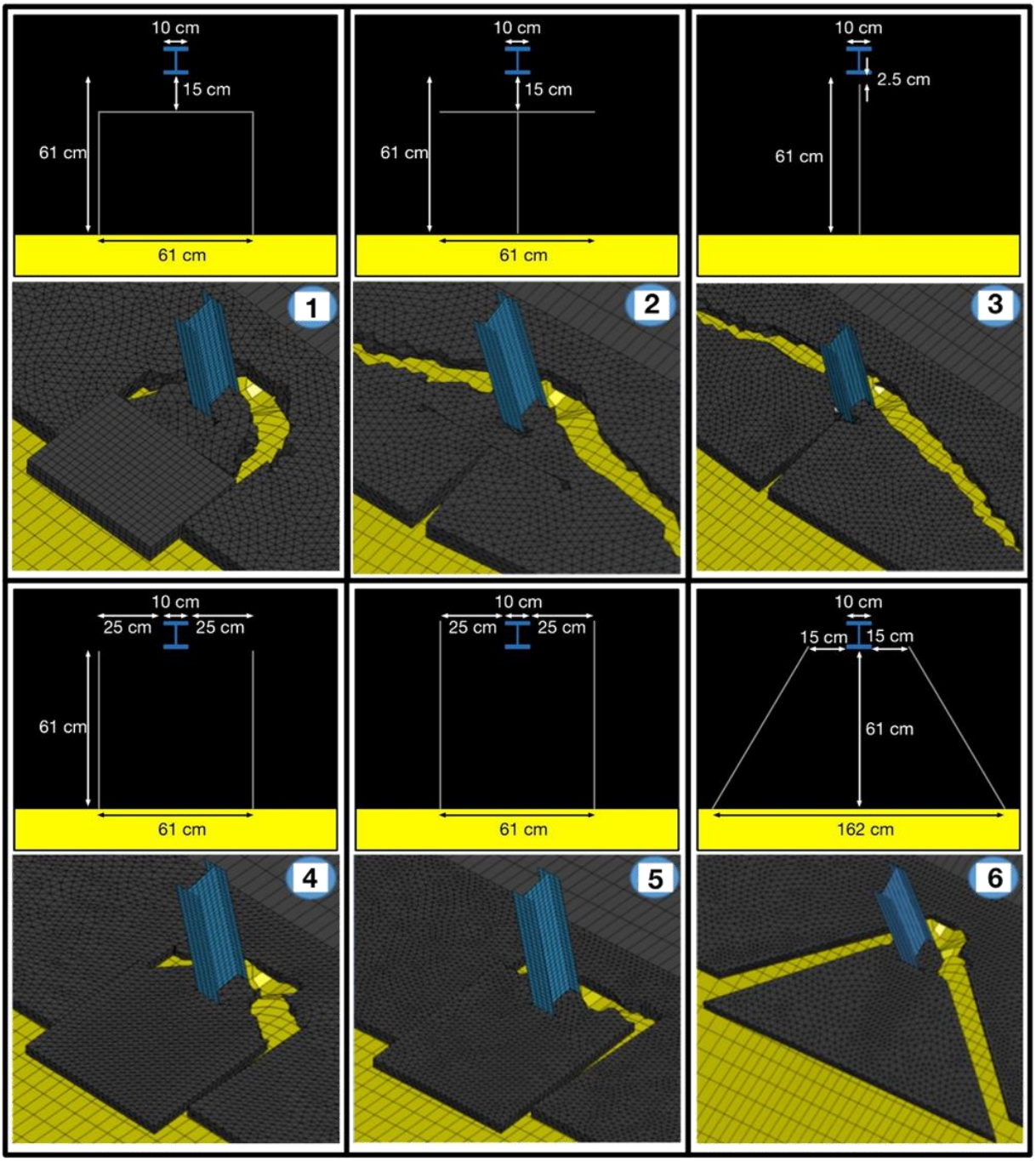

Figure 24. Pre-cutting designs for the asphalt mow strip with finite element model simulations.

Based on the FEA results and analysis of peak forces (Table 3) and stresses on the post, Design Numbers 2 and 3 are determined to be ineffective, since they do not significantly decrease the asphalt ground restraint. In Design Number 3, the cut is applied in the asphalt layer where the asphalt is in tension. Because asphalt is weak in tension, applying a cut in that area does not significantly decrease the asphalt layer's strength. Design Number 2 has the same cut as Design Number 3, along with an additional horizontal cut behind the post. Two sides of the horizontal cut are in compression when a force is applied to the post and, therefore, it does not cause a decrease in the strength of the layer. From the finite element results summarized in Table 3, Designs 1, 4, 5, and 6 are effective designs since they significantly decrease the peak load and ground restraint. These designs shorten the distance that the asphalt rupture needs to propagate until one part detaches from the rest of the layer.

Table 3. Peak force summary for pre-cutting designs.

Design Number	Peak Force (kN)
1	29.58
2	35.63
3	36.61
4	28.20
5	27.58
6	28.02
No pre-cut	37.50

3.4 System Assessment using Quantitative Performance Criteria

3.4.1 Parametric Studies on Asphalt Mow Strip Geometry

Varying asphalt mow strip geometry influences system performance. As the thickness and the rear distance behind the post increase, the ground-level restraint of the asphalt layer on the post-mow strip system increases. Parametric studies on the combination of different thicknesses and rear distances are a critical step to explore the impact of each of these parameters. The common asphalt thickness for a mow strip used in the state of Georgia is 90 mm, and the minimum feasible asphalt thickness based on constructability is estimated as 50 mm. Additionally, 25 mm, 125 mm, 175 mm, and 200 mm thick asphalt layers were included in the simulations to show the system response for very thin and very thick mow strips. Similarly, the rear distance values of 0 mm, 150 mm, 300 mm, 600 mm, and 1200 mm were used. Load-displacement curves, ground-level displacement of the post, work done on the system, and the maximum tensile strains in the post flanges were measured.

A set of quantitative performance criteria is required to evaluate the relative performance of mow strip designs with respect to the leave-out. Setups that show more restraint than the setup with leave-out are less likely to pass full-scale crash testing; setups that have less restraint than the setup with leave-out are more likely to pass crash testing. This is because previous researchers have demonstrated that setups with leave-out pass the crash testing, while setups with higher ground restraint might fail the crash testing [3].

Ground displacement associated with a target energy, peak force, and maximum strain [37] were chosen to evaluate the system performance, as discussed in the following sections.

3.4.2 Assessment using Peak Force Criterion

The first criterion that can be used to evaluate the relative performance is the peak force criterion. This criterion is based on the fact that higher peak force applied to the post before its failure yields higher ground restraint of the post. Figure 25 shows an FE simulation contour plot of peak force applied to the post. Experimental data [37] are marked on the plot with parentheses. Mow strip setups with the thicknesses and rear distances associated with the solid lines have less ground level restraint than setups with the leave-out. The dashed lines have more restraint than the leave-out setup. For example, guardrail posts installed in mow strips with 50 mm thickness and 300 mm rear distance are more likely to pass a full-scale crash test.

3.4.3 Assessment using Ground Level Displacement Criterion

Figure 26 shows an FE simulation contour plot of ground level displacement associated with 66.7 kip-in work done on the system. This amount of energy is equivalent to ten percent of the kinetic energy of a small crash test vehicle (Mass = 1100 kg) whose velocity is perpendicular to the guardrails. Larger ground level displacement associated with this target energy is an indication of less ground restraint of guardrail posts. Experimental data [37] are marked on the plot with parentheses. Mow strip setups with the

thicknesses and rear distances associated with the solid lines have less ground level restraint than setups with the leave-out. The dashed lines have more restraint than the leave-out setup. For example, guardrail posts installed in mow strips with 50 mm thickness and 450 mm rear distance are more likely to pass a full-scale crash test.

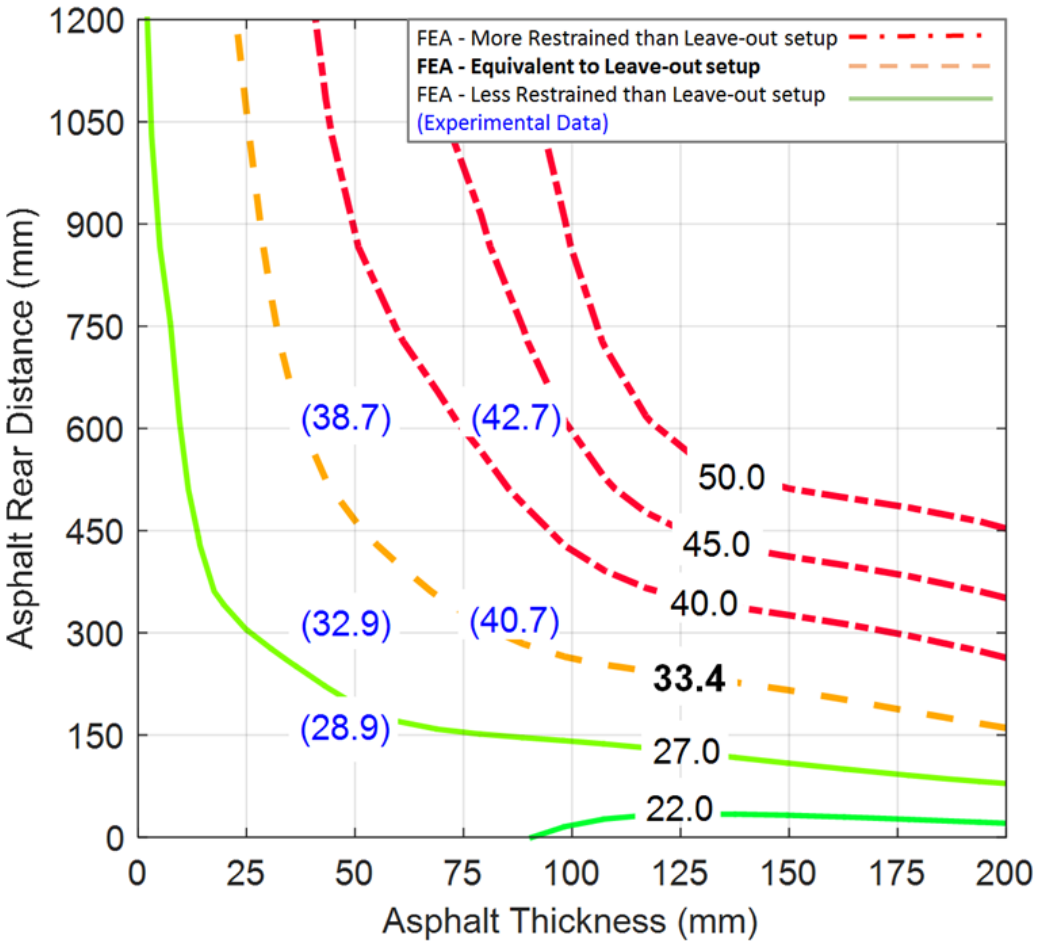

Figure 25. FEA Contour plots for combinations of thickness and rear distance. Curves are a representation of peak applied force to the post (kN). Experimental results are given in parentheses.

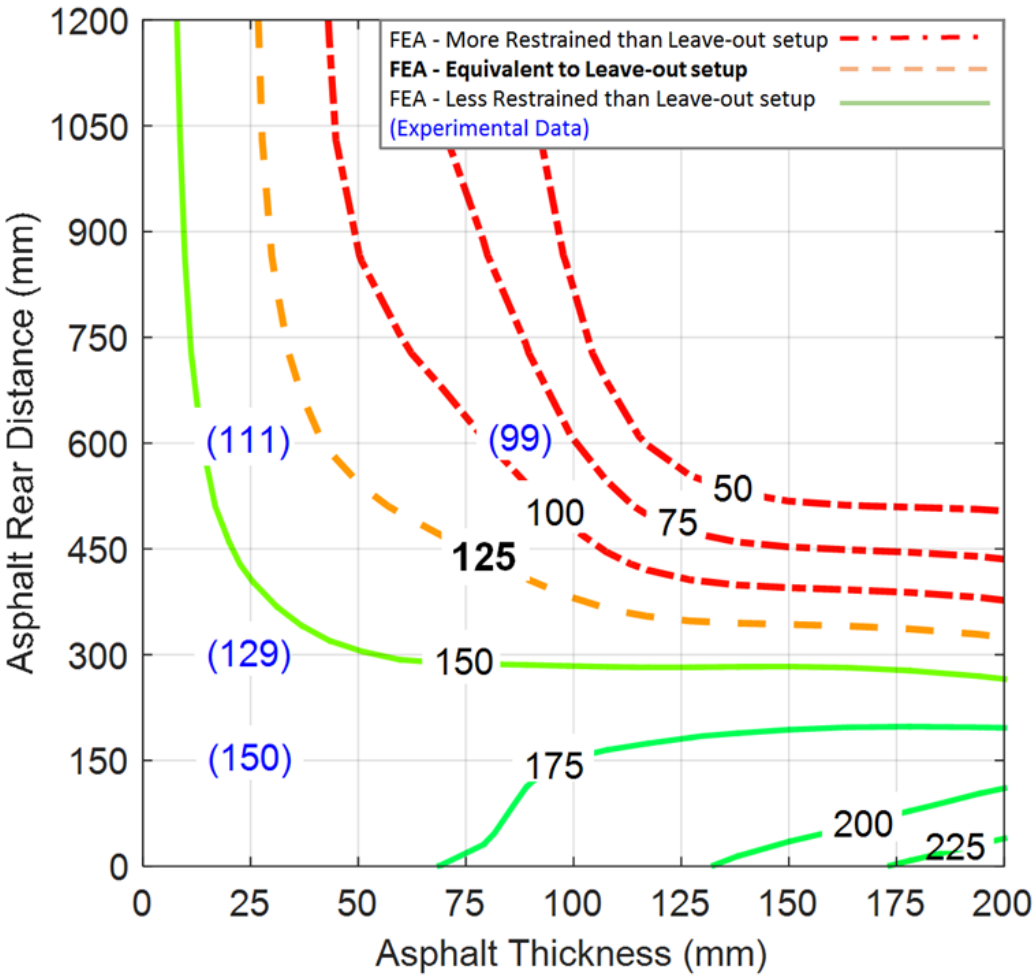

Figure 26. FEA Contour plots for combinations of thickness and rear distance. Curves are a representation of ground level displacement. Experimental results are given in parentheses.

3.4.4 Assessment using Maximum Strain Criterion

Figure 27 shows an FE simulation contour plot of normalized maximum longitudinal strain in the flanges of guardrail posts. The tensile longitudinal strain in the flange of guardrail posts was measured, and then it was divided by the yield strain of steel

to be normalized. Therefore, contours larger than 1 represent yielding in the guardrail posts. Experimental data [37] are marked on the plot with parentheses. Higher longitudinal strains in the guardrail posts are associated with higher ground restraint. Mow strip setups with the thicknesses and rear distances associated with the solid lines have less ground level restraint than setups with leave-out. The dashed lines have more restraint than the leave-out setup. For example, guardrail posts installed in mow strips with 50 mm thickness and 300 mm rear distance are more likely to pass a full-scale crash test.

3.4.5 Assessment using Combination of the Three Criteria

The three contour plots can be merged to draw a target performance envelope curve as shown in Figure 28. Any design below the three lines is expected to show less ground restraint than the typical leave-out design detailed in the Roadside Design Guide. These contours can conveniently be used to find guardrail post setups that are more likely to pass a full-scale crash test. For example, guardrail posts installed in mow strips with 50 mm thickness and 300 mm rear distance are more likely to pass a full-scale crash test, based on the combination the three criteria. These contours are used to better understand the behavior of guardrail post setups with mow strips and their relative performance. However, these curves cannot be the sole factor used to determine if a setup should be approved or rejected for road safety. The static testing results give insight for the next chapters, which will discuss dynamic subcomponent testing of various mow strip designs.

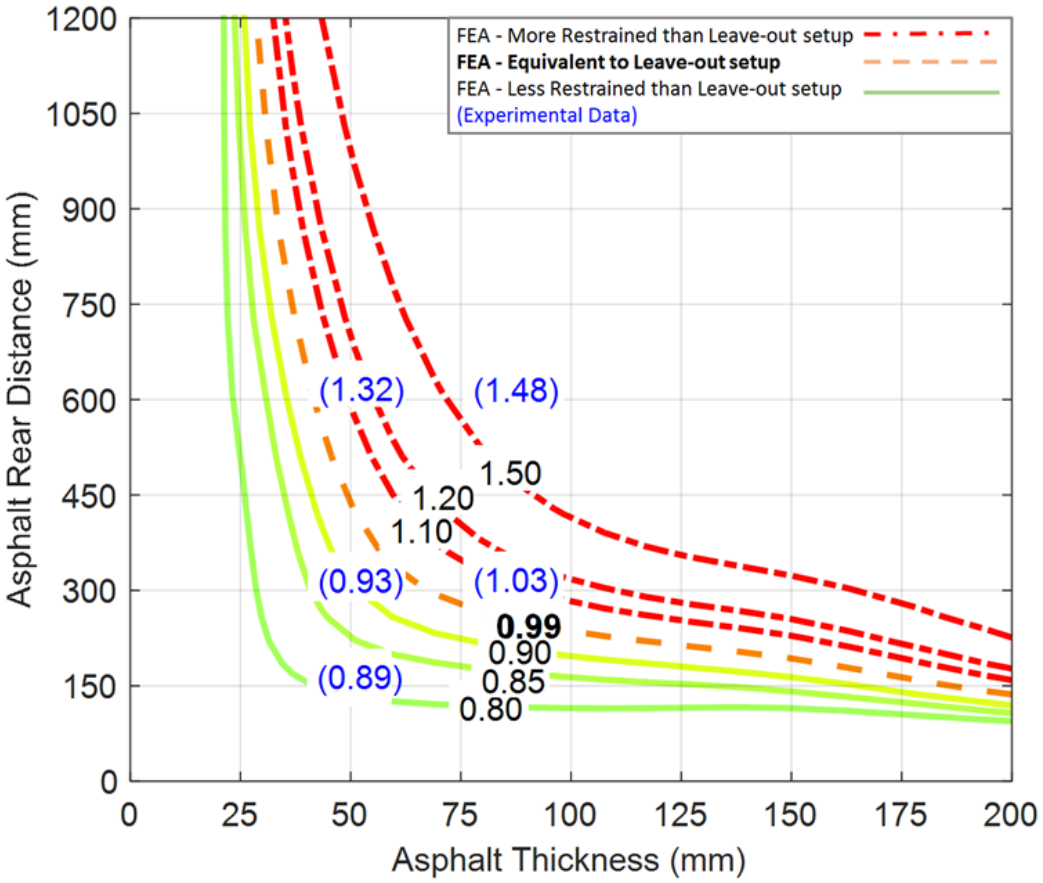

Figure 27. FEA Contour plots for combinations of thickness and rear distance. Curves are a representation of the ratio of measured strains to the yield strain of steel equal to 0.002 mm/mm. Experimental results are given in parentheses.

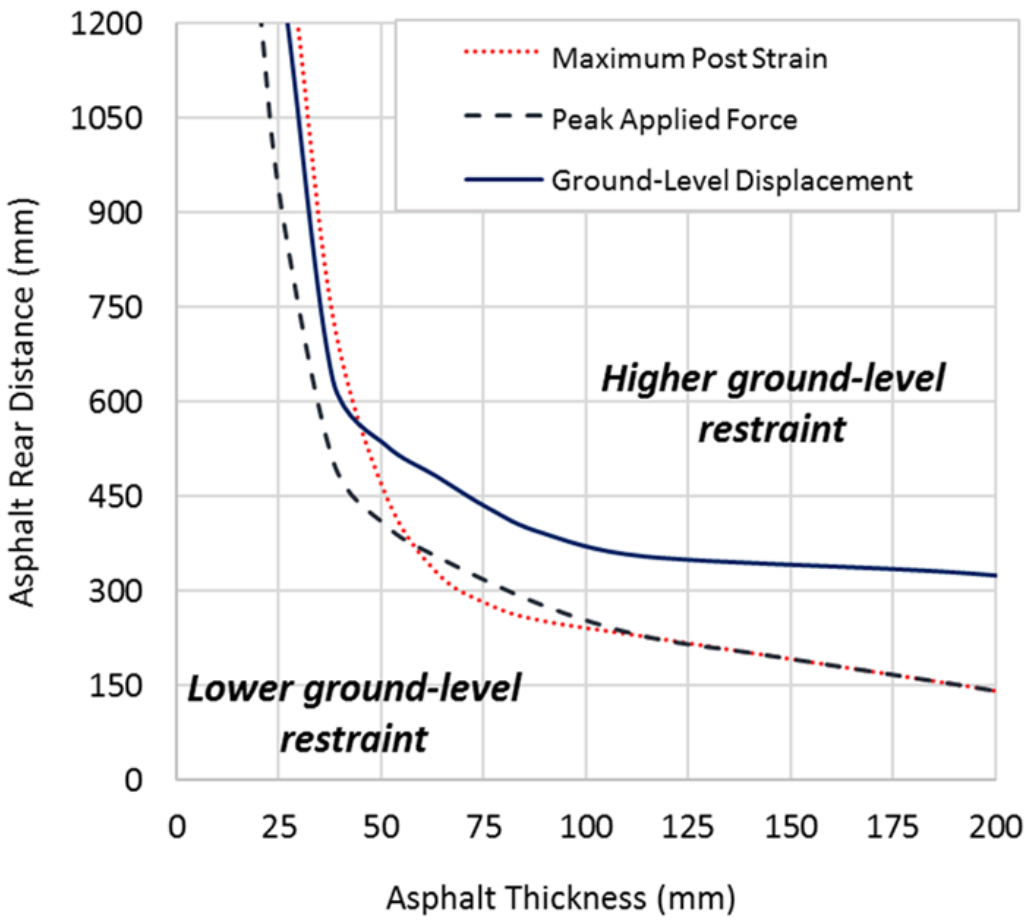

Figure 28. FEA Contour plots for combinations of thickness and rear distance. Curves are a representation of ground level displacement, peak applied force, and maximum longitudinal strain.

CHAPTER 4. DYNAMIC FINITE ELEMENT MODELING OF GUARDRAIL SYSTEMS WITH ASPHALT MOW STRIPS

Finite element models were constructed to perform mock-up dynamic simulations and subcomponent dynamic simulations. In the dynamic tests performed in this project, mock-up simulations were initially performed to determine the appropriate material properties and dimensions for the foam programmer used in the impactor. This model was used to determine the various parameters necessary for the test setup (i.e., impact mass, impact speed, instrumentation fixtures, etc.). Thereafter, dynamic subcomponent tests and simulations were conducted to assess the performance of guardrail posts embedded in soil and asphalt. These tests are less expensive than full-scale crash tests and are used to evaluate additional alternative designs for asphalt mow strips. The material models used for the soil, asphalt, and steel in the static tests were updated for use in the dynamic loading simulations.

4.1 Design of the Impactor

The impact loading was applied by impacting guardrail posts with a steel impactor that had a specified initial velocity. A dynamic actuator was used to give initial velocity to the steel mass. It was critical to determine appropriate impact speed and mass of the impactor. Based on the testing conditions, the safe maximum impact speed was limited to 15 m/s. Using this speed, the mass of the impactor could be specified for a given kinetic energy. The MASH guidelines specify the mass and speed of vehicles used for full-scale

crash testing. MASH test numbers 3-11 and 3-10 are used to evaluate the guardrail system discussed in this research. Vehicles with an impact angle equal to 25 deg and with masses of 2,270 kg and 1,100 kg are used for the tests 3-11 and 3-10, respectively. The kinetic energy for test 3-11 is used here as a reference in the subcomponent dynamic testing. It was assumed that the energy dissipated by guardrail posts and associated with the component of velocity perpendicular to guardrails is divided equally between ten posts. Therefore, the energy dissipated by one guardrail post can be obtained as

$$E_d = 0.5\frac{m_v(\mathrm{v}\ sin\,25^\circ)^2}{10} = 0.5{\times}2270kg{\times}\frac{\left(27.78\frac{m}{s}{\times}\,sin\,25^\circ\right)^2}{10} = 15.6\ kJ \qquad (2)$$

The mass required for a steel impactor to reach the above energy with a velocity of 15 m/s is approximately 135 kg. This mass is used in the experimental subcomponent tests. In the initial mock-up tests, a velocity of 10 m/s was used instead of 15 m/s in order to increase the safety of the tests. Also, 100 mm thick foam was used instead of 200 mm thick foam because the kinetic energy was less. However, the velocity of 15 m/s and foam thickness of 200 mm were used in the dynamic subcomponent tests with the guardrail post embedded in soil and asphalt.

When the steel impactor directly impacted the steel guardrail posts, the resultant acceleration due to the impact and based on the FEA simulations was more than 1,000 g. Vehicle ride down accelerations in acceptable full-scale crash tests on guardrails are typically less than 20 g based on MASH. Therefore, a crushable foam layer was attached

to the front of the impactor to reduce impact accelerations in the subcomponent tests. An 8-inch crushable foam with a density of 96 kg/m^3 was chosen for use in the tests. A neoprene rubber layer was placed between the crushable foam layer and the steel mass to protect the mass when the crushable foam was destroyed in an impact. A picture of the steel impactor with crushable foam and rubber layers is shown in Figure 29. The steel impactor has four wings that allow it to sit and slide on guidance rails.

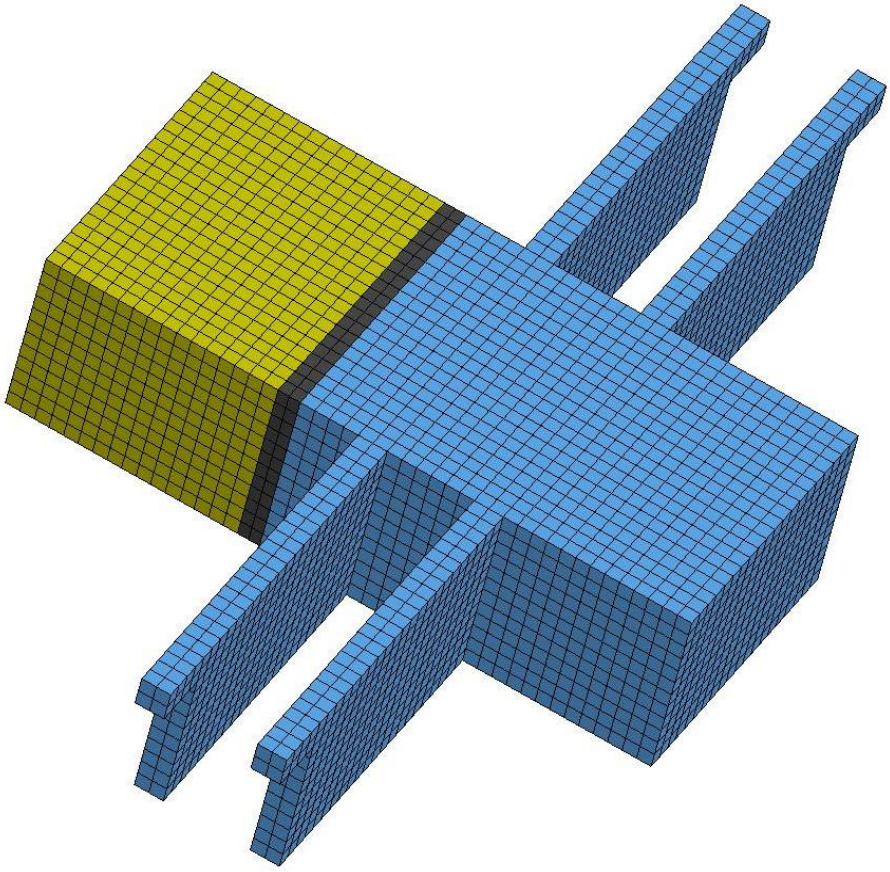

Figure 29. Steel impactor, crushable foam, and rubber.

4.2 Mock-up Testing

A simple dynamic mock-up test was constructed by attaching a 1.8 m length guardrail post to a steel beam. The connection between the steel beam and the guardrail post was made rigid using two flanges with bolted connections. A steel strut was used to support the guardrail post, using the rigid connection at the height of 1 m from the bottom of the post. This simple setup allowed for verifying the dynamic actuator setup and calibration of the foam finite element model. The post yielded upon impact immediately above the rigid connection to the steel strut. A finite element model of this mock-up test was made, and the results were compared by measuring the deformation of the foam layer and the displacement of the post at the point of impact. After verifying the finite element model of the steel post, foam, and rubber layer, the model for the impactor and the steel post were used in the subcomponent testing of guardrail posts embedded in soil and asphalt. A photo of the FE mock-up model is presented in Figure 30.

4.3 Dynamic Mock-up Simulations

4.3.1 Finite Element Model Description

4.3.1.1 Geometry

The length of the post used is 1.829 m. The impact point is 1.629 mm from the bottom of the post as shown in Figure 30. The steel mass length, width, and depth are 340 mm, 250 mm, and 150 mm, respectively. The width of the mass wings is 900 mm. The foam and rubber layer thicknesses are 100 mm, 25 mm, respectively.

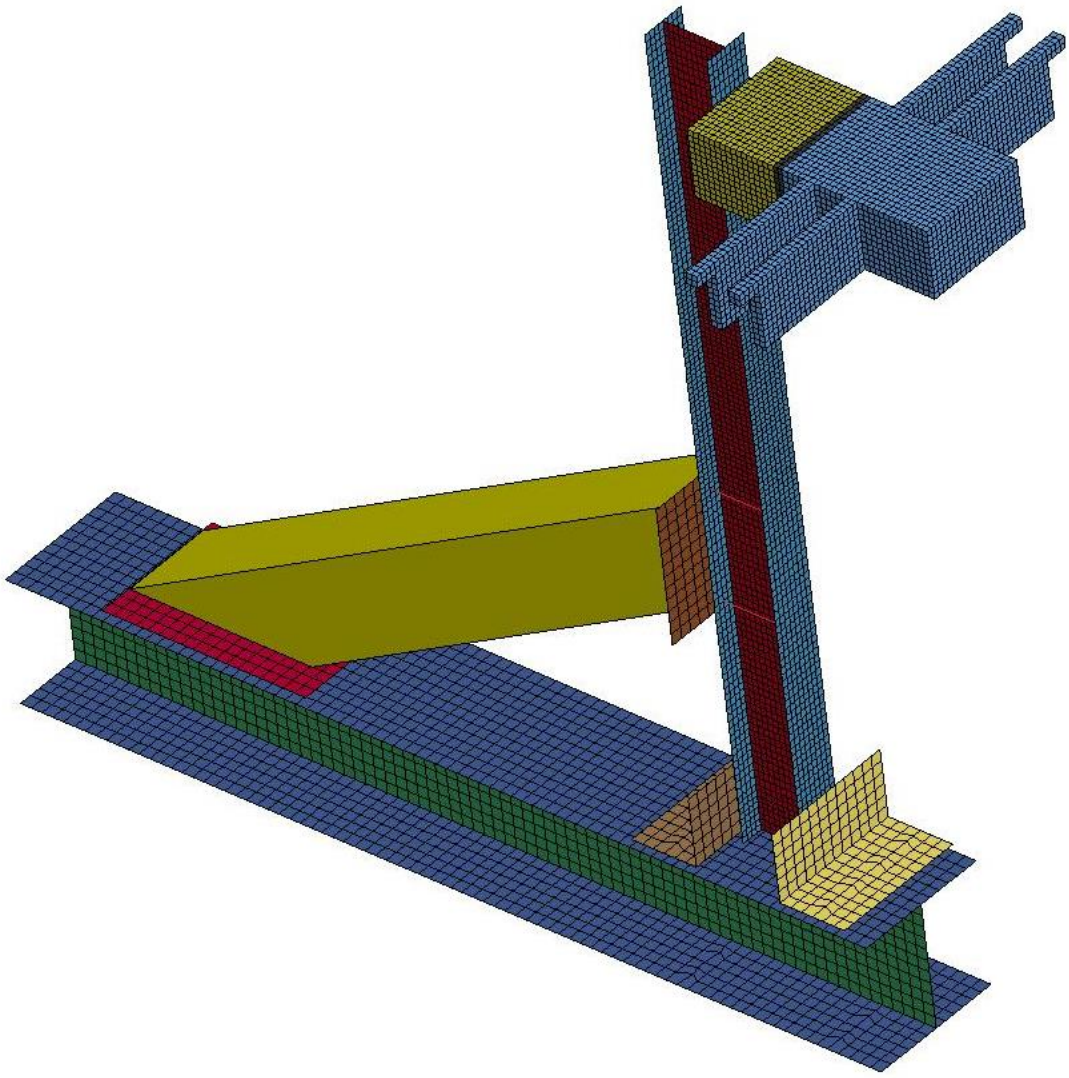

Figure 30. Representation of the mock-up setup.

4.3.1.2 Simulation of Initial Velocity and Impact

The initial velocity was modeled for the impactor by assigning an initial velocity equal to 10 m/s to all nodes of the impactor. The impactor flew for 1 mm and then impacted the post. The impactor stayed in contact with the post until its horizontal speed reached zero, and then the impactor bounced back; after a fraction of a second, the impactor lost contact with the post and flew freely away from the setup.

4.3.1.3 Mesh Sensitivity Analysis

The finite element mesh density for the guardrail post, foam, and rubber varied from 1 in. to 0.125 in. The post and foam deflection were monitored during the analysis. The results showed that using a mesh size of 0.125 in. gave results with less than 5 percent difference than using a mesh size of 0.25 in. Therefore, 0.125 in. was used as the mesh size for these parts. Further refining the mesh size was not feasible, as reducing the size of elements by a factor of 2.0 increased the simulation time by more than 100%.

4.3.1.4 Hourglass Controls and Energy Checks

Because fully integrated shell and solid elements were used in the model, the hourglass energy was zero, and no hourglass control was needed.

4.3.1.5 Steel

A piecewise linear metal plasticity model was used in LS-DYNA for the steel post. The static yield strength of the steel, modulus of elasticity, and Poisson's ratio were given as inputs. The common steel parameters, presented in Table 1 in Section 2.2.9, were employed in this model. The static stress-strain curves, presented in Figure 12, were used in the model for the web and flanges. These curves indicate significant strain hardening in the flanges and the web. Strain rate effects were accounted for by using a set of stress-strain curves associated with different strain rates [57]. These sets were shown in Figure 31 andFigure 32. The curves were extended to very high strains (up to 1.0) to account for large local strains that occur in the post during simulations. Shell element formulation number 16 was selected for the steel elements; this element did not exhibit hourglass modes.

4.3.1.6 Rubber

The rubber layer used in the impactor was modeled using simple Blatz-Ko rubber material with a shear modulus of 400 MPa [58]. The density of the rubber was estimated experimentally equal to 1,365 kg/m^3 [9].

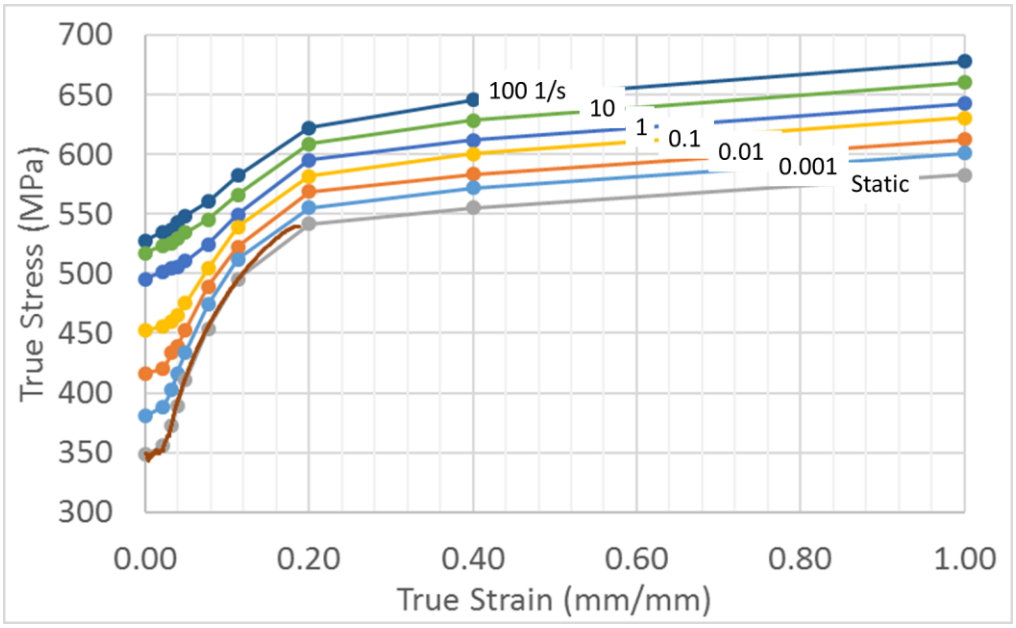

Figure 31. Stress-strain curves used for the post flanges. Strain rates are written on each curve.

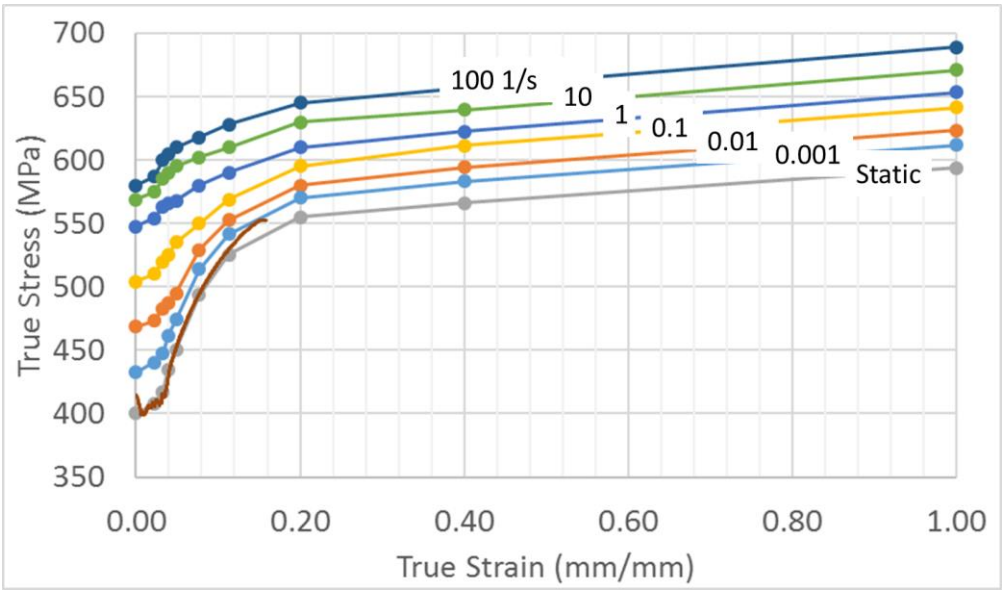

Figure 32. Stress-strain curves used for the post web. Strain rates are written on each curve.

4.3.1.7 Foam

The foam layer was modeled using a crushable foam material in LS-DYNA (material #63). The density of the foam was estimated experimentally to be equal to 96 kg/m^3 [9]. The stress-strain curve for compression loading of the foam under static loading was obtained experimentally [9]. This curve is presented in Figure 33.

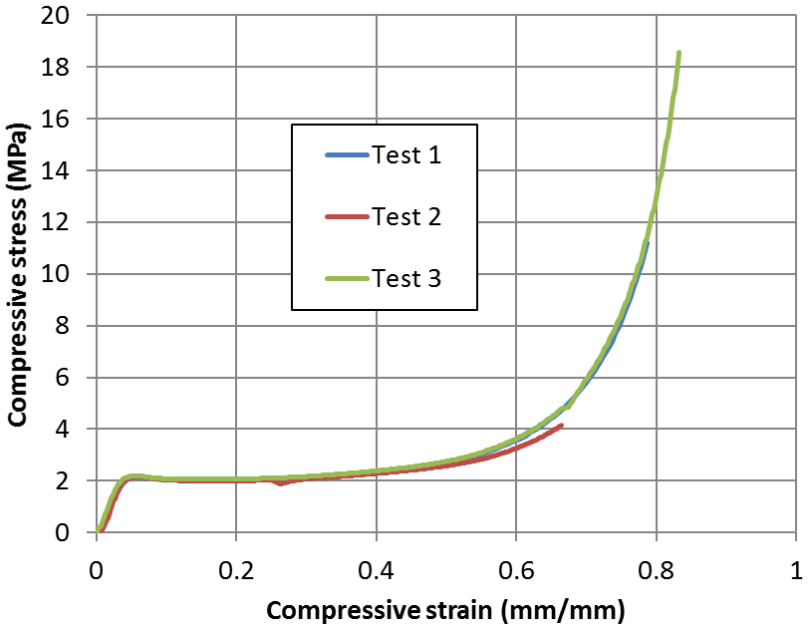

Figure 33. Stress-strain curve for the foam material.

After examination of the specimen during the compression test, no deformation was observed in the transverse direction, which implies that the Poisson's ratio of the foam material is zero. The initial and final cross-section areas of the crushable foam in compression remain constant. Therefore, the engineering and true stress-strain diagrams

are identical. The volume of the material is not conserved during compression and the density increases while the material is compressed. The volumetric strain is equal to the compressive strain. The crushable foam material model requires nominal yield stress vs. volumetric strain curve as an input. This curve was obtained using Figure 33 and is presented in Figure 34. This curve is based on static loading and was used initially in the model. Thereafter, in the calibration process of the model, a common dynamic rate factor equal to two was used to scale the stress values up at a given strain on the curve. This scale factor resulted in the same foam deformation in the FE results as observed in the experiments [9]. The results of the experiments and the simulations are compared in Table 4.

In the experiments [9] it was observed that the foam cracks and crushes during the impact. It is also known that foams are weak in tension. Therefore, an LS-DYNA element erosion criterion based on maximum principle strain was added to the foam model in order to capture the cracking and crushing of the foam. The elements were eroded when the principle strain reached a specified value. The value of the erosion principle strain equal to 0.1 mm/mm was found using model calibration by comparing foam deformation in the experiment and the finite element model at various times during the impact. This value is mesh-dependent, and lower values of maximum principle strain are needed for larger mesh sizes. This occurs because the average strain is smaller for a larger mesh than for a smaller mesh size.

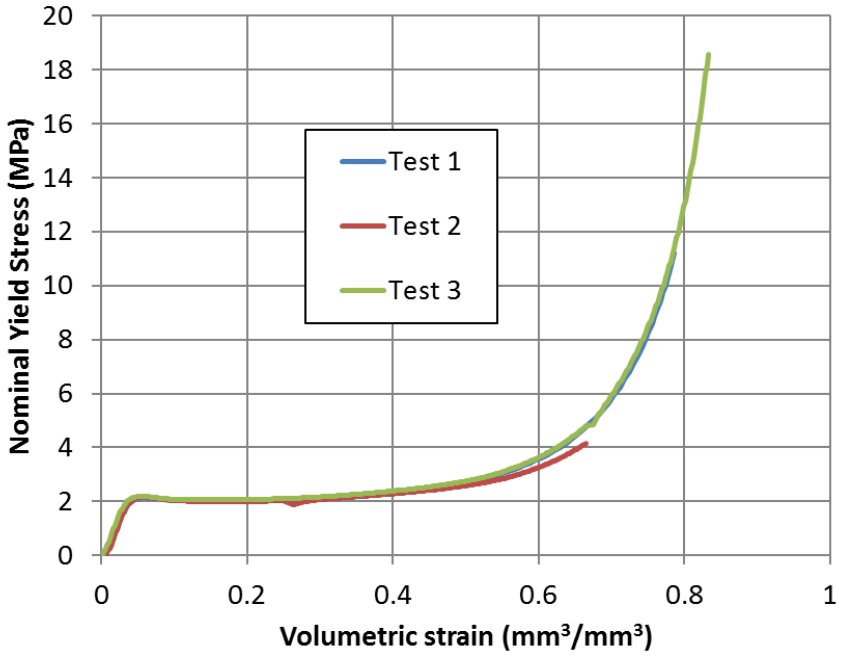

Figure 34. Nominal yield stress vs. volumetric strain for the foam material.

4.3.2 Comparison between Experiments and FE Simulations

The deflection of the post at the impact point and the deformation of the foam were measured in the simulations and the experiments [9]. The results are compared in Table 4. The accelerations were higher than common full-scale crash test accelerations, which are typically less than 20g; these higher accelerations are due to the lighter mass used in this research, compared with the mass of vehicles. However, the accelerations, velocities, and strain rates in the mock-up tests are still in the same order of magnitude as those in the full-scale crash tests. This indicates that the material response will not be considerably different between these tests and full-scale crash tests and these tests can be used to assess different components of guardrail systems separately.

Table 4. Comparison between FEA and Experimental results for the mock-up tests.

FEA	FEA	Experiment [9]	% Difference
Foam Deformation	37 mm	35 mm	6%
Post Disp. At Impact Point	145 mm	152 mm	5%
Impactor Max. Acceleration	65 g	52g and 71g[a]	25% and 8% [a]

a. Results from two separate accelerometers installed on the mass.

The plastic deformation of the post at the connection and the overall shape of the post after impact are shown in Figure 35 andFigure 36 for both the FEA and experimental results. These figures show that the FE model can accurately capture the plastic deformation of the post due to the impact. The crushed foam after impact is shown in Figure 37 for both the FEA and experimental results.

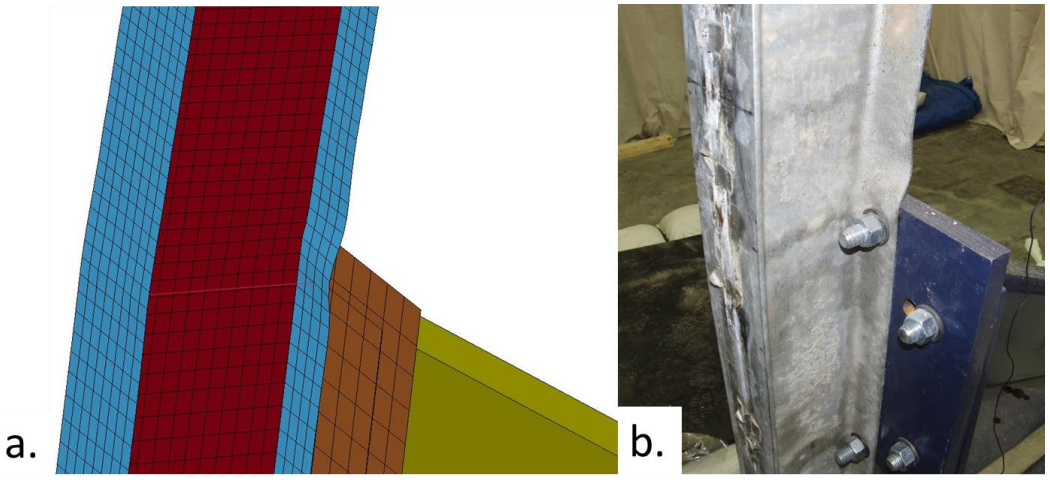

Figure 35. Plastic deformation of the post at the connection: a. FEA; b. Experiment [9]**.**

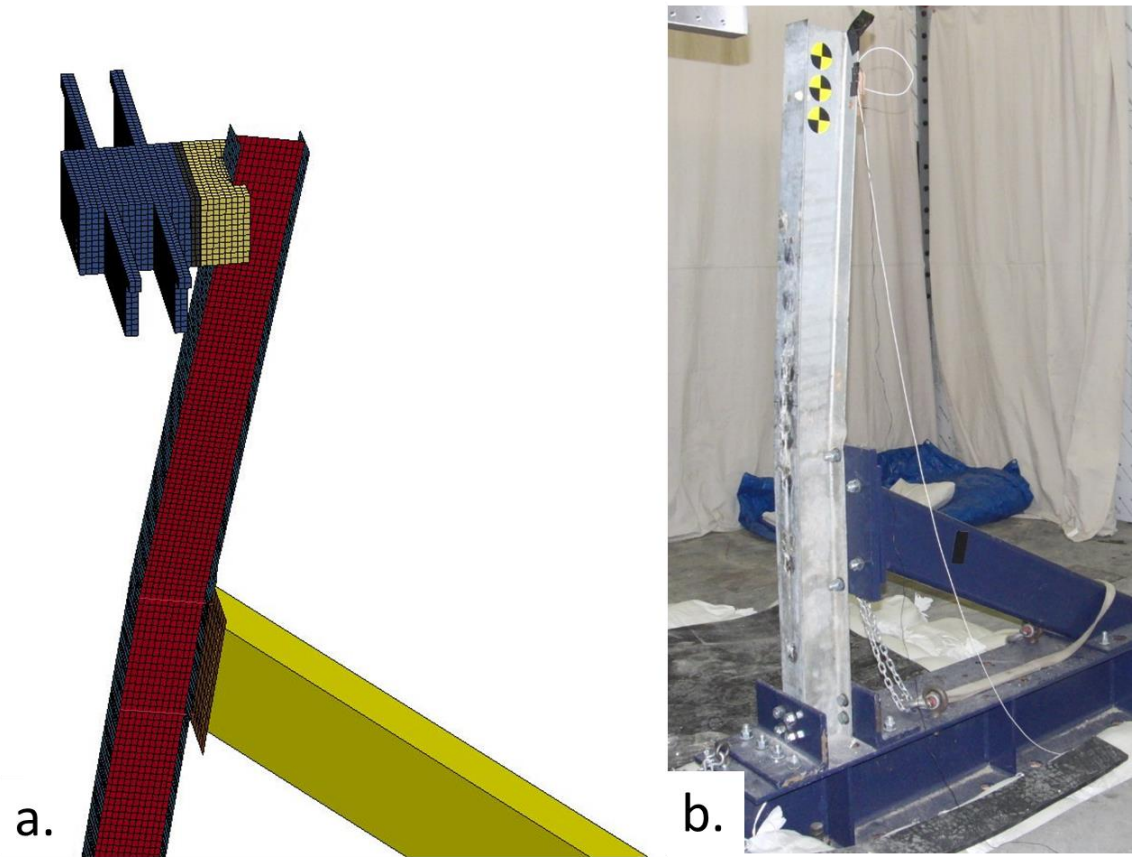

Figure 36. Representation of the system after impact: a. FEA; b. Experiment [9].

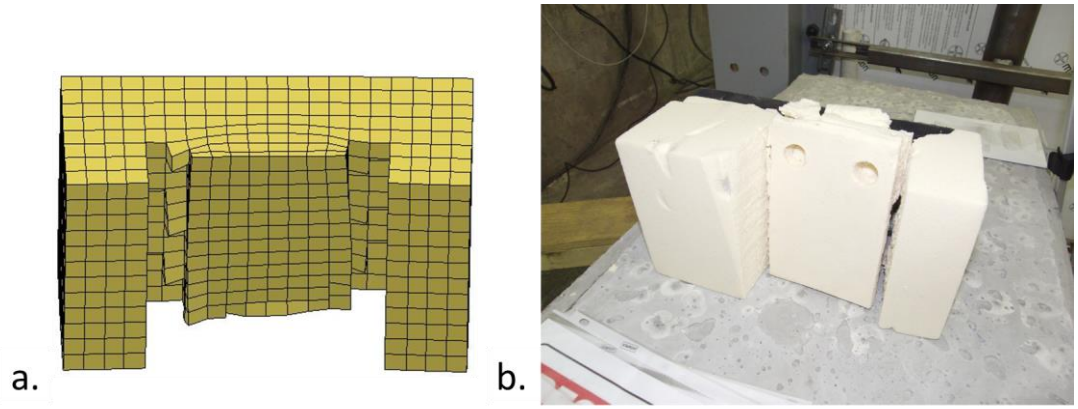

Figure 37. Crushed foam after the impact: a. FEA; b. Experiment [9].

4.4 Dynamic Subcomponent Simulations

4.4.1 Finite Element Model Description

4.4.1.1 Model Domain and Geometry

The soil was installed in a container with depth, width, and length of 1.575 m, 1.650 m, and 1.800 m, respectively. The container was filled with soil, which was compacted; then, asphalt layers with various thicknesses were installed and compacted over the soil. A guardrail post was driven through the asphalt and soil to the depth of 1.016 m, 1.219 m from the back of the container and 0.914 m from the front of the container. The impactor was located on two parallel rails [9] at an elevation of 0.635 m from ground level. The dynamic actuator pushed the impactor until it reached the speed of 15 m/s and then the impactor hit the guardrail post.

The finite element model had the same geometry as the test setup, as shown in Figure 38. The steel mass length, width, and depth were 340 mm, 250 mm, and 150 mm, respectively. The width of the mass wings was 900 mm. The foam and rubber layer thicknesses were 200 mm, 25 mm, respectively.

4.4.1.2 Element Formulations and Mesh Sensitivity Analysis

The same mesh sizes used in the mock-up simulations were repeated in this set of simulations. Constant stress solid elements (element formulation #1 in LS-DYNA) were

used to model the soil and the steel part of the impactor. The fully integrated formulation intended for solid elements with a poor aspect ratio (element formulation #-2 in LS-DYNA) was used for the foam and rubber layer. These types of elements show better stability in simulations with highly distorted foam elements with the possibility of high hourglass energy with constant stress elements. One-point integration tetrahedron elements (element formulation #10 in LS-DYNA) were used for the asphalt, which captures the asphalt rupture better than the element erosion formulation.

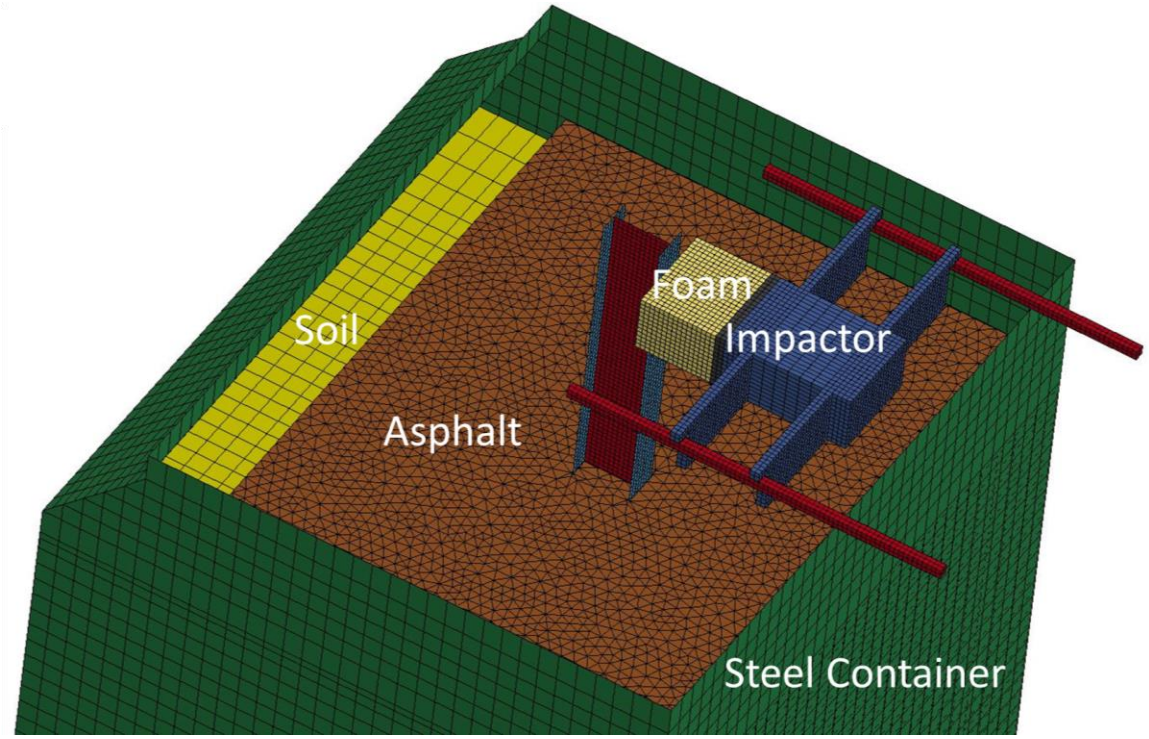

Figure 38. Finite Element Model used for dynamic subcomponent simulations.

4.4.1.3 Hourglass Controls and Energy Checks

The foam, rubber, steel post, and steel container were modeled using full integration elements. Therefore, there is no hourglass energy for these parts. Hourglass energy for the soil part and the steel part of the impactor was monitored, and it was less than 1 percent of the internal energy, which is acceptable.

4.4.1.4 Steel, Foam, and Rubber

The same material properties used in the mock-up simulations were used for the steel, foam, and rubber.

4.4.1.5 Soil

The soil type that was used in the road base has never been tested experimentally to investigate strain rate effects, and no data is available to adjust soil material properties for higher strain rates. Therefore, strain rate effects on the soil material were ignored, and the same soil material properties that were used in the static simulations were used in the dynamic simulations as initial inputs; then, the model was calibrated using experimental test results. The ground level displacement of the post in the FEA simulation was compared to the experimental result for the dynamic test with only soil and without an asphalt layer. The ground level displacement for the FEA simulation was considerably lower than the

experimental tests, which showed that the soil material properties in the simulations resulted in a stiffer response than the soil properties in the experiments. Therefore, the shear modulus was lowered to 25 MPa from 50 MPa, which was used in the static tests, and the cohesion value was set equal to zero. This difference occurred because the soil that was used in the dynamic tests was not exactly the same soil that was used in the static tests. Moreover, the dynamic tests were conducted in the laboratory with a controlled environment in contrast with the static tests that were performed in an open area exposed to rain and snow.

4.4.1.6 Asphalt

Strain rate effects were initially ignored for the asphalt, and the same material properties that were used as initial inputs in the static simulations were employed in the dynamic simulations; then the model was calibrated using experimental results. Material constants used in the dynamic finite element simulations are provided in Table 5.

After examining the dynamic simulation results, it was noted that the elements behind the post were eroding, which created a gap between the post and the asphalt layer until the post moved more and filled the gap. In the dynamic simulations, the asphalt elements behind the post and on the surface did not have overburden pressure. This caused the elements to expand upward under the sudden impact load. This expansion caused large positive principal strains although the element was compressed in the other directions. When the principle strain reached a high value, based on the erosion criterion, which was

used in the static tests, the element was eroded, and a gap occurred behind the post. To avoid this problem, the erosion criterion was changed in the dynamic simulations. A volumetric strain criterion was used to account for the average of principle strains in all directions.

Table 5. Material constants used in the dynamic finite element subcomponent and full-scale crash simulations.

Material	Constitutive Parameter	Value	Determined from
Steel	Density, ρ	7930 kg/m^3	Material test
	Young modulus, E	200 GPa	[3]
	Poisson's ratio, v	0.3	[3]
	Yield stress for flanges, σ_{yf}	348 MPa	Material test
	Yield stress for the web, σ_{yw}	400 MPa	Material test
Soil	Density, ρ	2300 kg/m^3	Material test
	Cohesion, C	1 kPa	Material test and via system test calibration[a]
	Peak friction angle, ϕ'_p	45^o	Material test and via system test calibration[a]
	Critical friction angle, ϕ'_{cr}	15^o	[1] and via system test calibration[a]
	Shear modulus, G	50 MPa	[47] and via system test calibration[a]
	Poisson's ratio, v	0.25	[48]
Asphalt	Density, ρ	2300 kg/m^3	Material test
	Cohesion, C	500 kPa	Material test
	Friction angle, ϕ'	35°	[49]
	Shear modulus, G	50 MPa	Via system test calibration[a]
	Poisson's ratio, v	0.35	[50]
	Failure volumetric strain, $\varepsilon_{v\text{-failure}}$	%2 mm/mm	Via system test calibration[a]
Rubber	Density, ρ	1365 kg/m3	Material test
	Shear modulus, G	400 MPa	[58]
Foam	Density, ρ	96 kg/m^3	Material test
	Shear modulus, G	100 MPa	[9]

a. The term “system test calibration” refers to the selection of particular material constants based on one selected system test as described above.

Using this criterion did not allow the elements behind the post to be eroded suddenly and made the model more stable under impact loads. Using erosion criterion of volumetric strain equal to 2 percent gave comparable results between FEA simulations and experiments. Although the model was not very sensitive to the value of this number, it was obtained based on the mesh size used in this model, and it is element formulation and mesh size dependent. Smaller meshes or higher order elements captured higher peaks in strains and stresses, and a higher value for erosion criterion was needed. Larger elements, with one point integration, made an average value of strain and stress throughout the element. For these elements, a lower value for the erosion criterion was required. However, slight changes in the element size (up to two times smaller or larger) or mesh did not affect the erosion criterion, and the same value for the erosion criterion could be used. The other material properties including cohesion, friction angle, shear modulus, and Poisson’s ratio remained unchanged after model calibration, and the same values used in the static simulations were employed in the dynamic simulations.

4.4.2 Comparisons between Experiments and FE Simulations

Lee [9] conducted dynamic loading experiments on systems with and without an asphalt layer. First, the system response for the case without an asphalt layer was tested. The results of these experiments were compared with the FEA results. Figure 39 and Figure

40 show the system after impact for FEA and experiments. As can be seen in these figures, the finite element model shows similar behavior to the experiments. The model effectively captured the foam deformation, movement of the post in the soil, and soil plowing behind the post. Element erosion for the soil material in tension was not included in the model. Including element erosion for the soil caused erosion of the elements behind the post due to soil plowing. When the elements were eroded from behind the post, the post could move freely, and the applied force to the post suddenly dropped, which caused instability in the model and did not match what happened in the experiments. Therefore, element erosion was not included for the soil material, and the model was not able to predict the gap in front of the post that occurred during experimental tests, as shown in Figure 40. Although the elements in front of the post experienced large tensile strains, because the cohesion value was given equal to zero, the tensile stresses in the elements in front of the post were approximately zero. Therefore, although there was no gap in the soil in front of the post, because tensile stresses were approximately zero, the tension force applied to the post by the soil was approximately zero, which is similar to a gap in the soil material.

The acceleration of the impactor mass was recorded using an accelerometer installed on the center top of the mass, as shown in Figure 41. Also, the accelerations were obtained using the FEA results. The acceleration-time history comparison is presented in Figure 42. The FEA model can predict the peak acceleration and late response of the system. However, in the experiments, the acceleration had a sharp peak versus a flat peak in the FEA. This occurred because, in the experiment, the foam crushed into separate pieces

and its strength decreased more rapidly than in the FEA. However, the peak acceleration was captured properly and the response of the system, after the foam is crushed, was similar in the FEA and the experiments.

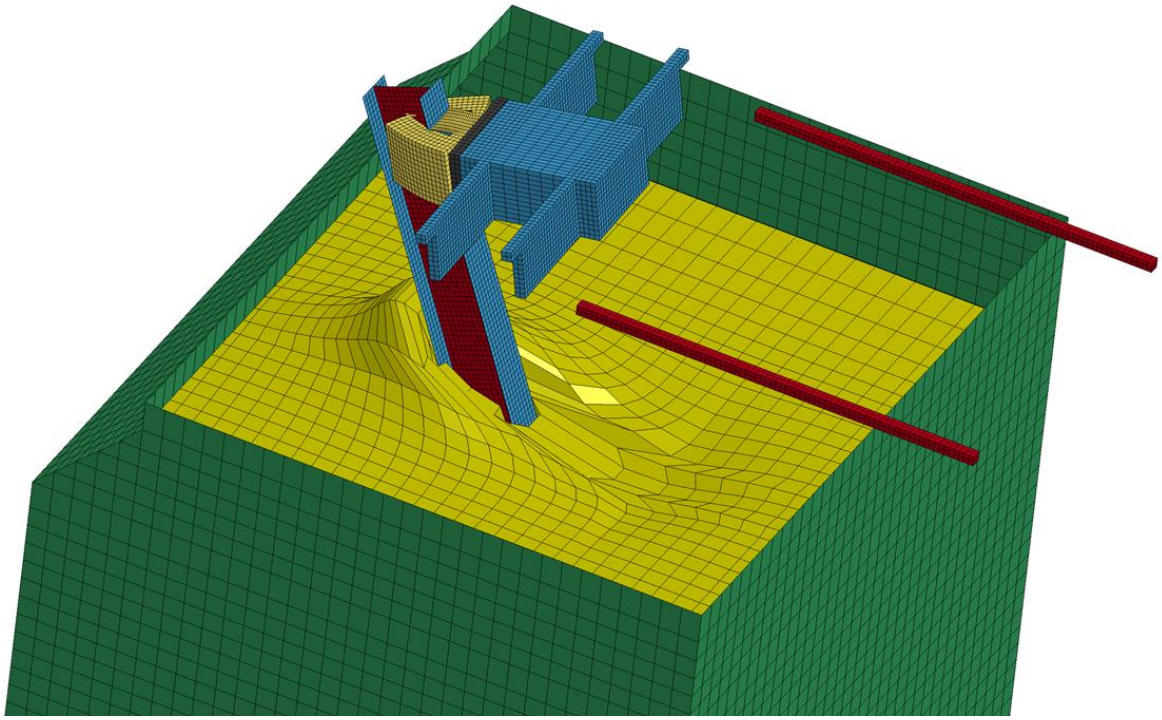

Figure 39. Simulation result for the model with only soil after the impact.

Figure 40. Experimental result for the model with only soil after the impact [9]**.**

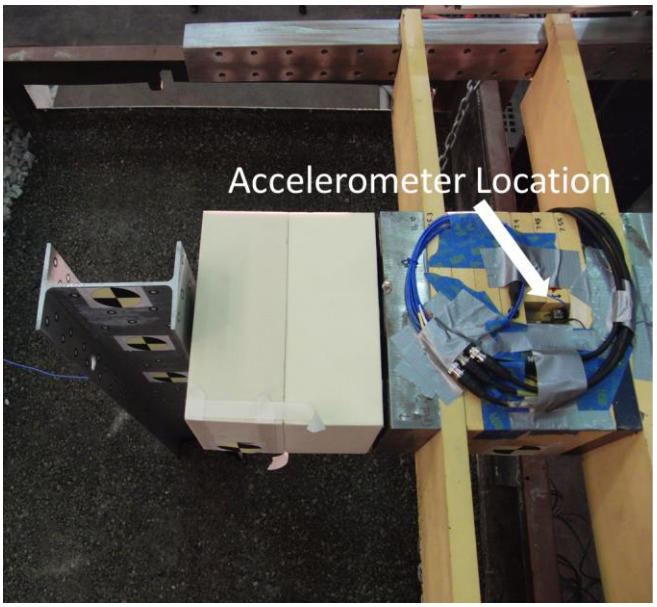

Figure 41. Location of the accelerometers installed on the impactor.

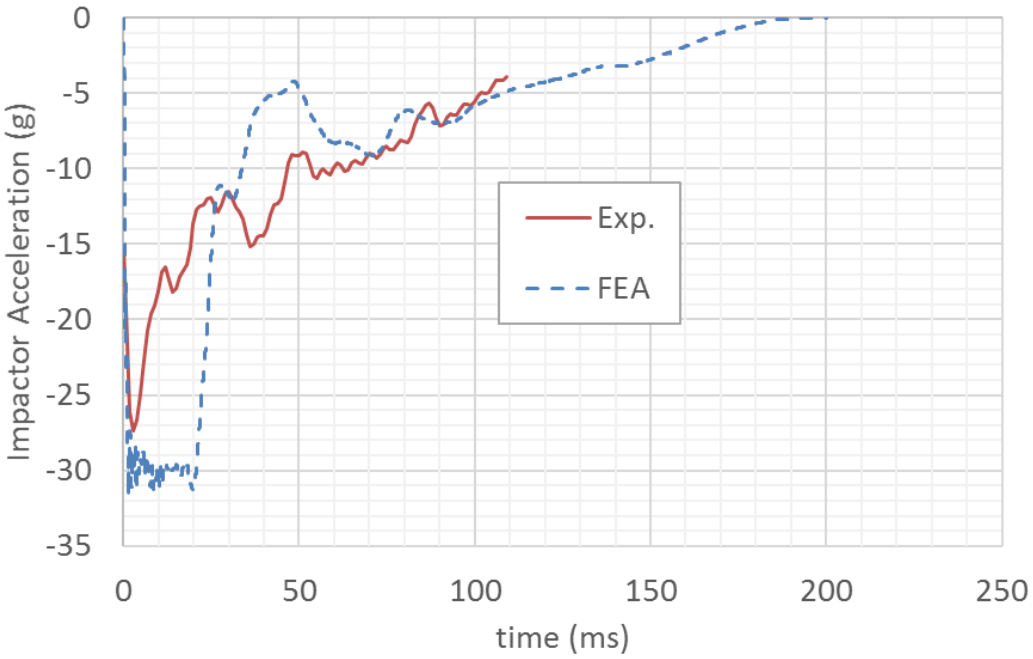

Figure 42. Acceleration-time history obtained from experiments [9] **and FEA.**

The asphalt thickness and rear distance were varied in the FEA simulations and experiments. In one of the cases, an asphalt thickness of 90 mm with a rear distance of 600 mm was used to examine the mow strip setup commonly used in Georgia. The after-impact result for this case is presented in Figure 43 and Figure 44 for the FEA and the experiments, respectively.

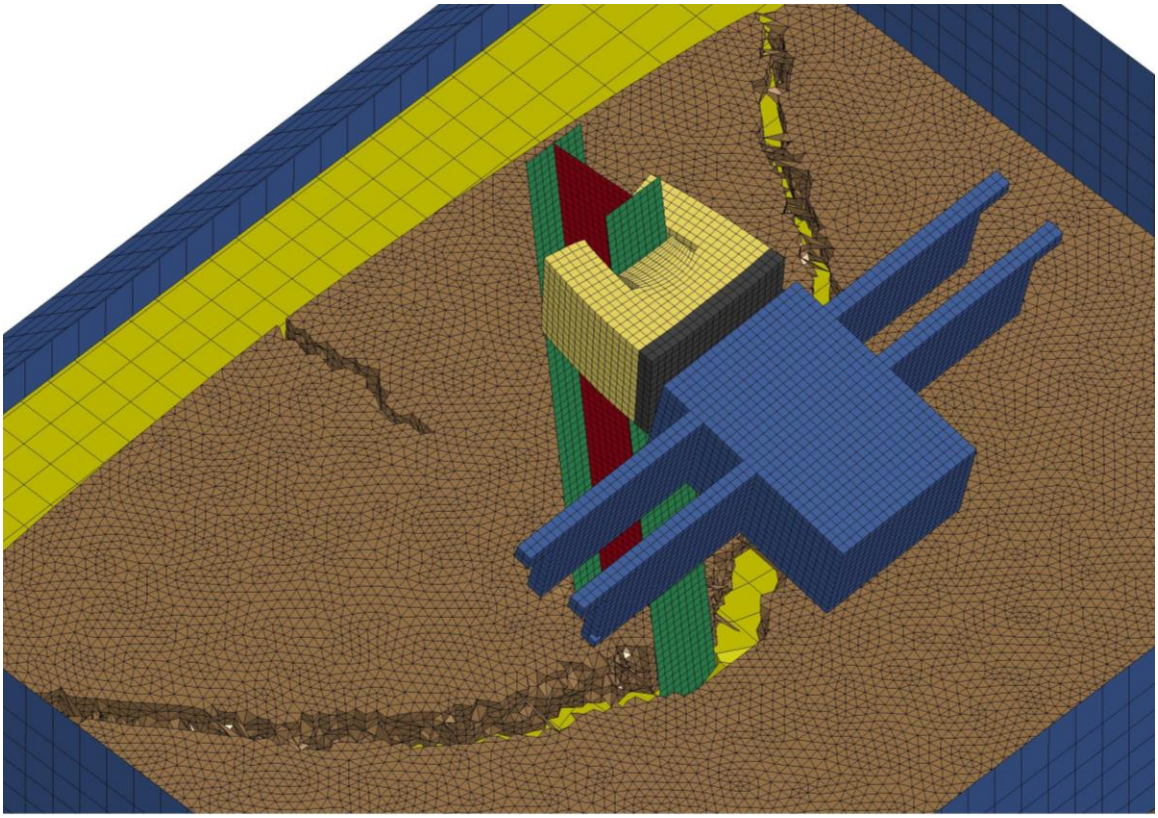

Figure 43. Simulation result for the model with 90 mm thick asphalt and rear distance of 610 mm.

Figure 44. Experimental result for the case with 90 mm thick asphalt and rear distance of 610 mm [9]**.**

The acceleration of the impactor mass was recorded using an accelerometer installed on the center top of the mass, as shown in Figure 41. The accelerations were also obtained using the FEA results. The acceleration-time history comparison is presented in **Figure 45**. The FEA model predicted a peak acceleration close to the one measured in the experiments. Moreover, the shape of the acceleration-time history is similar for both cases before and after the peak the force.

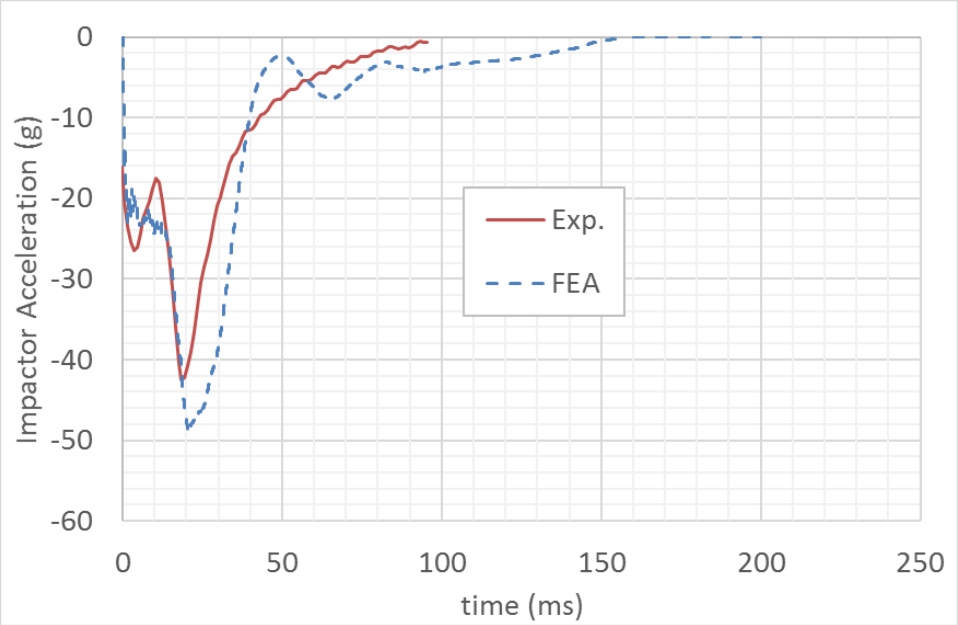

Figure 45. Acceleration-time history obtained from experiments [9] and the FEA.

CHAPTER 5. DYNAMIC PERFORMANCE OF GUARDRAIL SYSTEMS WITH ASPHALT MOW STRIPS

5.1 System Assessment using Quantitative Performance Criteria

5.1.1 Parametric Studies on Asphalt Mow Strip Geometry

As discussed in the previous chapters, changing asphalt mow strip geometry influences the system performance. As the thickness and the rear distance behind the post increase, the ground-level restraint of the asphalt layer on the post increases. Parametric studies on the combination of different thicknesses and rear distances are a critical step to explore the impact of each of these parameters. The asphalt thickness used for a mow strip in the state of Georgia is 90 mm, and the minimum feasible asphalt thickness based on constructability is estimated to be 50 mm. To show the system response for thicker mow strips, 150 mm thick asphalt was included in the simulations. Rear distance values of 0 mm, 300 mm, 600 mm, and 1200 mm were used. The time history of the impactor acceleration, post ground-level displacement, post displacement at the impact point, and post velocity at ground level were measured experimentally [9] and with FE simulations. The results are compared in Table 6. The effective force parameter shown in Table 6 is obtained by dividing the kinetic energy of the impactor (150 kJ) by the peak displacement at the impact point. This parameter is representative of the effective force applied to the post during the impact.

Table 6. Comparison between measurements using subcomponent dynamic tests [9] **and FE simulations.**

Test Description	Mow Strip Size (mm)		Peak Disp. at Impact Point (mm)		Ground Level Disp. (mm)		Peak Ground Level Velocity (m/s)	Peak Force (kN)		Effective Force (kN)	
	Thick.	Rear Dis.	FEA	Exp.	FEA	Exp.	FEA	FEA	Exp.	FEA	Exp.
Thick - Extended Rear Distance	150	1200	175	-	19	-	3.49	79	-	87	-
Thick - Regular Rear Distance	150	600	256	266	61	107	4.53	68	71	59	57
Thick - Reduced Rear Distance	150	300	438	445	184	209	4.81	55	45	35	34
Thick - Zero Rear Distance	150	0	876	-	450	-	5.8	32	-	17	-
GDOT - Extended Rear Distance	90	1200	201	-	48.5	-	3.72	74	-	76	-
GDOT	90	600	317	348	155	130	4.54	65	61	48	44
GDOT - Reduced Rear Distance	90	300	447	656	242	298	4.96	49	29	34	23
GDOT - Zero Rear Distance	90	0	758	-	400	-	5.73	37	-	20	-
Thin - Extended Rear Distance	50	1200	352	-	177	-	4.42	62	-	43	-
Thin - Regular Rear Distance	50	600	455	536	250	267	4.52	53	35	33	28
Thin - Reduced Rear Distance	50	300	517	-	275	-	5.32	47	-	29	-
Thin - Zero Rear Distance	50	0	657	-	349	-	5.74	42	-	23	-
Only Soil	0"	0	600	587	327	275	5.17	41	20	25	26
GDOT with Leave-out	90	600	-	404	-	170	-	-	43	-	38
GDOT with Parallel Pre-Cut	90	600	574	559	299	241	5.39	52	39	26	27
GDOT with Diagonal Pre-Cut	90	600	464	371	237	147	4.91	58	59	33	41
GDOT with Stiffer Asphalt	90	600	169	-	35	-	2.86	80	-	89	-

- Experimental tests or finite element simulations were not performed for setups indicated by a dashed line.

A set of quantitative performance criteria is necessary to evaluate alternative mow strip designs. Ground level displacement, displacement at the impact point, peak force applied to the post, and the effective applied force to the post were chosen to evaluate the system performance [9]. These criteria can be used to compare setups with various mow

strip thicknesses and rear distances with setups incorporating a leave-out. Setups that show more restraint than the setup with a leave-out are less likely to pass full-scale crash tests. Setups that have less restraint than the setup with a leave-out are more likely to pass the crash tests. This is because researchers in the past have demonstrated that setups with leave-out passed the crash tests; therefore, setups with lower ground restraint are expected to pass the tests [3].

5.1.2 Assessment using Peak Force Criterion

The first criterion considered is the peak force criterion. This criterion is based on the fact that higher peak force applied to the post before its failure shows higher ground restraint of the post. Figure 46 shows an FE simulation contour plot of peak force applied to the post. Experimental data [9] are marked on the plot with parentheses. Mow strip setups with the thicknesses and rear distances associated with the dashed lines have less ground level restraint than setups with leave-out. The dotted lines have more restraint than leave-out setup, which is shown with a solid line. For example, as shown in Figure 46, guardrail posts installed in mow strips with 50 mm thickness and 300 mm rear distance are more likely to pass a full-scale crash test.

5.1.3 Assessment using Peak Displacement Criterion

Figure 47 shows an FE simulation contour plot of the peak displacement of the post at the impact point. Larger displacement is an indication of less restraint of the posts.

Experimental data [9] are marked on the plot with parentheses. For example, as shown in Figure 47, guardrail posts installed in mow strips with 50 mm thickness and 600 mm rear distance are more likely to pass a full-scale crash test.

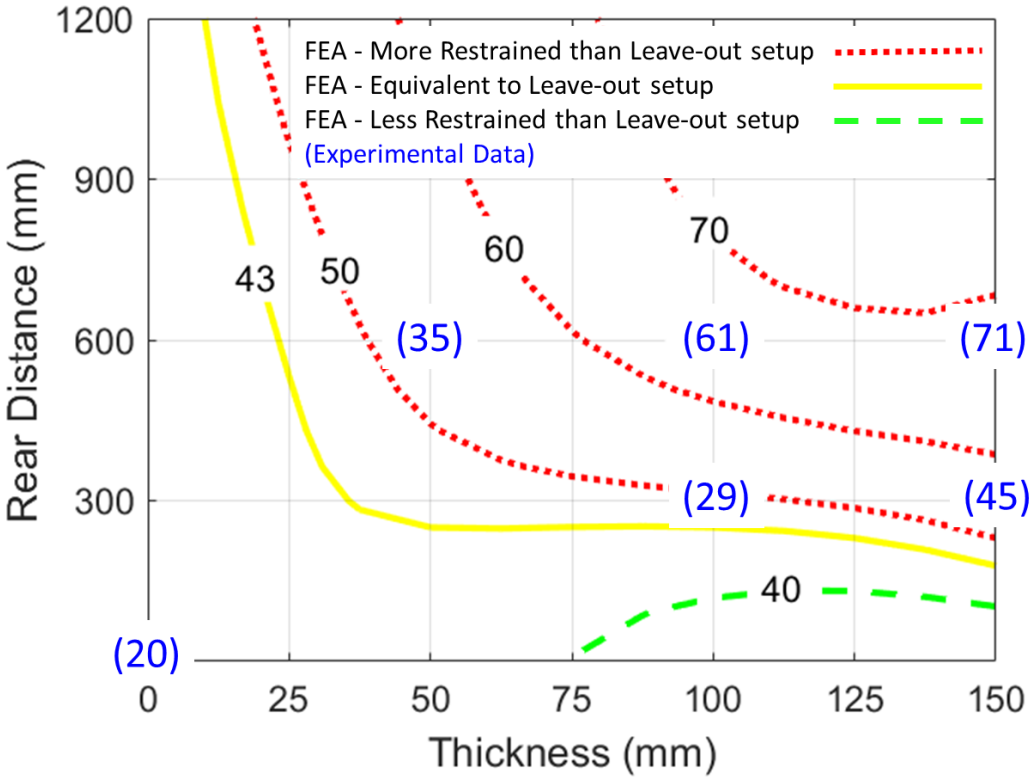

Figure 46. FEA contour plots for combinations of thickness and rear distance. Curves are a representation of peak applied force to the post (kN). Experimental results are given in parentheses [9]**.**

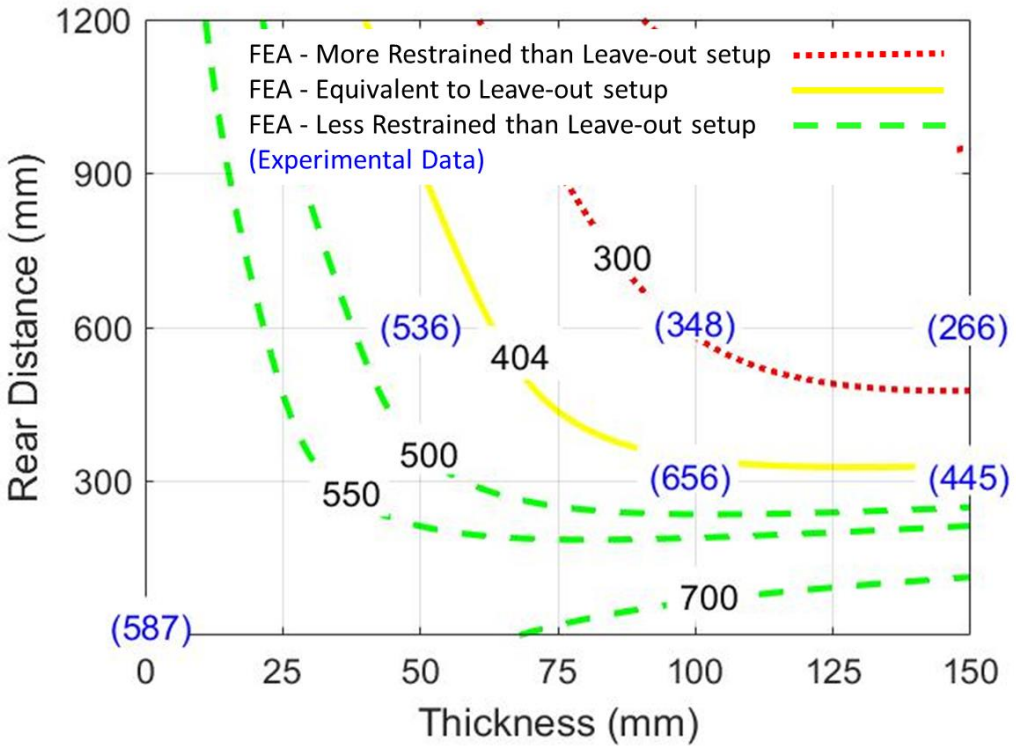

Figure 47. FEA Contour plots for combinations of thickness and rear distance. Curves are a representation of peak displacement at impact point (mm). Experimental results are given in parentheses [9]**.**

5.1.4 Assessment using Ground Level Displacement Criterion

Figure 48 shows an FE simulation contour plot of residual ground level displacement of the post after the impact. Larger ground level displacement is an indication of less ground restraint of guardrail posts. Experimental data [9] are marked on the plot with parentheses. For example, as shown in Figure 48, guardrail posts installed in mow strips with 50 mm thickness and 450 mm rear distance are more likely to pass a full-scale crash test.

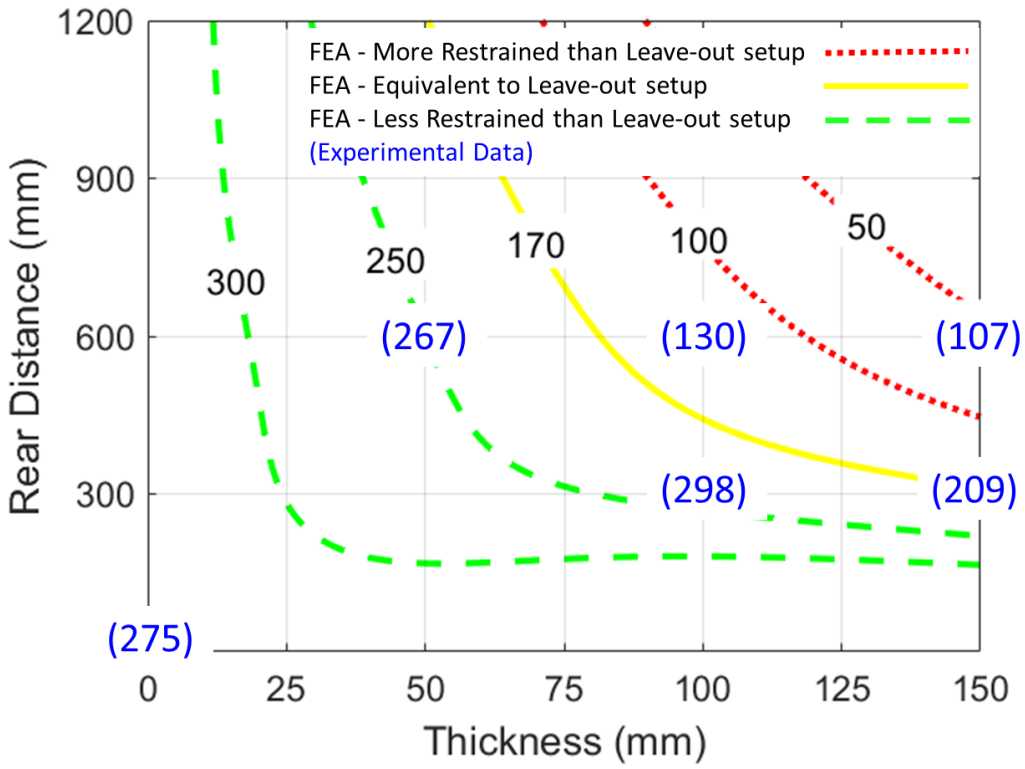

Figure 48. FEA Contour plots for combinations of thickness and rear distance. Curves are a representation of ground level displacement (mm). Experimental results are given in parentheses [9]**.**

5.1.5 Assessment using Effective Force Criterion

Figure 49 shows an FE simulation contour plot of effective force, which is obtained by dividing the kinetic energy of the impactor (150 kJ) by the displacement of the impact point. Larger effective applied force is an indication of higher ground restraint. Experimental data [9] are marked on the plot with parentheses. For example, as shown in Figure 49, guardrail posts installed in mow strips with 50 mm thickness and 300 mm rear distance are more likely to pass a full-scale crash test.

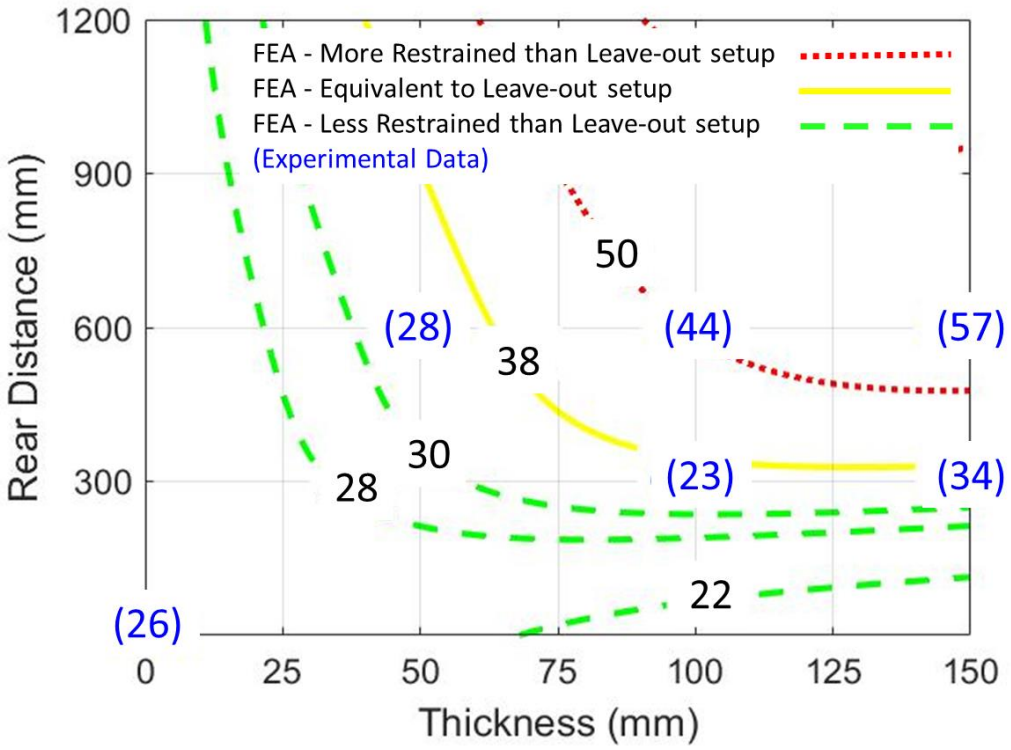

Figure 49. FEA Contour plots for combinations of thickness and rear distance. Curves are a representation of effective applied force to the post (kN). Experimental results are given in parentheses.

5.1.6 Assessment using Combination of the Four Criteria

The four contour plots are plotted together in Figure 50. Because the peak displacement criterion and the effective force criterion have the same shape, they are shown with only one curve. Any design below all criteria lines is expected to show less ground restraint than the typical leave-out design introduced in the Roadside Design Guide. On the other hand, a setup that is above the criteria lines is expected to exhibit a higher level of ground restraint than setups with a leave-out. These contours are used to better understand

the behavior of guardrail post setups with mow strip and their relative performance. However, these curves cannot be used solely to reject or approve a setup to be used for road safety. The dynamic testing results give insight into the anticipated behavior in full-scale crash simulations of various mow strip designs, which are discussed in the next chapter.

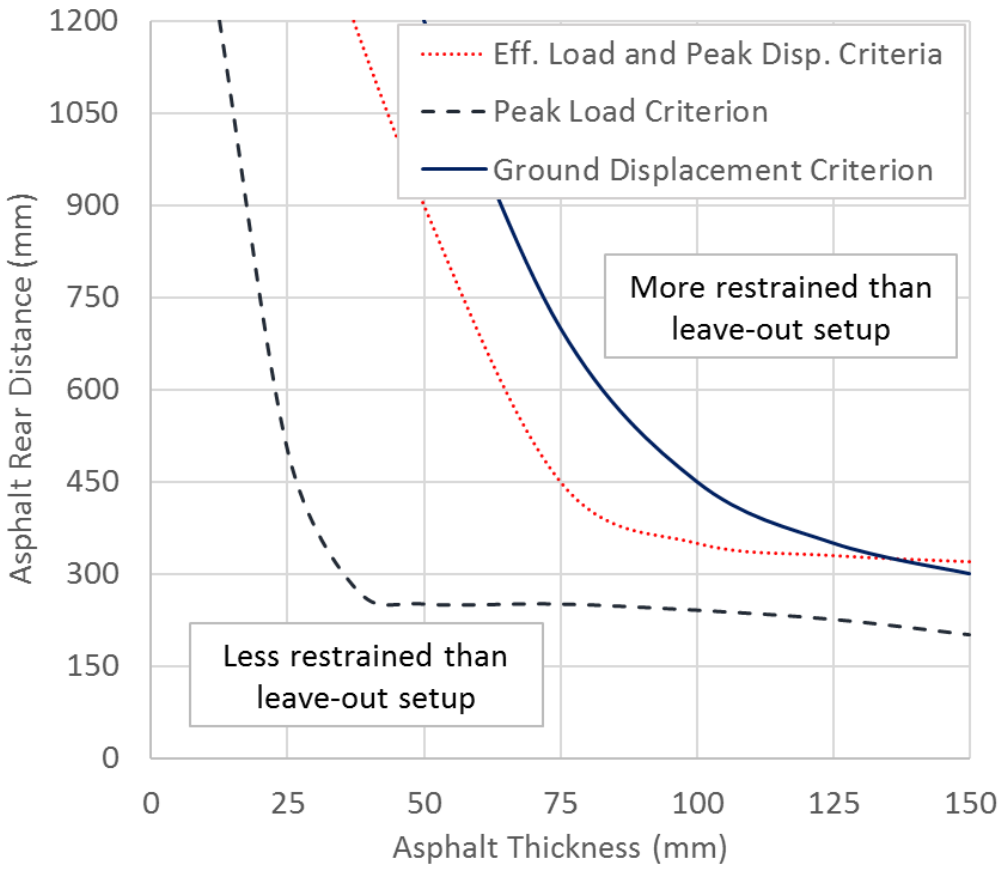

Figure 50. FEA contour plots for combinations of thickness and rear distance. Curves are a representation of ground level displacement (mm), peak displacement at the impact point (mm), peak applied force (kN), and effective applied force (kN) for setups with equivalent restraint to the leave-out setup.

5.1.7 Effect of Asphalt Pre-Cutting

Based on the experimental results [9], rupture is the primary mechanism of the asphalt failure around the guardrail post. As the rupture propagates, the strength of the asphalt layer decreases up to the point that a portion of the asphalt detaches from the rest of the mow strip. After this occurs, the asphalt has a negligible impact on the system and the soil is the only source of ground restraint. Therefore, one potentially effective way to decrease mow strip restraint is to add pre-cuts to the asphalt layer. Based on the results discussed in Section 3.3, the two most effective cuts were selected for the dynamic tests: diagonal (Figure 51) and parallel (Figure 52) cuts. The cuts were selected based on the experimental and numerical investigations of various rupture patterns. These designs shorten the distance that the asphalt rupture needs to propagate until one part detaches from the rest of the layer. These two cut patterns were tested experimentally [9] and using numerical simulations. The results are presented in Table 6. Comparing the values of various parameters for the asphalt layer with pre-cuts and for the leave-out setup shows that the peak force is higher for setups with pre-cuts because the peak force occurs in early system response, which is more affected by the asphalt layer. Pre-cut setups provide less restraint based on the comparison of ground level displacement, displacement at the impact point, and the effective applied force. Considering these three criteria,, guardrail systems utilizing these pre-cuts show less ground restraint than the leave-out. However, based on

the peak force criterion, they show higher ground level stiffness for the early system response.

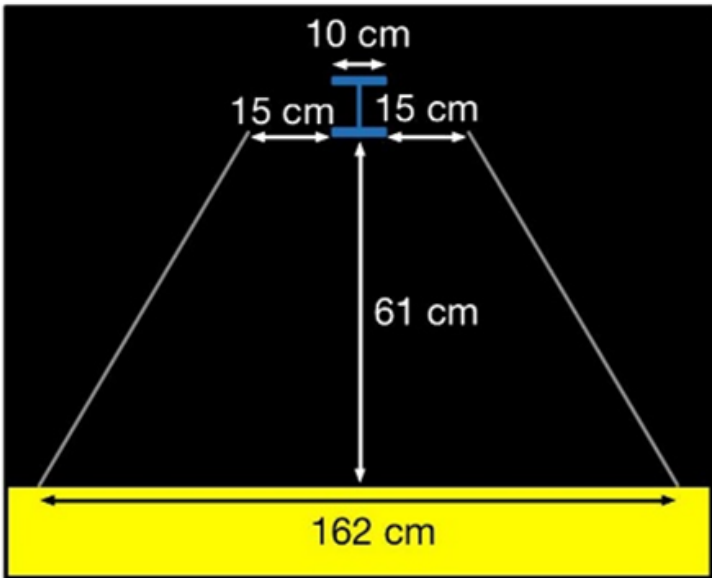

Figure 51. Diagonal asphalt pre-cut used in the dynamic tests and simulations.

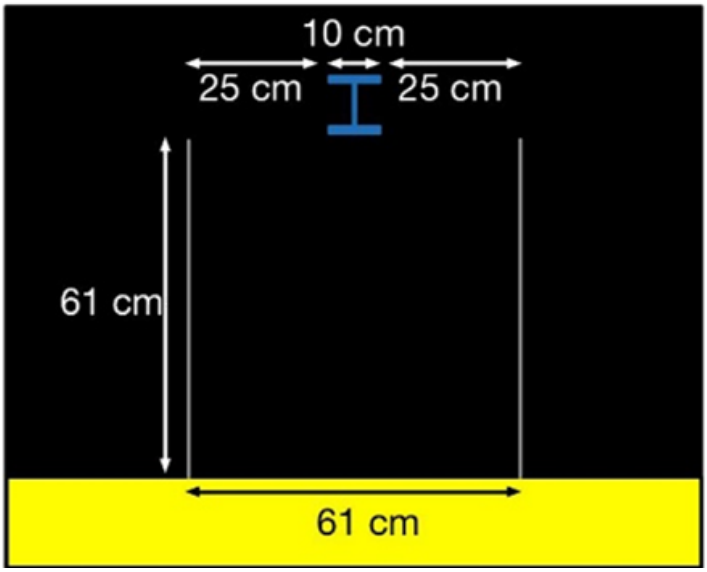

Figure 52. Parallel asphalt pre-cut used in the dynamic tests and simulations.

5.1.8 Effect of Asphalt Material Properties

In some cases, the asphalt layer could be extremely cold, or an asphalt mix other than the one classified as PG 76-22 binder and 19 mm aggregate size could be used, leading to stiffer and stronger asphalt than the asphalt used in this research, which had 500 kPa cohesion and 35 degree friction angle. Therefore, the GDOT setup with 90 mm thickness and 600 mm rear distance was simulated with a stiffer and stronger asphalt layer to show how the system would respond when the asphalt layer could potentially be stiffer than normal. The value of cohesion, shear modulus, and the volumetric failure strain were increased to 930 kPa, 93 MPa, and 0.04 mm/mm based on the specimen tests done by Lee [9] on the stiffer asphalt. The simulation result is presented in Table 6 and Figure 53.

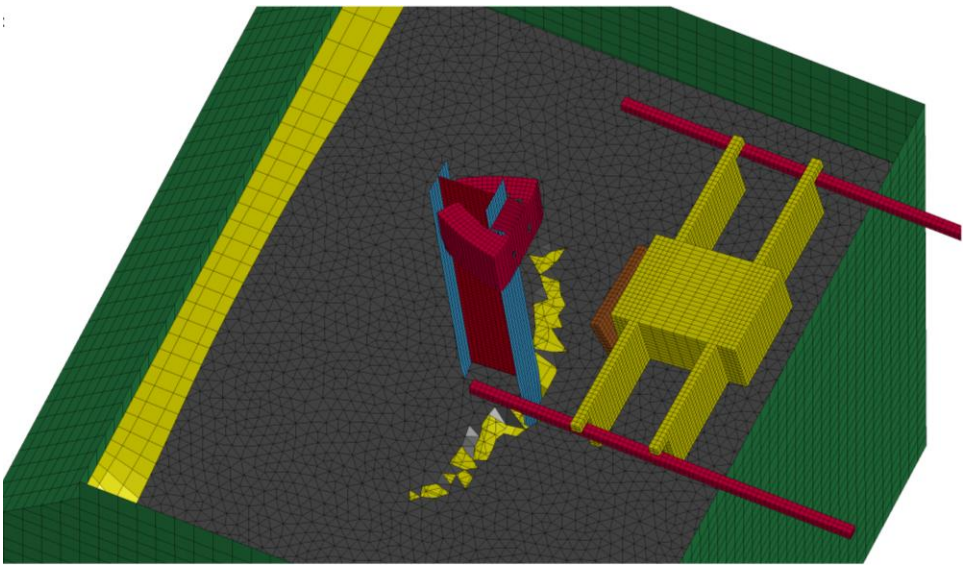

Figure 53. Simulation result for 90 mm thick asphalt with 600 mm rear distance and a stiffer asphalt.

Only a limited asphalt rupture occurs, and the results show that this change in the material properties makes the asphalt layer significantly stronger than the asphalt used in this research. This decreases the likelihood that a guardrail system with these asphalt properties will pass a full-scale crash test.

The rupture capacity of an asphalt layer per unit of thickness can be estimated using Eq. 19 (derived in Section 7.2.1.3): $p_r = c\,(r+h)(a_r + f_r\phi)$. c is the asphalt cohesion, r is the mow strip rear distance, h is the post cross-section depth, and a_r and f_r are constants equal to 2.87 and -0.025, respectively. Based on this equation, the rupture capacity is a function of the mow strip material properties and geometry. The full rupture capacity of the asphalt layer can be obtained as

$$P_r = t \ p_r \tag{3}$$

where *t* is the asphalt layer thickness. The contour plots presented in this chapter (Figure 46 through Figure 50) and Chapter 3 (Figure 25 throughFigure 28) are for the type of asphalt with cohesion equal to 500 kPa, friction angle equal to 35 degrees, and shear modulus equal to 50 MPa. Based on Eq. 19, if the asphalt material properties change, the rupture capacity changes, and therefore the contour plots change. However, the contour plots can still be used to estimate the system performance for other asphalt types with cohesion *c*, friction angle ϕ, and thickness *t* using an equivalent thickness obtained as $t_e =$

$$\frac{\acute{c}(a_r + f_r \acute{\phi}\ )t}{c(a_r + f_r\ \phi)} \tag{4}$$

where the reference cohesion $\acute{c}$ and reference friction angle $\acute{\phi}$ are equal to 500 kPa and 35 deg, which were used to draw the contour lines. For example, for the stiffer asphalt with cohesion equal to 930 kPa, rear distance equal to 600 mm, and friction angle equal to 35 degrees, the asphalt layer becomes 1.86 times (computed from 930/500) stronger than the asphalt layer with cohesion equal to 500 kPa. Therefore, a 90 mm thick layer with the stiffer asphalt has an equivalent thickness of 167 mm (computed from 1.86 * 90mm). The peak force, peak displacement, ground level displacement, and effective force for a guardrail post with 90 mm thick layer and the stiffer asphalt, with 600 mm rear distance can be estimated using the points on the contours (Figure 25 through Figure 28 and Figure 46 through Figure 50) associated with 167 mm thickness and 600 mm rear distance. The

estimated values of these parameters using the equivalent thickness method are compared with the results obtained from finite element simulations in Table 7. The values of the parameters predicted by finite element simulations differ up to 27% from the values estimated using the equivalent thickness method. Although the estimates are not as accurate as the simulation results, they can be used as a fast estimate of the system response.

Moreover, using the results presented in Chapter 6 for other asphalt cohesion values and friction angles, the equivalent thickness method can be utilized to estimate the full-scale crash simulation results, assuming that changes in shear modulus do not significantly change the system response.

Table 7. Comparison between measurements predicted by FE simulations and estimated using the equivalent thickness method for a mow strip with the stiffer asphalt and 600 mm rear distance.

Test Description	Peak Disp. at Impact Point (mm)	Ground Level Disp. (mm)	Peak Force (kN)	Effective Force (kN)
Estimated Using the Equivalent Thickness Method	215	40	74	73
Predicted by the FE Simulations	169	35	80	89
Percent Difference	27%	14%	8%	18%

CHAPTER 6. ASSESSMENT USING MASH FULL-SCALE CRASH SIMULATIONS

6.1 Finite Element Model Description

The vehicle model used for the simulation in this research was the 2007 Chevrolet Silverado, which was developed and verified by National Crash Analysis Center (NCAC) [59]. This vehicle model represents the *MASH* 2270P test vehicle and has approximately one million elements. A validated model for the guardrail system was also obtained from NCAC. The model was updated for this research by increasing the rail height to match MGS W-beam guardrail system with 31-inch rail height. The guardrail splices were originally located at the posts. The splices were moved to between guardrail posts in the model to match the current MGS designs. An asphalt layer was added to the model, and the material properties of the soil and steel were updated. The hourglass formulation, element size, and material properties used in Chapter 4 for modeling of one guardrail post system were used here for the full-scale crash model. The material properties are summarized in Table 8. The model had 29 posts. Initial vehicle impact was to occur 13 ft – 3½ in. (4051.3 mm) upstream of the middle post in the model (post #15), as shown in Figure 54, which was selected using the critical impact point (CIP) plots in MASH guidelines. The complete model had approximately 1.3 million elements.

Table 8. Material constants used in the full-scale crash simulations.

Material	Constitutive Parameter	Value	Determined from
Steel	Density, ρ	7930 kg/m^3	Material test
	Young modulus, E	200 GPa	[3]
	Poisson's ratio, v	0.3	[3]
	Yield stress for flanges, σ_{yf}	348 MPa	Material test
	Yield stress for the web, σ_{yw}	400 MPa	Material test
Soil	Density, ρ	2300 kg/m^3	Material test
	Cohesion, C	1 kPa	Material test and via system test calibration[a]
	Peak friction angle, ϕ'_p	45^o	Material test and via system test calibration[a]
	Critical friction angle, ϕ'_{cr}	15^o	[1] and via system test calibration[a]
	Shear modulus, G	50 MPa	[47] and via system test calibration[a]
	Poisson's ratio, v	0.25	[48]
Asphalt	Density, ρ	2300 kg/m^3	Material test
	Cohesion, C	500 kPa	Material test
	Friction angle, ϕ'	35°	[49]
	Shear modulus, G	50 MPa	Via system test calibration[a]
	Poisson's ratio, v	0.35	[50]
	Failure volumetric strain, $\varepsilon_{v\text{-failure}}$	%2 mm/mm	Via system test calibration[a]

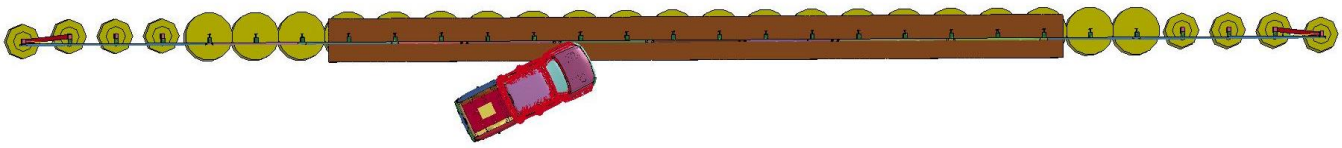

Figure 54. FE model with 29 posts.

First, the model was validated for the case without mow strips by comparing the simulation results with available experimental test results [60]. Thereafter, the validated model was used to simulate guardrail systems with various mow strip designs (Table 9) to assess the effect of mow strip geometric and material properties on the system performance.

Table 9. Full-Scale Crash Simulations.

Test Number	Mow Strip Thickness (mm)	Mow Strip Rear Distance (mm)	Mow Strip Modification
Soil Only	No Mow Strip	No Mow Strip	No Mow Strip
T50-R600	50	600	None
T90-R300	90	300	None
R90-R600	90	600	None
T150-R600	150	600	None
T90-R600-C	90	600	Diagonal Pre-cuts
T90-R600-S	90	600	Stiffer Asphalt

6.2 Evaluation Based on MASH Guidelines

The simulations presented here are based on MASH test 3-11 with a 2270P vehicle on MGS 31-inch guardrail systems embedded in asphalt mow strips. In this test, a 2,270 kg vehicle (a 2007 Chevy Silverado in this research) impacts the guardrails with an angle of 25 degrees and speed of 100 km/h. Several parameters must be obtained from full-scale crash simulations and tests based on MASH guidelines. These parameters are used in this research and are briefly explained in the following.

Based on MASH, occupant risk is assessed by the response of a hypothetical, unrestrained front seat occupant whose motion relative to the occupant compartment is dependent on vehicle accelerations. The occupant, as an assumed point mass, moves through space until striking a hypothetical instrument panel, windshield, or side structure and subsequently is assumed to experience the remainder of the vehicle acceleration pulse by remaining in contact with the interior surface. There are two performance factors:

1. Lateral and longitudinal occupant impact velocities (OIV) at the time of initial contact with interior surfaces of the vehicle. The following expression is used for the occupant impact velocity

   $$\mathrm{OIV}_{x,y} = \int_0^{t^*} a_{x,y}\,dt \qquad (5)$$

   where $\mathrm{OIV}_{x,y}$ is occupant-to-car interior impact velocity in *x* and *y* directions; $a_{x,y}$ is vehicle acceleration in *x* and *y* directions; and t^* is the smaller of the time when

the occupant has traveled 610 mm forward or 305 mm lateral. Time t^* is determined by incremental integration as follows

$$X = \int_0^{t_x^*} \int_0^{t_x^*} a_x dt^2 \quad (6)$$

$$Y = \int_0^{t_y^*} \int_0^{t_y^*} a_y dt^2 \quad (7)$$

$$t^* = min\left(t_x^*, t_y^*\right) \quad (8)$$

where X is 0.610 mm, and Y is 0.305 mm. The preferred limit for the longitudinal and lateral OIVs is 9.1 m/s, and the maximum allowed limit is 12.2 m/s.

2. Largest lateral and longitudinal vehicular or occupant ride down acceleration, ORA, averaged over every 10 m/s interval for the collision pulse subsequent to occupant impact time, t^*. After the occupant impact with the vehicle interior, the occupant, vehicle acceleration, and velocity are assumed to be equal. The interval of 0.010 s is chosen because spikes of minimum duration to produce injury range from 0.007 s to 0.04 s. ORA can be obtained using accelerometers at the center of mass of the vehicle. The preferred limit for the longitudinal and lateral ORAs is 15 g, and the maximum allowed limit is 20.49 g.

Moreover, the vehicle should remain upright during and after the collision. The maximum roll and pitch angles are not to exceed 75 degrees. All accelerations and rotations of the vehicle are measured using a local coordinate system located at the center of mass of the vehicle. The standard coordinate system suggested by MASH is shown in Figure 55.

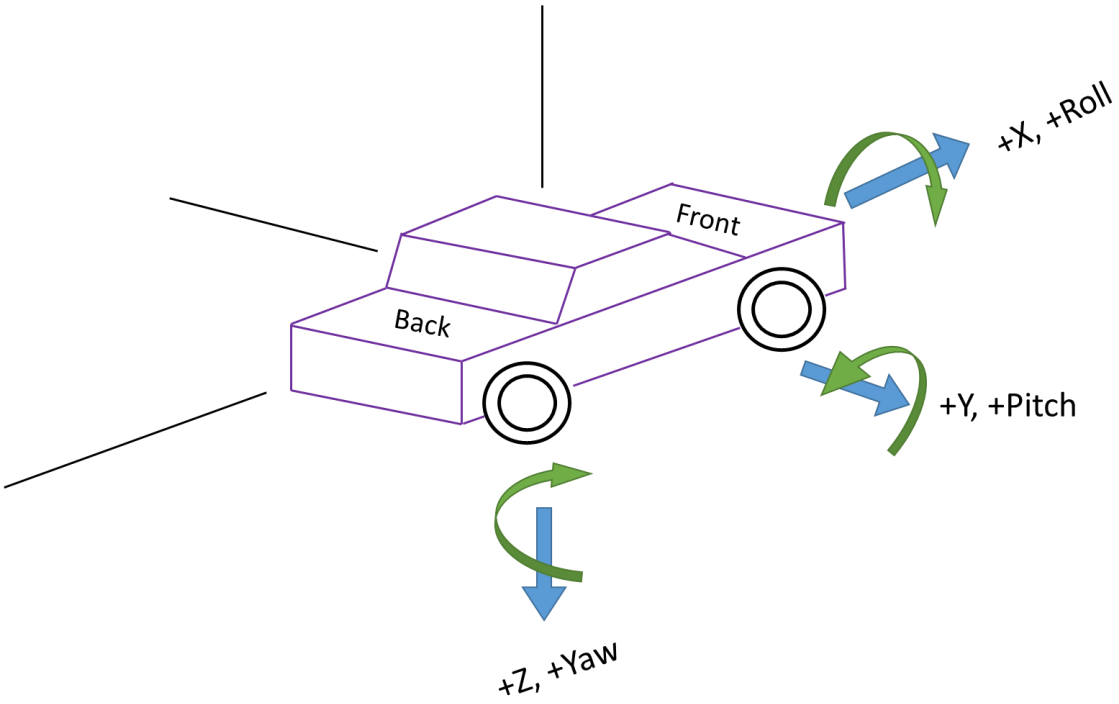

Figure 55. The suggested coordinate system in MASH.

The deformation of the guardrail system can be assessed by measuring the maximum deflection of the rails during the collision (dynamic deflection) and the permanent deflection at the end of the collision. These two parameters were obtained from the simulations and are reported in this research. Although these parameters give a good measure of guardrail system deflection, they are not completely representative of the relative ground stiffness of systems with different mow strips. The guardrail posts close to the impact point usually fail, and their tops move considerably even with very stiff asphalt mow strips. However, if the mow strip is extremely strong, then the ground level displacement of the posts is very limited. Therefore, the summation of ground level

displacement of all posts is used as an additional parameter to better assess the relative ground stiffness of the various mow strips considered in this research. This parameter is a direct measure of ground level stiffness and ground level translation of the guardrail system, which is critical in this research. If the guardrail posts do not translate sufficiently at the ground level, then the likelihood of wheel snagging and vehicle pocketing increases. Pocketing failure causes the vehicle to get stuck into the guardrail, and it does not get redirected back to the road. A sudden stop of the vehicle during pocketing failure causes large deformations of the vehicle and extremely high vehicle deceleration, leading to a crash test failure.

6.3 Full-Scale Crash Simulation Results

6.3.1 Guardrail System without Mow Strip (Soil Only)

First, a baseline model without added asphalt mow strips was considered for validation and to establish a baseline for comparison with cases with asphalt mow strips. The simulation results are graphically presented in Figure 56 throughFigure 61. During the collision, the leading front wheel of the vehicle hit a guardrail post at approximately 0.1 sec (Figure 56 and Figure 58 at 0.1 sec). The wheel failed partially but stayed connected to the vehicle and continued to rotate throughout the remainder of the simulation, as shown in Figure 61. At approximately 0.2 sec the vehicle hit the second post (Figure 56 and Figure 58 at 0.2 sec) and passed over this post. The vehicle moved forward and hit the third post at approximately 0.3 sec (Figure 56 and Figure 58 at 0.3 sec).

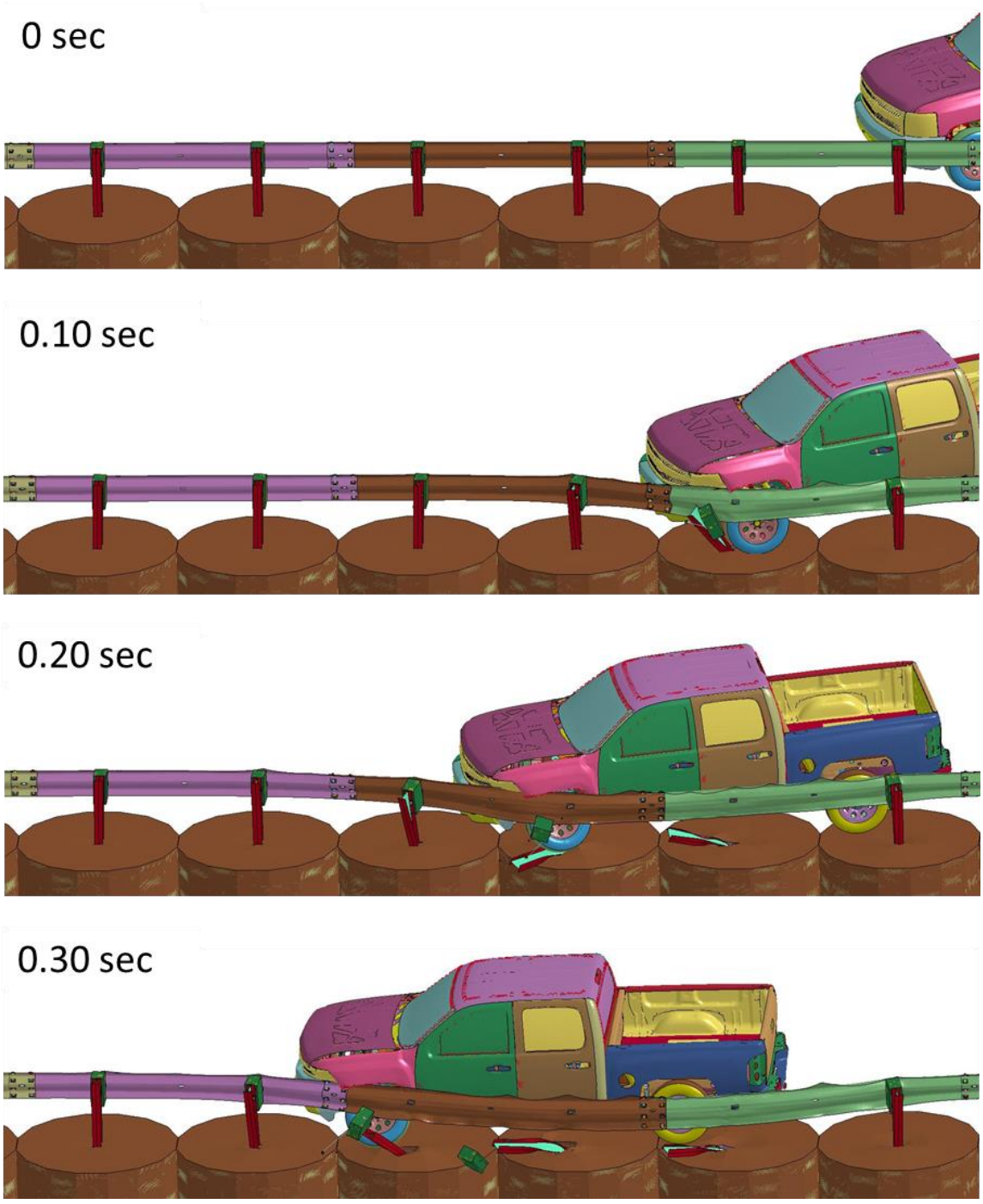

Figure 56. Simulation result for the guardrail system without mow strip – up to 0.3 sec.

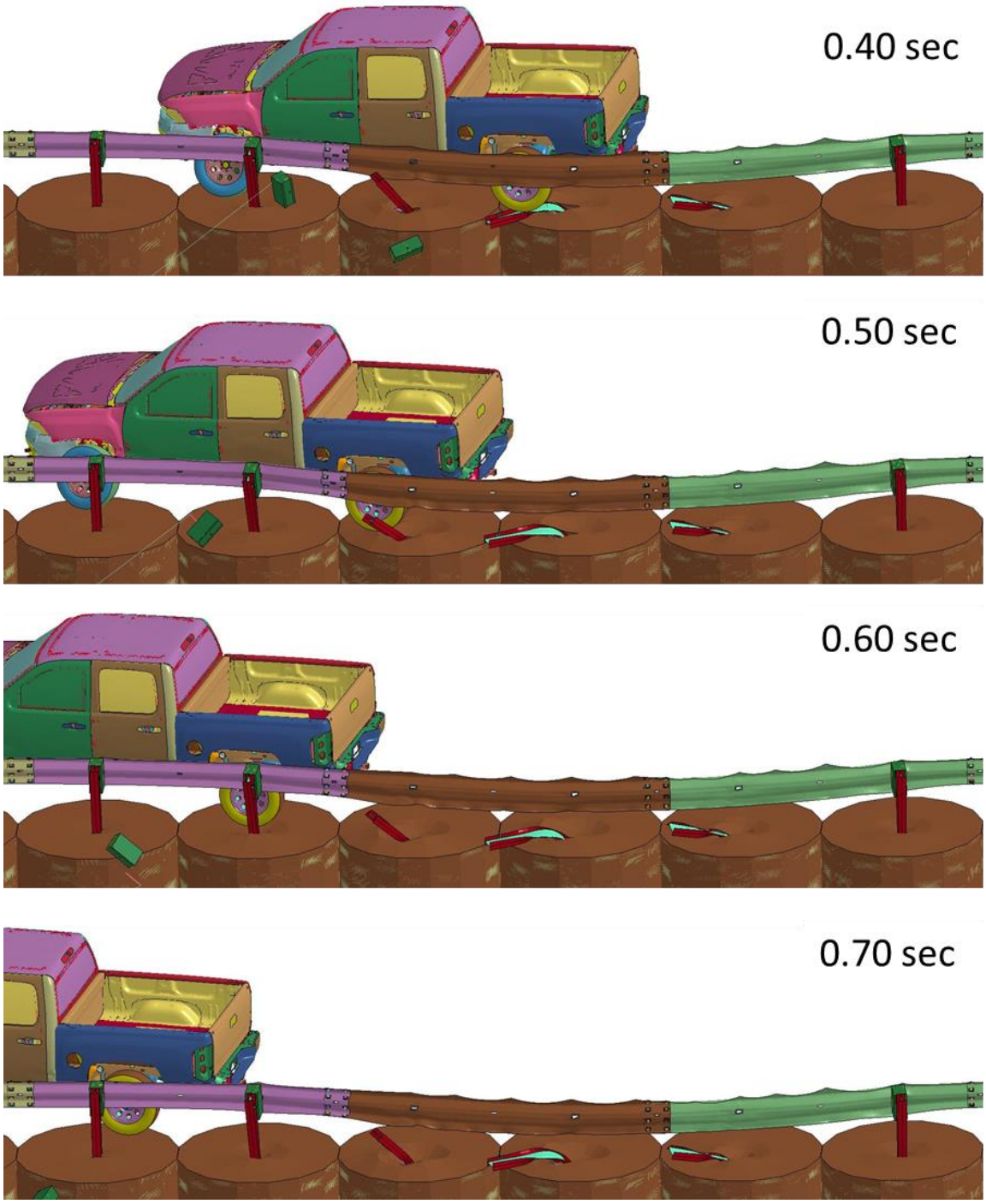

Figure 57. Simulation result for the guardrail system without mow strip–after 0.3 sec.

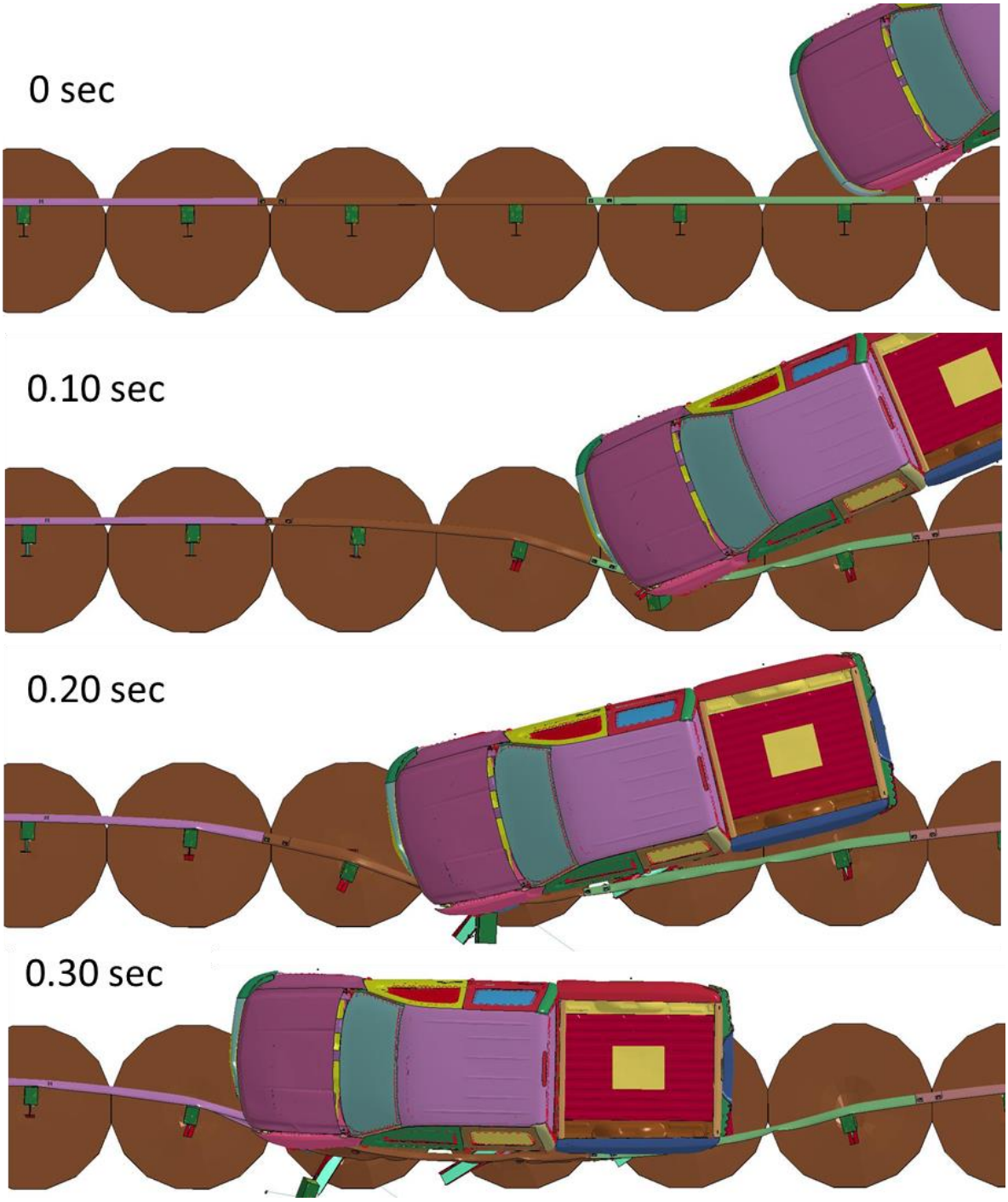

Figure 58. Simulation result for the guardrail system without mow strip – up to 0.3 sec.

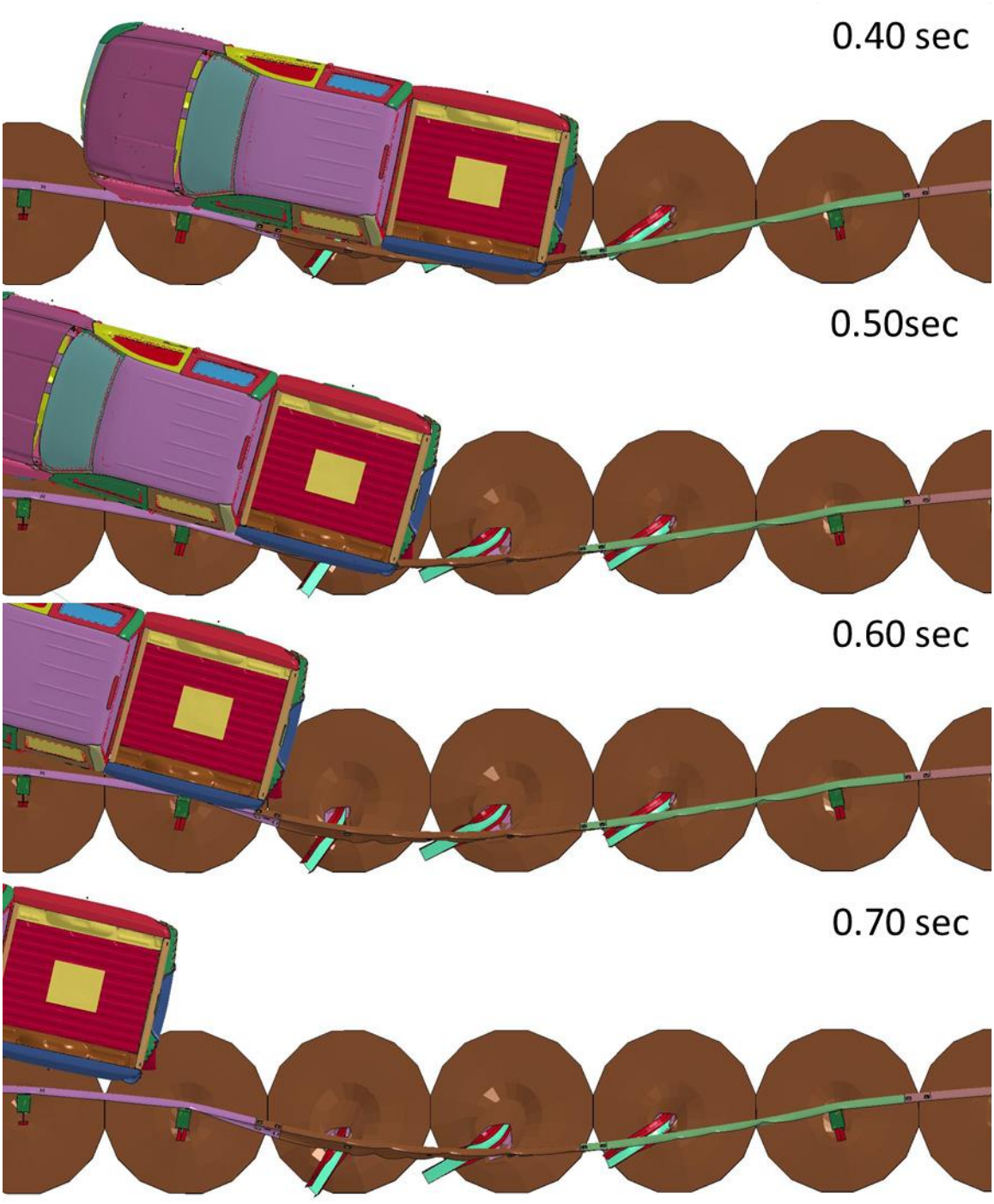

Figure 59. Simulation result for the guardrail system without mow strip–after 0.3 sec.

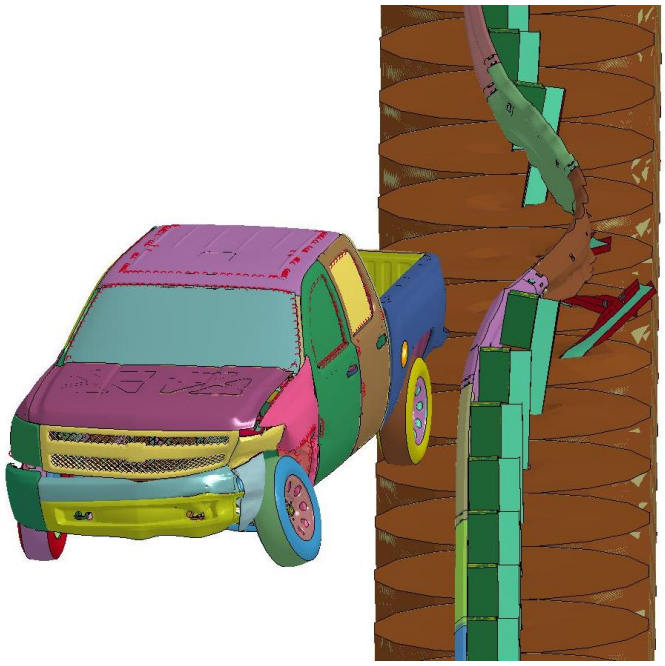

Figure 60. Simulation result for the guardrail system without mow strip.

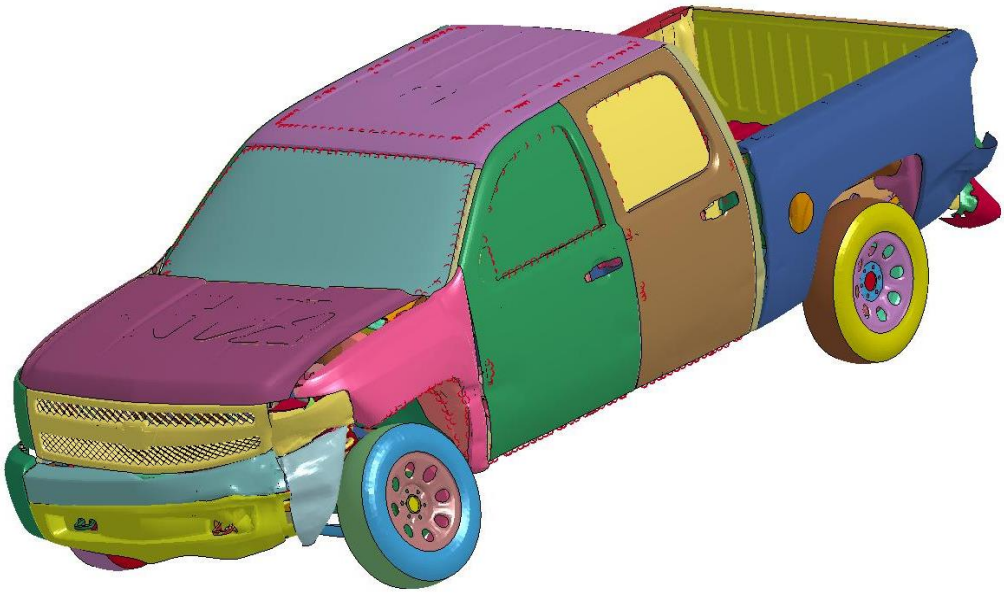

Figure 61. Vehicle deformation for the guardrail system with soil only.

However, the wheel did not completely go over the post, which happened to the first and second posts. At this point, the vehicle was parallel to the guardrail. The vehicle was redirected back to the road and lost contact with the guardrail at approximately 0.65 sec. Vehicle pocketing did not occur during this simulation.

The longitudinal and lateral accelerations of the vehicle were obtained and are shown in Figure 62 andFigure 65. The integration of these accelerations over time produced the velocity of the occupant relative to the vehicle in longitudinal and lateral directions that are presented in Figure 63 andFigure 66. Integration of the velocity resulted in the displacement of the occupant relative to the vehicle, as presented in Figure 64 and Figure 67. The times when the lateral displacement became equal to 305 mm and when the longitudinal displacement became equal to 610 mm were found using the relative displacement curves (Figure 64 andFigure 67). The smaller of these two was for the lateral displacement equal to 0.142 sec. This means that the occupant first hit the interior of the vehicle on his sides before hitting somewhere in front of him in the vehicle. After the occupant hit the interior, it is assumed that his velocity and acceleration were the same as the vehicle. This is why the horizontal axis is extended only up to 0.2 sec, which was slightly after the time when the occupant hit the interior of the vehicle, in Figure 63 and Figure 64 where relative displacement or velocity of the occupant is presented. The longitudinal and lateral occupant impact velocities (OIVs) were found using the relative velocity curves (Figure 63 andFigure 66) by finding the relative velocities at 0.142 sec. Thereafter, the peak accelerations from the acceleration curves (Figure 62 and Figure 65)

were found for the period of time after 0.142 sec until the end of the collision. The OIVs and ORAs were smaller than the maximum limit in MASH guidelines. The results are reported in Table 10.

The roll, pitch, and yaw angles of the vehicle were recorded during the simulation. The time histories for these parameters are shown in Figure 68 throughFigure 70. The peak values of roll and pitch were less than MASH limit, which is equal to 75 deg. The initial impact angle of 25 degrees was subtracted fom the yaw angle at the time when the vehicle lost contact with the guardrail to determine the exit angle. The peak values of yaw, roll, and pitch angles, the exit angle, and the exit speed of the vehicle are reported in Table 10.

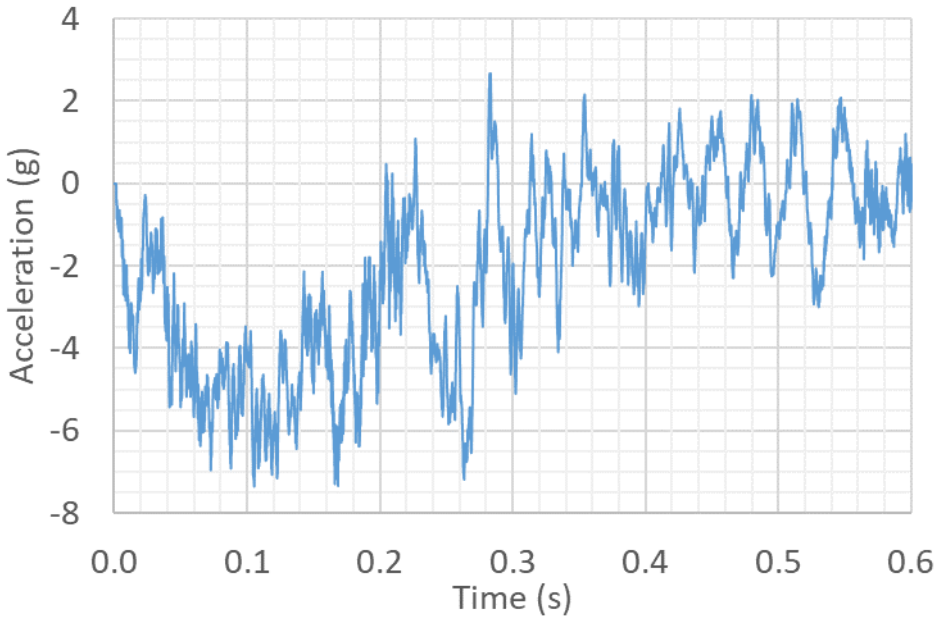

Figure 62. 10 m/s average vehicle longitudinal acceleration (g) – soil only.

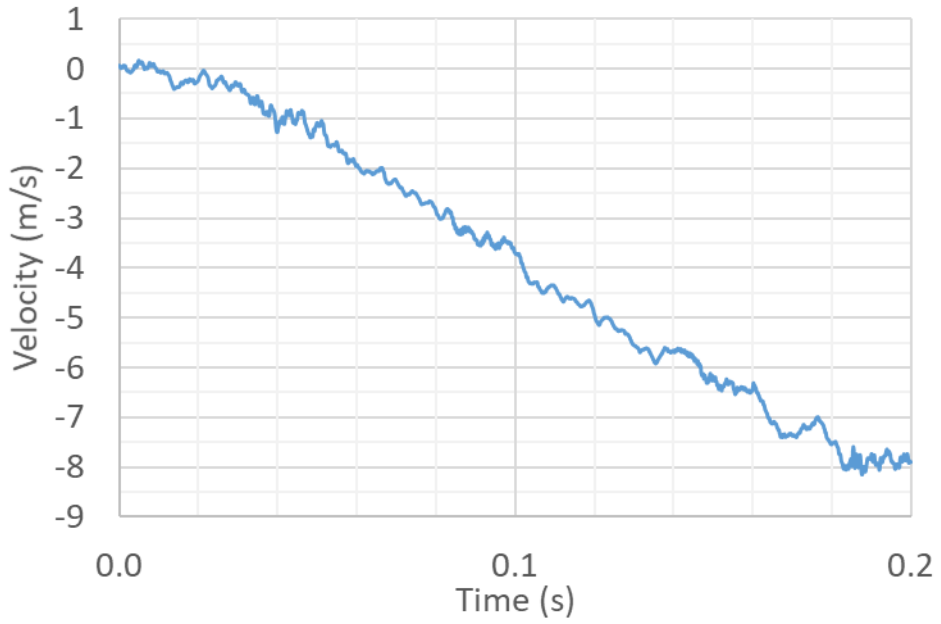

Figure 63. Relative longitudinal velocity of the occupant (m/s) – soil only.

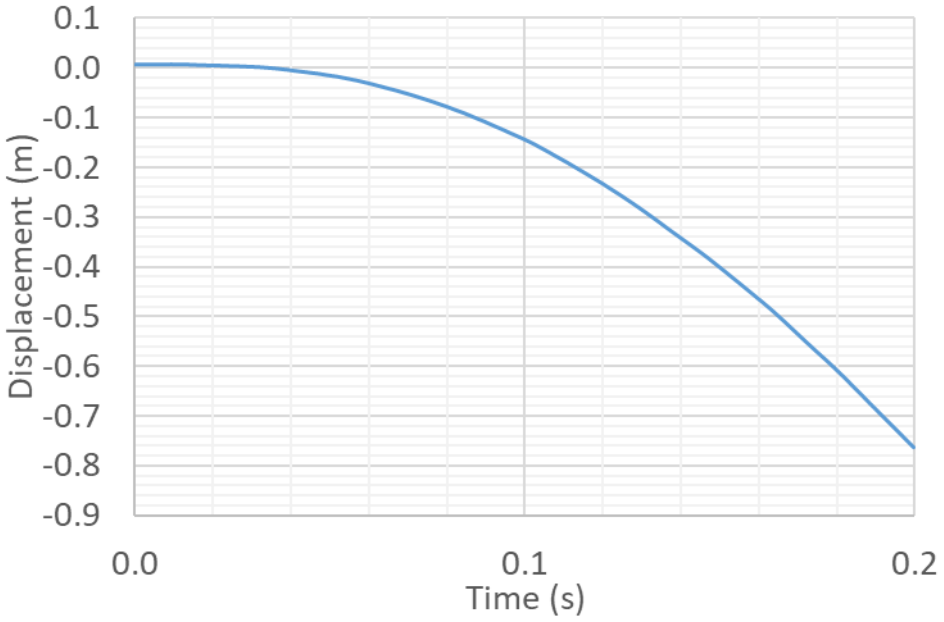

Figure 64. Relative longitudinal displacement of the occupant (m) – soil only.

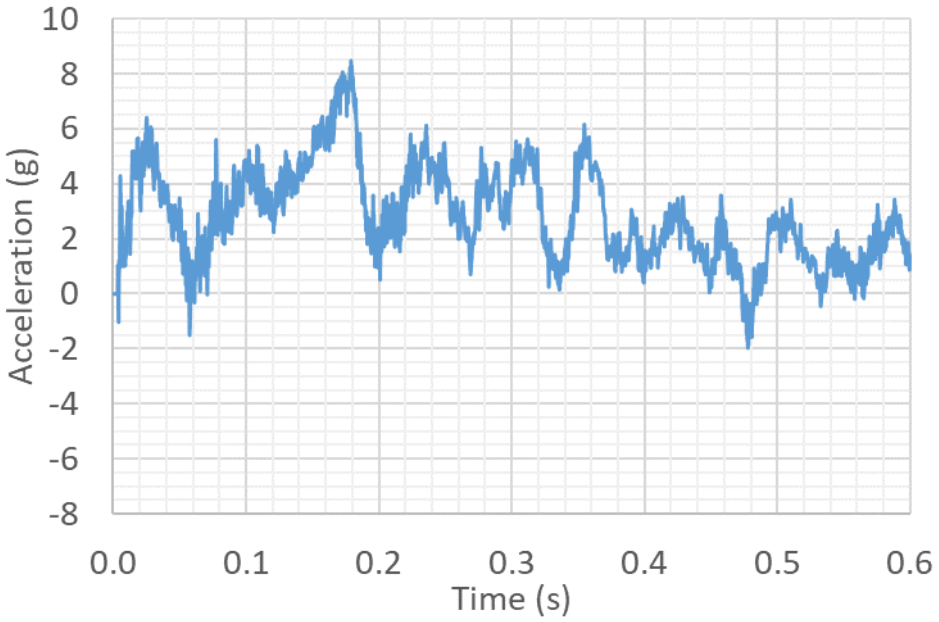

Figure 65. 10 m/s average vehicle lateral acceleration (g) – soil only.

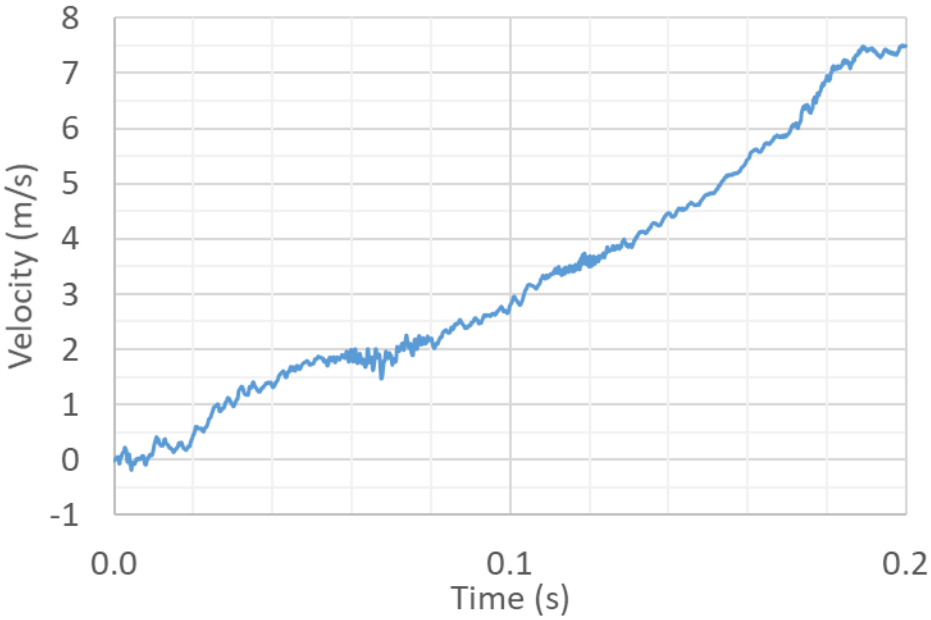

Figure 66. Relative lateral velocity of the occupant (m/s) – soil only.

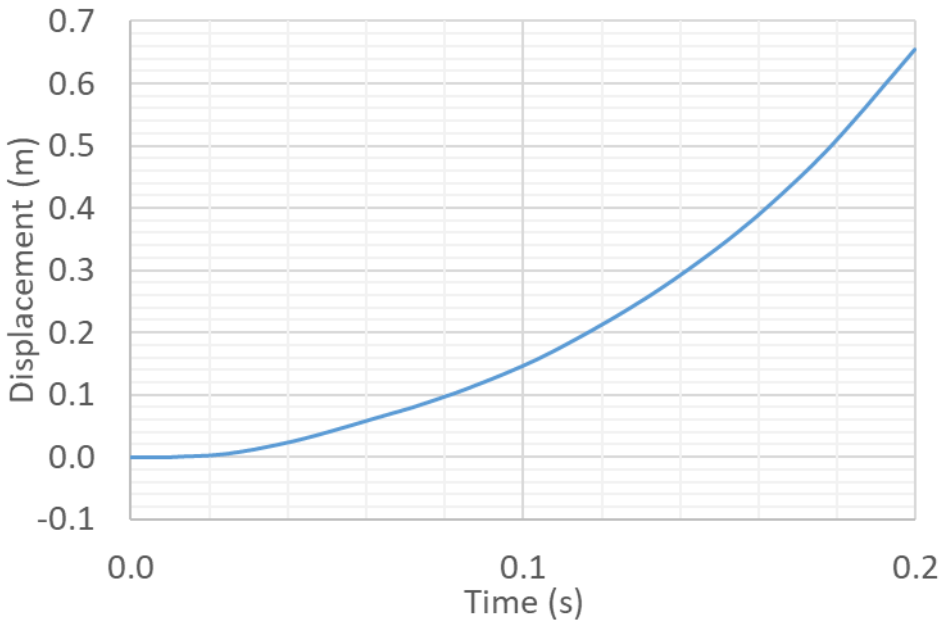

Figure 67. Relative lateral displacement of the occupant (m) – soil only.

The maximum deflection of the guardrail, the permanent deflection of the guardrail, and the summation of ground level displacement of all posts were measured and reported in Table 10. None of the posts was pulled out of the ground during the simulation, and three posts were detached from the guardrail. The model was validated using the experimental results [60]. Table 10 compares the results obtained from the simulations and an experimental MASH test on 31-inch MGS guardrail system [60]. The comparison shows that all the parameters predicted by the finite element model were close to those measured in the experimental test. Therefore, the model was used for other simulations with added asphalt mow strips. The simulation results for the cases with asphalt mow strips will be compared in Section 6.4 with the results for the case with soil only to show how much ground restraint is added when the guardrail posts are encased in asphalt mow strips.

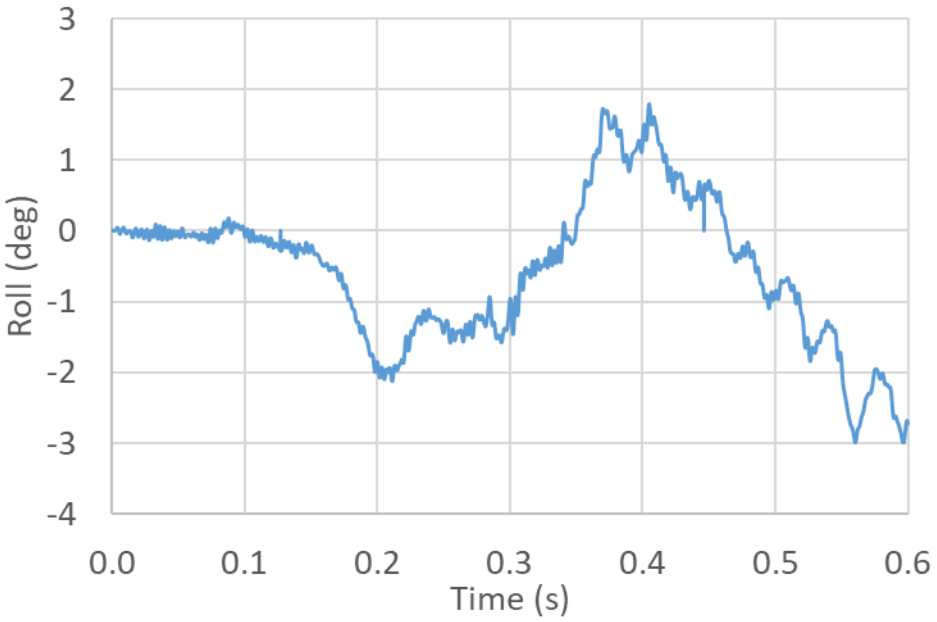

Figure 68. Vehicle roll for the setup with soil only (deg).

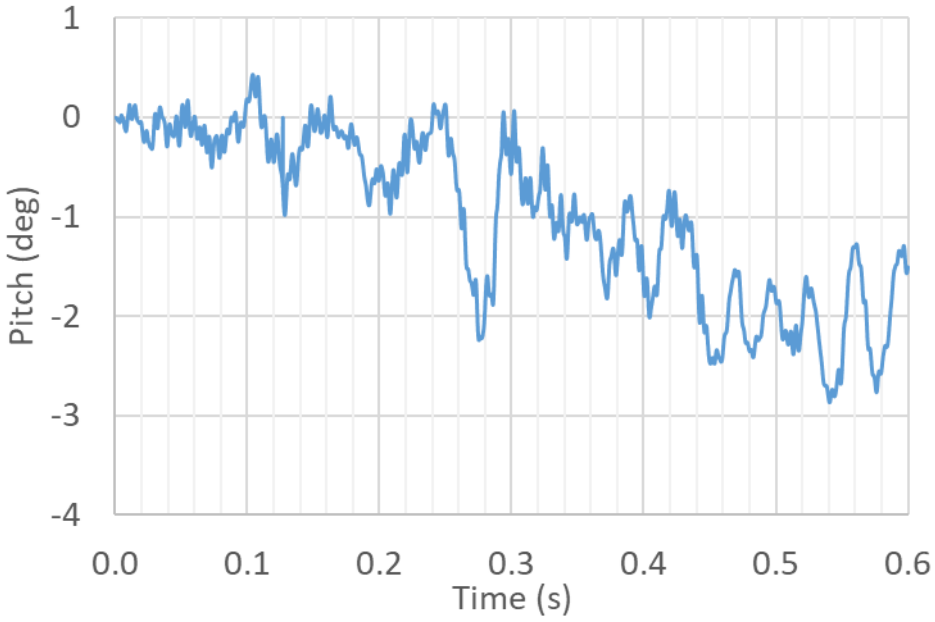

Figure 69. Vehicle pitch for the setup with soil only (deg).

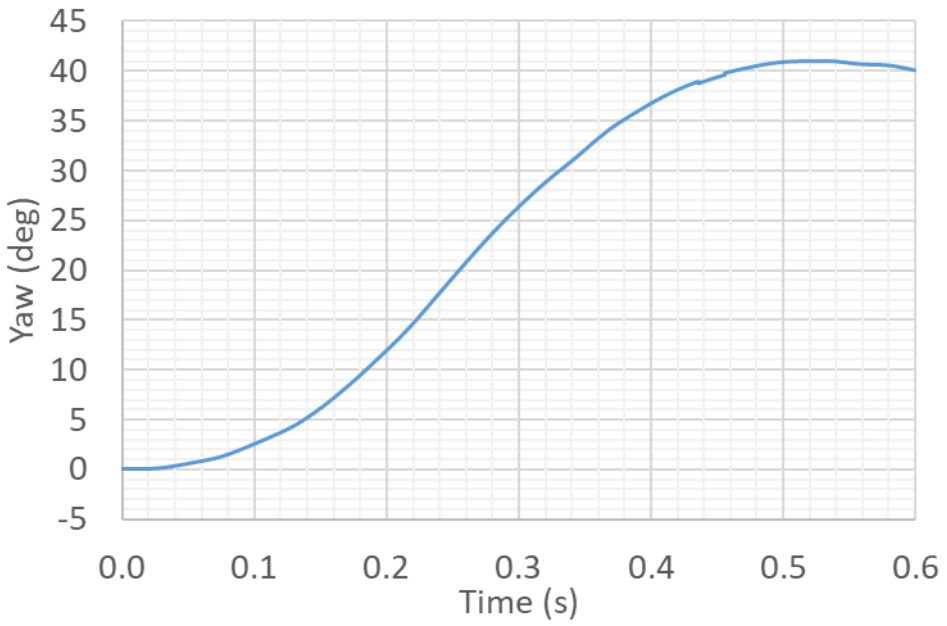

Figure 70. Vehicle yaw for the setup with soil only (deg).

Table 10. Comparison between results from FEA in this research and experiment [60] **for the setup without an asphalt layer.**

Parameters		**Experiment** [60]	**FEA in this research**
Test Number		MASH Test 3-11	MASH Test 3-11
Vehicle	Designation	2270P	2270P
	Test Inertial, kg	2,268	2,270
Impact Conditions	Speed, km/h	101.1	100
	Angle, deg	25.5	25.0
Exit Conditions	Speed (km/h)	63.7	57.6
	Trajectory Angle, deg	13.5	12.8
ORA, g's < 20.49 g	Longitudinal	8.2	7.4
	Lateral	6.9	8.5
OIV, m/s < 12.2 m/s	Longitudinal	4.7	4.7
	Lateral	4.8	4.5
Test Article Deflections, m	Dynamic	1.1	1.0
	Permanent	0.8	0.8
Impact Time for the Occupant t*, sec		N/A	0.142
Sum. of Ground Level Displacement of Posts (m)		N/A	1.686
Max. Yaw Angle, deg		46	41
Max. Roll Angle, deg < 75 deg		-5	-3.5
Max. Pitch Angle, deg < 75 deg		-2	-2.9
Posts detached from rail during impact		4 posts	3 posts
Posts hit by leading tire (wheel snag)		3 posts	3 posts
Posts pulled out of ground		none	none
Leading tire/wheel disengaged		mostly	mostly

6.3.2 Guardrail System with Asphalt Mow Strip with 50 mm Thickness and 600 mm Rear Distance (Test T50-R600)

The model with soil only was updated by including an asphalt layer with a thickness of 50 mm and rear distance of 600 mm to the model. The simulation results are presented graphically in Figure 71 through Figure 76. During the collision, the leading front wheel of the vehicle hit a guardrail post at approximately 0.1 sec (see Figure 71 andFigure 73 at 0.1 sec). The suspension system failed partially but stayed connected to the vehicle, and the wheel continued to rotate throughout the rest of the simulation as shown in Figure 76. At approximately 0.2 sec the vehicle hit the second post and passed over this post (see Figure 71 and Figure 73 at 0.2 sec). The vehicle moved forward and hit the third post at approximately 0.3 sec (see Figure 71 and Figure 73 at 0.3 sec). The leading wheel did not completely go over the post, which happened to the first and second posts. The wheel snagging for this case was similar to the simulation of the case without an asphalt layer, which was discussed in the previous Section. The vehicle moved parallel to the guardrail at approximately 0.3 sec. The vehicle was redirected back to the road and lost contact with the guardrail at approximately 0.63 sec. Vehicle pocketing did not occur during this simulation. Asphalt rupture propagated for each post and was connected to the ruptures around other posts. This created a continuous rupture that ran parallel to the guardrail as shown in Figure 72 and Figure 74. Moreover, asphalt rupture occurred at the edge of the mow strip and behind each post, with a substantial ground level displacement.

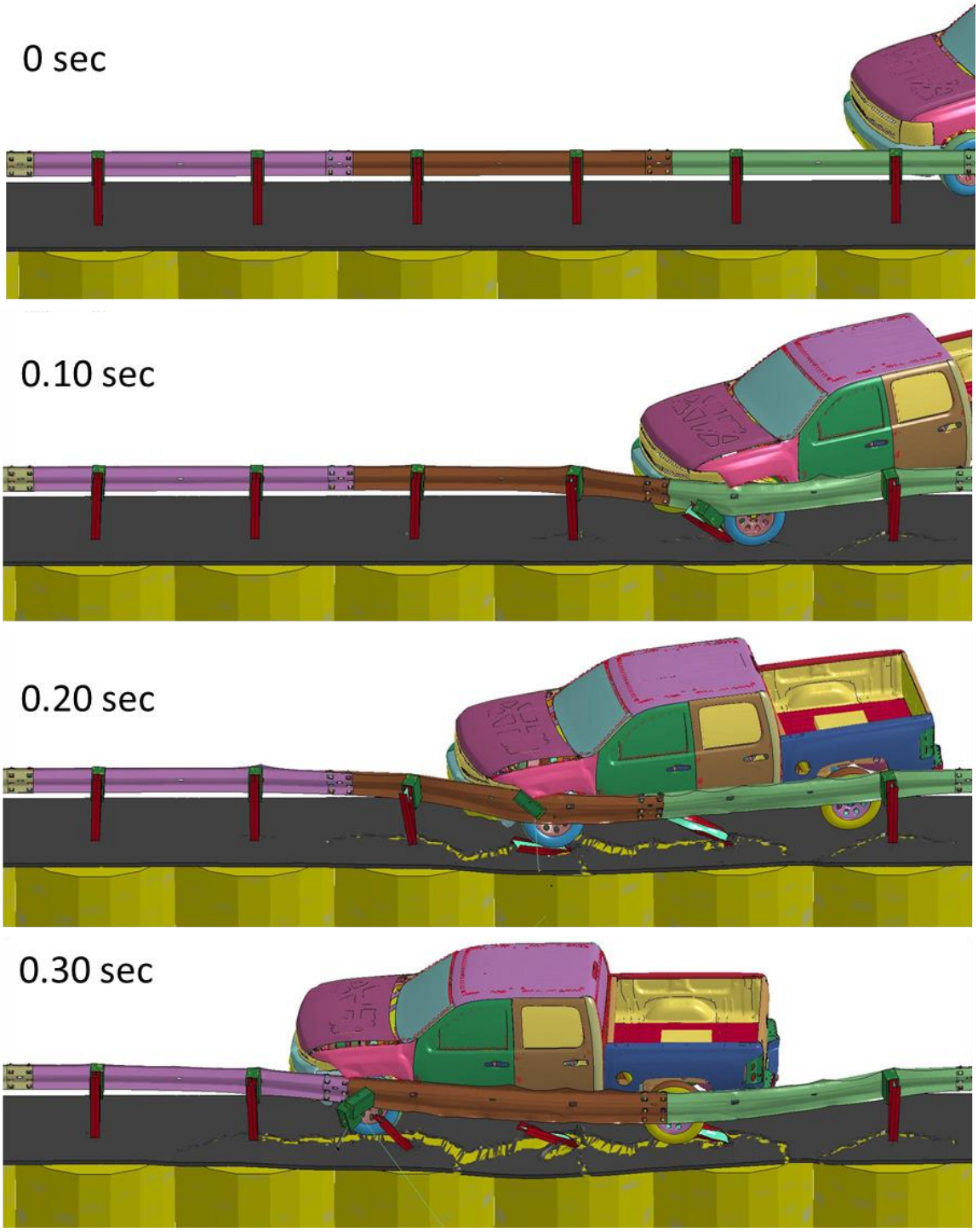

Figure 71. Simulation result for Test T50-R600 – up to 0.3 sec.

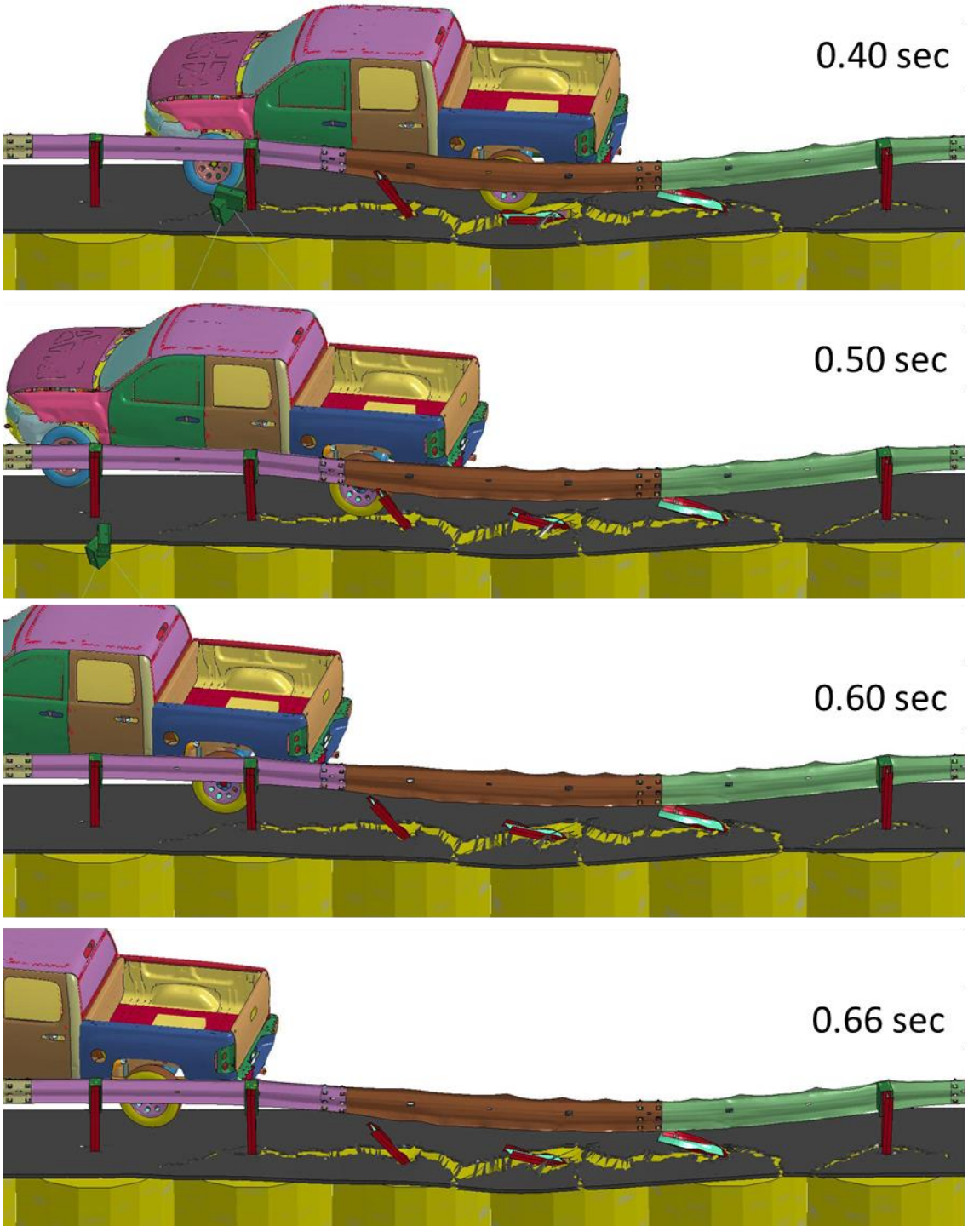

Figure 72. Simulation result for Test T50-R600 – after 0.3 sec.

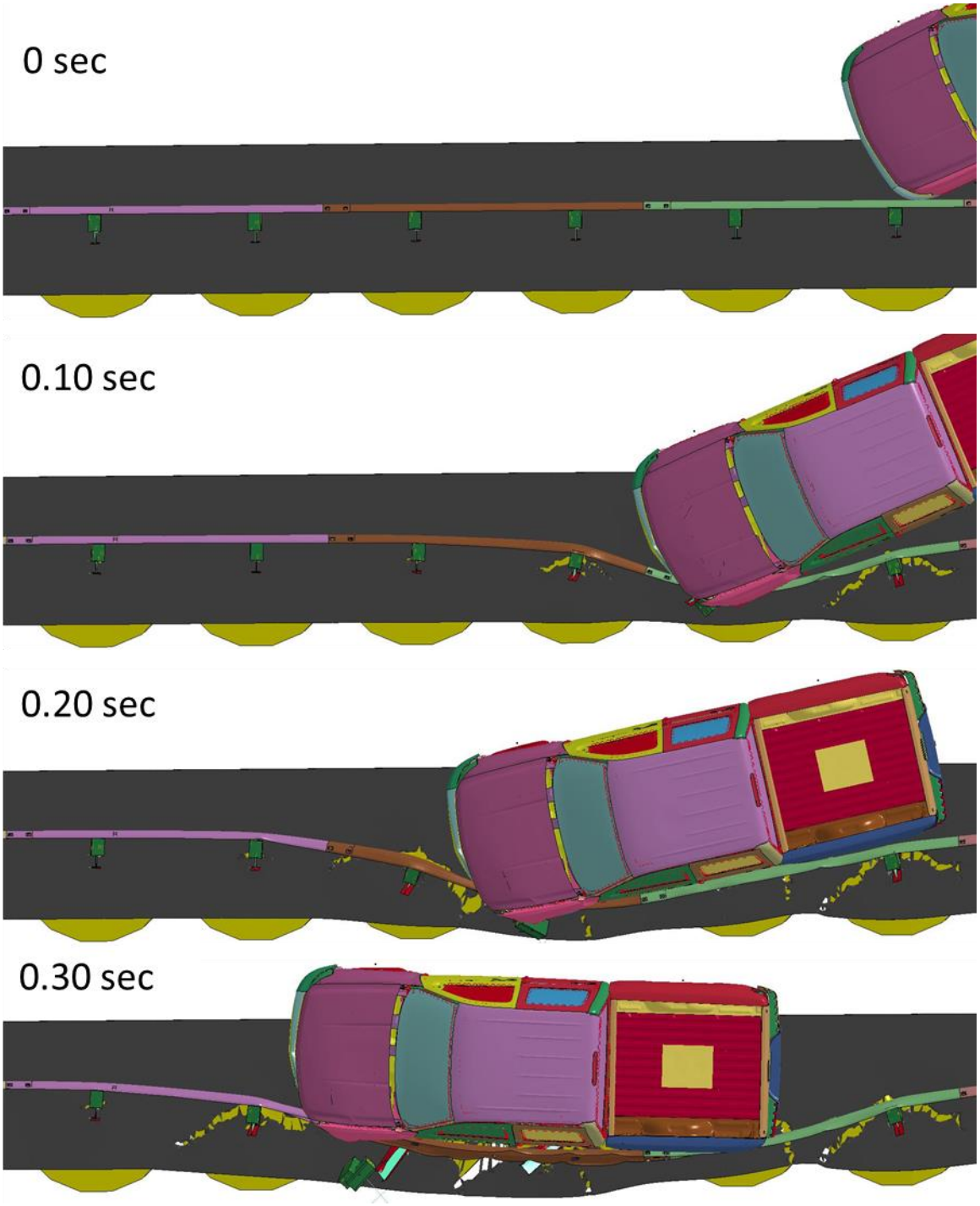

Figure 73. Simulation result for Test T50-R600 – up to 0.3 sec.

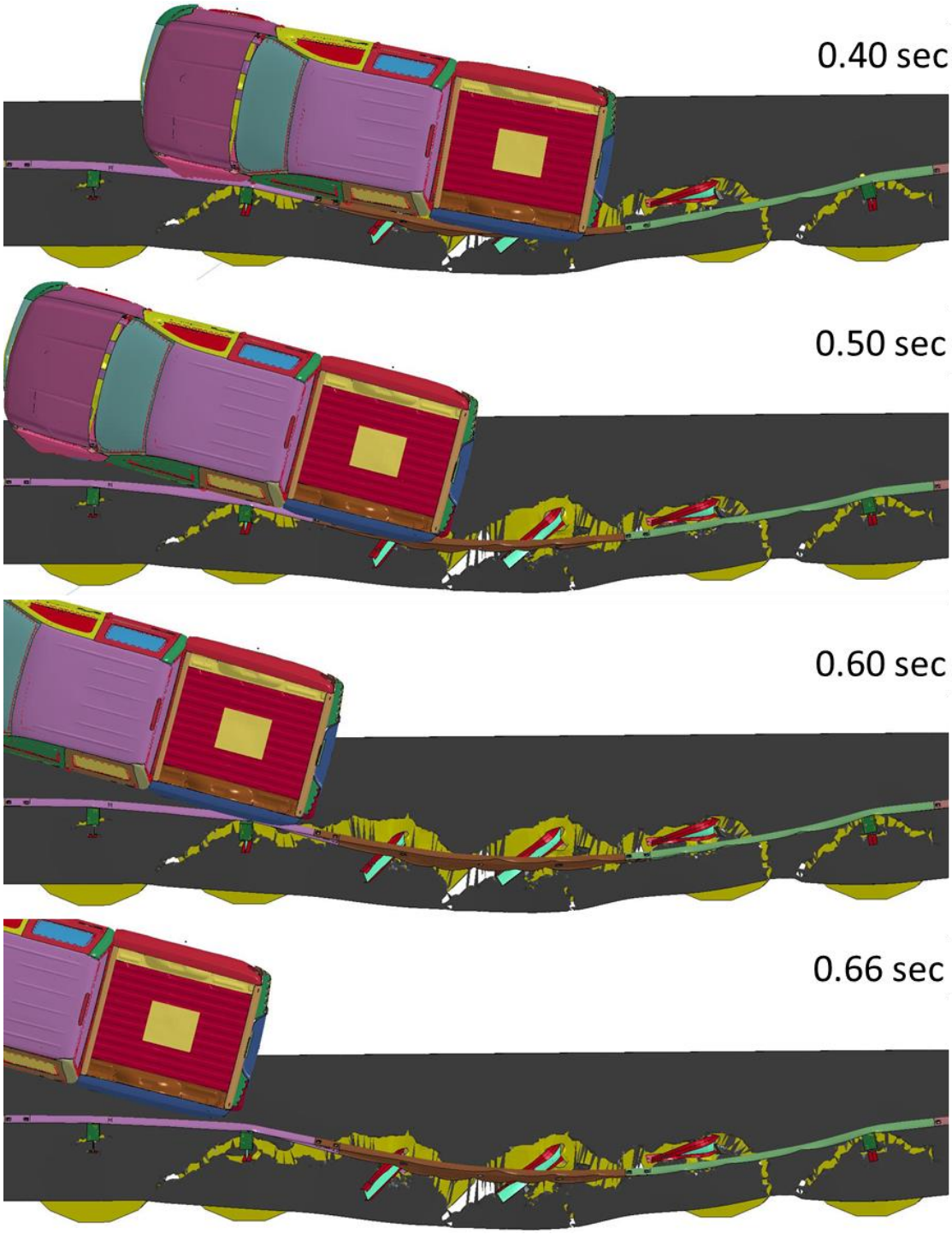

Figure 74. Simulation result for Test T50-R600 – after 0.3 sec.

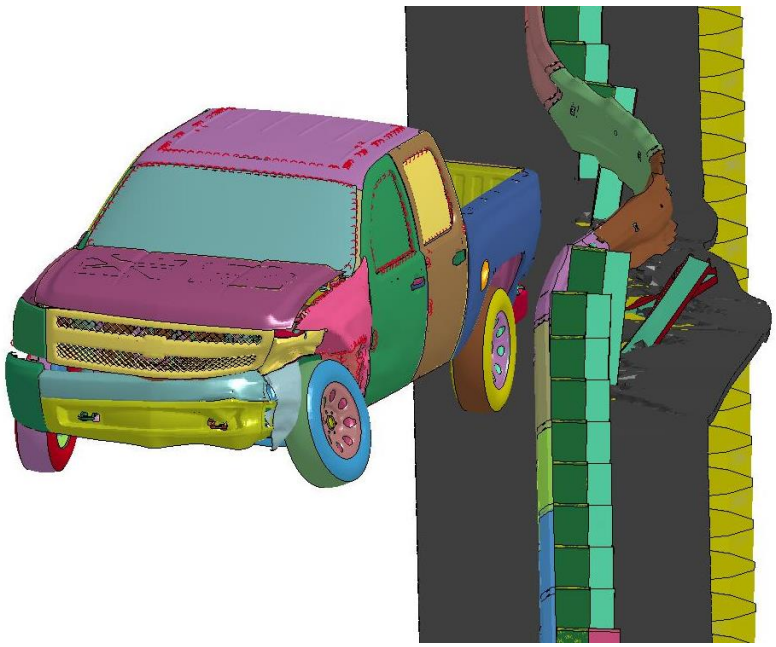

Figure 75. Simulation result for Test T50-R600.

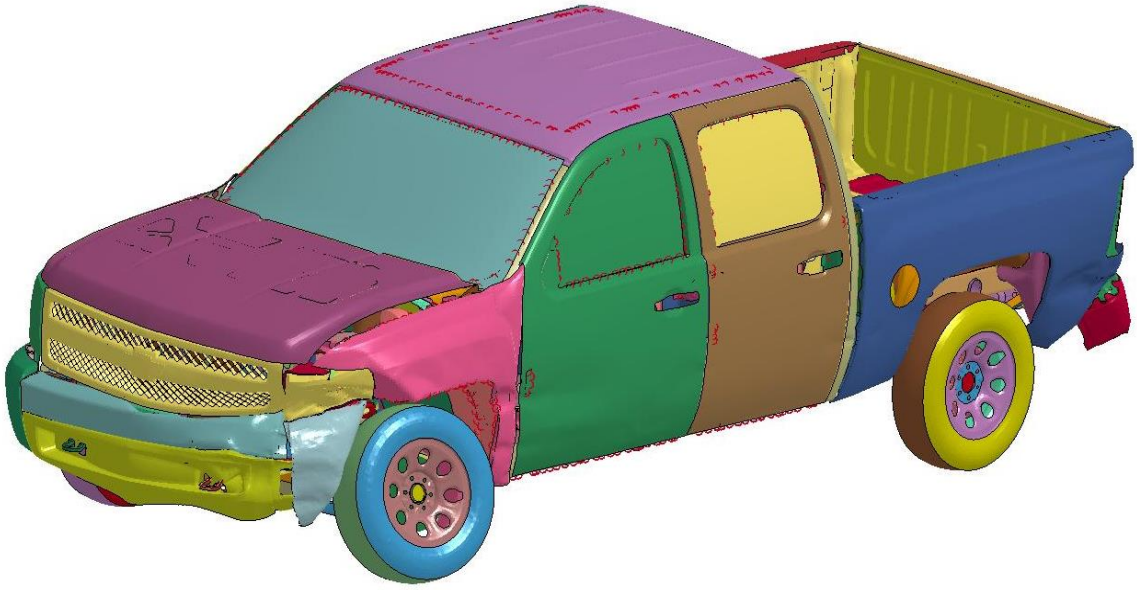

Figure 76. Vehicle Deformation for Test T50-R600.

The four posts that had the largest ground level displacement caused large asphalt ruptures, and one large part of the asphalt mow strip behind these four posts was nearly detached from the rest of the mow strip. This asphalt rupture limited the effect of the mow strip on the ground level restraint.

The longitudinal and lateral accelerations of the vehicle were obtained and are shown in Figure 77 and Figure 80. The integration of these accelerations over time produced the velocity of the occupant relative to the vehicle in longitudinal and lateral directions as presented in Figure 78 and Figure 81. Another integration over time resulted in the displacement of the occupant relative to the vehicle, as presented in Figure 79 and Figure 82. The times when the lateral displacement was equal to 305 mm and when the longitudinal displacement was equal to 610 mm were found using relative displacement curves (Figure 79 and Figure 82). The smaller of these two was for the lateral displacement equal to 0.135 sec, meaning that the occupant first hit the interior of the vehicle on his sides before hitting somewhere in front of him in the vehicle. After the occupant hit the interior, it is assumed that his velocity and acceleration were the same as the vehicle for the remainder of the collision. The longitudinal and lateral occupant impact velocities, OIVs, were then found using the relative velocity curves (Figure 78 and Figure 81) by finding the relative velocities at 0.135 sec. Thereafter, the peak accelerations from the acceleration curves (Figure 77 and Figure 80) were found for the period of time after 0.135 sec until the end of the collision. The OIVs and ORAs were less than the maximum limit in MASH guidelines. The results are reported in Table 11.

The roll, pitch, and yaw angles of the vehicle were recorded during simulations. The time histories for these parameters are shown in Figure 83 to Figure 85. The peak values of roll and pitch were less than MASH limit, which is equal to 75 deg. The initial impact angle of 25 degrees was subtracted from the yaw angle at the time when the vehicle lost contact with the guardrail to determine the exit angle. The peak values of yaw, roll, and pitch angles, the exit angle, and the exit speed of the vehicle are reported in Table 11. The maximum deflection of the guardrail, permanent deflection of the guardrail, and summation of ground level displacement of all posts are reported in Table 11. None of the posts was pulled out of the ground during the simulation; three posts were detached from the guardrail.

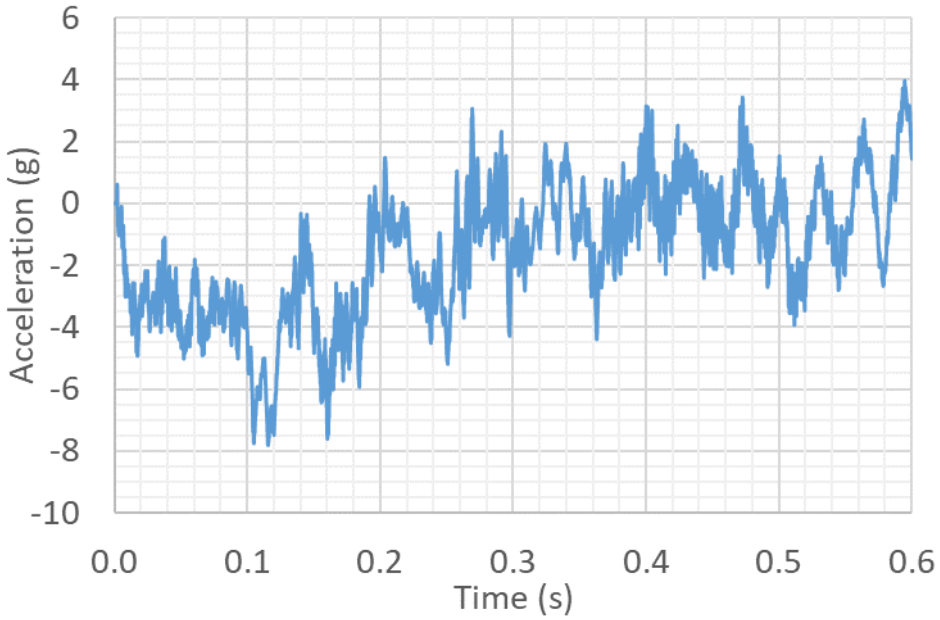

Figure 77. 10 m/s average vehicle longitudinal acceleration (g) - Test T50-R600.

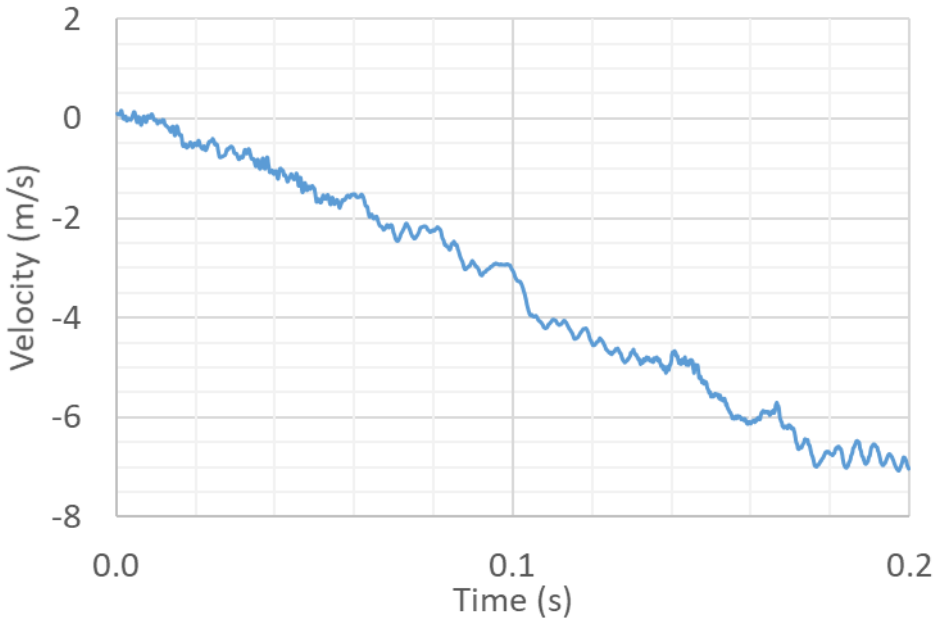

Figure 78. Relative longitudinal velocity of the occupant (m/s) - Test T50-R600.

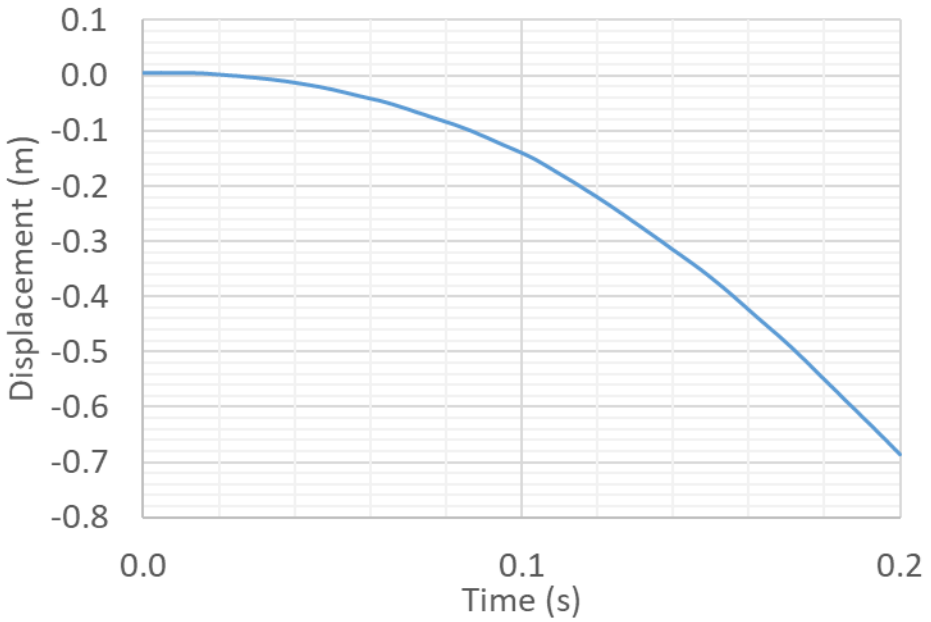

Figure 79. Relative longitudinal displacement of the occupant (m) – Test T50-R600.

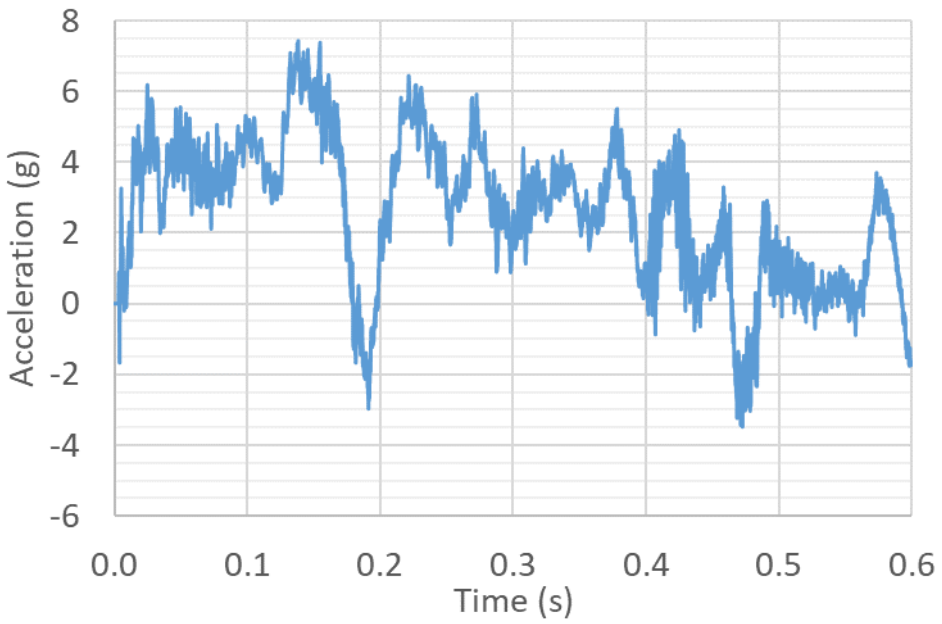

Figure 80. 10 m/s average vehicle lateral acceleration (g) – Test T50-R600.

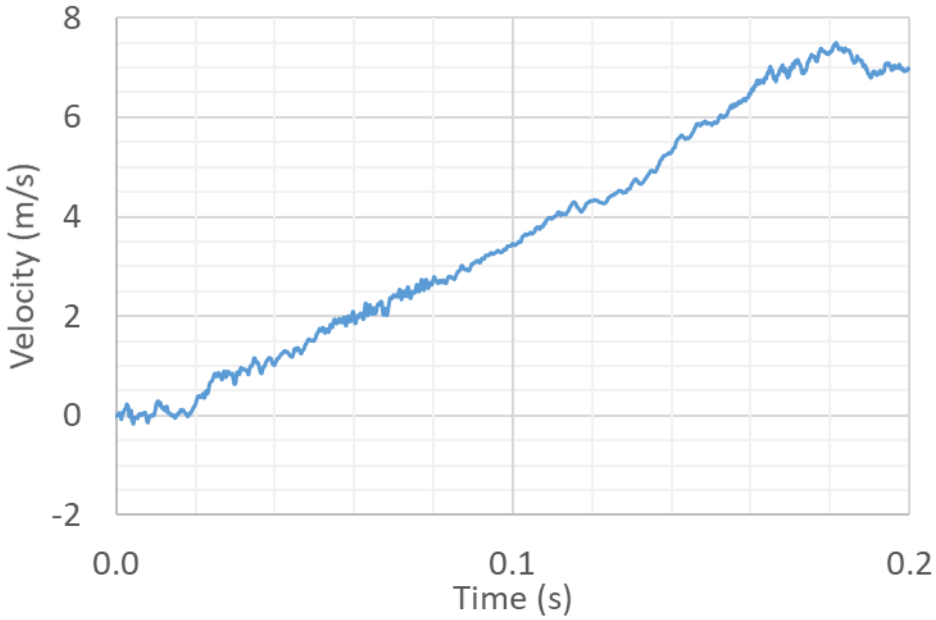

Figure 81. Relative lateral velocity of the occupant (m/s) - Test T50-R600.

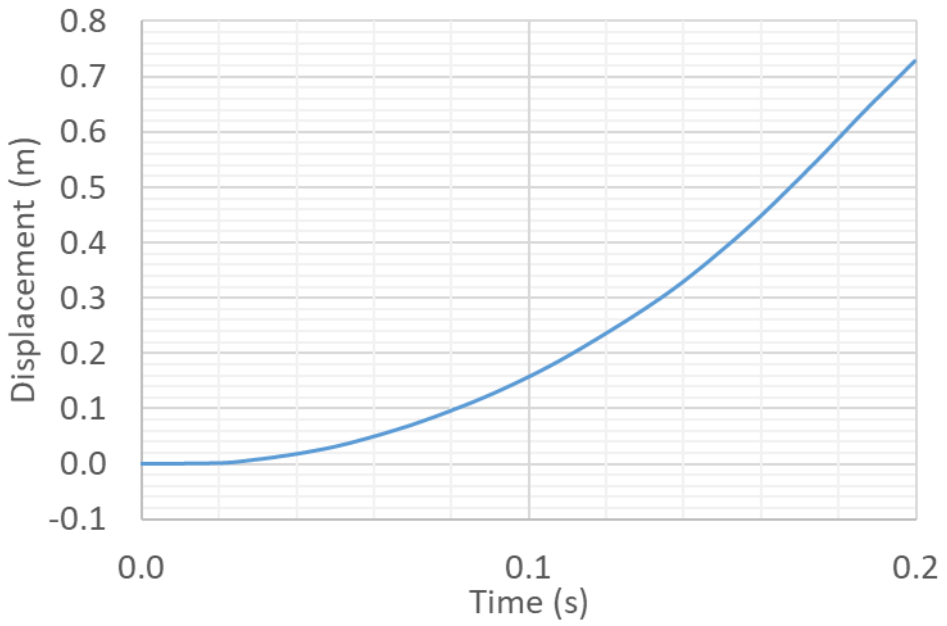

Figure 82. Relative lateral displacement of the occupant (m) - Test T50-R600.

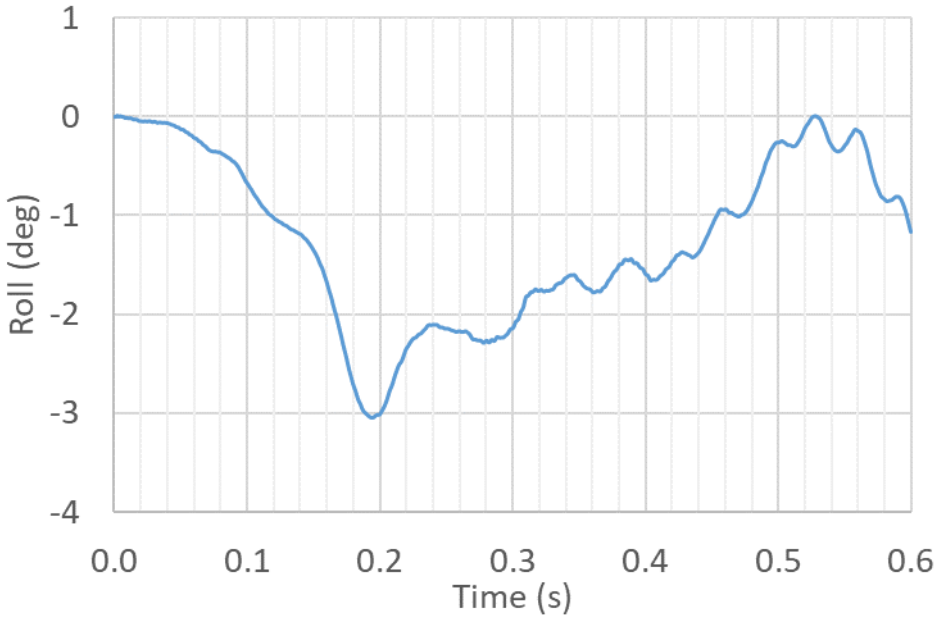

Figure 83. Vehicle roll (deg) - Test T50-R600.

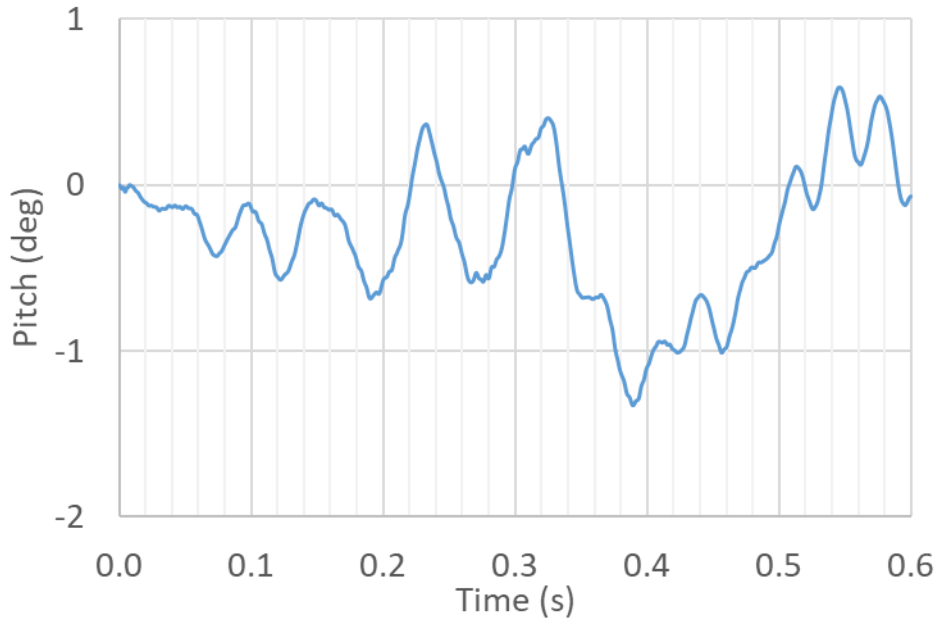

Figure 84. Vehicle pitch (deg) - Test T50-R600.

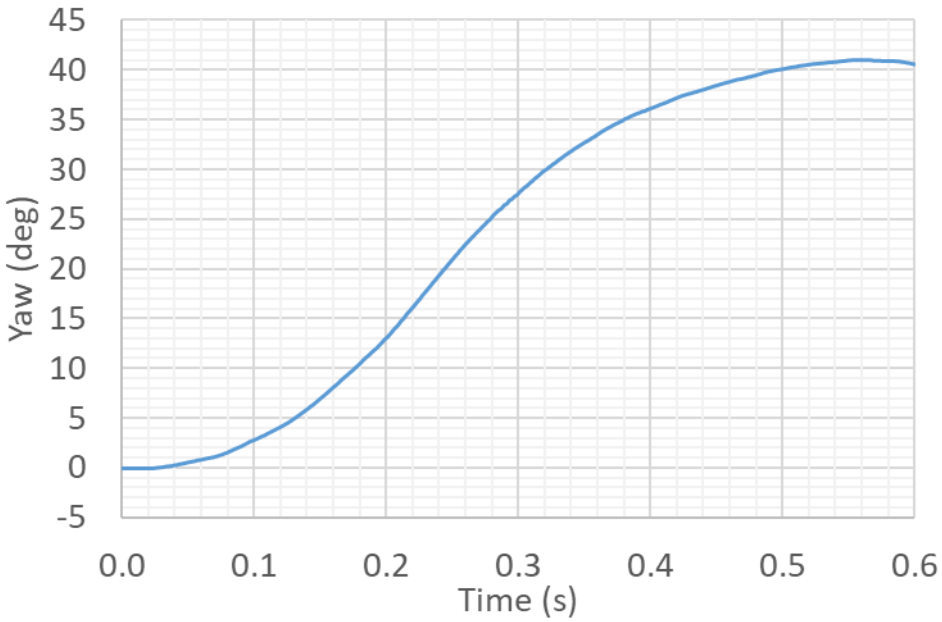

Figure 85. Vehicle yaw (deg) - Test T50-R600.

Table 11. Summary of full-scale crash simulation results for Test T50-R600.

Test Number		T50-R600
Vehicle	Designation	2270P
	Test Inertial, kg	2,270
Impact Conditions	Speed, km/h	100
	Angle, deg	25.0
Exit Conditions	Speed (km/h)	60
	Trajectory Angle, deg	15
ORA, g's < 20.49 g	Longitudinal	-7.8
	Lateral	7.4
OIV, m/s < 12.2 m/s	Longitudinal	4.9
	Lateral	4.9
Test Article Deflections, m	Dynamic	0.909
	Permanent	0.707
Impact time for the Occupant t^*, sec		0.135
Sum. of all posts ground level displacement (m)		1.042
Max. Yaw Angle, deg		41
Max. Roll Angle, deg < 75 deg		-3
Max. Pitch Angle, deg < 75 deg		-1
Posts detached from rail during impact		3 posts
Posts hit by leading tire (wheel snag)		3 posts
Posts pulled out of ground		none
Leading tire/wheel disengaged		mostly

6.3.3 Guardrail System with Asphalt Mow Strip with 90 mm Thickness and 300 mm Rear Distance (Test T90-R300)

The model was updated by changing the asphalt layer geometry, increasing the thickness to 90 mm, and decreasing the rear distance to 300 mm. The simulation results are presented graphically in Figure 86 through Figure 91. During the collision, the leading front wheel of the vehicle hit a guardrail post at approximately 0.1 sec (Figure 86 and Figure 88 at 0.1 sec). Similar to the previous simulations, the suspension system failed partially but stayed connected to the vehicle and the wheel continued to rotate throughout the rest of the simulation as shown in Figure 91. At approximately 0.2 sec the vehicle hit and then passed over the second post (Figure 86 and Figure 88 at 0.2 sec). The vehicle moved forward and hit the third post at approximately 0.3 sec. The leading wheel did not completely go over the third post as it did with the first and second posts (Figure 86 and Figure 88 at 0.3 sec). The wheel snagging for this case was similar to the case with 50 mm thickness and 600 mm rear distance, test T50-R600. The vehicle ran parallel to the guardrail at approximately 0.3 sec. The vehicle was redirected back to the road and lost contact with the guardrail at approximately 0.64 sec. Vehicle pocketing did not occur during this simulation. Asphalt rupture propagated around each post; however, unlike test T50-R600, the ruptures remained local to each post and did not connect with the ruptures around other posts. This occurred because the rear distance here was half of the rear distance in test T50-R600. Therefore, the rupture for each post reached the edge of the mow strip before joining with ruptures around other posts.

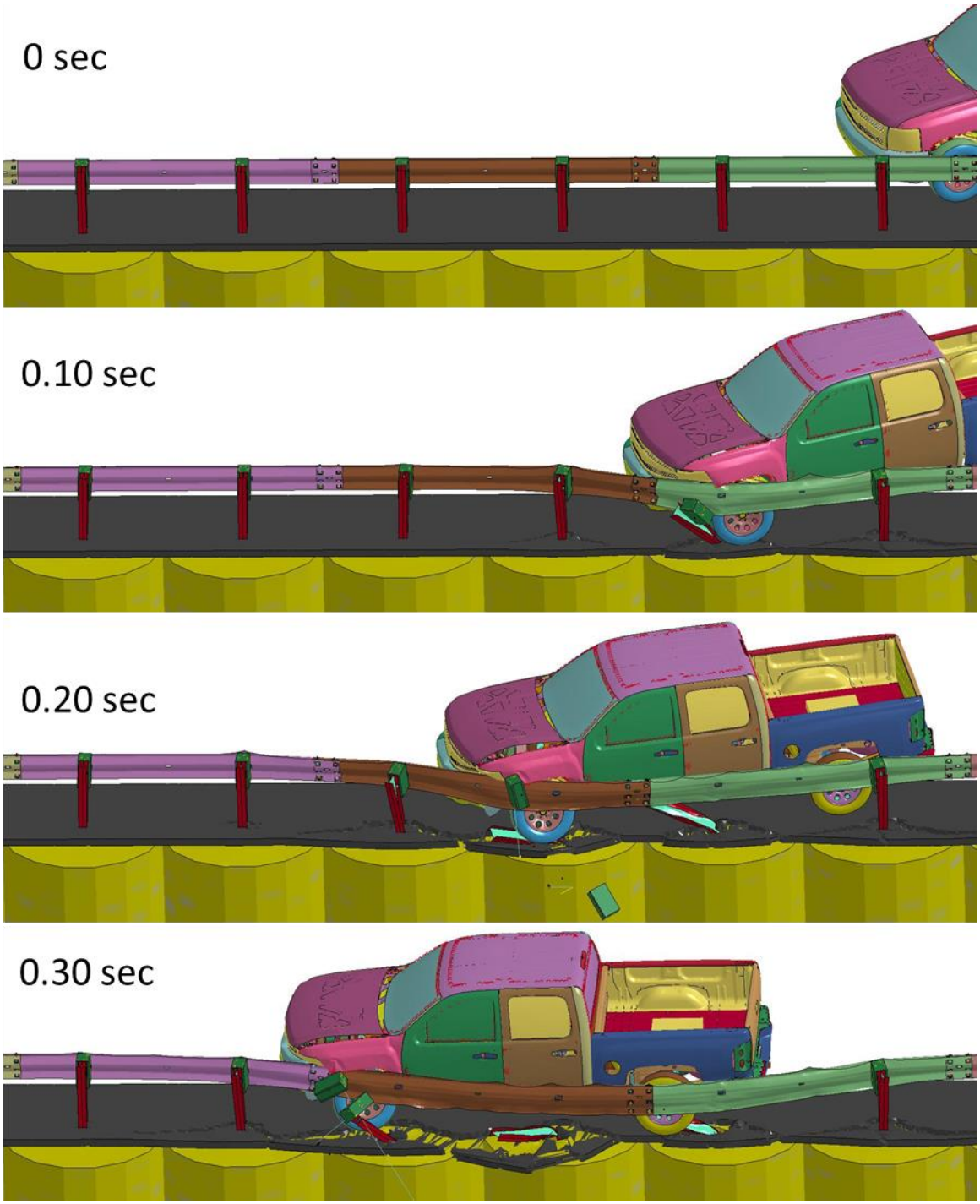

Figure 86. Simulation result for Test T90-R300 – up to 0.3 sec.

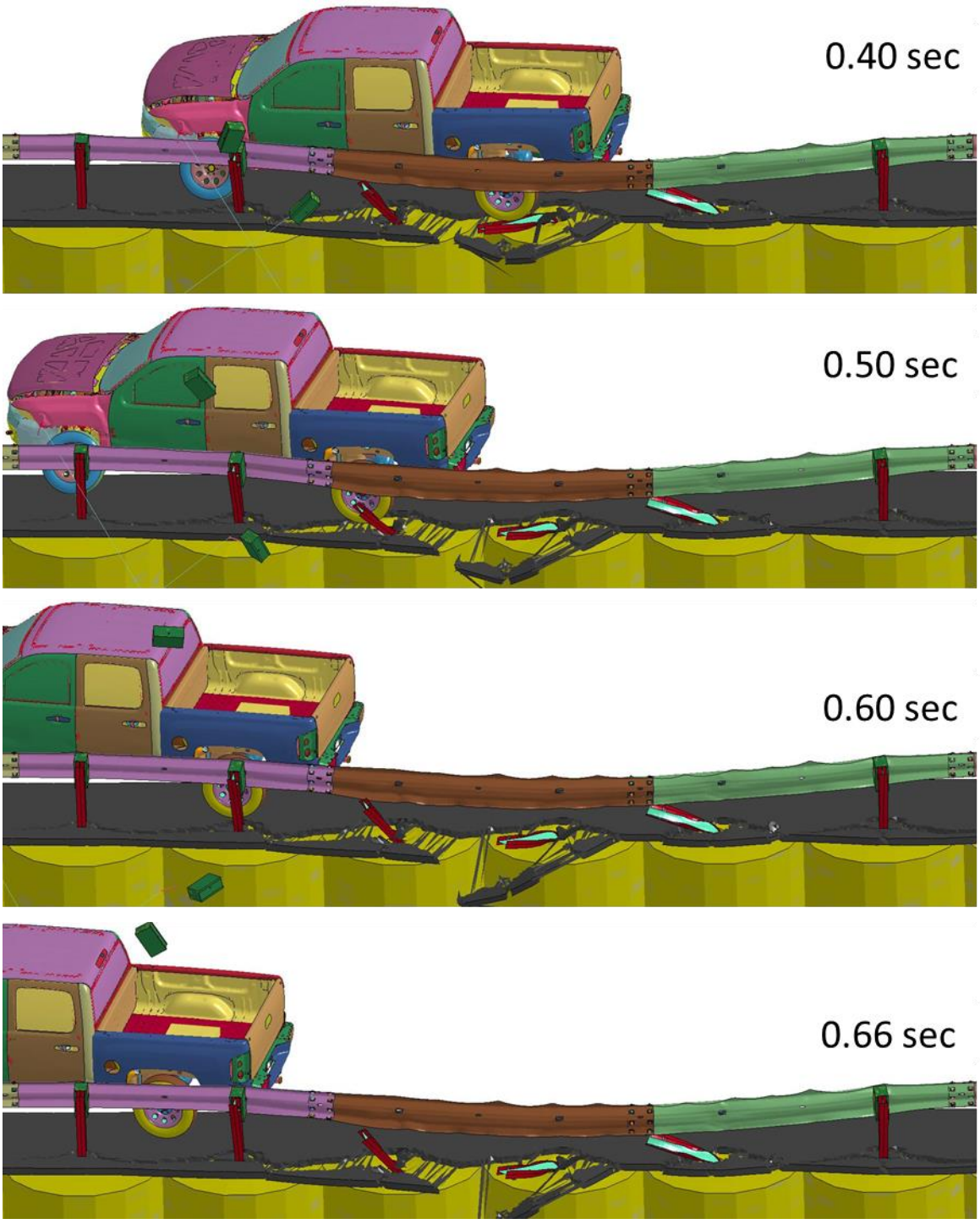

Figure 87. Simulation result for Test T90-R300 – after 0.3 sec.

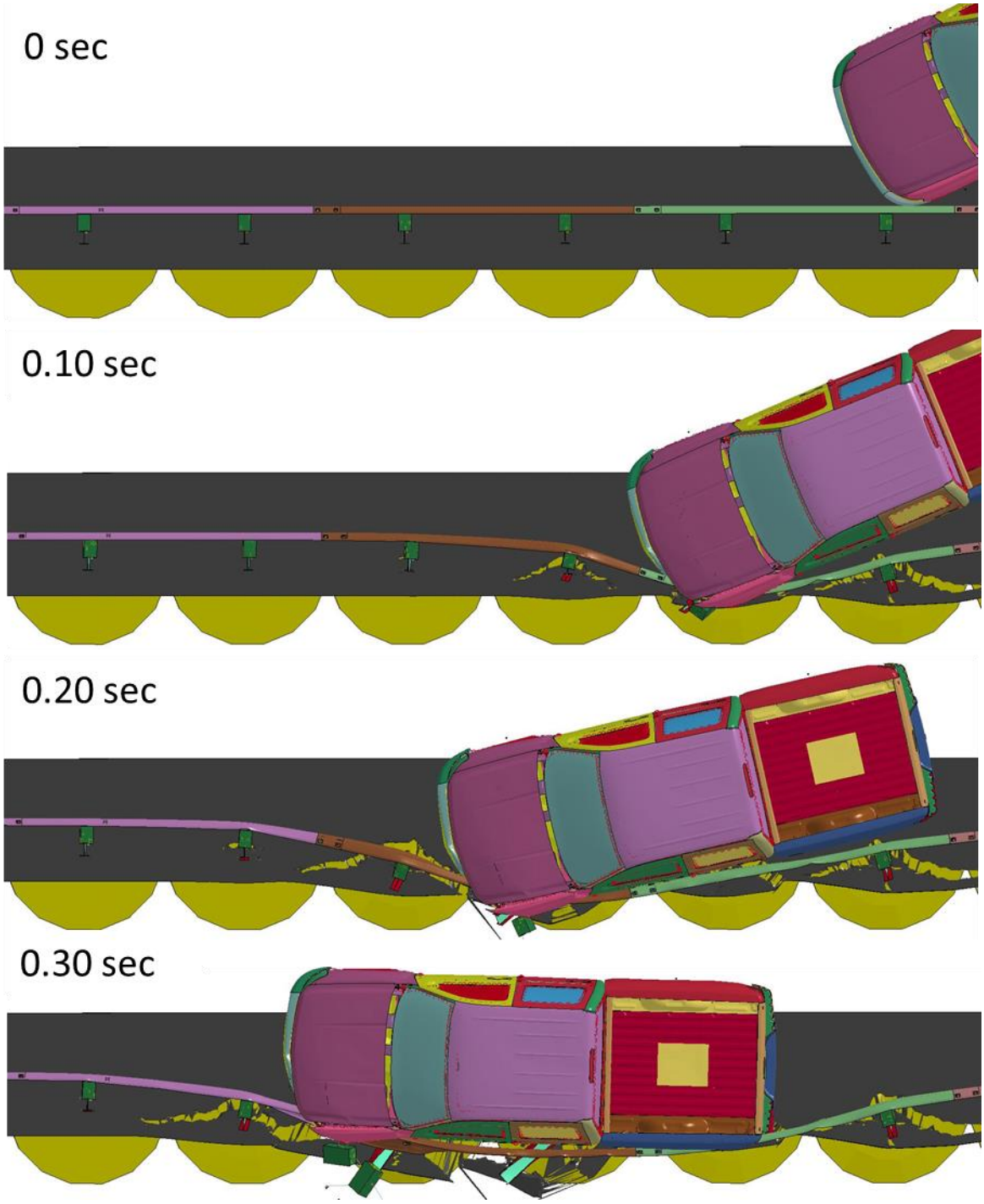

Figure 88. Simulation result for Test T90-R300 – up to 0.3 sec.

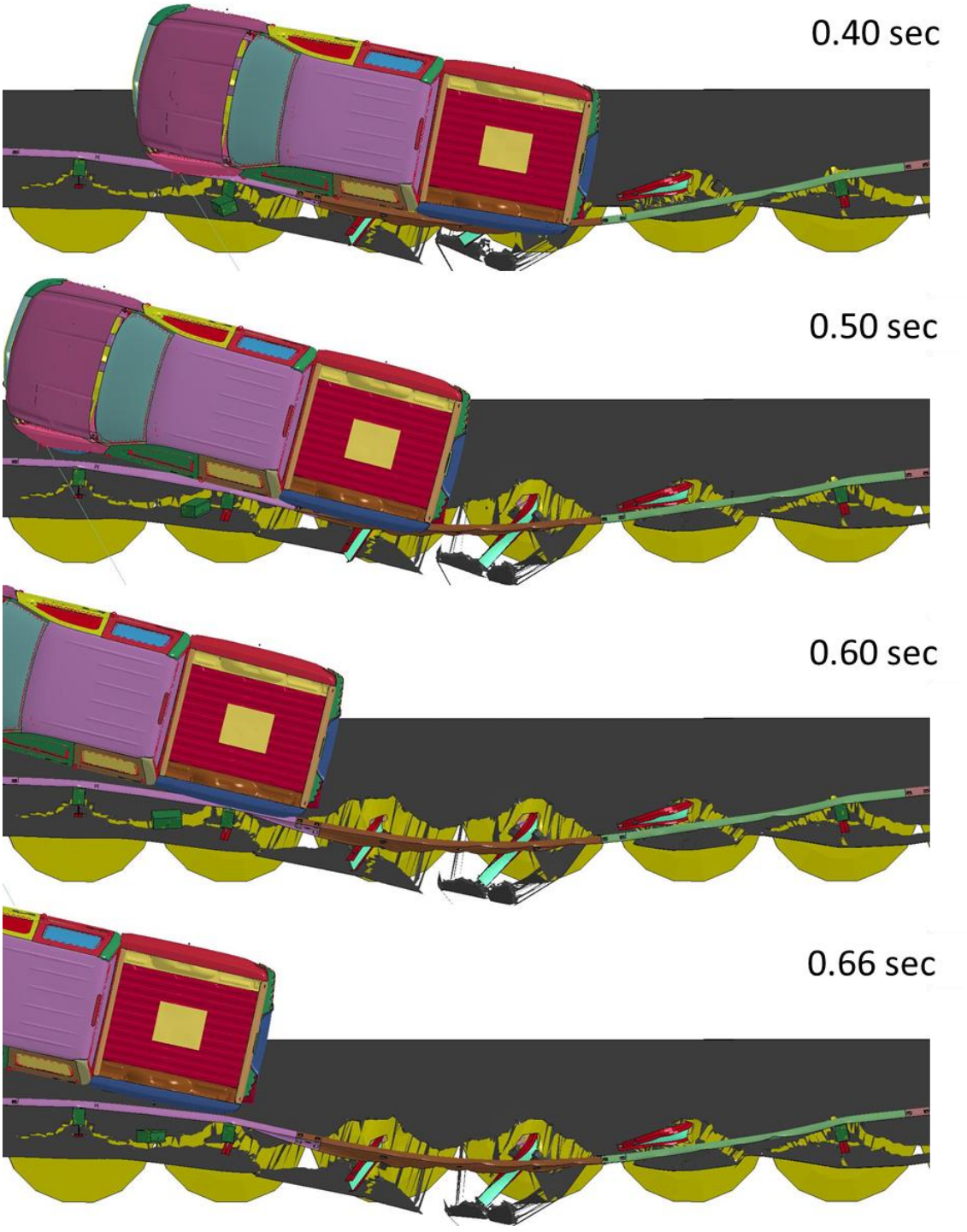

Figure 89. Simulation result for Test T90-R300 – after 0.3 sec.

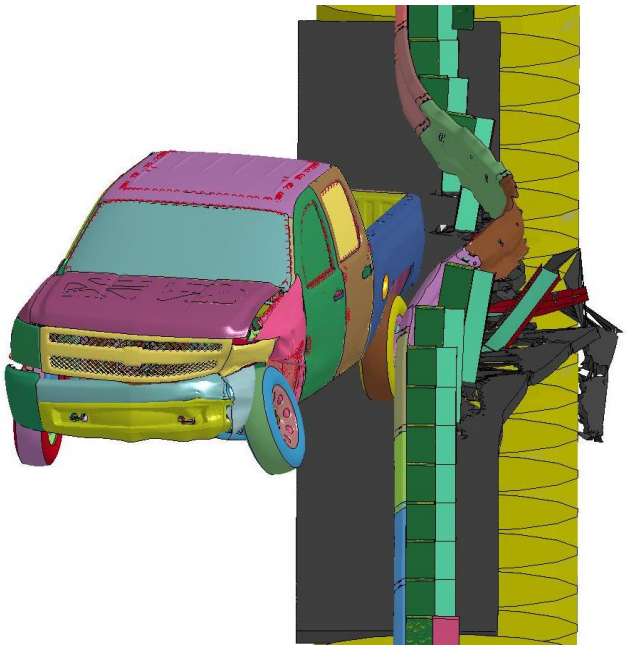

Figure 90. Simulation result for Test T90-R300.

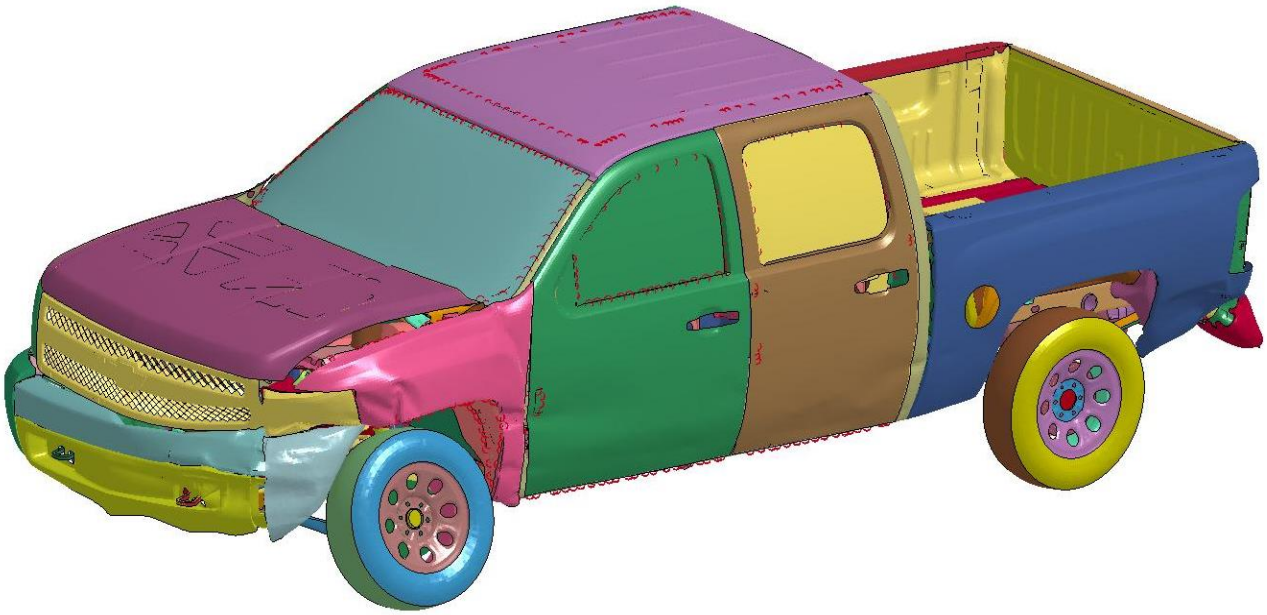

Figure 91. Vehicle Deformation for Test T90-R300.

When the rupture around each post reached the edge of the mow strip, the part of the mow strip behind each post was locally detached from the rest of the mow strip. This local asphalt rupture around the posts considerably decreased the ground level restraint caused by the asphalt mow strip.

The longitudinal and lateral accelerations of the vehicle were obtained and are shown in Figure 92 and Figure 95. The integration of these accelerations over time produces the velocity of the occupant relative to the vehicle in longitudinal and lateral directions as presented in Figure 93 and Figure 96. Another integration over time resulted in the displacement of the occupant relative to the vehicle, as presented in Figure 94 and Figure 97. The times when the lateral displacement equalled 305 mm and when the longitudinal displacement equalled 610 mm were found using the relative displacement curves (Figure 94 and Figure 97). The smaller of these two was for the lateral displacement equal to 0.136 sec, which is close to the occupant impact time for Test T50-R600, which was 0.135 sec. After the occupant hit the interior, it is assumed that his velocity and acceleration were the same as the vehicle for the remainder of the collision. The longitudinal and lateral occupant impact velocities, OIVs, were then found using relative velocity curves (Figure 93 and Figure 96) by determining the relative velocities at 0.136 sec. Thereafter, the peak accelerations from the acceleration curves (Figure 92 and Figure 95) were found for the period of time after 0.136 sec until the end of the collision. The OIVs and ORAs were lower than the maximum limit in MASH guidelines. The results are reported in Table 12.

The roll, pitch, and yaw angles of the vehicle were recorded during simulations. The time histories for these parameters are shown in Figure 98 through Figure 100. The peak values of roll and pitch are lower than the MASH limit, which is equal to 75 deg. The peak values of yaw, roll, and pitch angles, the exit angle, and the exit speed of the vehicle are reported in Table 12. The maximum deflection of the guardrail, the permanent deflection of the guardrail, and the summation of ground level displacement of all posts are reported in Table 12. None of the posts was pulled out of the ground during the simulation, and three posts were detached from the guardrail.

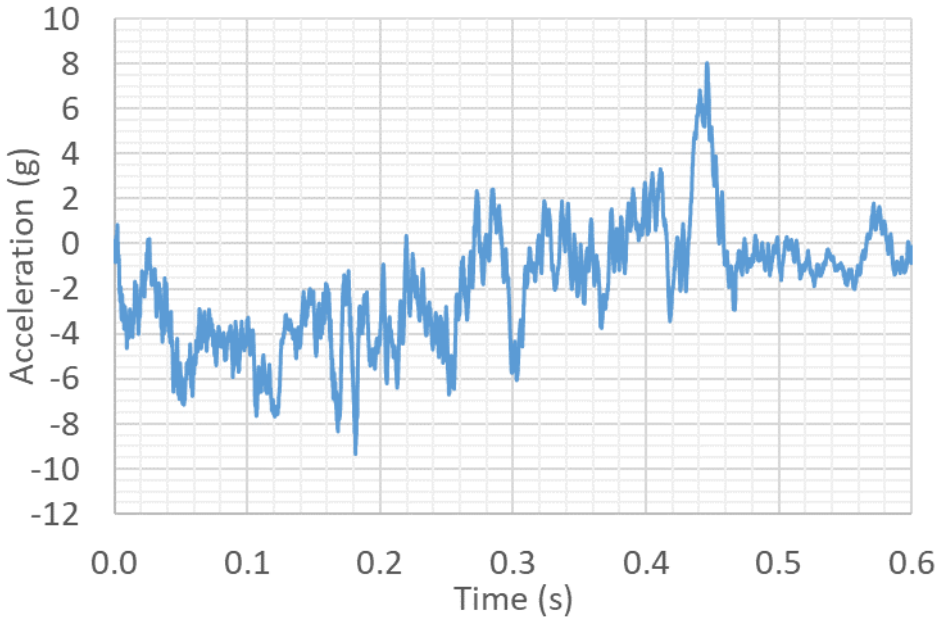

Figure 92. 10 m/s average vehicle longitudinal acceleration (g) - Test T90-R300.

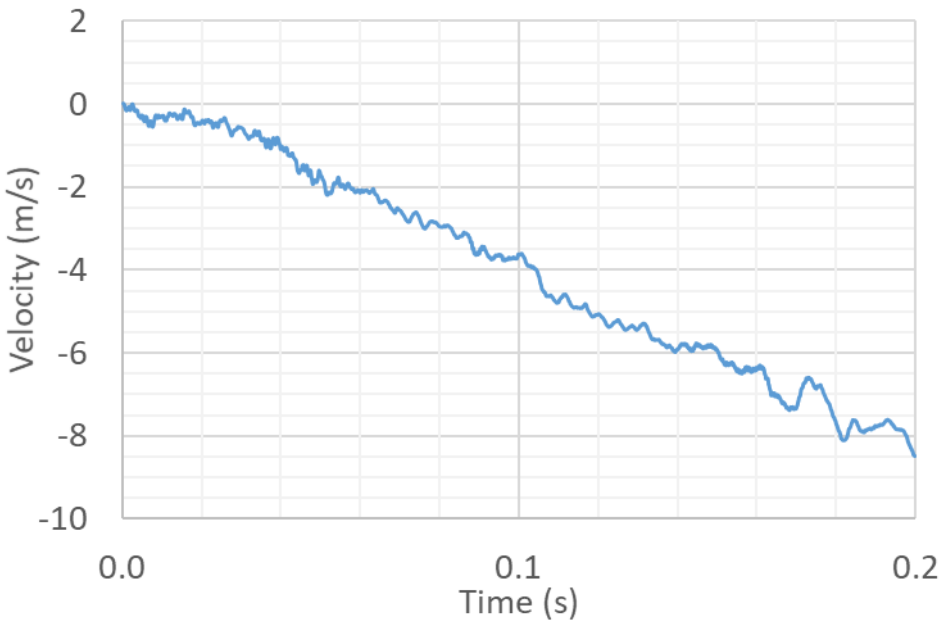

Figure 93. Relative longitudinal velocity of the occupant (m/s) - Test T90-R300.

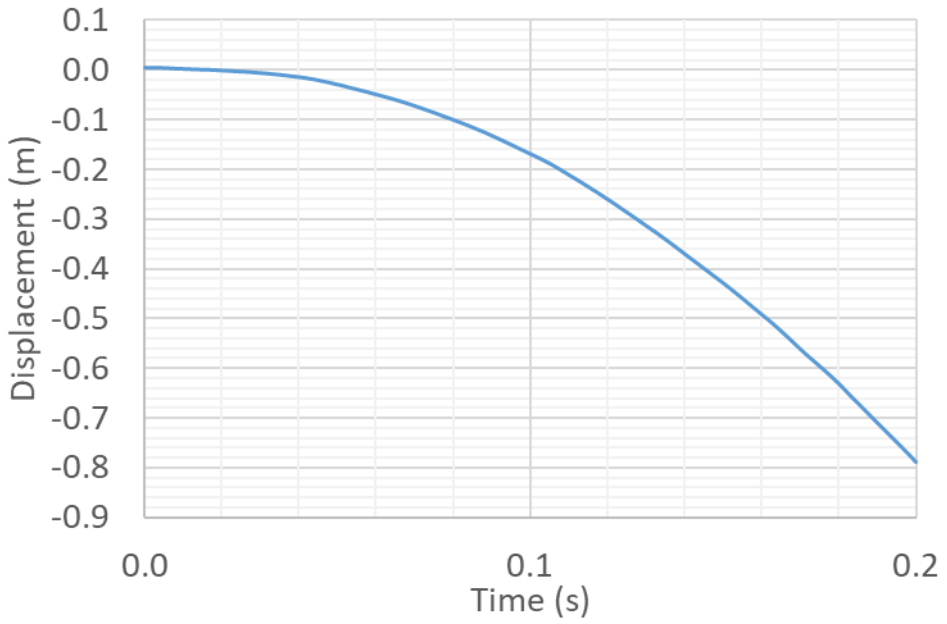

Figure 94. Relative longitudinal displacement of the occupant (m)–Test T90-R300.

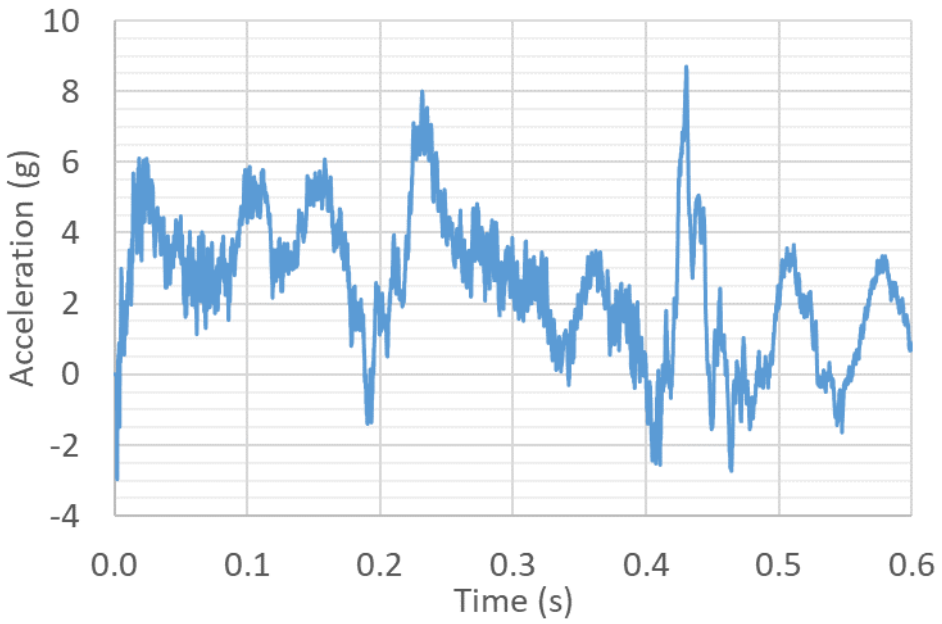

Figure 95. 10 m/s average vehicle lateral acceleration (g) – Test T90-R300.

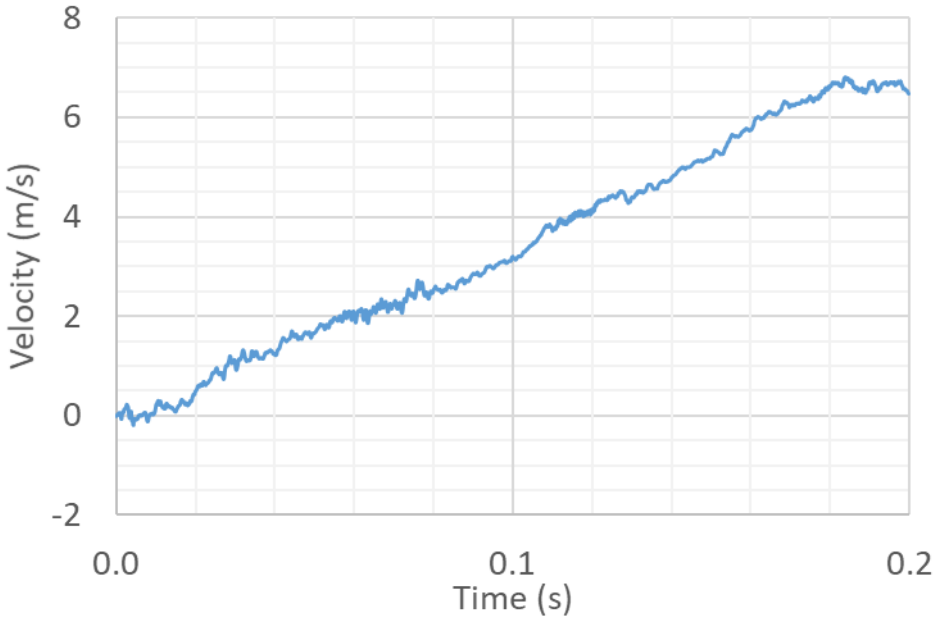

Figure 96. Relative lateral velocity of the occupant (m/s) - Test T90-R300.

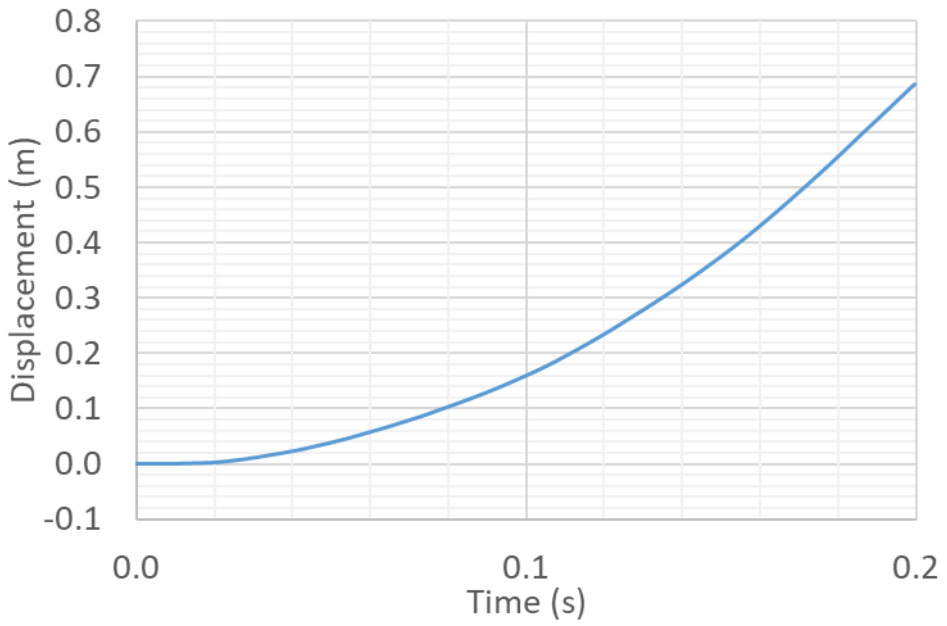

Figure 97. Relative lateral displacement of the occupant (m) - Test T90-R300.

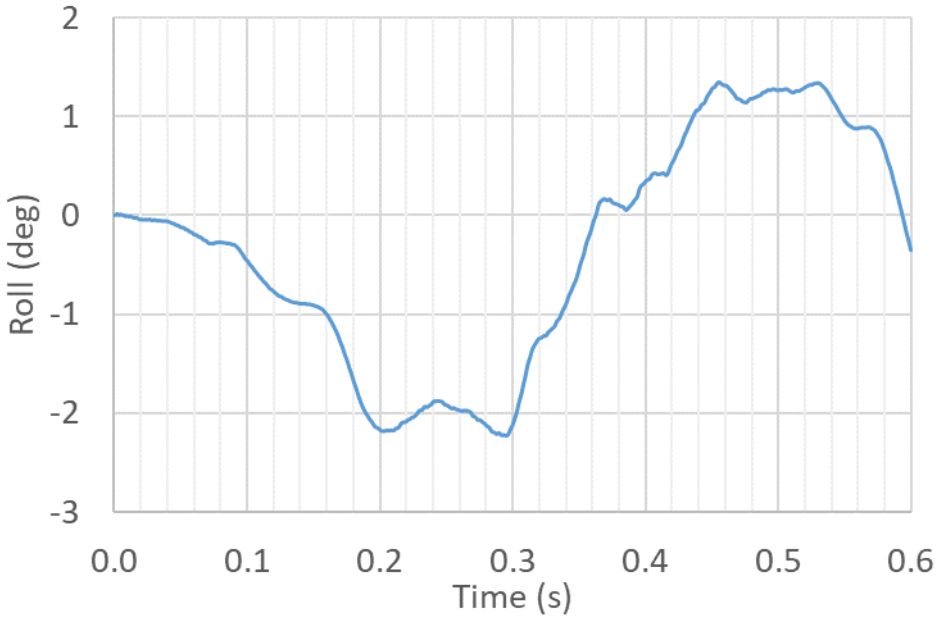

Figure 98. Vehicle roll (deg) - Test T90-R300.

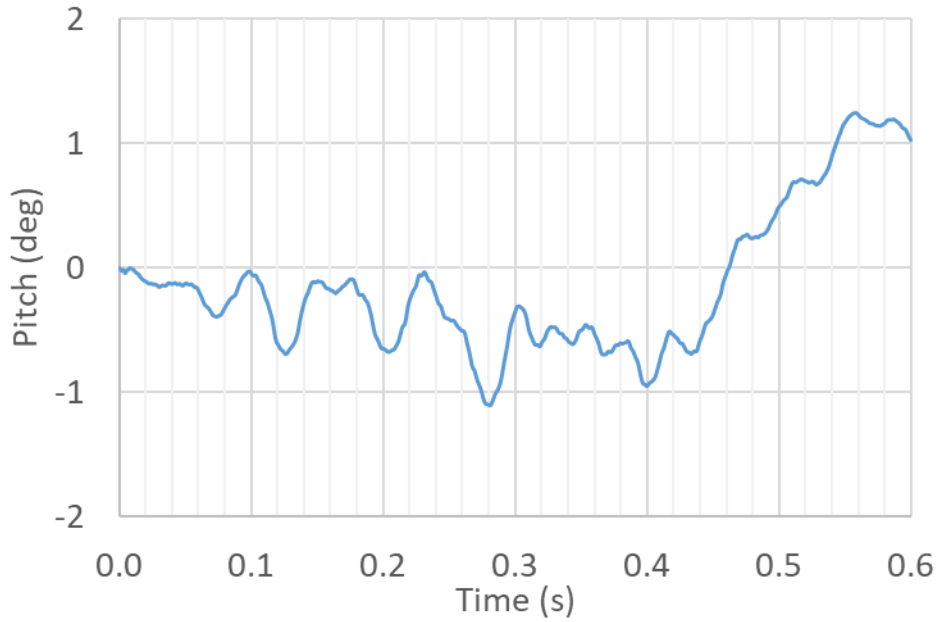

Figure 99. Vehicle pitch (deg) - Test T90-R300.

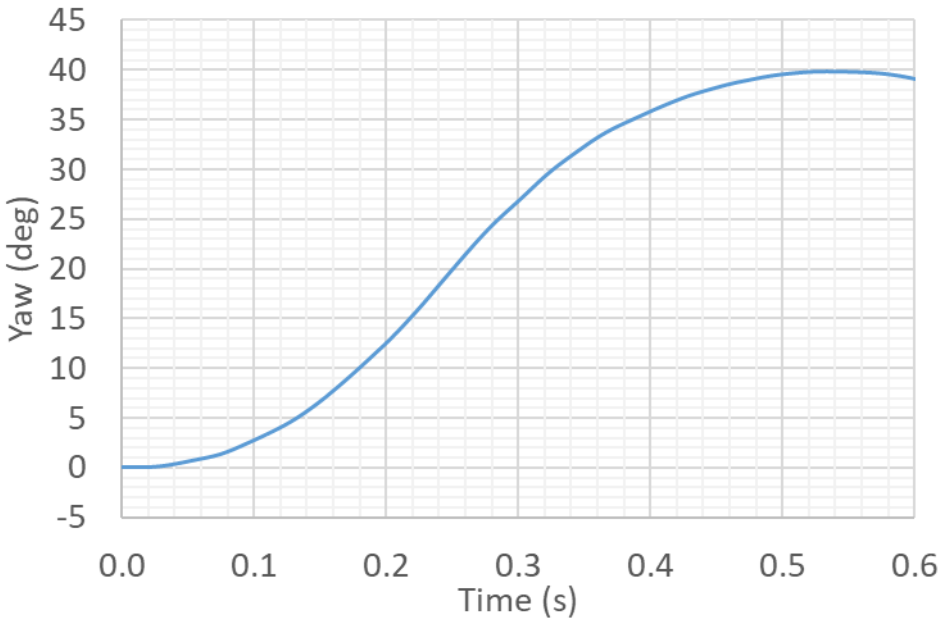

Figure 100. Vehicle yaw (deg) - Test T90-R300.

Table 12. Summary of full-scale crash simulation results for Test T90-R300.

Test Number		T90-R300
Vehicle	Designation	2270P
	Test Inertial, kg	2,270
Impact Conditions	Speed, km/h	100
	Angle, deg	25.0
Exit Conditions	Speed (km/h)	57
	Trajectory Angle, deg	13
ORA, g's < 20.49 g	Longitudinal	-9.3
	Lateral	8.7
OIV, m/s < 12.2 m/s	Longitudinal	5.8
	Lateral	4.6
Test Article Deflections, m	Dynamic	0.96
	Permanent	0.81
Impact Time for the Occupant, sec		0.136
Sum. of all posts ground level displacement (m)		1.473
Max. Yaw Angle, deg		40
Max. Roll Angle, deg < 75 deg		-2
Max. Pitch Angle, deg < 75 deg		1
Posts detached from rail during impact		3 posts
Posts hit by leading tire (wheel snag)		3 posts
Posts pulled out of ground		none
Leading tire/wheel disengaged		mostly

6.3.4 Guardrail System with Asphalt Mow Strip with 90 mm Thickness and 600 mm Rear Distance (Test T90-R600)

The model was updated by increasing the rear distance to 600 mm while keeping the thickness unchanged at 90 mm. This asphalt mow strip geometry is the recommended GDOT setup. The simulation results are graphically presented in Figure 101 through Figure 106. During the collision, the leading front wheel of the vehicle hit a guardrail post at approximately 0.1 sec (Figure 101 and Figure 103 at 0.1 sec), which is same as in previous simulations. However, this time the wheel passed behind the post instead of going over the post. This is due to the fact that the ground level displacement of the post for this case was noticeably lower than in previous cases. Again, the suspension system failed partially but stayed connected to the vehicle; the wheel continued to rotate throughout the rest of the simulation, as shown in Figure 106. At approximately 0.2 sec the vehicle hit and passed over the second post (Figure 101 and Figure 103 at 0.2 sec). The vehicle moved forward and hit the third post at approximately 0.3 sec. Unlike with the first and second posts, the leading wheel did not completely go over the third post. The wheel snagging for this case was worse than Tests T50-R600 and T90-R300. The vehicle ran parallel to the guardrail at approximately 0.3 sec, and was then redirected back to the road, losing contact with the guardrail at approximately 0.65 sec. Vehicle pocketing did not occur during this simulation. Asphalt rupture propagated around each post; however, it was much more limited than in Tests T50-R600 and T90-R300. The ruptures for each post connected to the ruptures

around other posts. This is similar to the ruptures that occurred in Test T50-R600, which had the same rear distance.

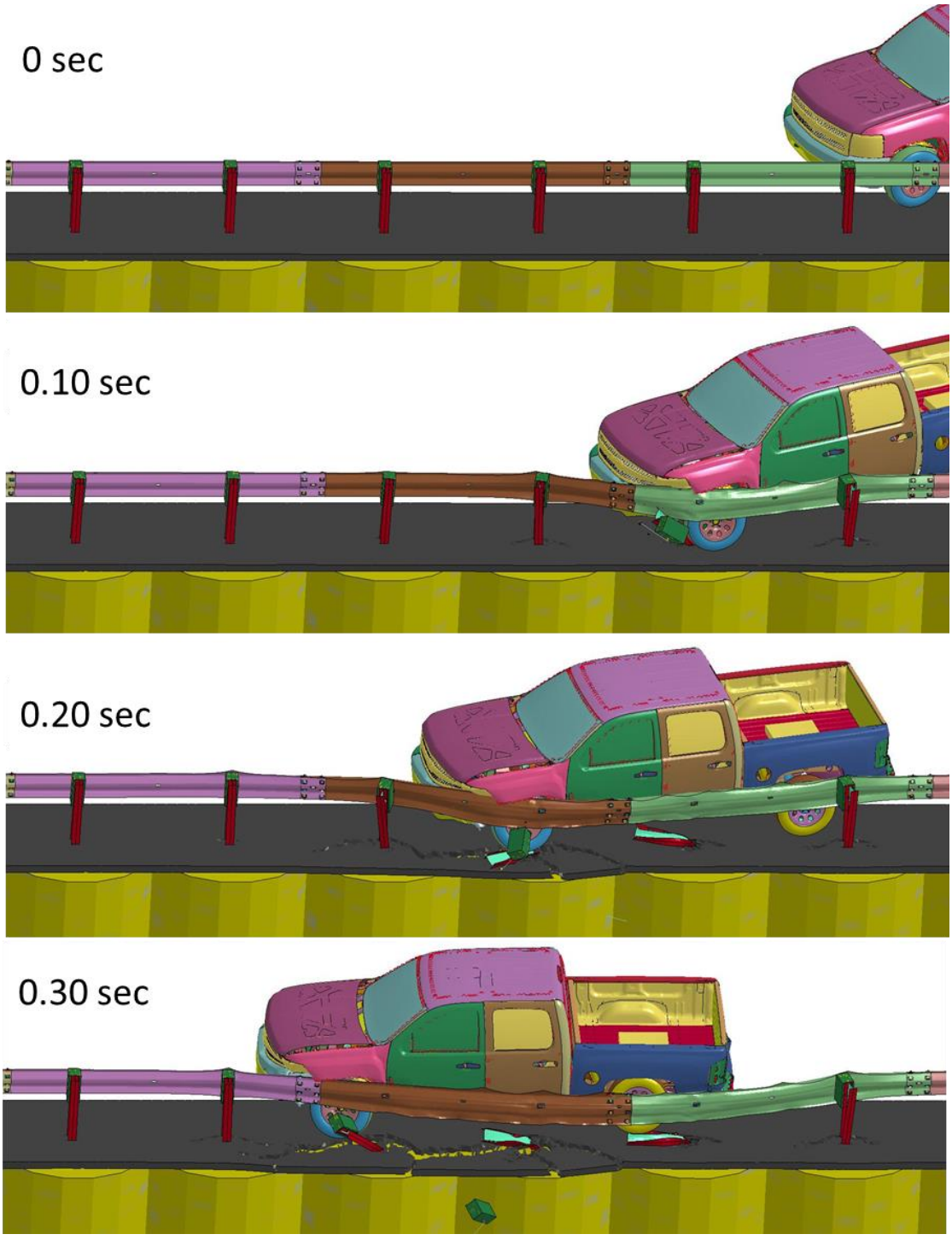

Figure 101. Simulation result for Test T90-R600 – up to 0.3 sec.

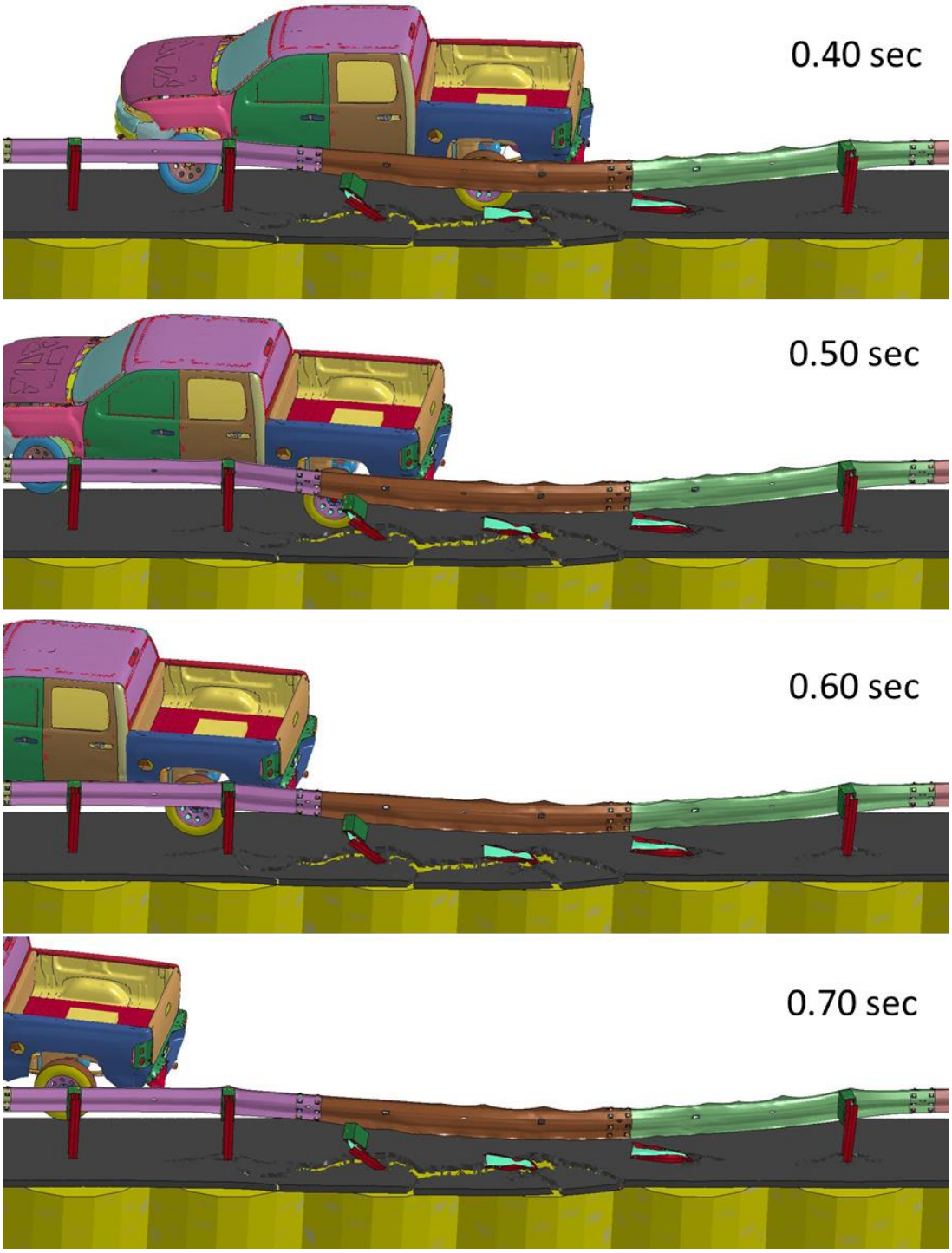

Figure 102. Simulation result for Test T90-R600 – after 0.3 sec.

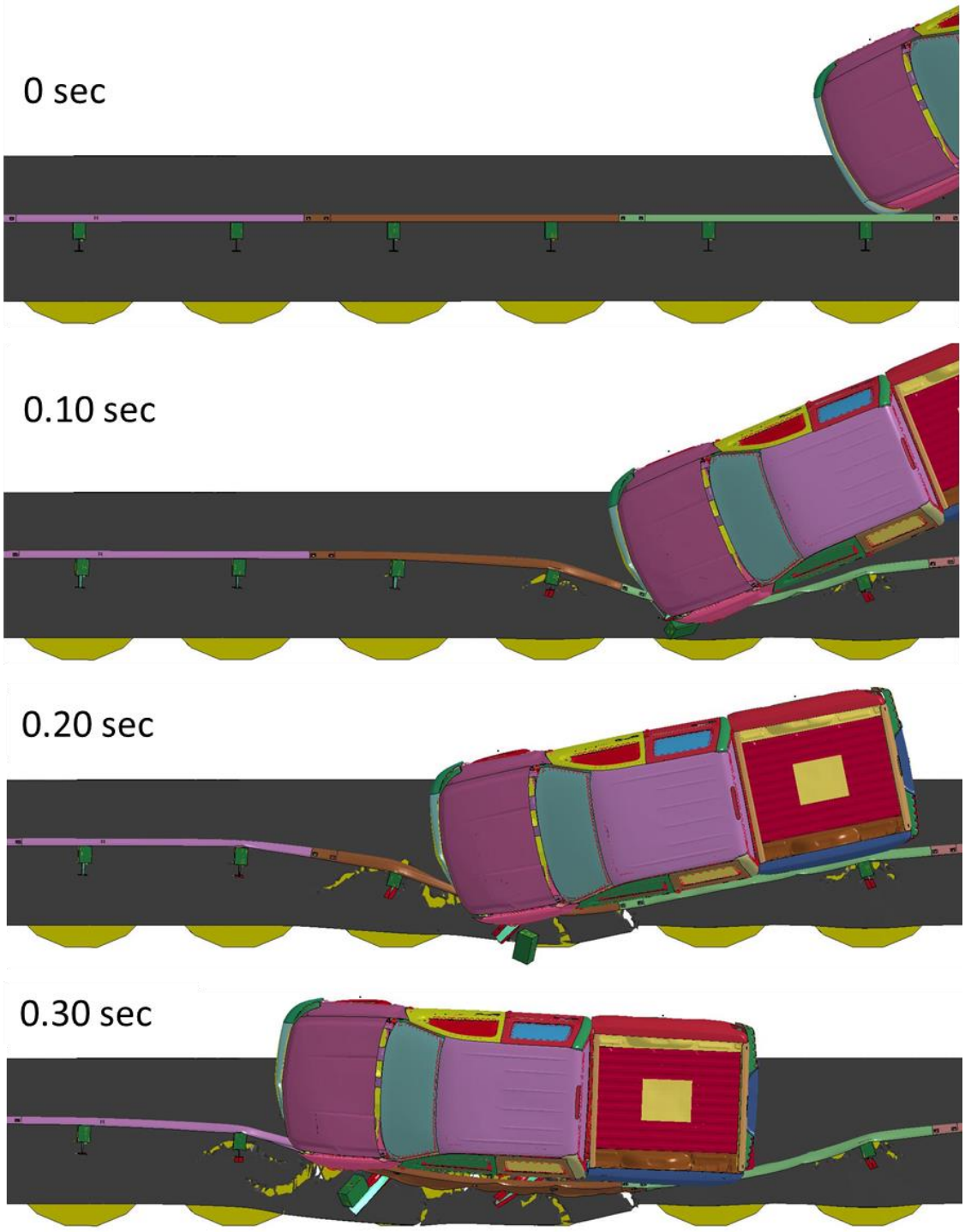

Figure 103. Simulation result for Test T90-R600 – up to 0.3 sec.

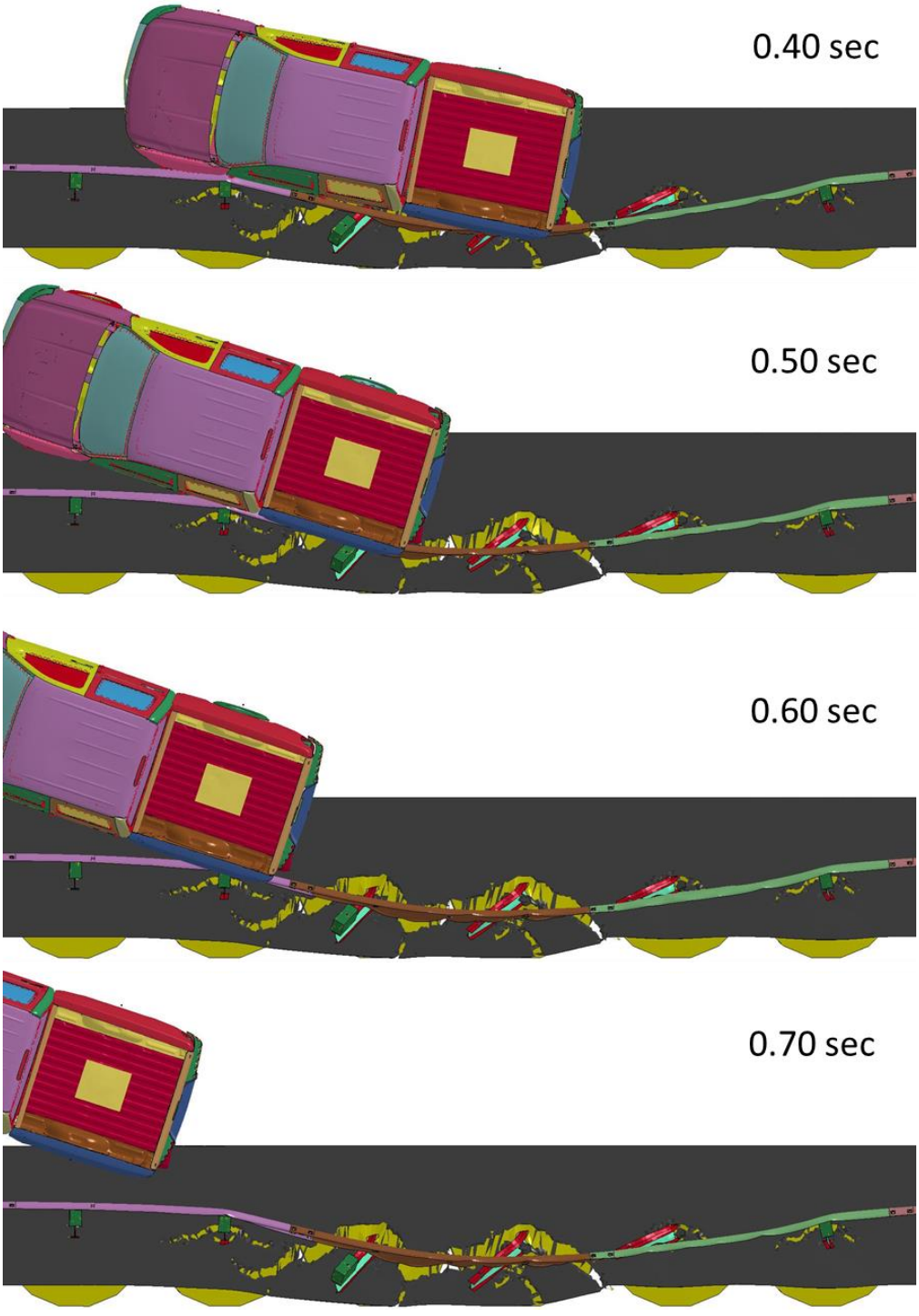

Figure 104. Simulation result for Test T90-R600 – after 0.3 sec.

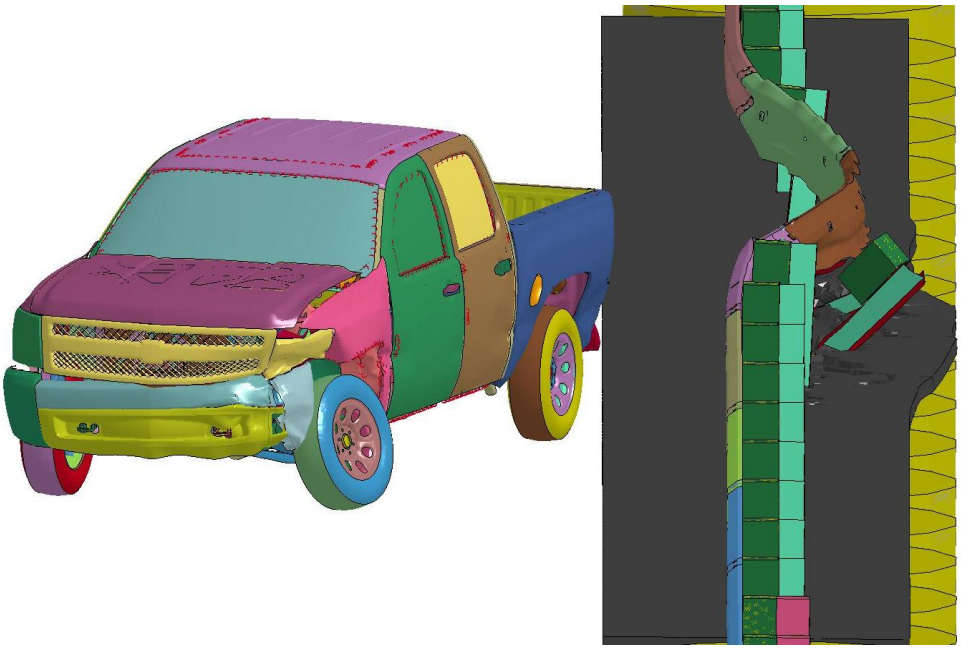

Figure 105. Simulation result for Test T90-R600.

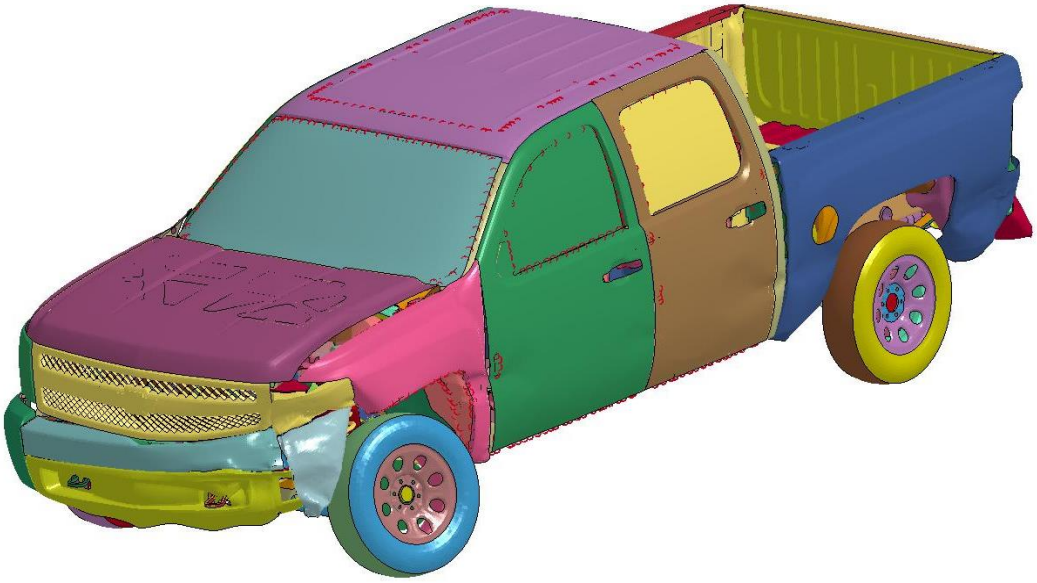

Figure 106. Vehicle Deformation for Test T90-R600.

Ruptures behind only two posts reached the edge of the mow strip. Those segments of asphalt became detached from the rest of the asphalt. This considerably decreased the ground level restraint for these two posts. However, the other posts remained encased in asphalt through the end of the simulation and experienced much higher ground level restraint.

The longitudinal and lateral accelerations of the vehicle were obtained and are shown in Figure 107 and Figure 110. The integration of these accelerations over time produced the velocity of the occupant relative to the vehicle in the longitudinal and lateral directions as presented in Figure 108 and Figure 111. Another integration over time resulted in the displacement of the occupant relative to the vehicle as presented in Figure 109 and Figure 112. The times when the lateral displacement equalled 305 mm and when the longitudinal displacement equalled 610 mm were found using the relative displacement curves (Figure 109 and Figure 112). The smaller of these two was for the lateral displacement, equal to 0.140 sec, which was close to the occupant impact time for previous test simulations. After the occupant hit the interior, it is assumed that he moved with the vehicle. The longitudinal and lateral occupant impact velocities, OIVs, were then determined using relative velocity curves (Figure 108 and Figure 111) by finding the relative velocities at 0.140 sec. Thereafter, the peak accelerations from the acceleration curves (Figure 107 and Figure 110) were found for the period of time after 0.140 sec until the end of the collision. The OIVs and ORAs were lower than the maximum limit in MASH guidelines. The results are reported in Table 13.

The roll, pitch, and yaw angles of the vehicle were recorded during simulations. The time histories for these parameters are shown in Figure 113 to Figure 115. The peak values of roll and pitch were lower than the MASH limit of 75 deg. The peak values of yaw, roll, pitch, the exit angle, the exit speed of the vehicle, the maximum deflection of the guardrail, the permanent deflection of the guardrail, and summation of ground level displacement of all posts are reported in Table 13. None of the posts was pulled out of the ground during the simulation, and three posts were detached from the guardrail, which is the same as all previously discussed test simulations.

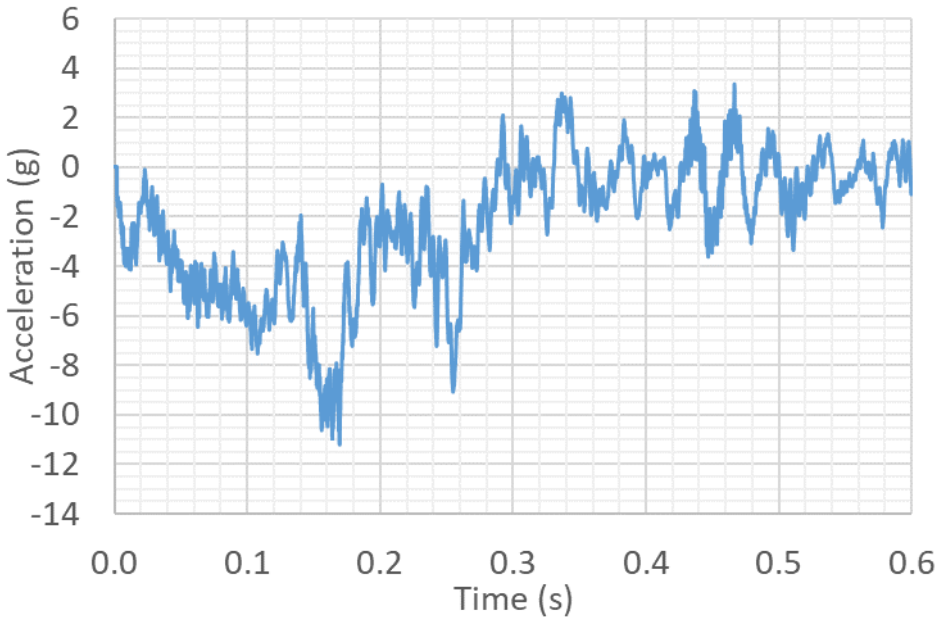

Figure 107. 10 m/s average vehicle longitudinal acceleration (g) - Test T90-R600.

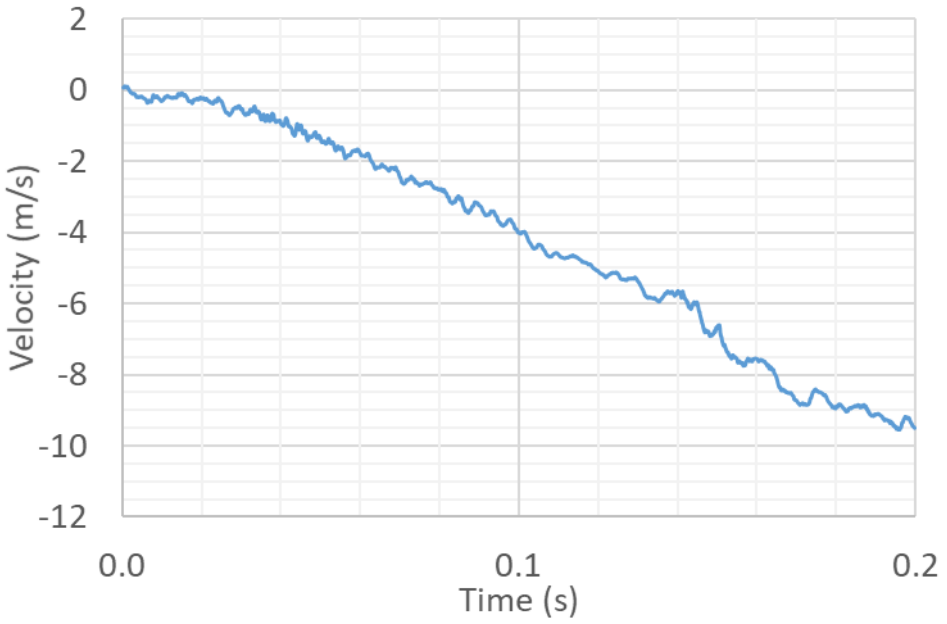

Figure 108. Relative longitudinal velocity of the occupant (m/s) - Test T90-R600.

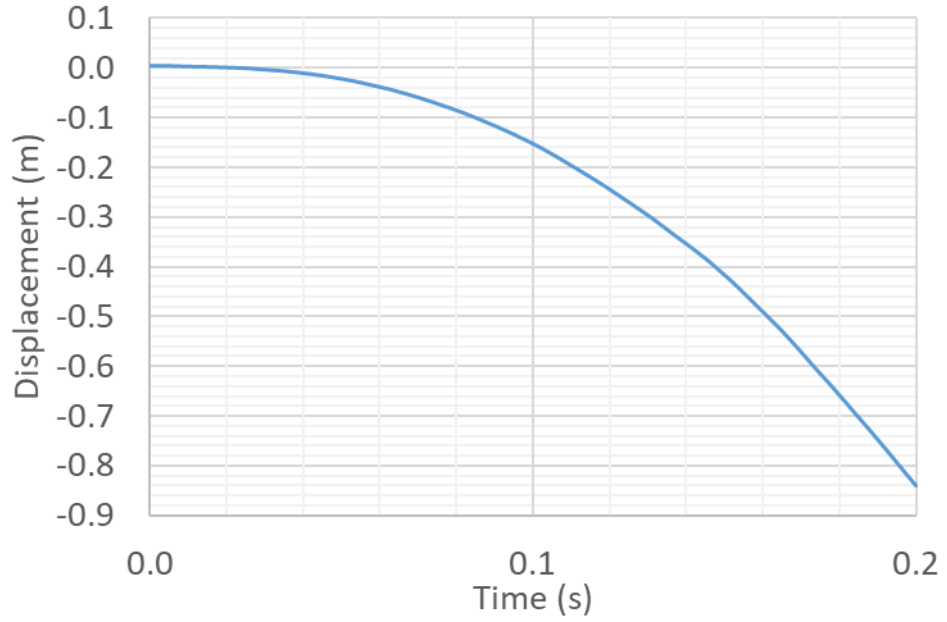

Figure 109. Relative longitudinal displacement of the occupant (m) – Test T90-R600.

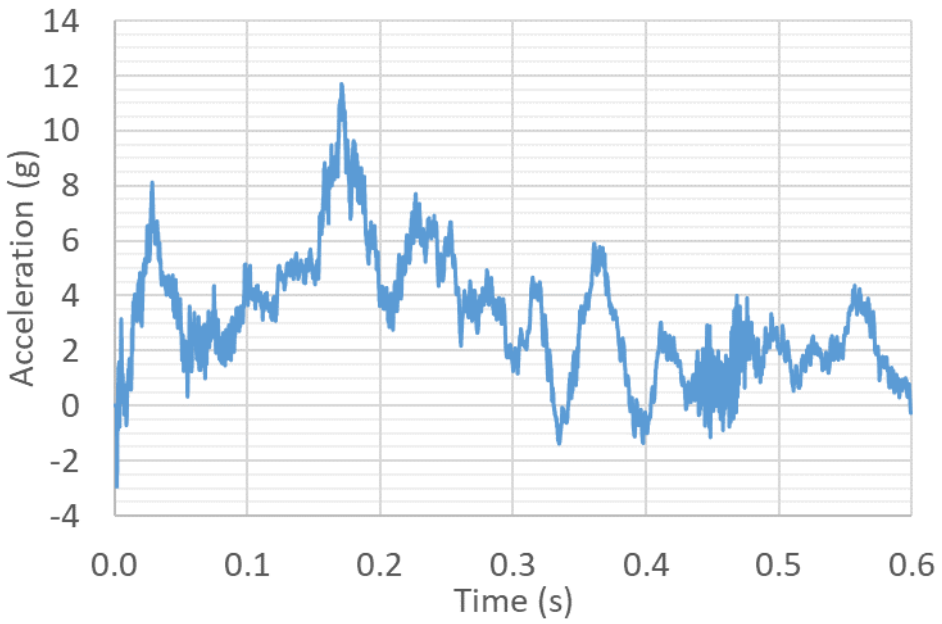

Figure 110. 10 m/s average vehicle lateral acceleration (g) – Test T90-R600.

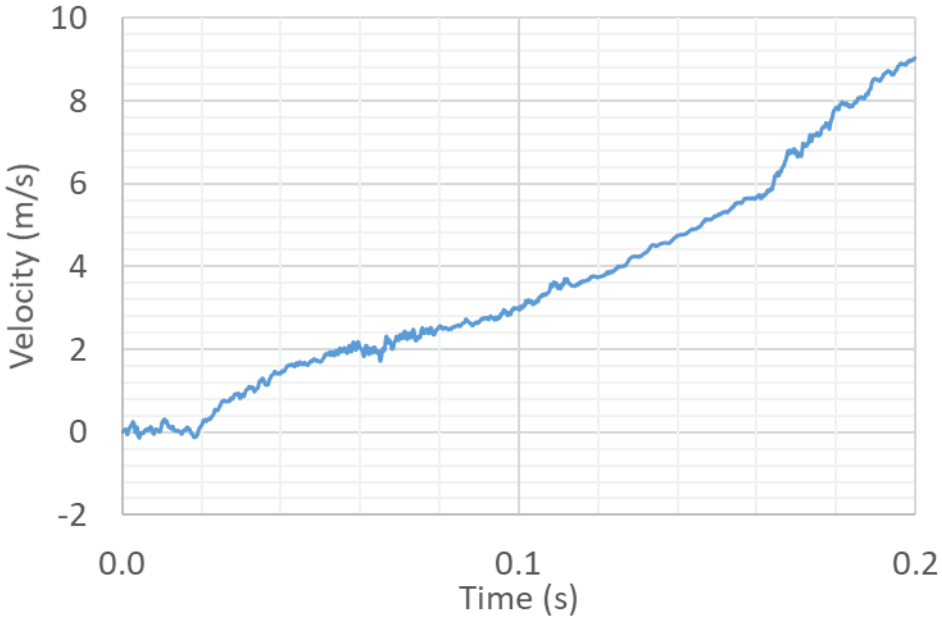

Figure 111. Relative lateral velocity of the occupant (m/s) - Test T90-R600.

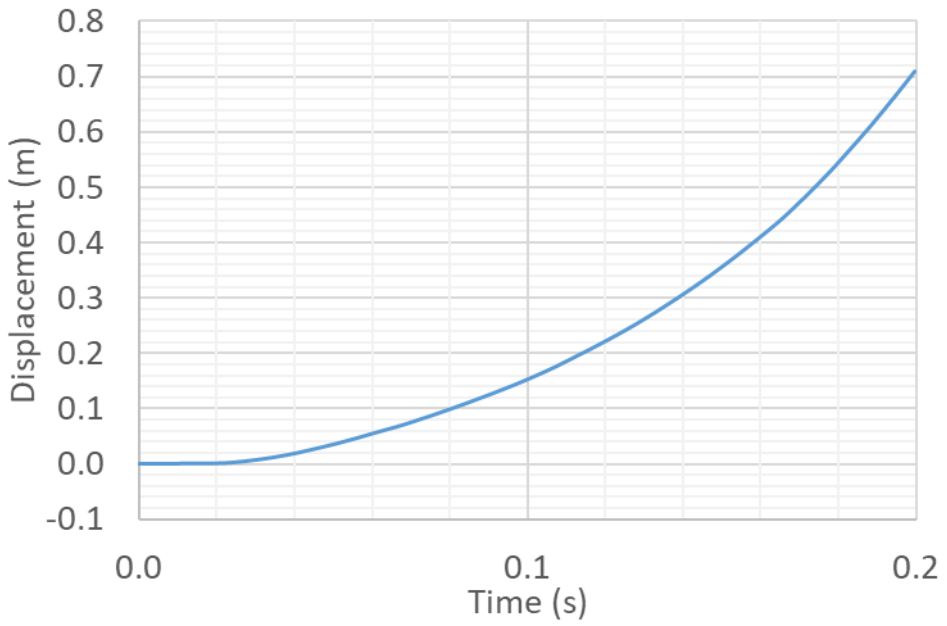

Figure 112. Relative lateral displacement of the occupant (m) - Test T90-R600.

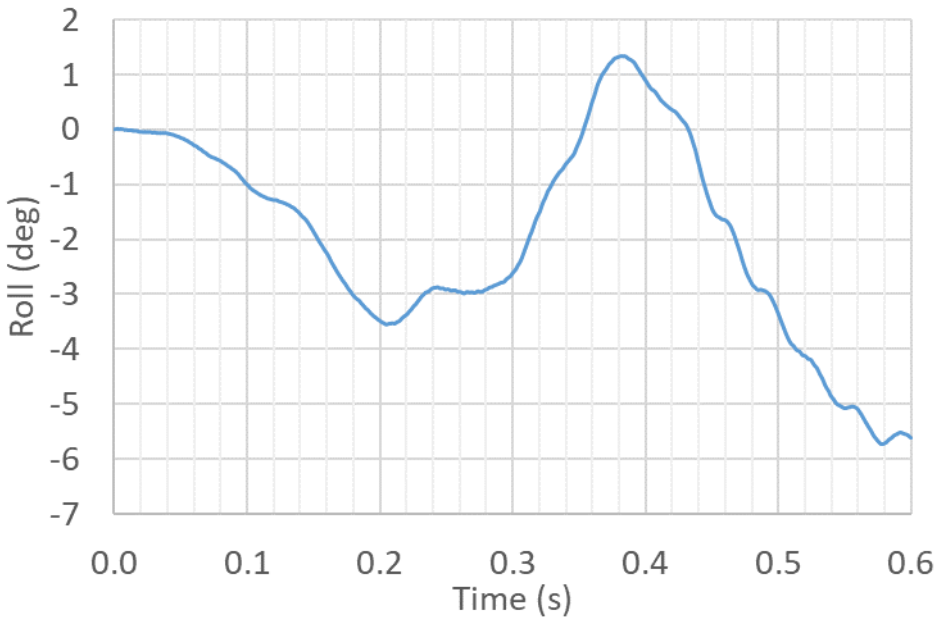

Figure 113. Vehicle roll (deg) - Test T90-R600.

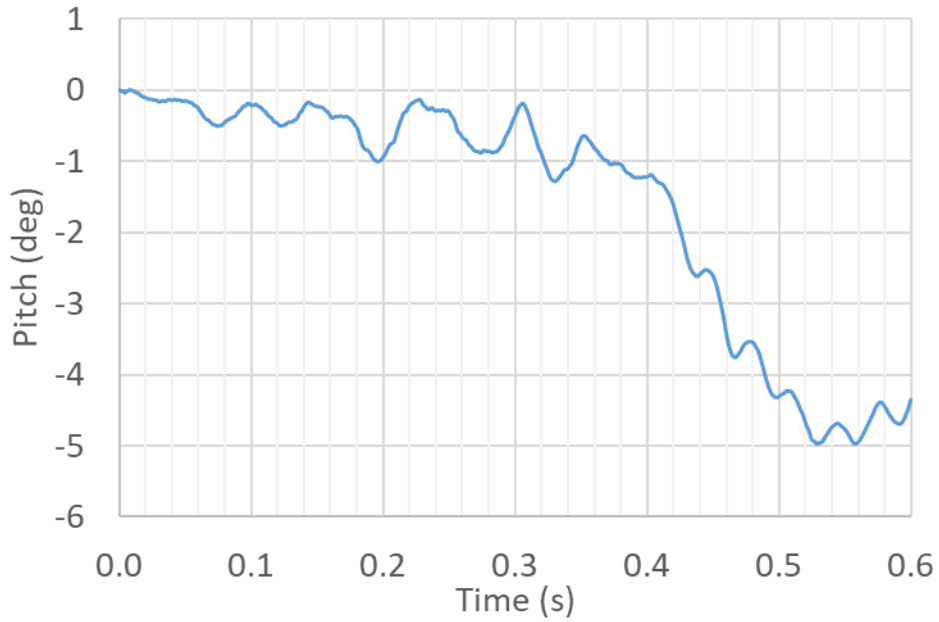

Figure 114. Vehicle pitch (deg) - Test T90-R600.

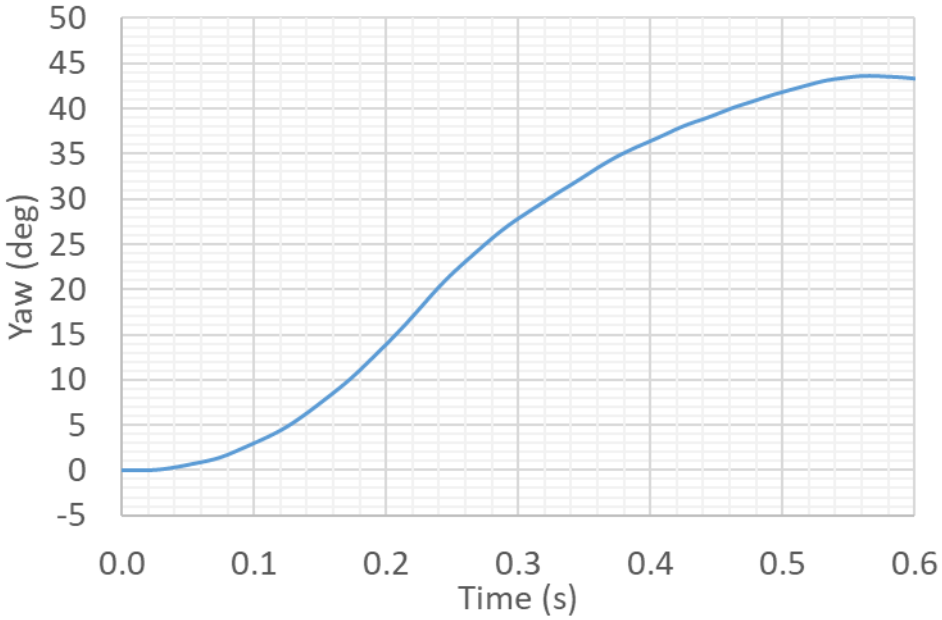

Figure 115. Vehicle yaw (deg) - Test T90-R600.

Table 13. Summary of full-scale crash simulation results for Test T90-R600.

Test Number		T90-R600
Vehicle	Designation	2270P
	Test Inertial, kg	2,270
Impact Conditions	Speed, km/h	100
	Angle, deg	25.0
Exit Conditions	Speed (km/h)	58
	Trajectory Angle, deg	18
ORA, g's < 20.49 g	Longitudinal	-11.2
	Lateral	11.7
OIV, m/s < 12.2 m/s	Longitudinal	5.6
	Lateral	4.7
Test Article Deflections, m	Dynamic	0.842
	Permanent	0.753
Impact time for the Occupant, sec		0.140
Sum. of all posts ground level displacement (m)		0.734
Max. Yaw Angle, deg		44
Max. Roll Angle, deg < 75 deg		-6
Max. Pitch Angle, deg < 75 deg		-5
Posts detached from rail during impact		3 posts
Posts hit by leading tire (wheel snag)		3 posts
Posts pulled out of ground		none
Leading tire/wheel disengaged		mostly

6.3.5 Guardrail System with Asphalt Mow Strip with 150 mm Thickness and 600 mm Rear Distance (Test T150-R600)

The model was updated by increasing the thickness to 90 mm; the rear distance remained unchanged at 600 mm. This asphalt mow strip geometry is the thickest and has the longest rear distance among all the setups investigated in this research. The simulation results are graphically presented in Figure 116 through Figure 121. During the collision, the leading front wheel of the vehicle hit a guardrail post at approximately 0.1 sec, which is same as previous simulations. However, this time the wheel passed far behind the post instead of going over the post as in previous simulations (Figure 116 and Figure 118 at 0.1 Sec). This shows that the ground level displacement of the post for this case was considerably lower than previous cases. In all simulations discussed so far, the suspension system failed partially but remained connected to the vehicle, and the wheel continued to rotate throughout the rest of the simulation as shown in Figure 121. At approximately 0.2 sec, the vehicle hit the second post and passed behind it (Figure 116 and Figure 118 at 0.2 Sec). This did not happen in Tests T50-R600, T90-R300, T90-R600, or in the test with soil only. The vehicle moved forward and hit the third post at approximately 0.3 sec (Figure 116 and Figure 118 at 0.3 Sec). The leading wheel passed over the post, which did not happen in Tests T50-R600, T90-R300, and T90-R600. The wheel snagging for this case was much more pronounced than in Tests T50-R600 and T90-R300. The vehicle ran parallel to the guardrail at approximately 0.3 sec, and was redirected back to the road,

losing contact with the guardrail at approximately 0.65 sec. Vehicle pocketing did not occur during this simulation.

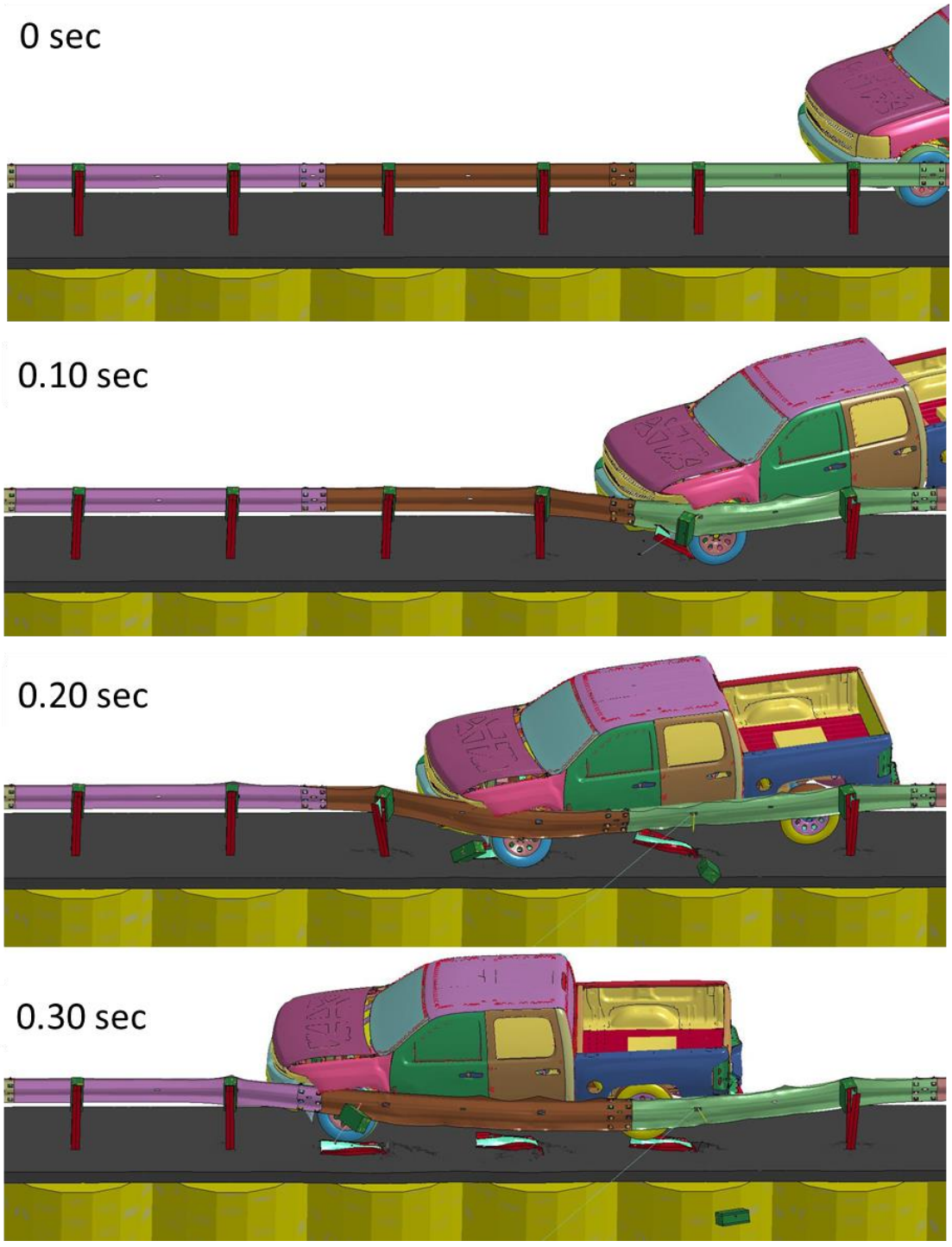

Figure 116. Simulation result for Test T150-R600 – up to 0.3 sec.

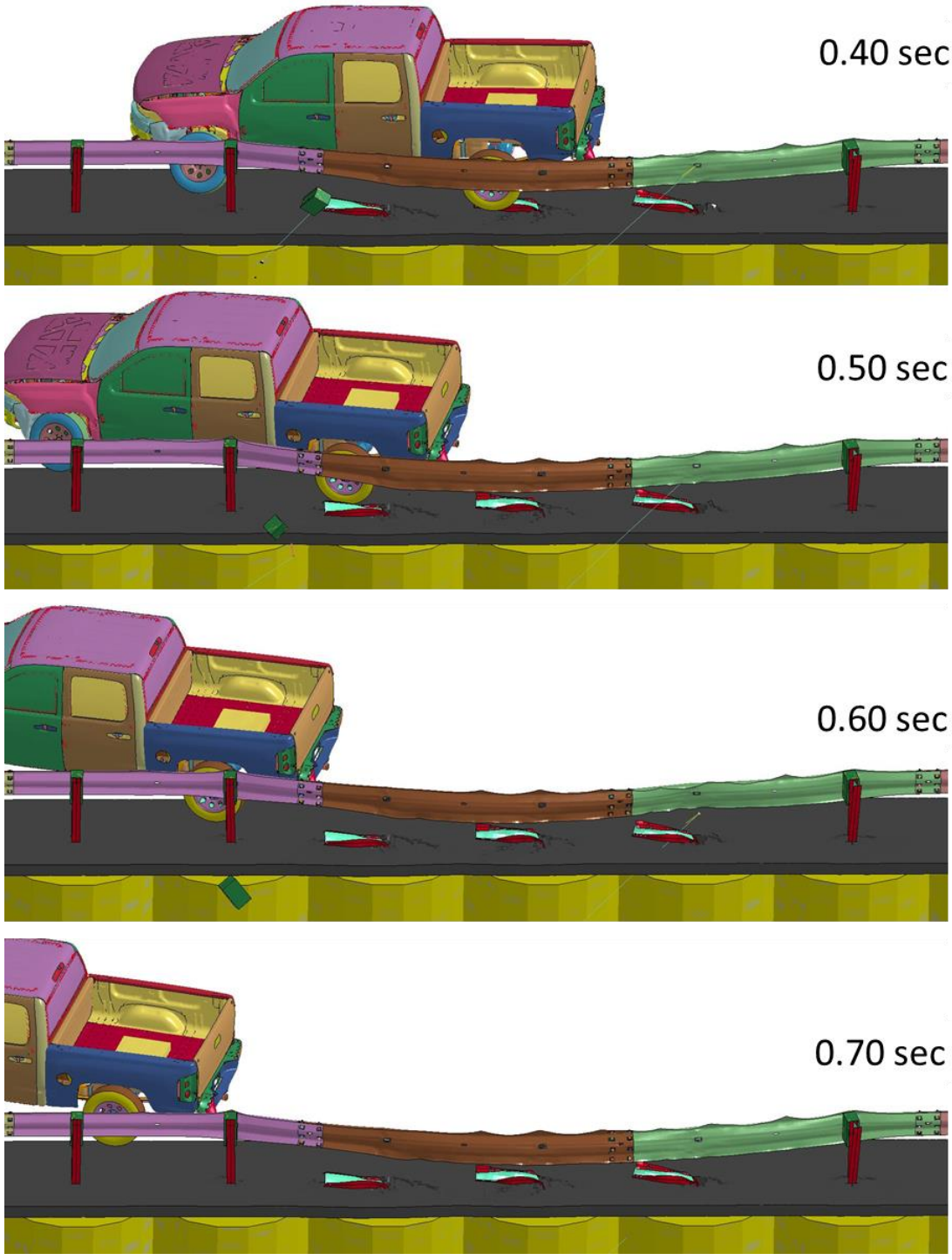

Figure 117. Simulation result for Test T150-R600 – after 0.3 sec.

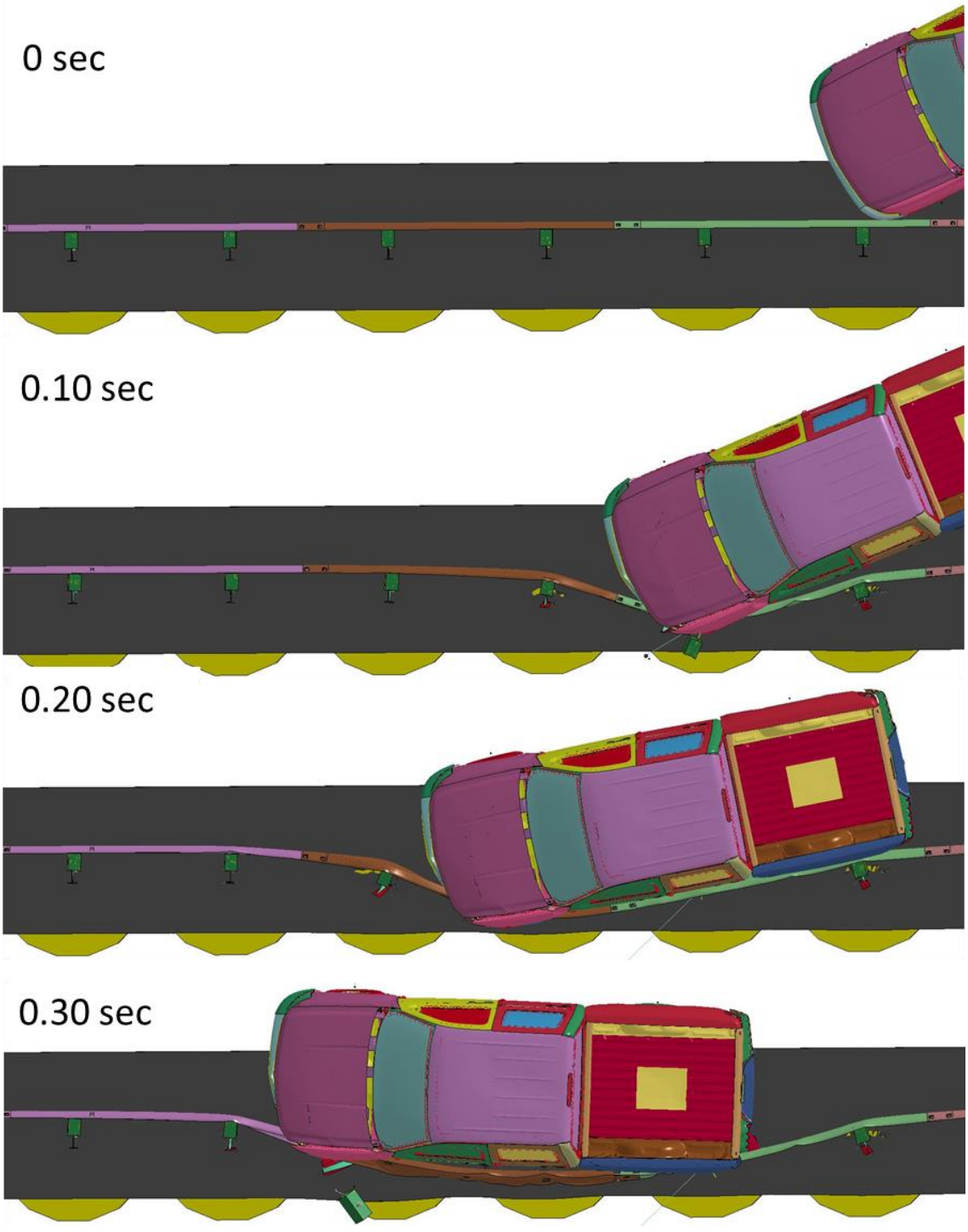

Figure 118. Simulation result for Test T150-R600 – up to 0.3 sec.

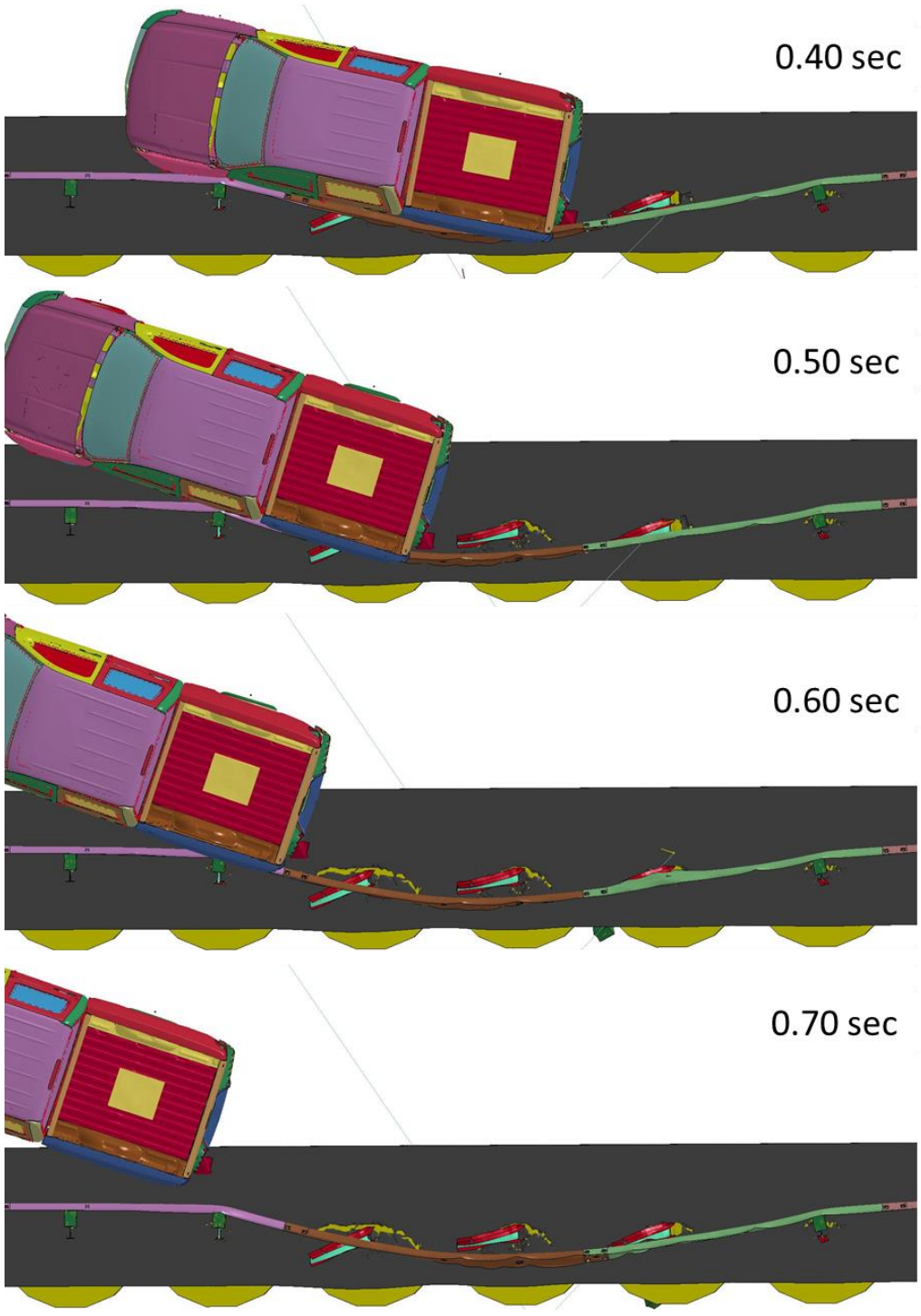

Figure 119. Simulation result for Test T150-R600 – after 0.3 sec.

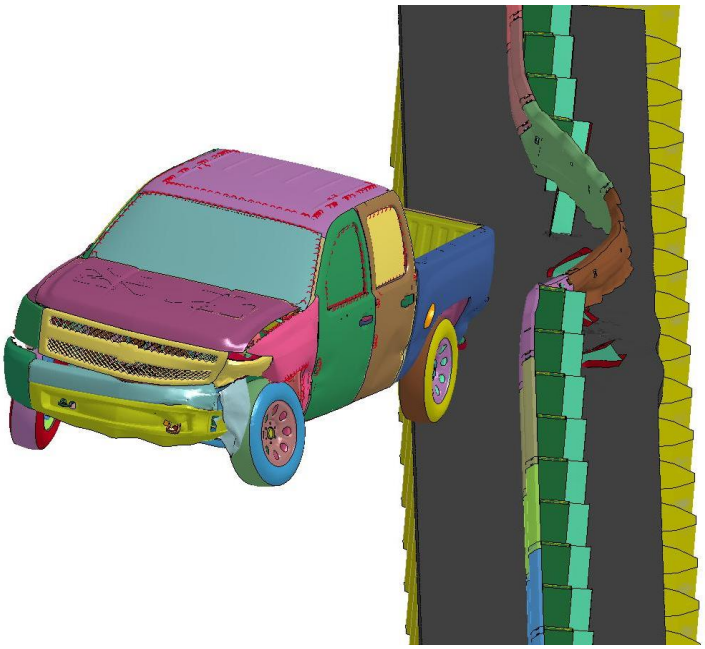

Figure 120. Simulation result for Test T150-R600.

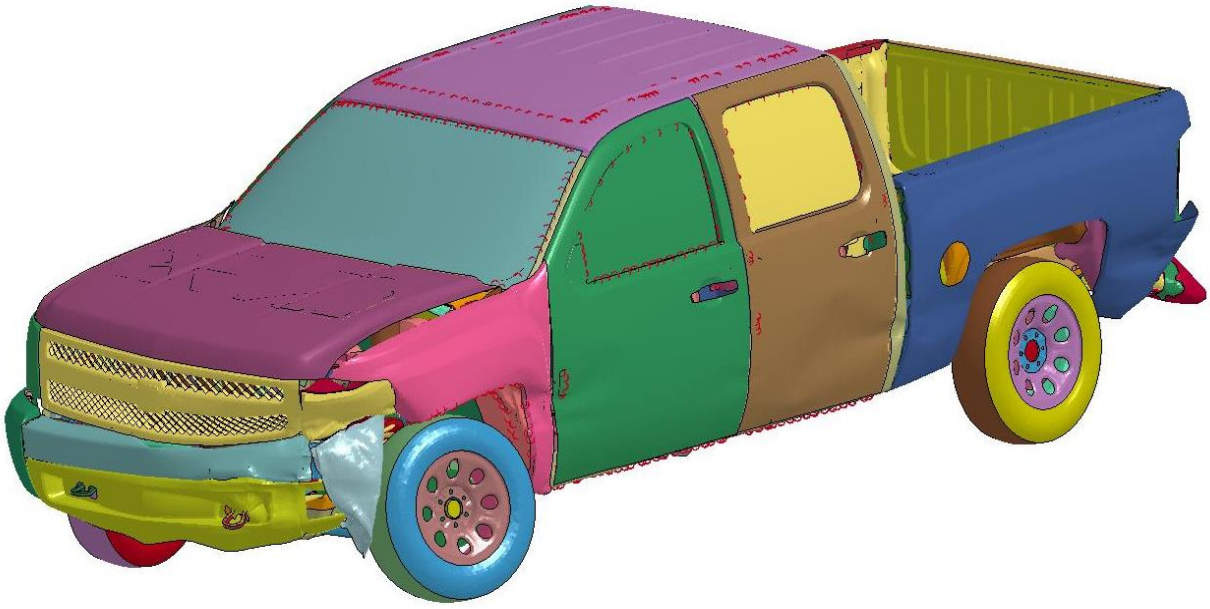

Figure 121. Vehicle Deformation for Test T150-R600.

There were very limited asphalt ruptures around each post. These ruptures did no connect to any of the ruptures from other posts. This means all posts remained encased in asphalt through the end of the simulation and experienced extreme ground level restraint.

The longitudinal and lateral acceleration, velocity, and displacement of the vehicle were obtained and are shown in Figure 122 to Figure 127. The occupant impact time is governed by the lateral impact of the occupant and was determined to be equal to 0.136. The OIVs and ORAs were obtained based on the occupant impact time and are reported in Table 14. They are lower than the maximum limit in the MASH guidelines. The roll, pitch, and yaw angles of the vehicle were recorded during simulations. The time histories for these parameters are shown in Figure 128 to Figure 130. The peak values of roll and pitch were lower than the MASH limit of 75 deg. The peak values of yaw, roll, pitch, the exit angle, the exit speed of the vehicle, the maximum deflection of the guardrail, the permanent deflection of the guardrail, and summation of ground level displacement of all posts are reported in Table 14. None of the posts was pulled out of the ground during the simulation, and three posts detached from the guardrail, which is same as all previously discussed test simulations.

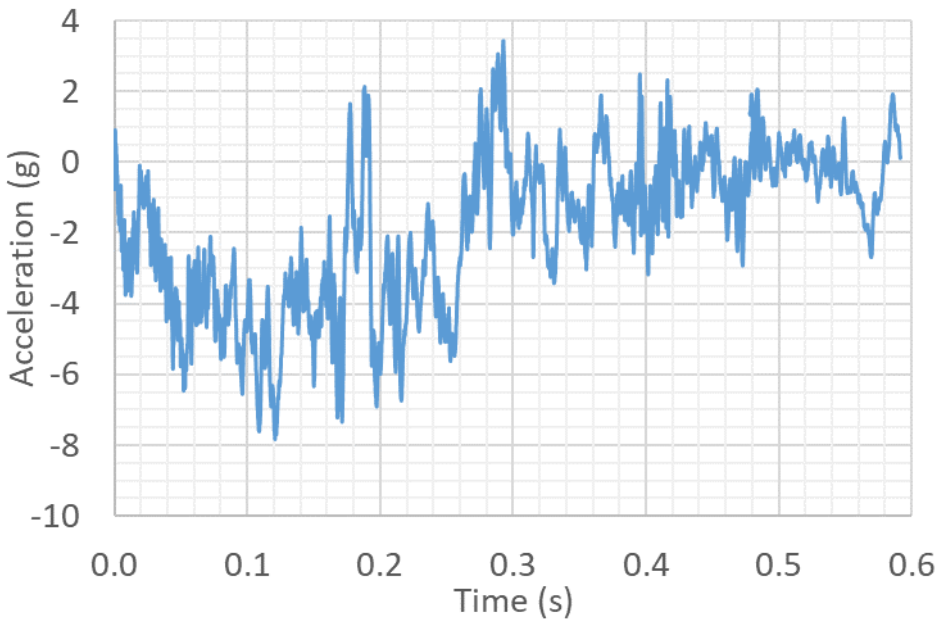

Figure 122. 10 m/s average vehicle longitudinal acceleration (g) - Test T150-R600.

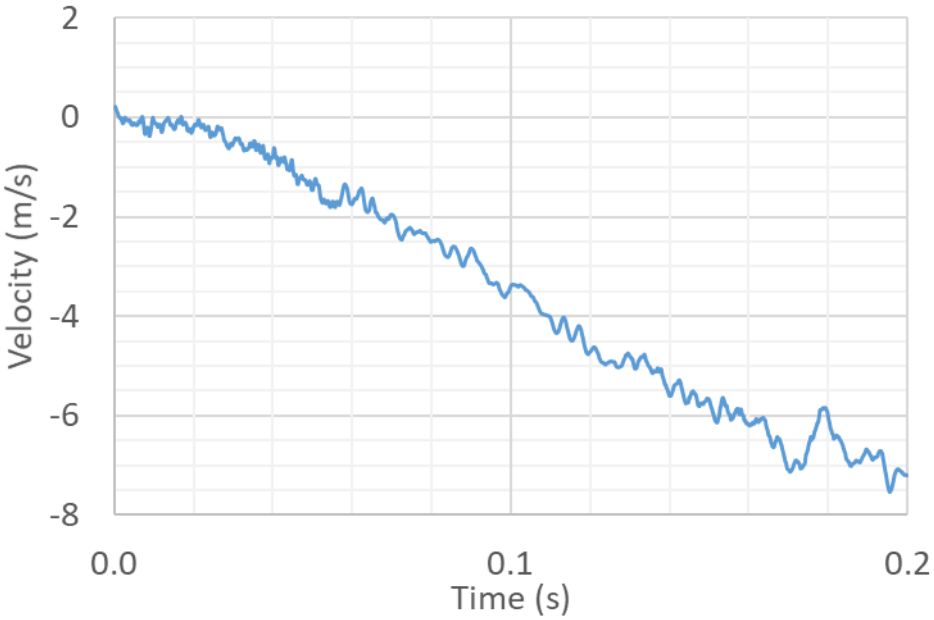

Figure 123. Relative longitudinal velocity of the occupant (m/s) - Test T150-R600.

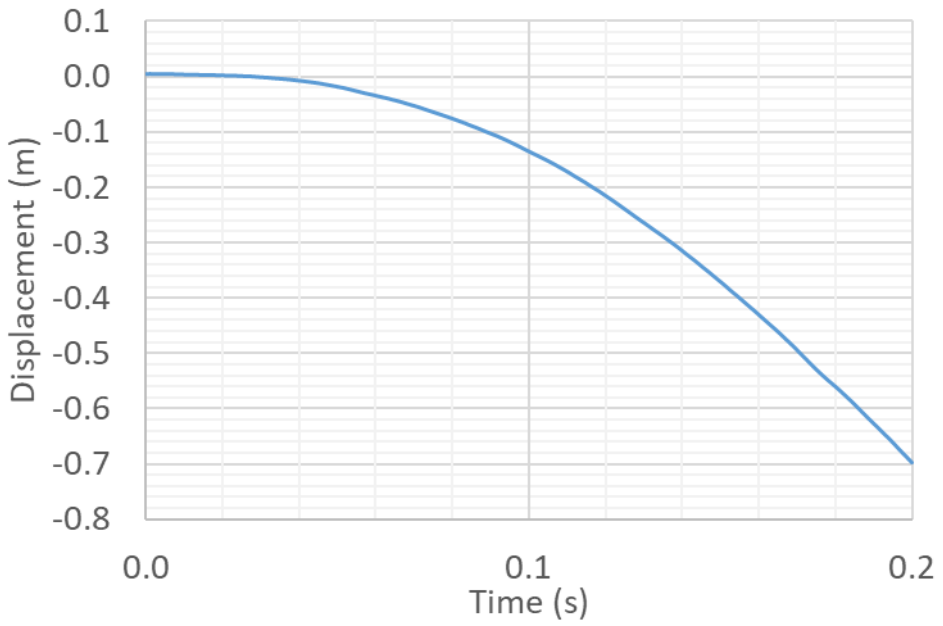

Figure 124. Relative longitudinal displacement of the occupant(m)–Test T150-R600.

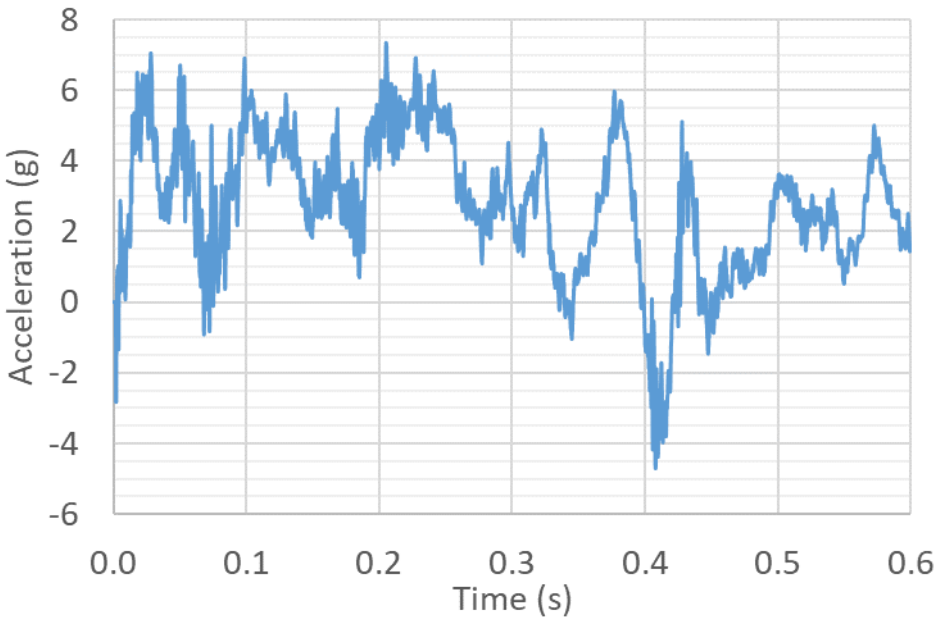

Figure 125. 10 m/s average vehicle lateral acceleration (g) – Test T150-R600.

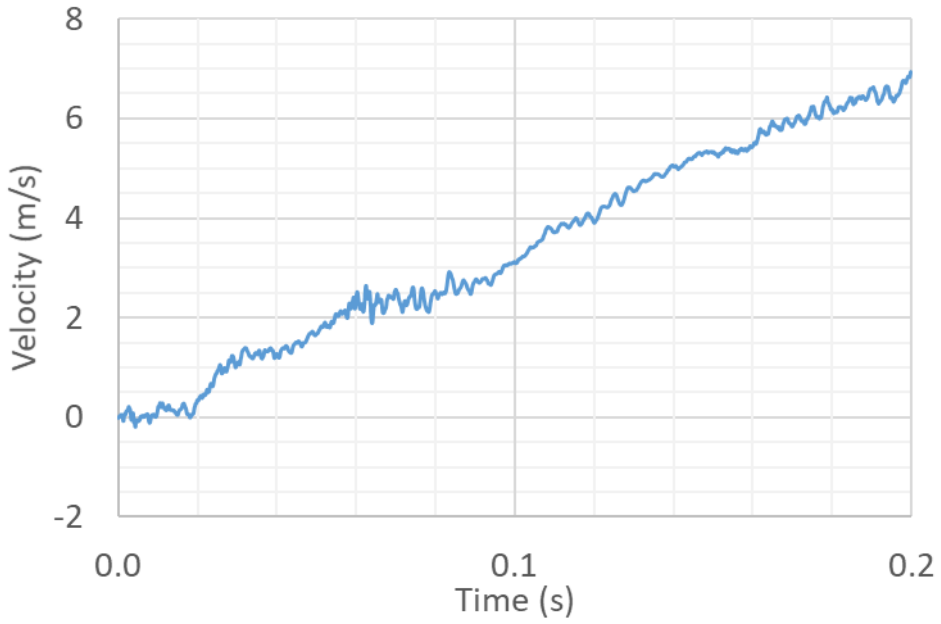

Figure 126. Relative lateral velocity of the occupant (m/s) - Test T150-R600.

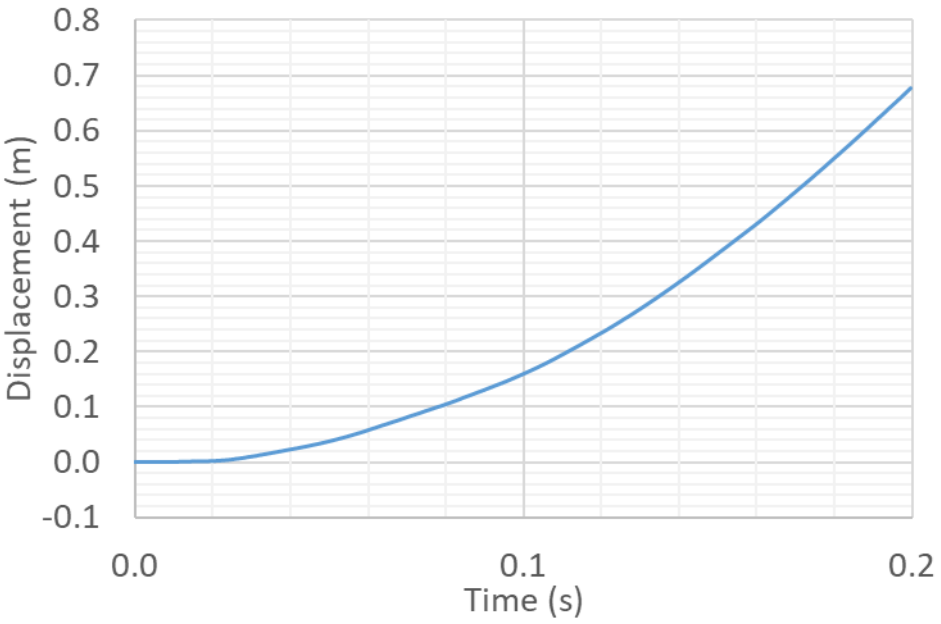

Figure 127. Relative lateral displacement of the occupant (m) - Test T150-R600.

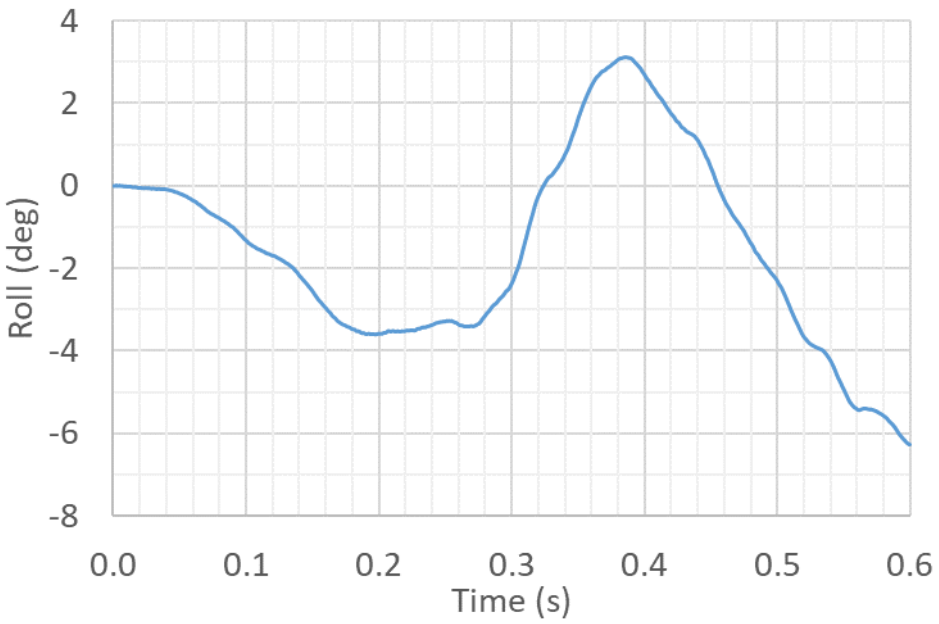

Figure 128. Vehicle roll (deg) - Test T150-R600.

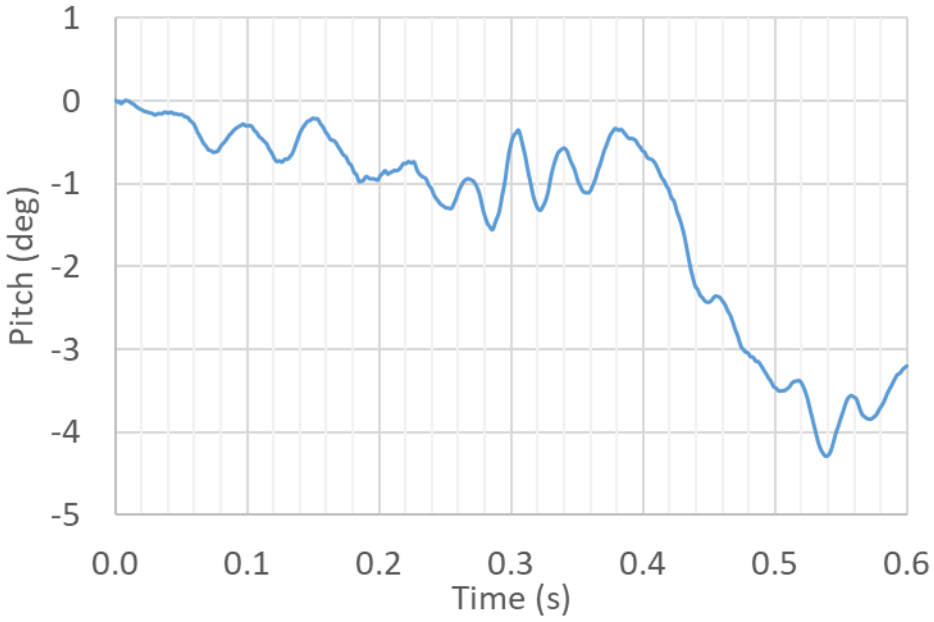

Figure 129. Vehicle pitch (deg) - Test T150-R600.

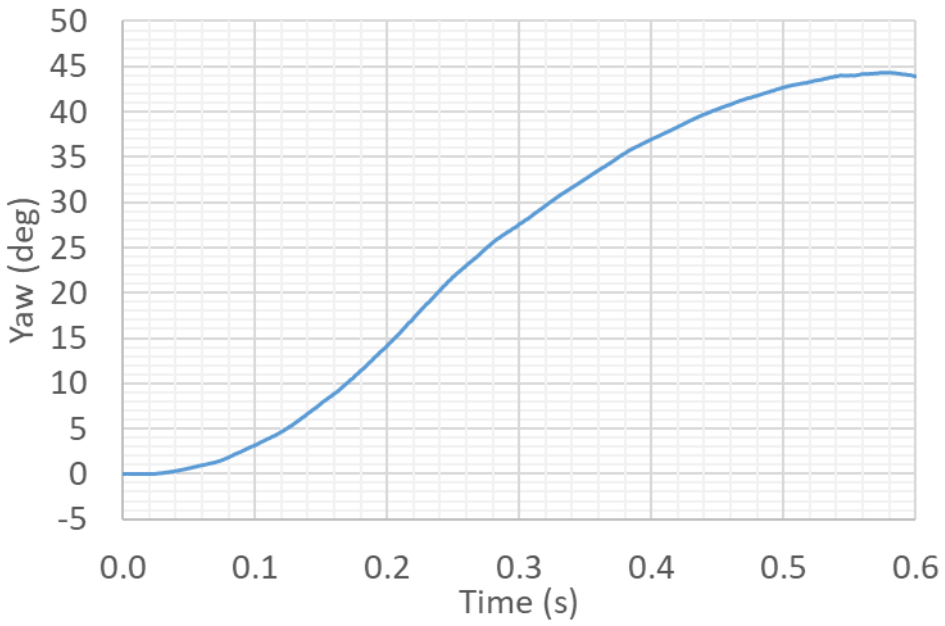

Figure 130. Vehicle yaw (deg) - Test T150-R600.

Table 14. Summary of full-scale crash simulation results for Test T150-R600.

Test Number		T150-R600
Vehicle	Designation	2270P
	Test Inertial, kg	2,270
Impact Conditions	Speed, km/h	100
	Angle, deg	25.0
Exit Conditions	Speed (km/h)	57
	Trajectory Angle, deg	18
ORA, g's < 20.49 g	Longitudinal	-7.4
	Lateral	7.3
OIV, m/s < 12.2 m/s	Longitudinal	5.1
	Lateral	4.8
Test Article Deflections, m	Dynamic	0.81
	Permanent	0.65
Impact time for the Occupant, sec		0.136
Sum. of all posts ground level displacement (m)		331
Max. Yaw Angle, deg		44
Max. Roll Angle, deg < 75 deg		-7
Max. Pitch Angle, deg < 75 deg		-4
Posts detached from rail during impact		3 posts
Posts hit by leading tire (wheel snag)		3 posts
Posts pulled out of ground		none
Leading tire/wheel disengaged		mostly

6.3.6 Guardrail System with Asphalt Mow Strip with 90 mm Thickness and 600 mm Rear Distance and Asphalt Diagonal Pre-Cuts (Test T90-R600-C)

The model for Test T90-R600 was modified by adding diagonal pre-cuts to the asphalt layer behind all posts. The simulation results are graphically presented in Figure 131 through Figure 136. During the collision, the leading front wheel of the vehicle hit a guardrail post at approximately 0.1 sec (Figure 131 and Figure 133 at 0.1 sec). The suspension system failed partially but remained connected to the vehicle, and the wheel continued to rotate throughout the rest of the simulation as shown in Figure 136. At approximately 0.2 sec the vehicle hit and passed over the second post. The vehicle moved forward and hit the third post at approximately 0.3 sec. The leading wheel did not completely go over the post, which happened to the first and second posts. The wheel snagging for this case was much less than Tests T90-R600; it was very similar to the baseline test without any asphalt mow strips. The vehicle moved parallel to the guardrail at approximately 0.3 sec. The vehicle was redirected back to the road and lost contact with the guardrail at approximately 0.63 sec. Vehicle pocketing did not occur during this simulation.

Asphalt rupture for each post started to propagate from the edge of each post's flanges and became connected to the pre-cuts. After the ruptures on the sides of a post connected with the pre-cuts behind that post, the asphalt resistance became zero for that post, and the post behaved as if there was no asphalt mow strip around it. The detached

section of mow strip behind the posts slid freely and translated with little to no resistance. This occured for five posts.

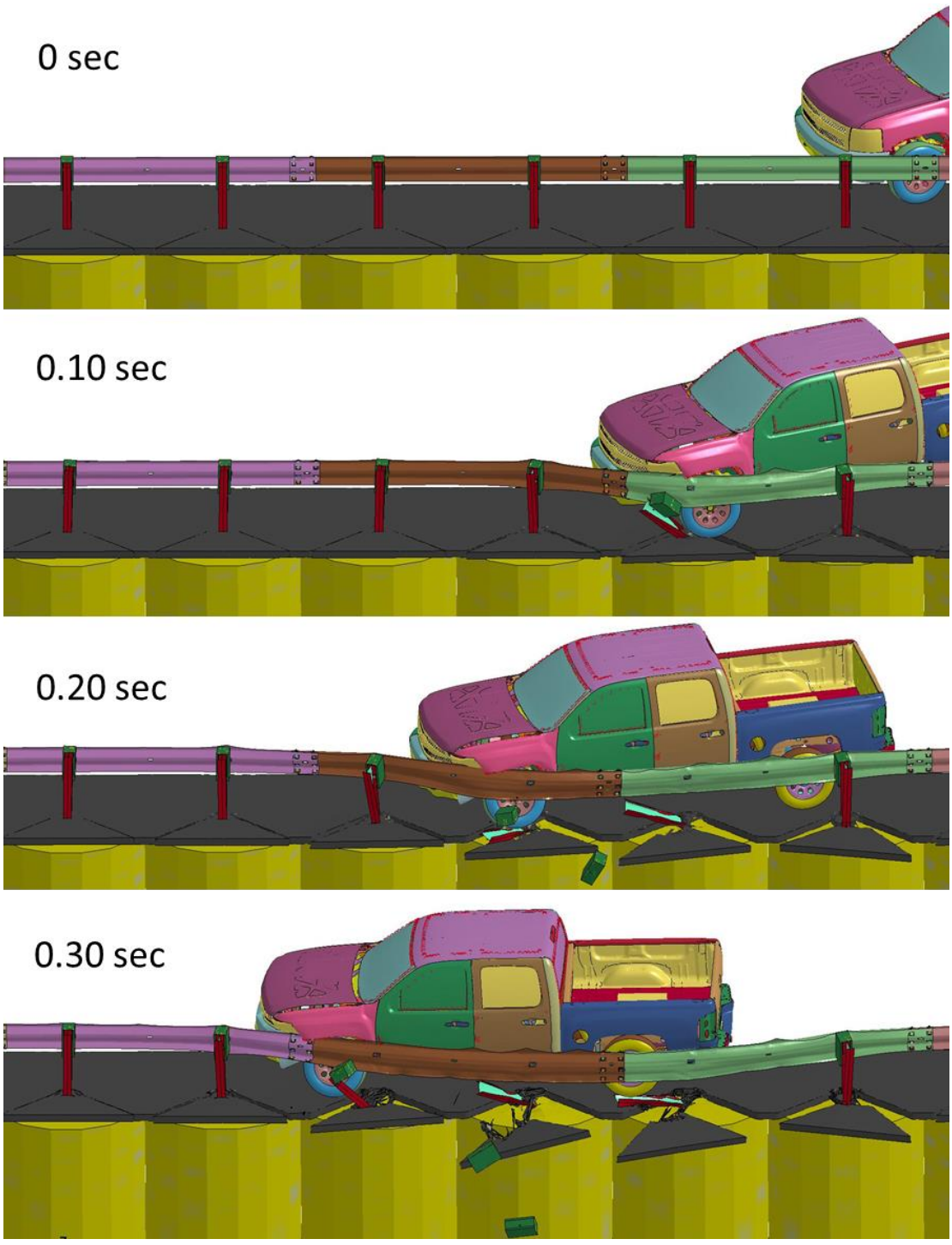

Figure 131. Simulation result for Test T90-R600-C – up to 0.3 sec.

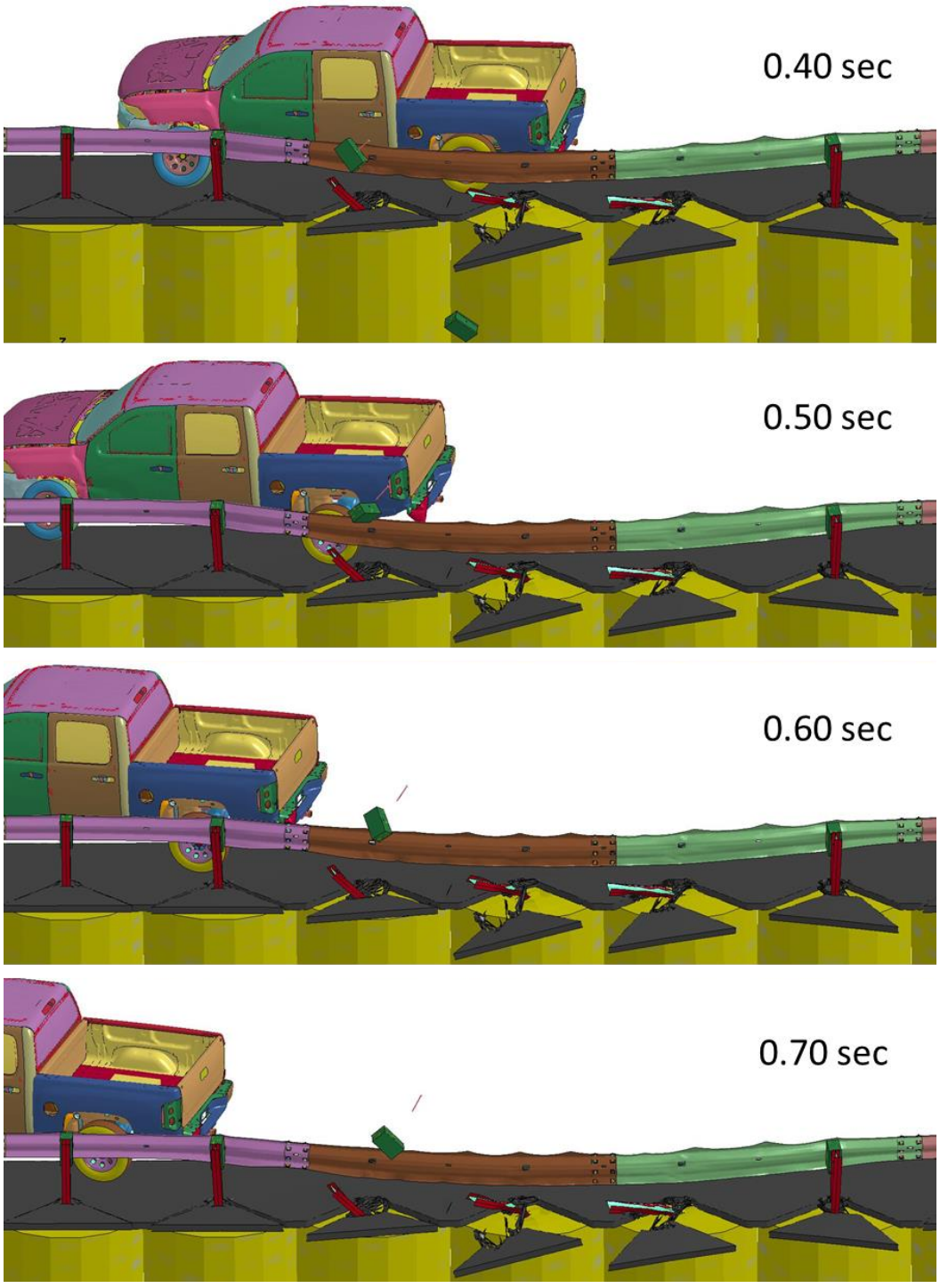

Figure 132. Simulation result for Test T90-R600-C – after 0.3 sec.

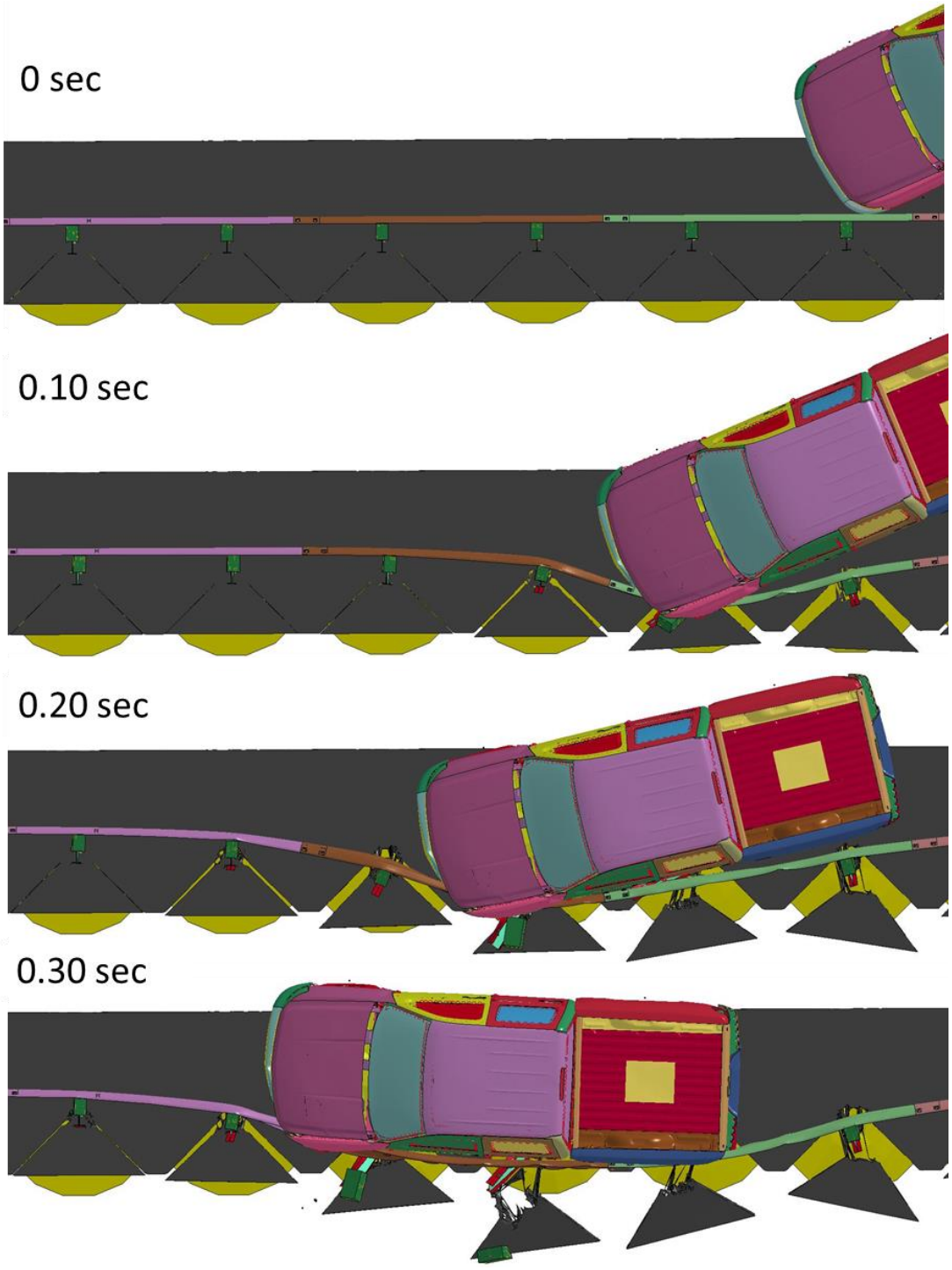

Figure 133. Simulation result for Test T90-R600-C – up to 0.3 sec.

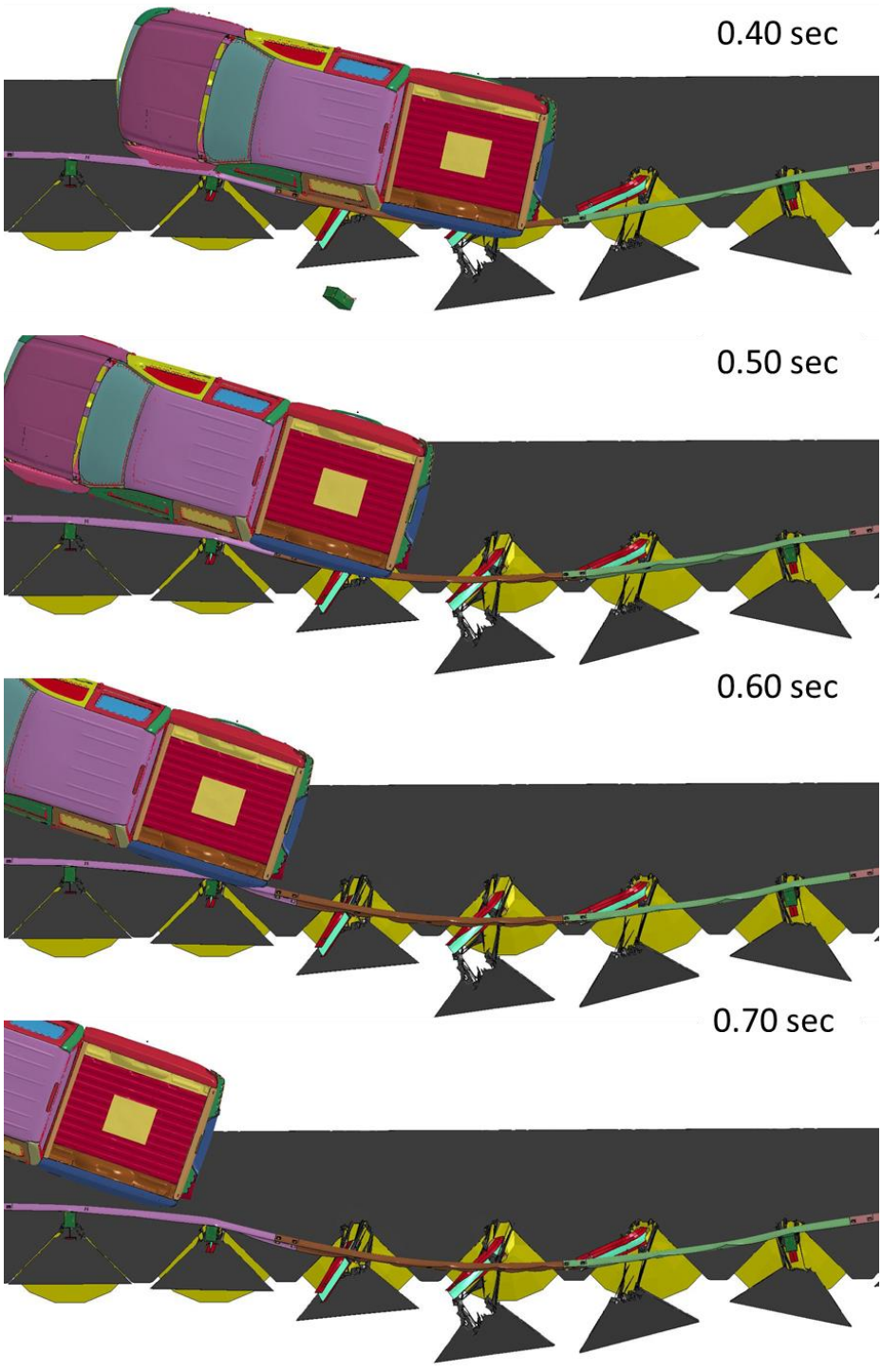

Figure 134. Simulation result for Test T90-R600-C – after 0.3 sec.

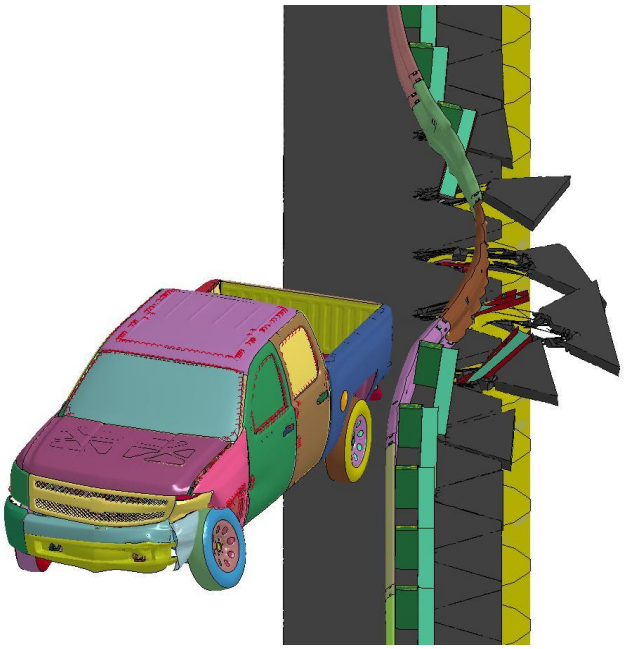

Figure 135. Simulation result for Test T90-R600-C.

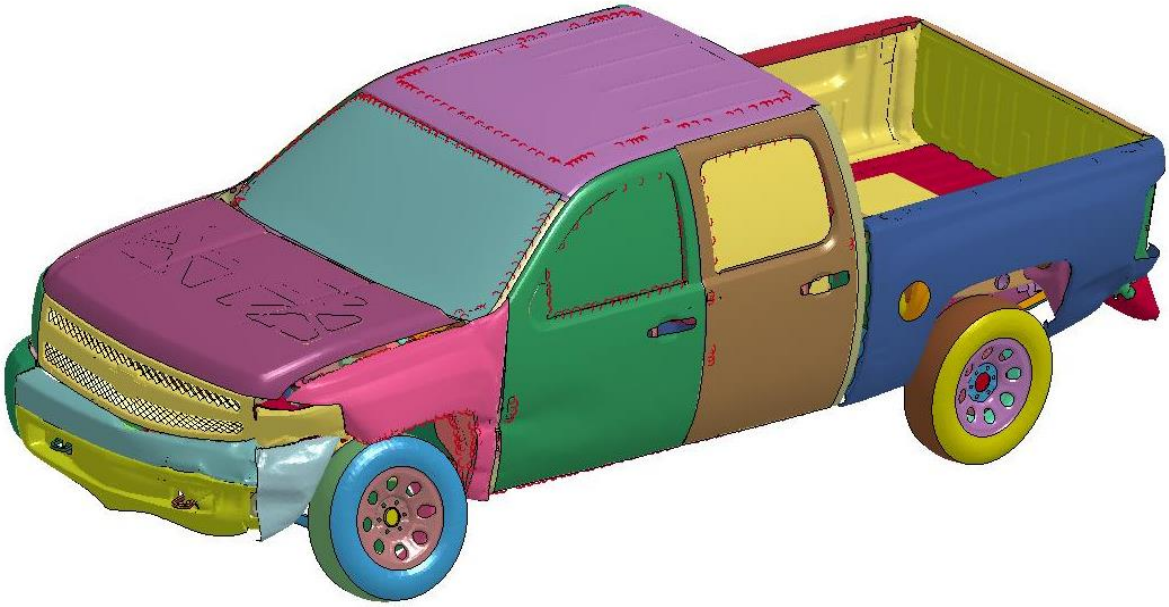

Figure 136. Vehicle Deformation for Test T90-R600-C.

The longitudinal and lateral acceleration, velocity, and displacement of the vehicle were obtained and are shown in Figure 137 to Figure 142. The occupant impact time was governed by the lateral impact of the occupant and was determined to be equal to 0.143. The OIVs and ORAs were obtained based on the occupant impact time and are reported in Table 15. They were less than the maximum limit in MASH guidelines. The roll, pitch, and yaw angles of the vehicle were recorded during simulations. The time histories for these parameters are shown in Figure 143 toFigure 145. The peak values of roll and pitch were lower than the MASH limit, which is equal to 75 deg. The peak values of yaw, roll, pitch, the exit angle, the exit speed of the vehicle, the maximum deflection of the guardrail, the permanent deflection of the guardrail, and summation of ground level displacement of all posts are reported in Table 14. None of the posts were pulled out of the ground during the simulation and three posts were detached from the guardrail, which is same as all previously discussed simulations.

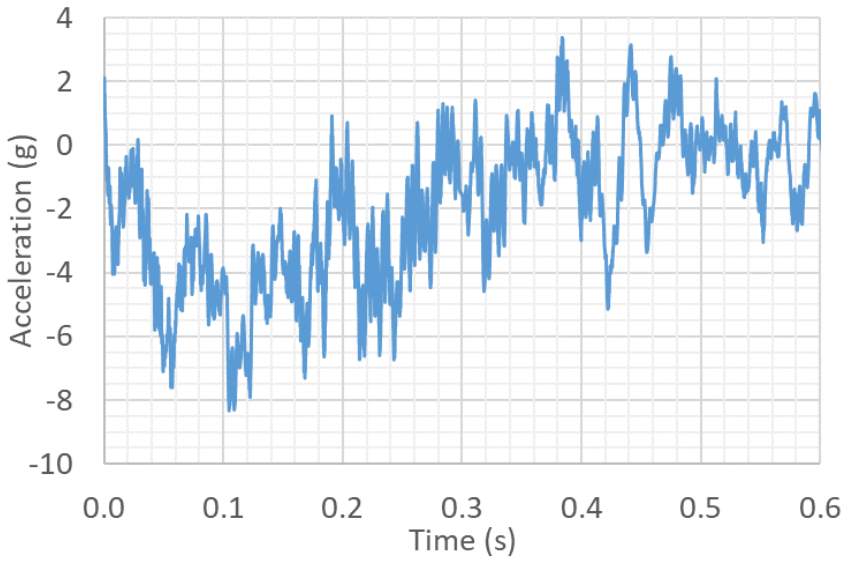

Figure 137. 10 m/s average vehicle longitudinal acceleration (g) - Test T90-R600-C.

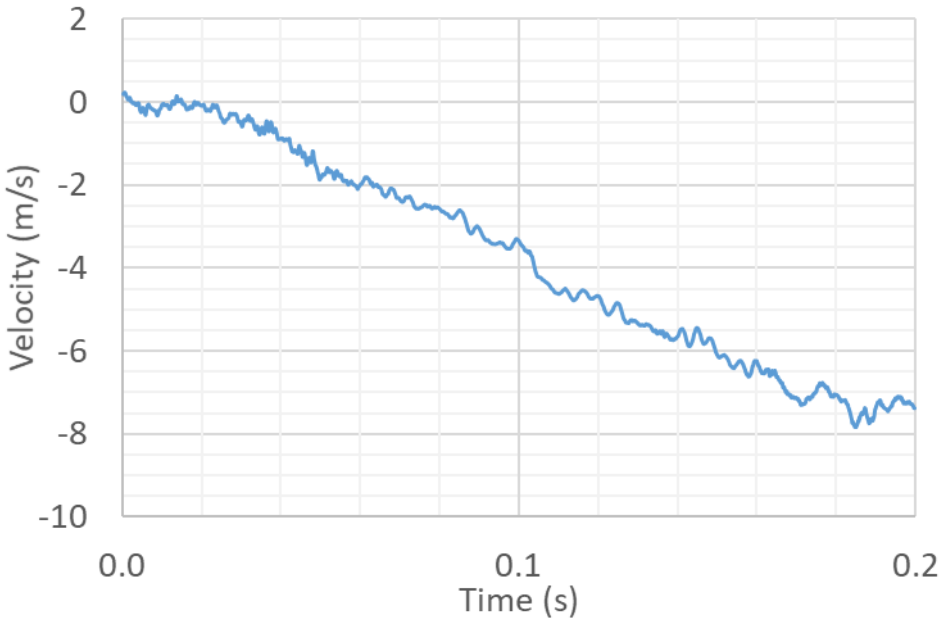

Figure 138. Relative longitudinal velocity of the occupant (m/s) - Test T90-R600-C.

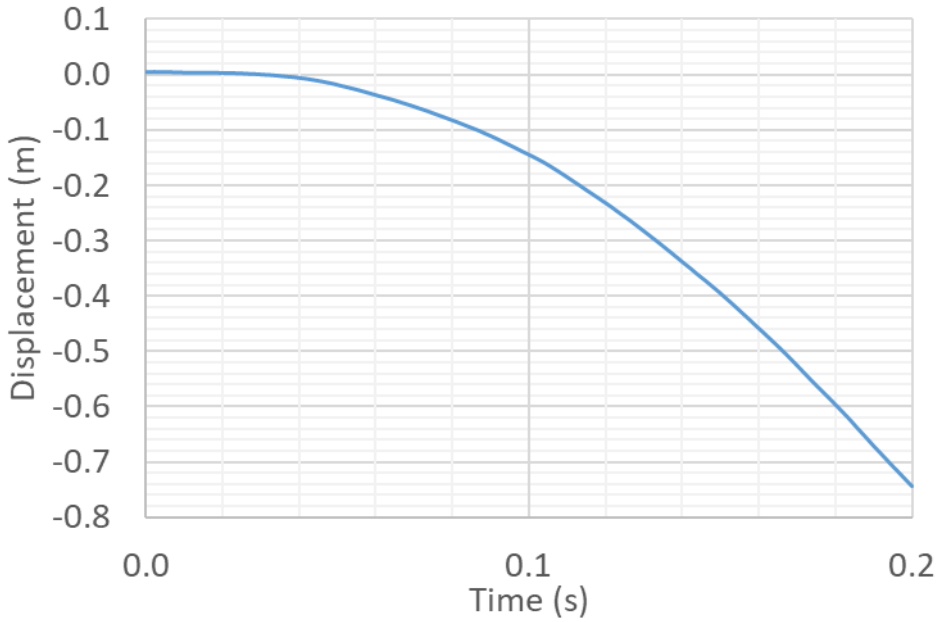

Figure 139. Relative longitudinal displacement of occupant (m) – Test T90-R600-C.

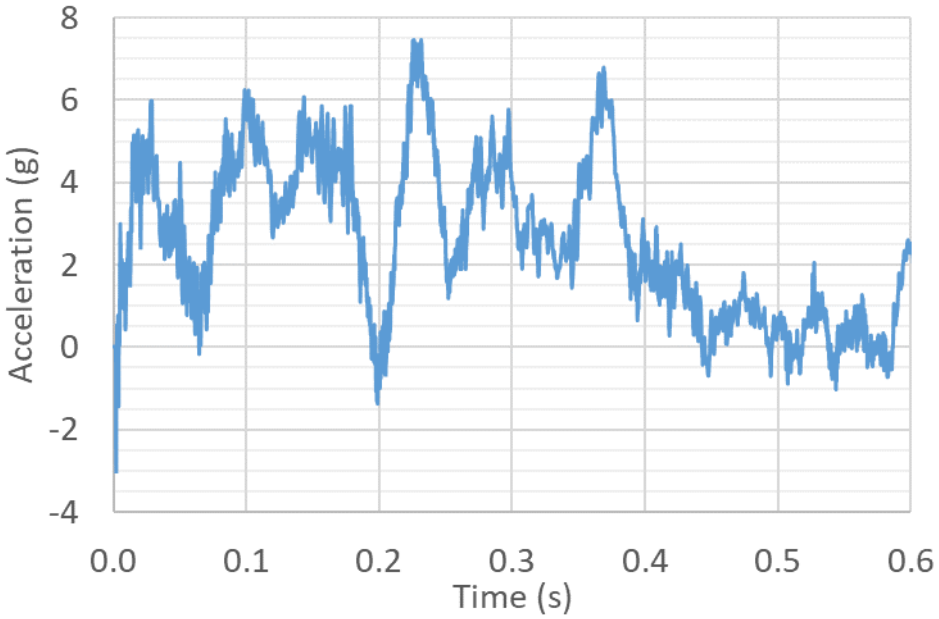

Figure 140. 10 m/s average vehicle lateral acceleration (g) – Test T90-R600-C.

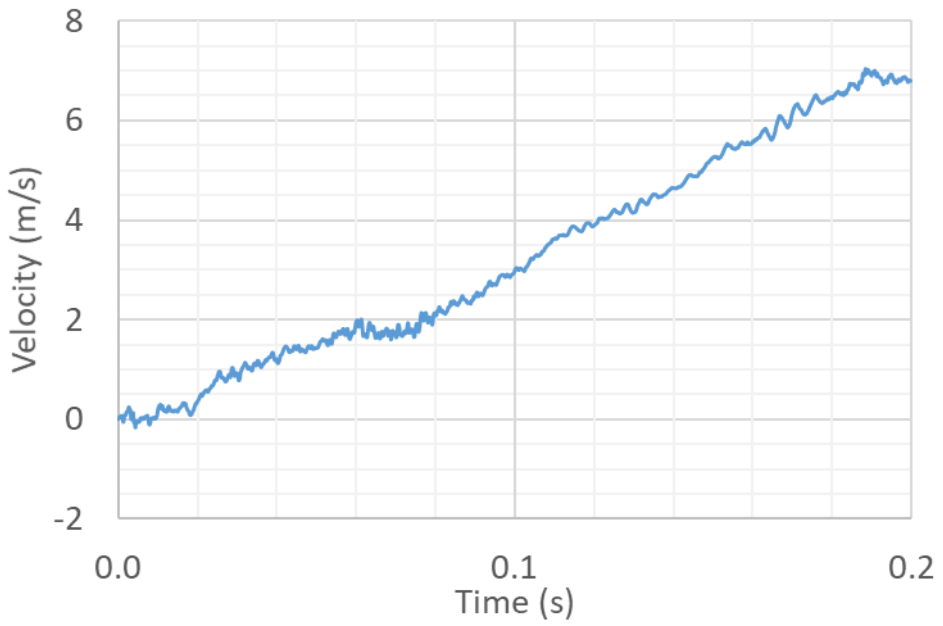

Figure 141. Relative lateral velocity of the occupant (m/s) - Test T90-R600-C.

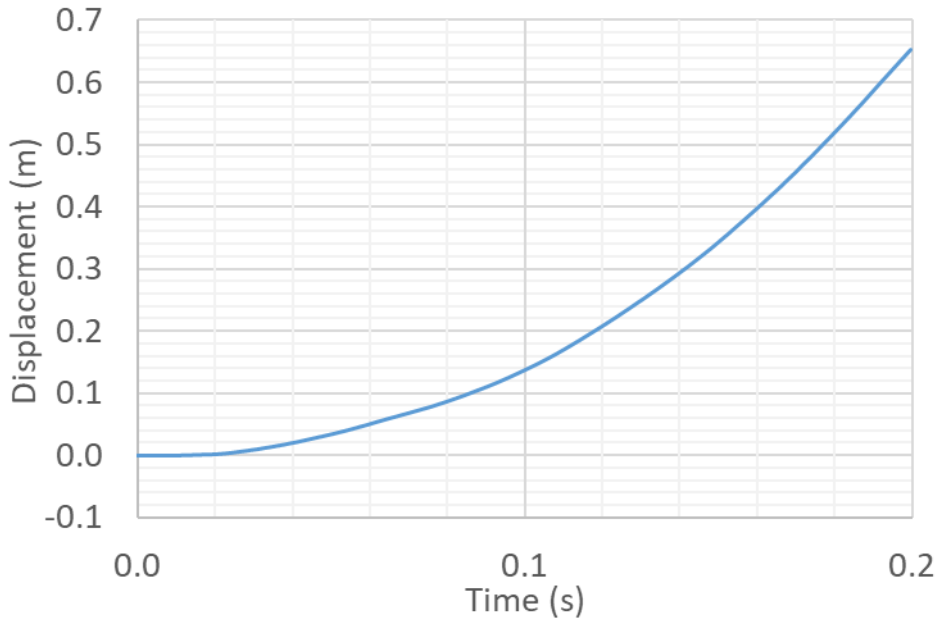

Figure 142. Relative lateral displacement of the occupant (m) - Test T90-R600-C.

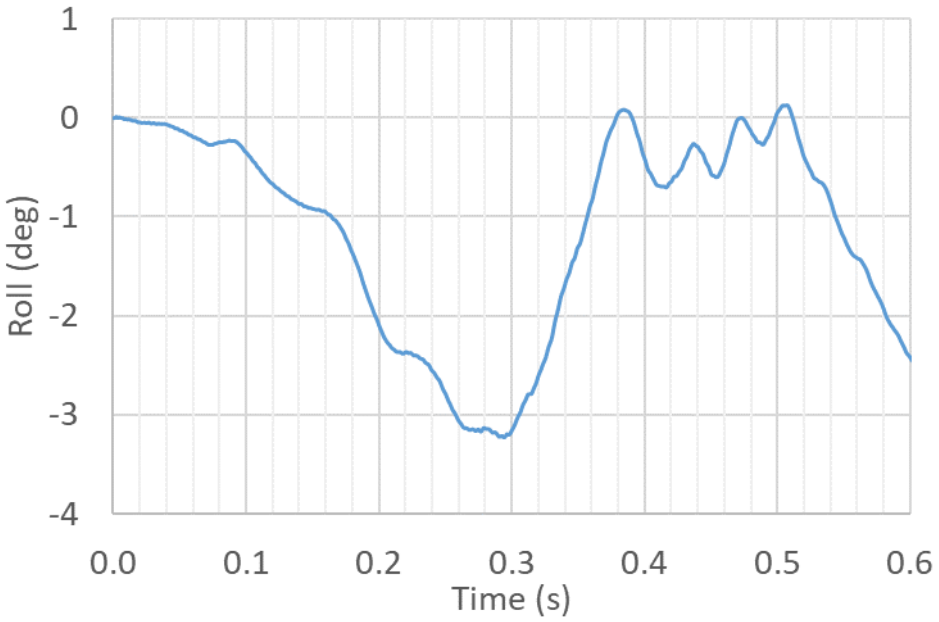

Figure 143. Vehicle roll (deg) - Test T90-R600-C.

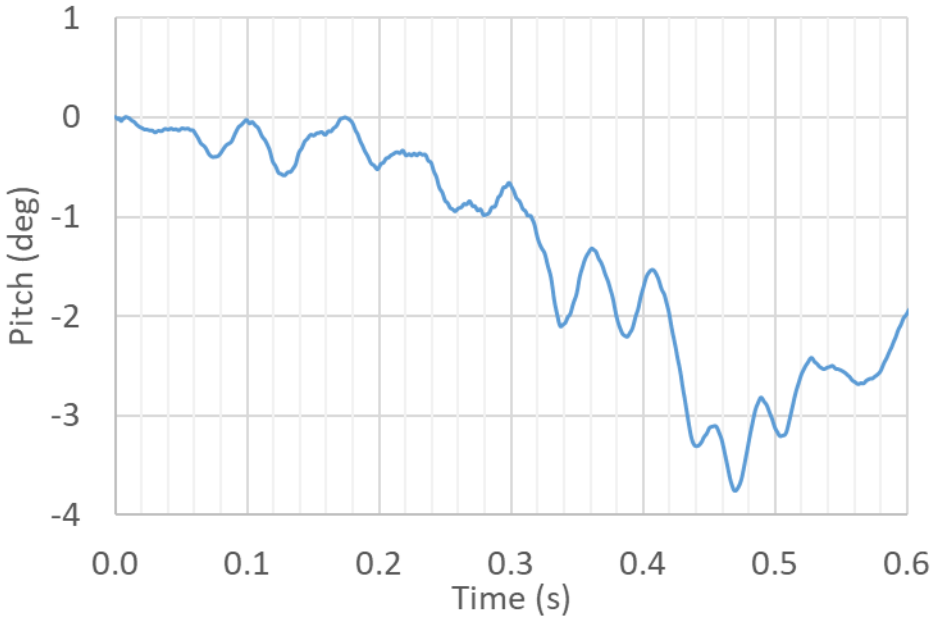

Figure 144. Vehicle pitch (deg) - Test T90-R600-C.

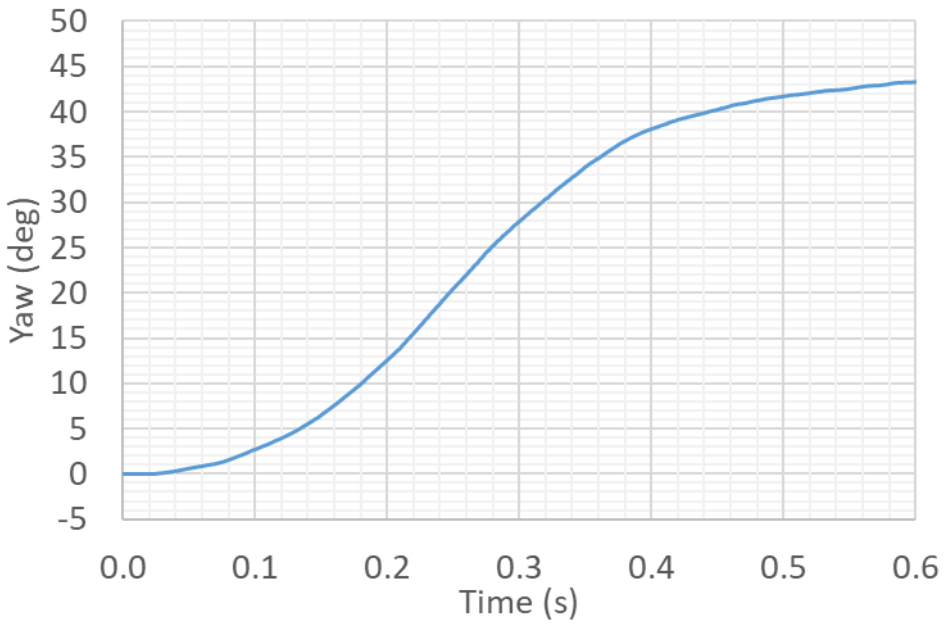

Figure 145. Vehicle yaw (deg) - Test T90-R600-C.

Table 15. Summary of full-scale crash simulation results for Test T90-R600-C.

Test Number		T50-R600
Vehicle	Designation	2270P
	Test Inertial, kg	2,270
Impact Conditions	Speed, km/h	100
	Angle, deg	25.0
Exit Conditions	Speed (km/h)	58
	Trajectory Angle, deg	19
ORA, g's < 20.49 g	Longitudinal	-7.3
	Lateral	7.4
OIV, m/s < 12.2 m/s	Longitudinal	5.5
	Lateral	4.8
Test Article Deflections, m	Dynamic	1.01
	Permanent	0.81
Impact time for the Occupant t^*, sec		0.143
Sum. of all posts ground level displacement (m)		1.474
Max. Yaw Angle, deg		44
Max. Roll Angle, deg < 75 deg		-4
Max. Pitch Angle, deg < 75 deg		-4
Posts detached from rail during impact		3 posts
Posts hit by leading tire (wheel snag)		3 posts
Posts pulled out of ground		none
Leading tire/wheel disengaged		mostly

6.3.7 Guardrail System with Asphalt Mow Strip with 90 mm Thickness and 600 mm Rear Distance and a Stiffer Asphalt (Test T90-R600-S)

The model for Test T90-R600 was updated by increasing the asphalt thickness and stiffness while using the same material properties used in Section 5.1.8. This asphalt was approximately two times stronger and stiffer than the asphalt type used in this research for all other test simulations. The simulation results are graphically presented in Figure 146 through Figure 151. During the collision, the leading front wheel of the vehicle hit a guardrail post at approximately 0.1 sec, which was same as previous simulations. However, in this case, the wheel passed far behind the post instead of going over the post's web. This shows that the ground level displacement of the post in this scenario is extremely limited. As in all the other simulations in this research, the suspension system failed partially but stayed connected to the vehicle and the wheel continued to rotate throughout the rest of the simulation. At approximately 0.2 sec, the vehicle hit the second post and passed far behind this post (Figure 146 and Figure 148 at 0.2 sec). This did not happen in Tests T50-R600, T90-R300, T90-R600, T90-R600-C, or the test with soil only. The vehicle moved forward and hit the third post at approximately 0.3 sec. The leading wheel passed over this post, which did not happen in Tests T50-R600, T90-R300, T90-R600, T90-R600-C, or the test with soil only. The wheel snagging for this case was the worst among all test simulations. The vehicle ran parallel to the guardrail at approximately 0.3 sec, was redirected back to the road, and lost contact with the guardrail at approximately 0.61 sec.

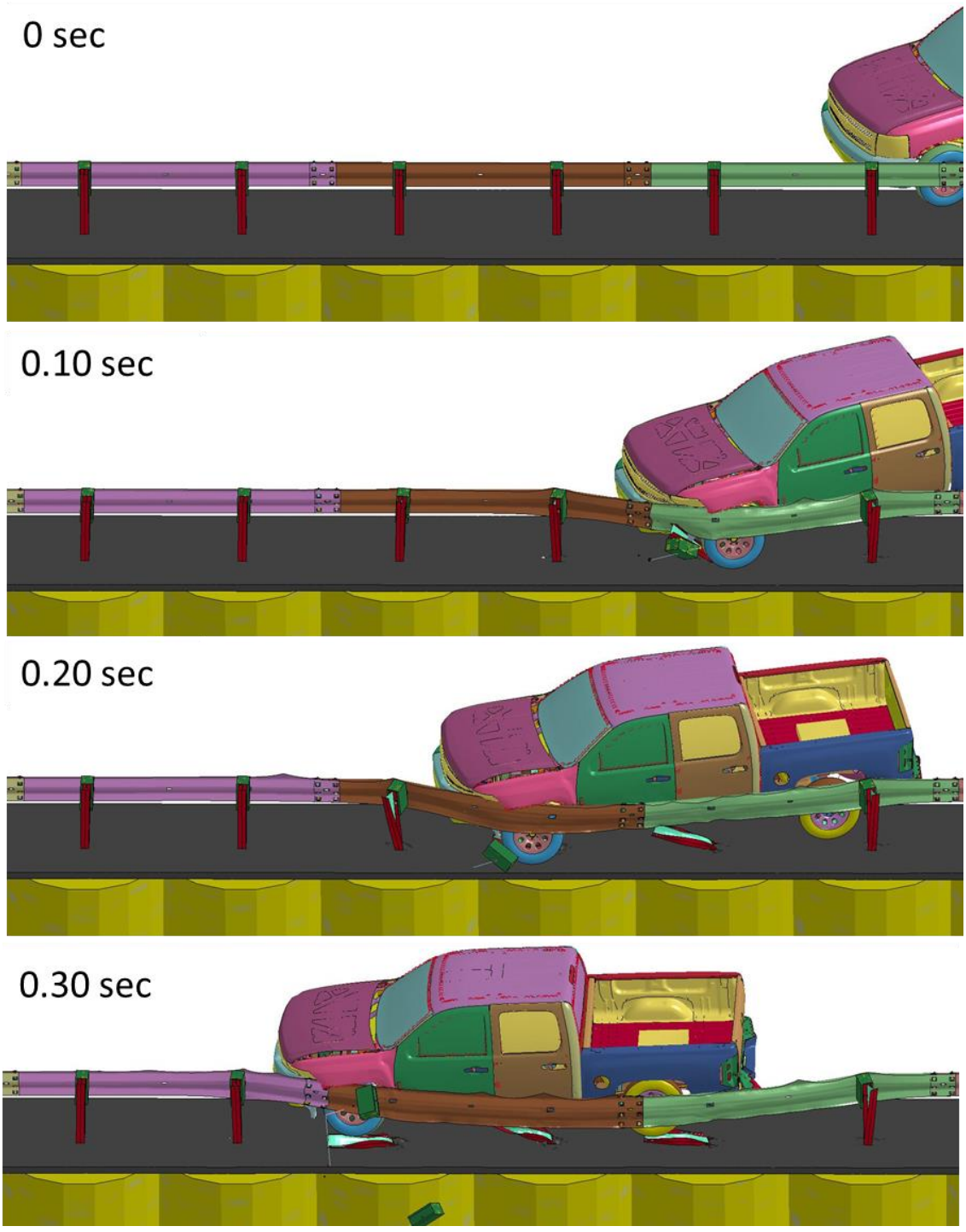

Figure 146. Simulation result for Test T90-R600-S – up to 0.3 sec.

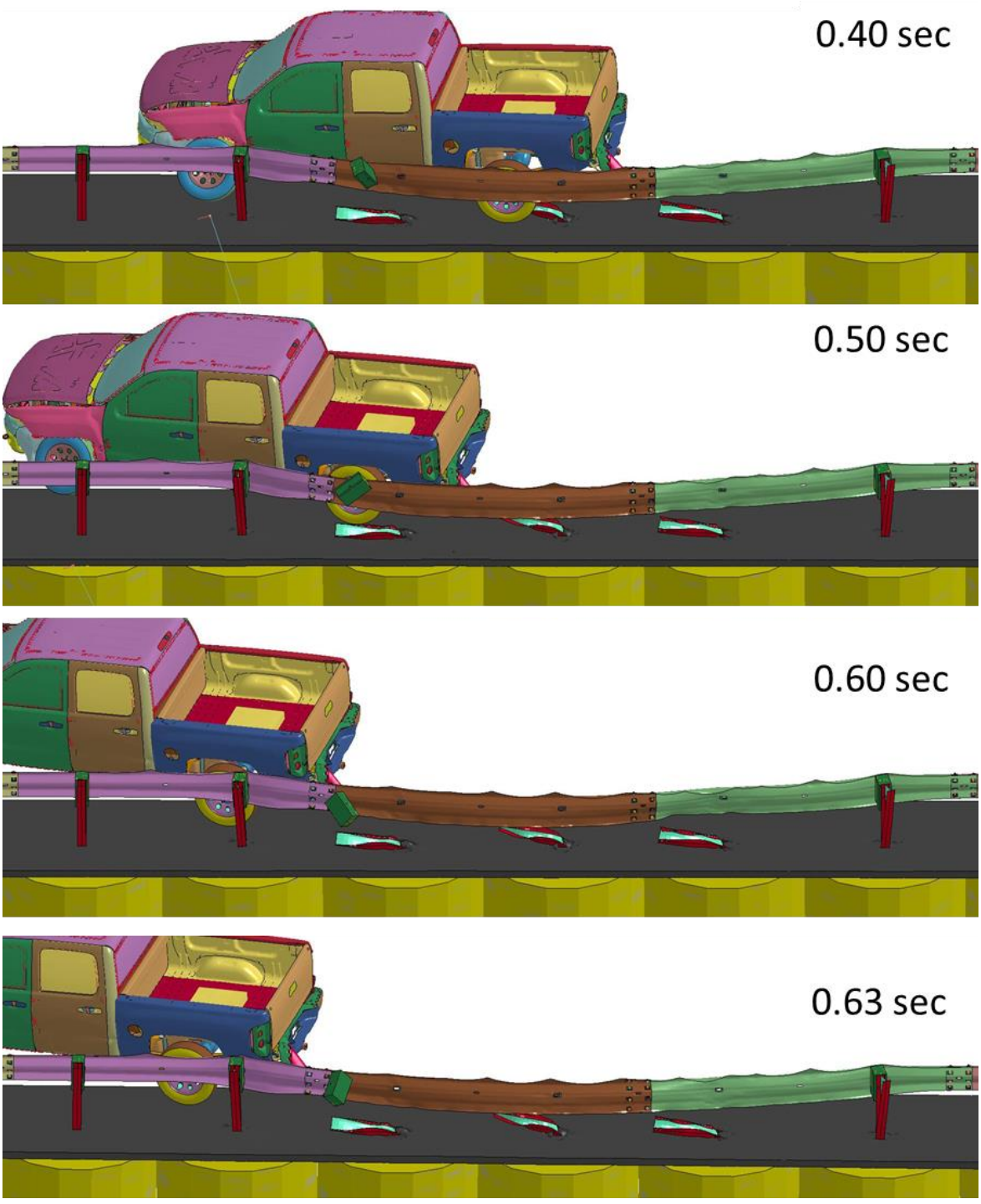

Figure 147. Simulation result for Test T90-R600-S – after 0.3 sec.

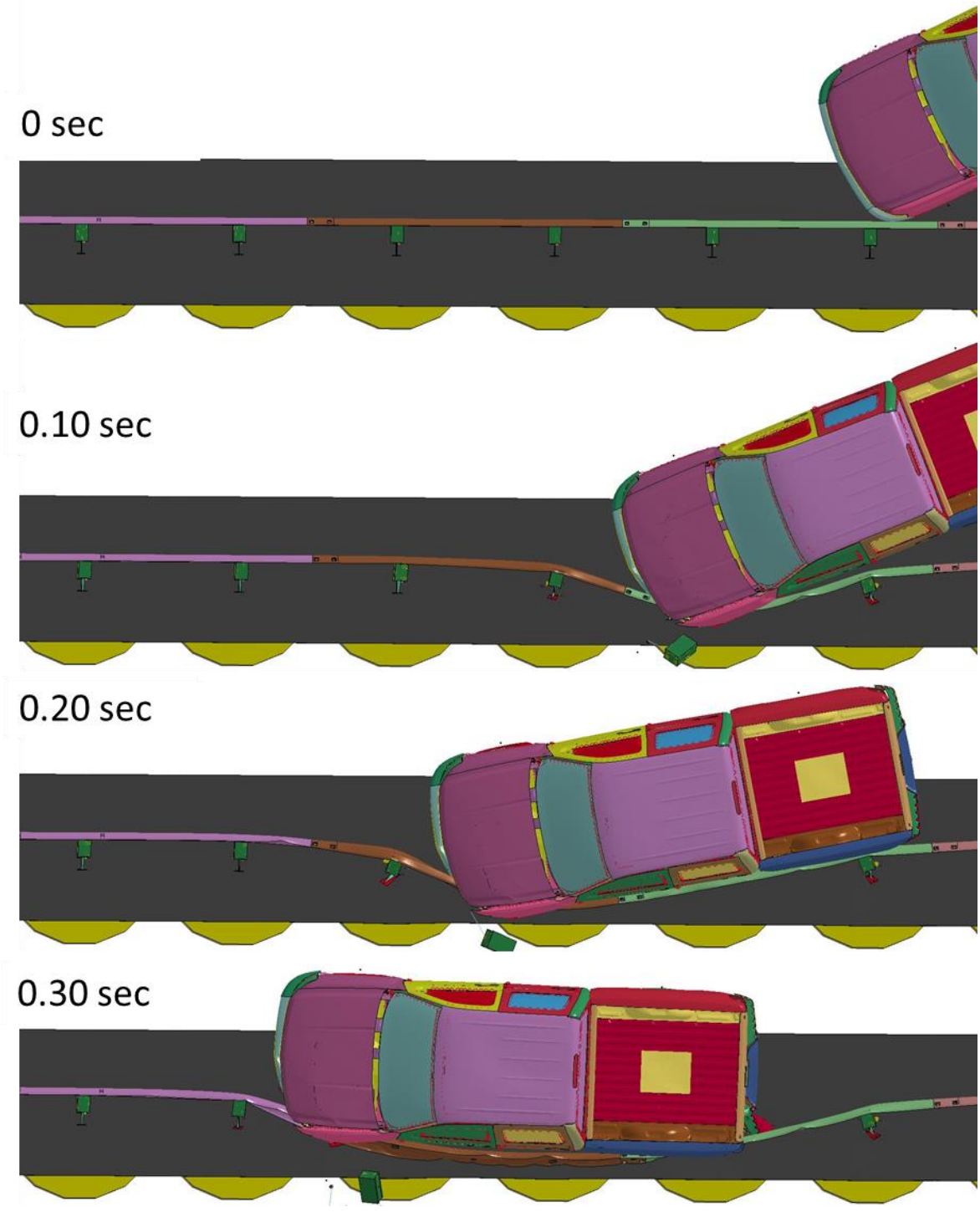

Figure 148. Simulation result for Test T90-R600-S – up to 0.3 sec.

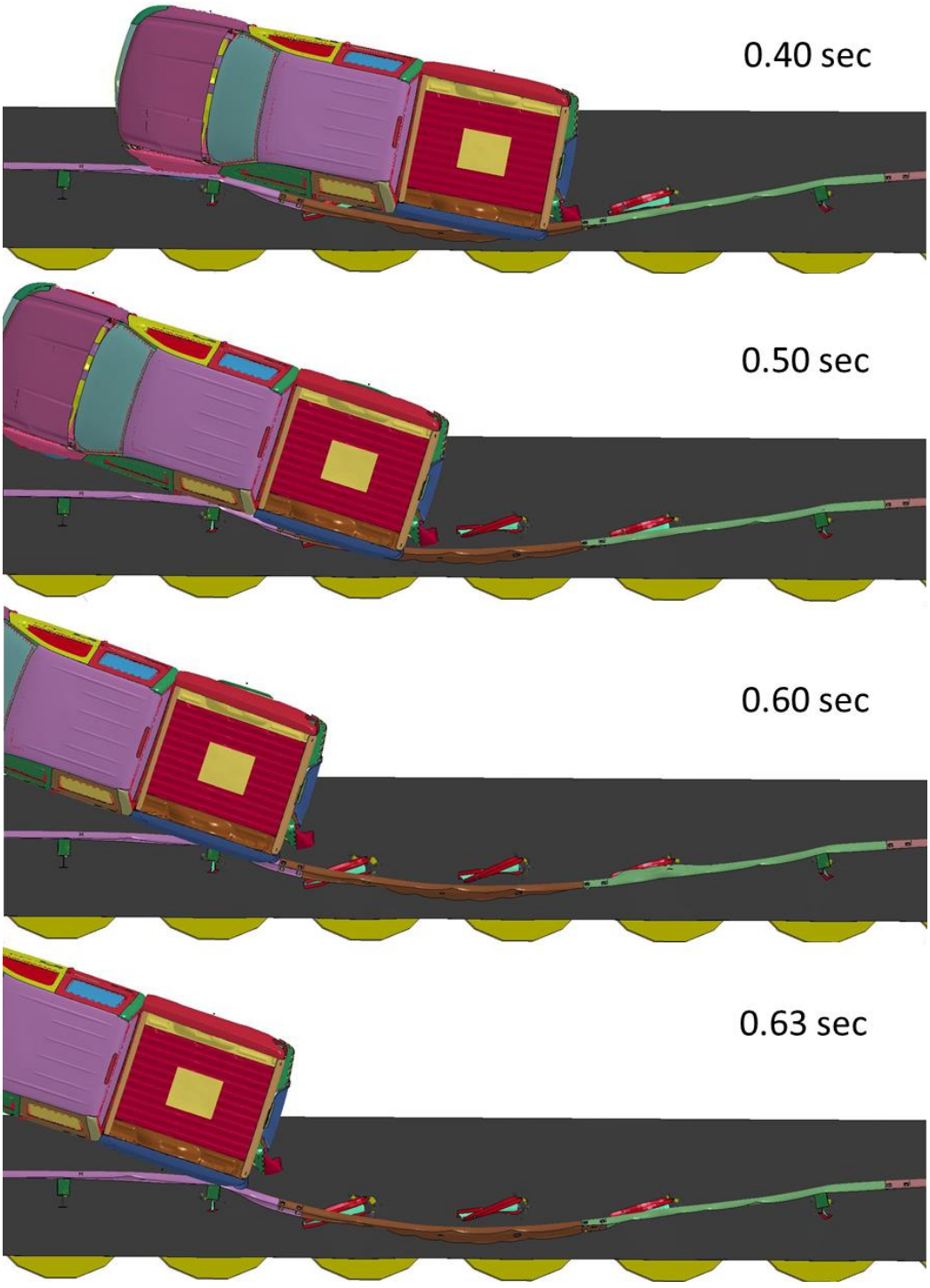

Figure 149. Simulation result for Test T90-R600-S – after 0.3 sec.

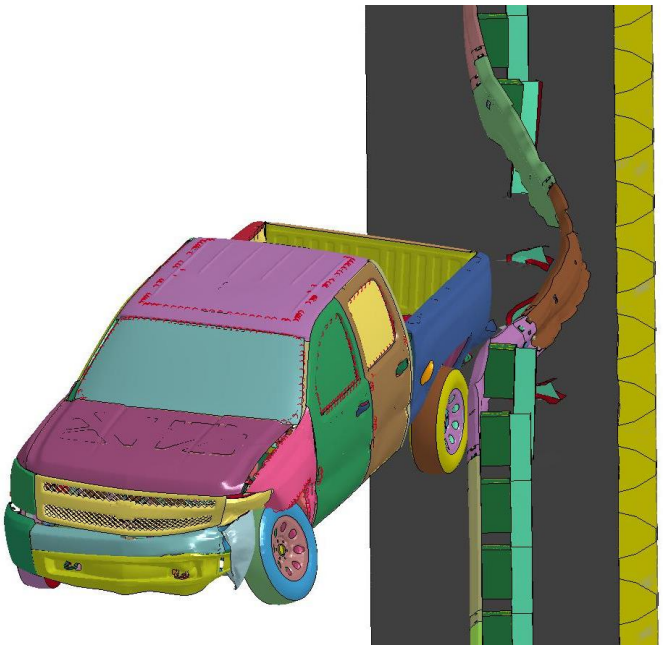

Figure 150. Simulation result for Test T90-R600-S.

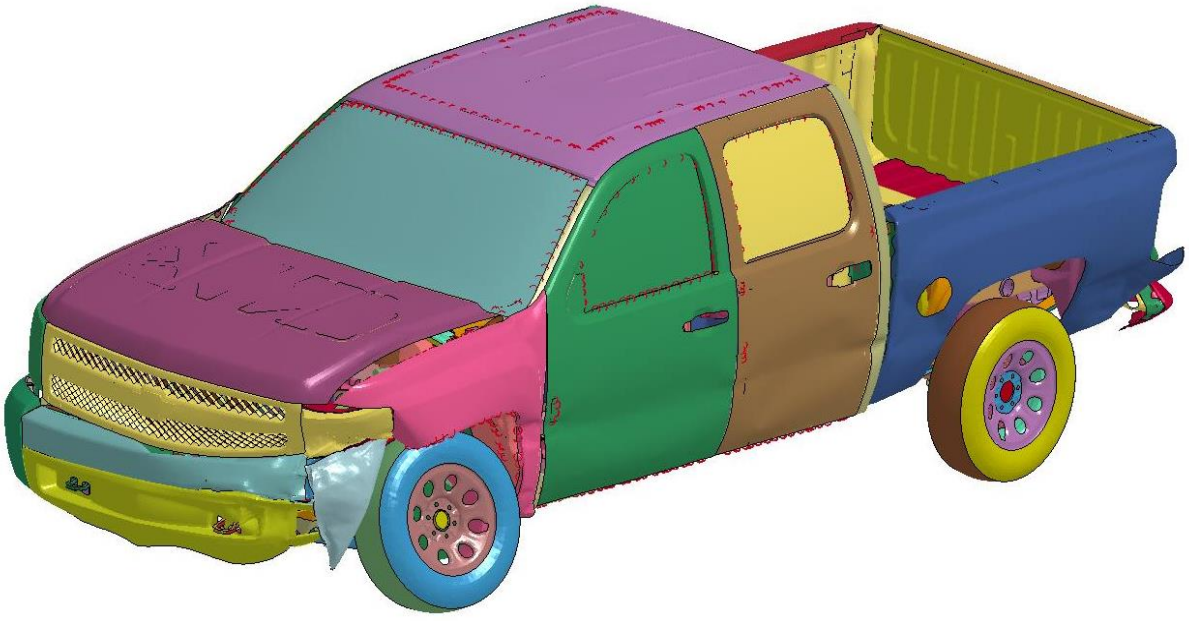

Figure 151. Vehicle deformation for Test T90-R600-S.

The vehicle lost contact with the guardrail earlier than any other case discussed in this research. Vehicle pocketing did not occur during this simulation. Very limited asphalt rupture occurred around the posts. This means all of the posts remained fully encased in asphalt through the end of the simulation and experienced extreme ground level restraint that was close to having a rigid mow strip.

The longitudinal and lateral acceleration, velocity, and displacement of the vehicle were obtained and are shown in Figure 152 to Figure 157. The occupant impact time was governed by the lateral impact of the occupant and was determined to be equal to 0.140. The OIVs and ORAs were obtained based on the occupant impact time and are reported in Table 16. They were lower than the maximum limit in MASH guidelines. The roll, pitch, and yaw angles of the vehicle were recorded during simulations. The time histories for these parameters are shown in Figure 143 to Figure 145. The peak values of roll and pitch were lower than the MASH limit, which is equal to 75 deg. The peak values of yaw, roll, pitch, the exit angle, the exit speed of the vehicle, the maximum deflection of the guardrail, the permanent deflection of the guardrail, and summation of ground level displacement of all posts are reported in Table 16. None of the posts were pulled out of the ground during the simulation and three posts were detached from the guardrail, which is same as all previously discussed test simulations so far.

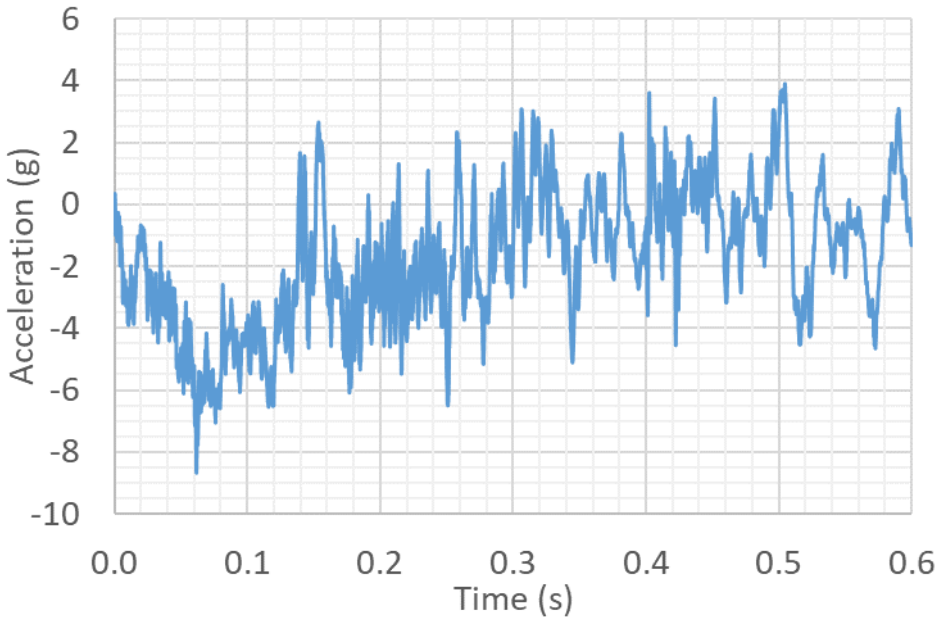

Figure 152. 10 m/s average vehicle longitudinal acceleration (g) - Test T90-R600-S.

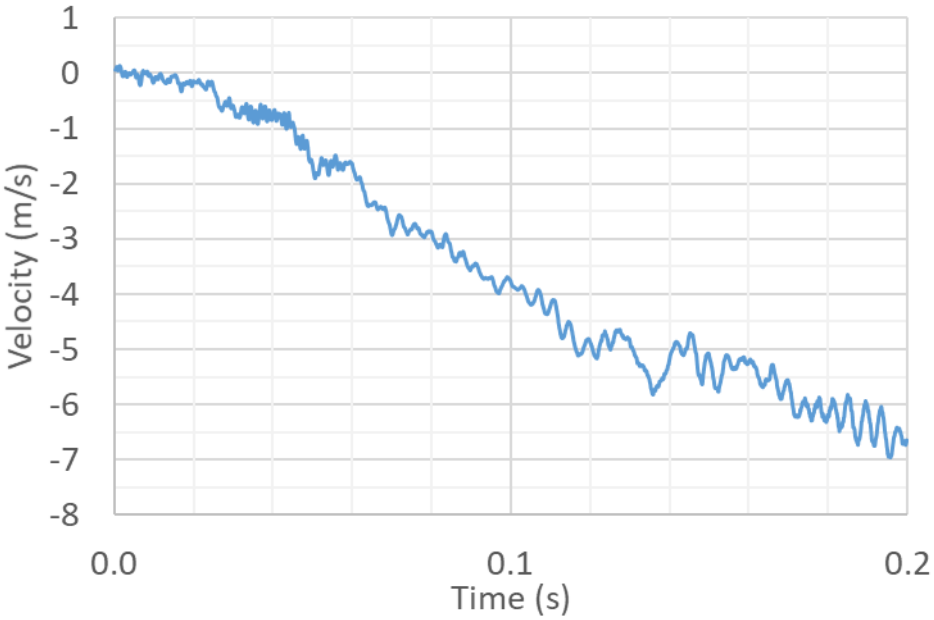

Figure 153. Relative longitudinal velocity of the occupant (m/s) - Test T90-R600-S.

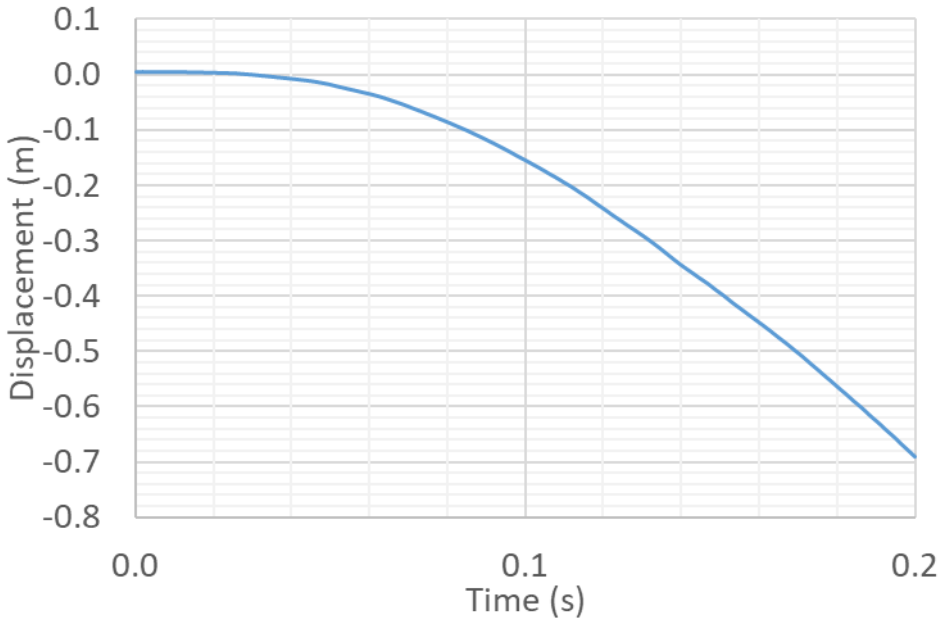

Figure 154. Relative longitudinal displacement of occupant (m) – Test T90-R600-S.

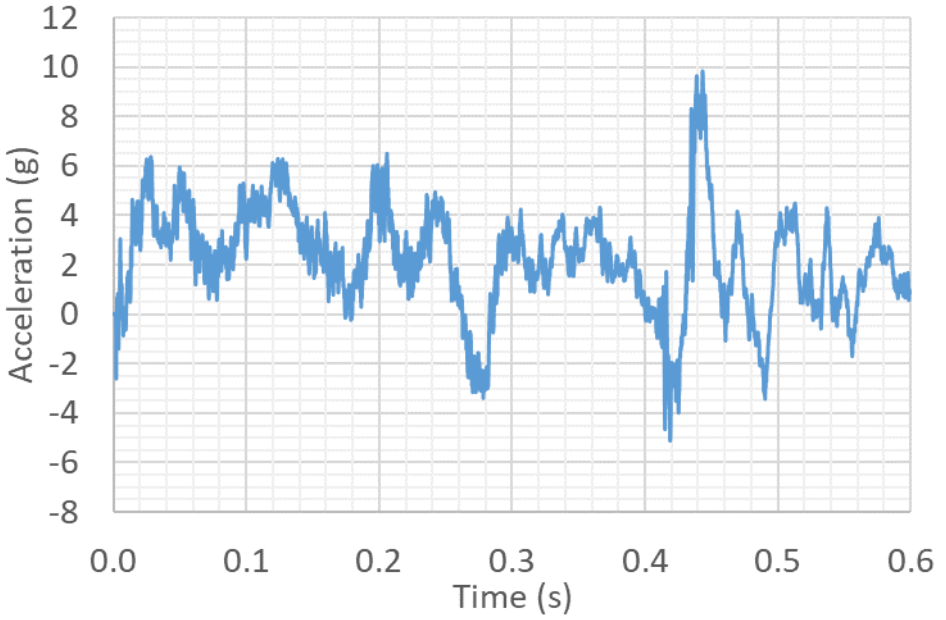

Figure 155. 10 m/s average vehicle lateral acceleration (g) – Test T90-R600-S.

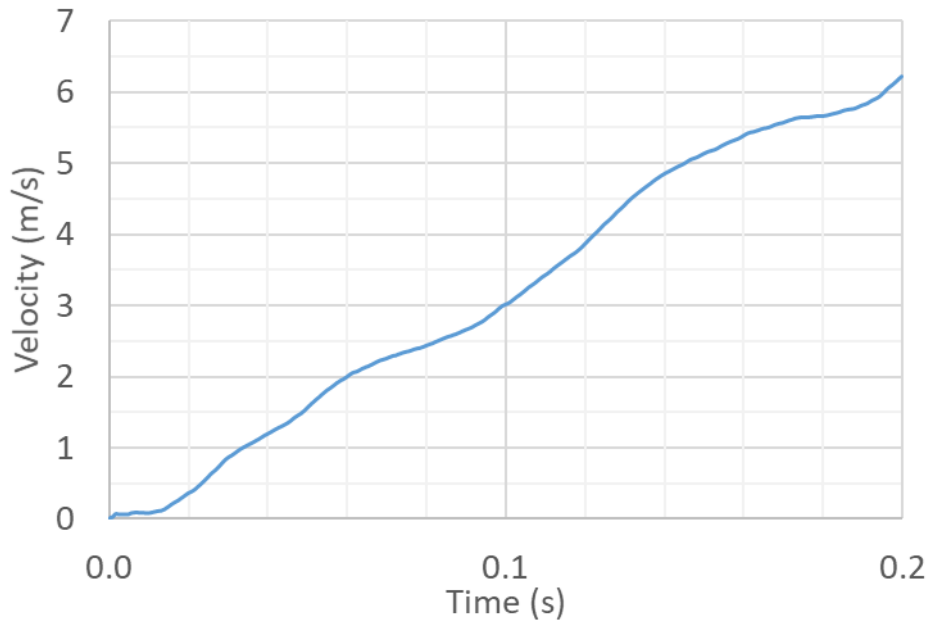

Figure 156. Relative lateral velocity of the occupant (m/s) - Test T90-R600-S.

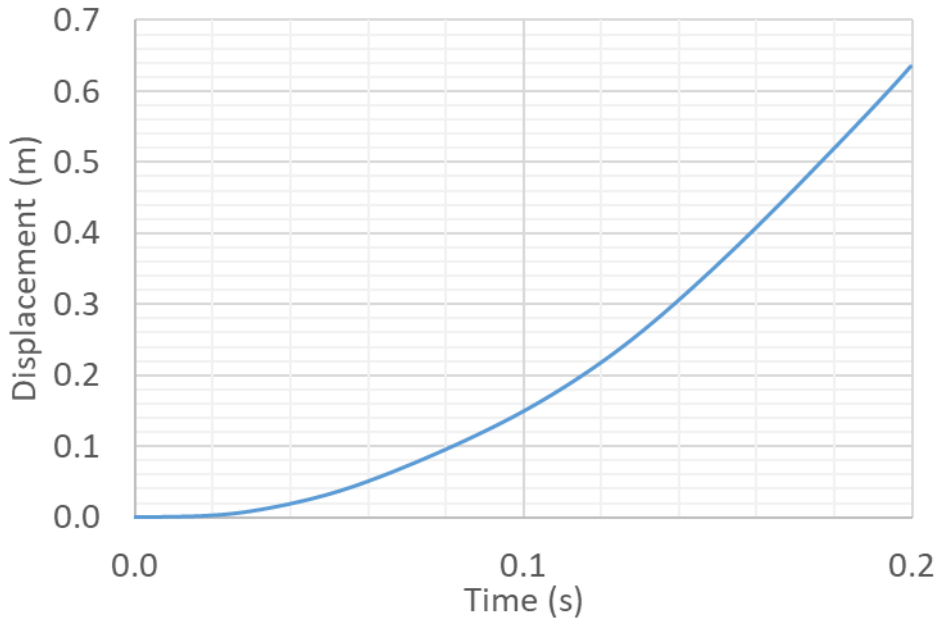

Figure 157. Relative lateral displacement of the occupant (m) - Test T90-R600-S.

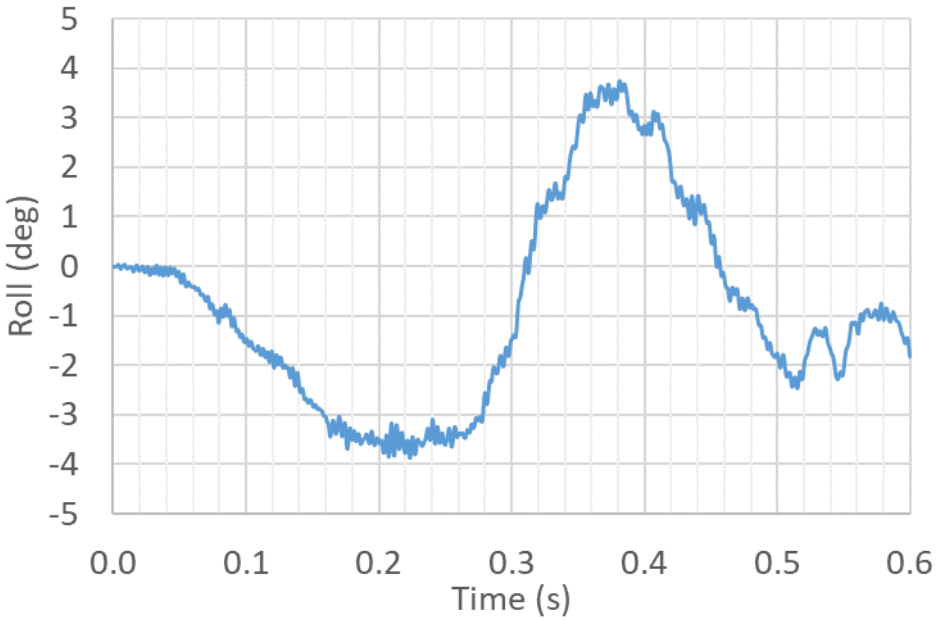

Figure 158. Vehicle roll (deg) - Test T90-R600-S.

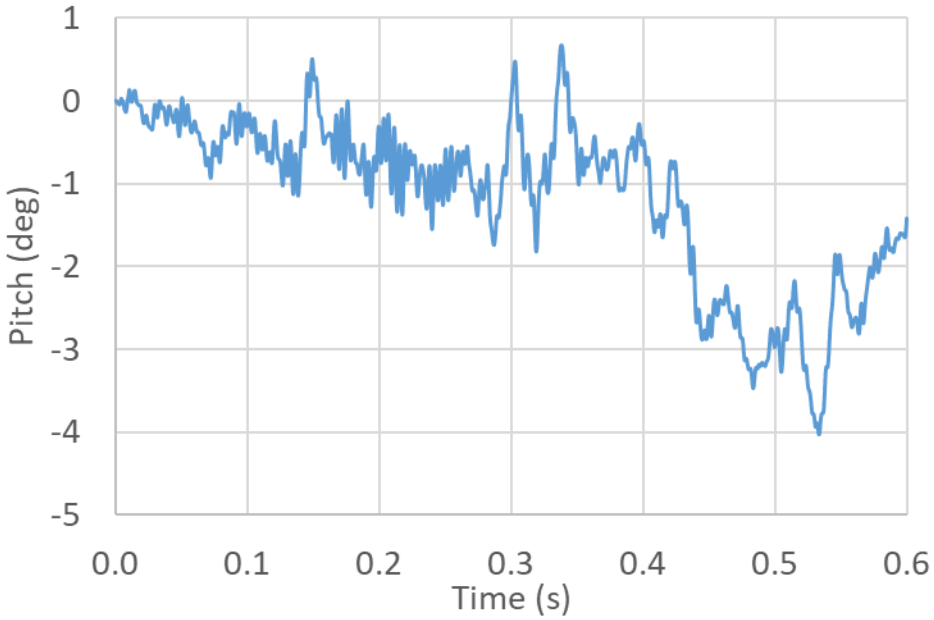

Figure 159. Vehicle pitch (deg) - Test T90-R600-S.

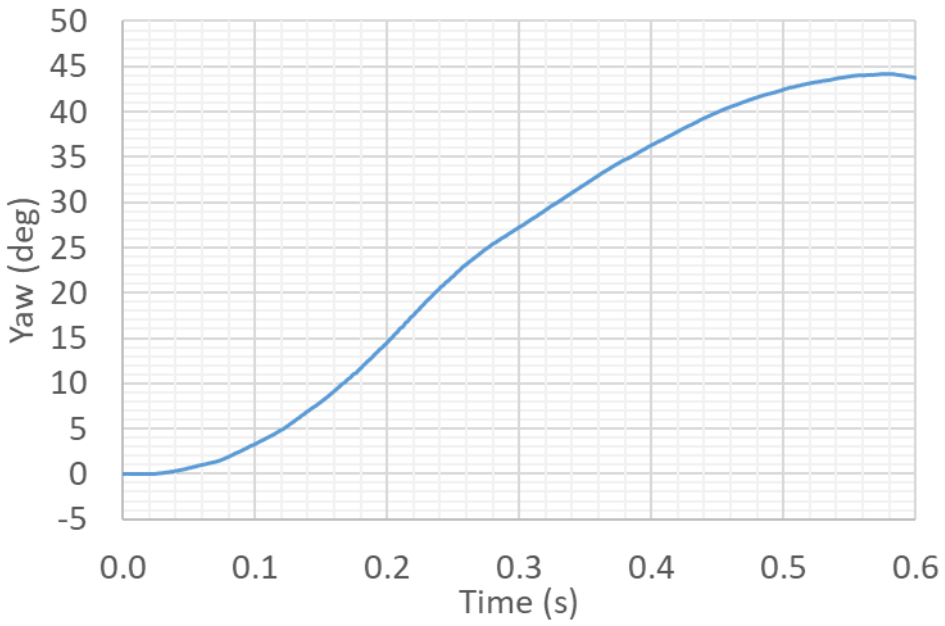

Figure 160. Vehicle yaw (deg) - Test T90-R600-S.

Table 16. Summary of full-scale crash simulation results for Test T90-R600-S.

Test Number		T90-R600-S
Vehicle	Designation	2270P
	Test Inertial, kg	2,270
Impact Conditions	Speed, km/h	100
	Angle, deg	25.0
Exit Conditions	Speed, km/h	56
	Trajectory Angle, deg	18
ORA, g's < 20.49 g	Longitudinal	-6.5
	Lateral	9.8
OIV, m/s < 12.2 m/s	Longitudinal	-4.7
	Lateral	4.9
Test Article Deflections, m	Dynamic	0.81
	Permanent	0.64
Impact time for the Occupant, sec		0.140
Sum. of all posts ground level displacement (m)		0.191
Max. Yaw Angle, deg		44
Max. Roll Angle, deg < 75 deg		-4
Max. Pitch Angle, deg < 75 deg		-4
Posts detached from rail during impact		3 posts
Posts hit by leading tire (wheel snag)		3 posts
Posts pulled out of ground		none
Leading tire/wheel disengaged		mostly

6.4 Quantitative Comparison between Guardrail Systems with Different Mow Strips

Finite element crash simulations have limitations that prohibit them from being used to determine if a particular safety structure passes MASH requirements. MASH guidelines specify that experimental tests are the only acceptable method for deciding whether a safety structure passes or fails its requirements. However, finite element simulations can be used to test additional alternatives, help design future experimental crash tests, and optimize the design of safety structures. The limitations of the finite element model used in this research include:

- Steel rupture was not included. Therefore, rupture could not occur in guardrails and posts.
- The vehicle wheels did not fail and detach as easily as they failed in experimental tests.
- Rupture was not modeled for the bolted connections in the guardrails.
- Material failure was not modeled for the blockouts between the posts and guardrails.
- The friction coefficient between the vehicle and the guardrail system is an important parameter in crash simulations. In this research, the friction

coefficient was assumed to be the same between all surfaces of the vehicle and all parts of the guardrail system. Through calibration of the model for the case with soil only and by comparing the simulation results with experimental crash test results, the friction coefficient was determined to be equal to 0.15. Higher values of friction angle resulted in too much loss of energy and lower vehicle exit speeds than what was observed in the experimental test. Considerably higher values of friction coefficient (0.3 and higher) caused vehicle pocketing because the vehicle got stuck in the guardrail system. Friction values less than 0.15 resulted in too little loss of energy and higher vehicle exit speeds than what was observed in the experimental test.

Because of these limitations and based on MASH guidelines, the crash simulation results presented in this dissertation cannot be used to decide whether a guardrail system with a specific mow strip specification passes MASH requirements. Instead, the results are used to determine the relative performance of guardrail systems with different asphalt mow strips.

In the previous sections of this chapter, guardrail systems with different mow strips were compared based on wheel snagging, ground level displacement of the guardrail posts, and rupture patterns of asphalt mow strips. This comparison shows that Tests T50-R600, T90-R300, and T90-R600-C show much less ground restraint than other tests with asphalt mow strips.

A quantitative comparison is presented in this section. The simulation results for all cases considered are summarized in Table 17. The summation of ground level displacement of all posts in each simulation is used as the primary parameter. The cases presented in Table 17 are sorted in such a way that summation of ground level displacement of posts decreases from left to right. The results are also presented in Figure 161. As can be seen in the table, the dynamic and permanent test article deflections did not have the same pattern as the ground level displacement. This is because the rails detached from three of the posts in all simulations; therefore, the guardrail displacement was less dependent on the posts' ground level displacements, which is critical in this research. This table also shows that, with the exception of the summation of ground level displacement of posts, other parameters in the table do not show a consistent pattern as a function of mow strip thickness, rear distance, and material properties. Therefore, only the ground level displacement of posts is used here as a parameter to compare the different setups. This parameter clearly shows that Tests T90-R300 and T90-R600-C behaved similarly to the case without an asphalt mow strip. The other setups had considerably less ground level displacement of the posts when compared to Tests T90-R300, T90-R600-C, and the test with soil only. This indicates that these two setups are more likely to pass an experimental full-scale crash test based on the quantitative comparison of full-scale crash simulation results.

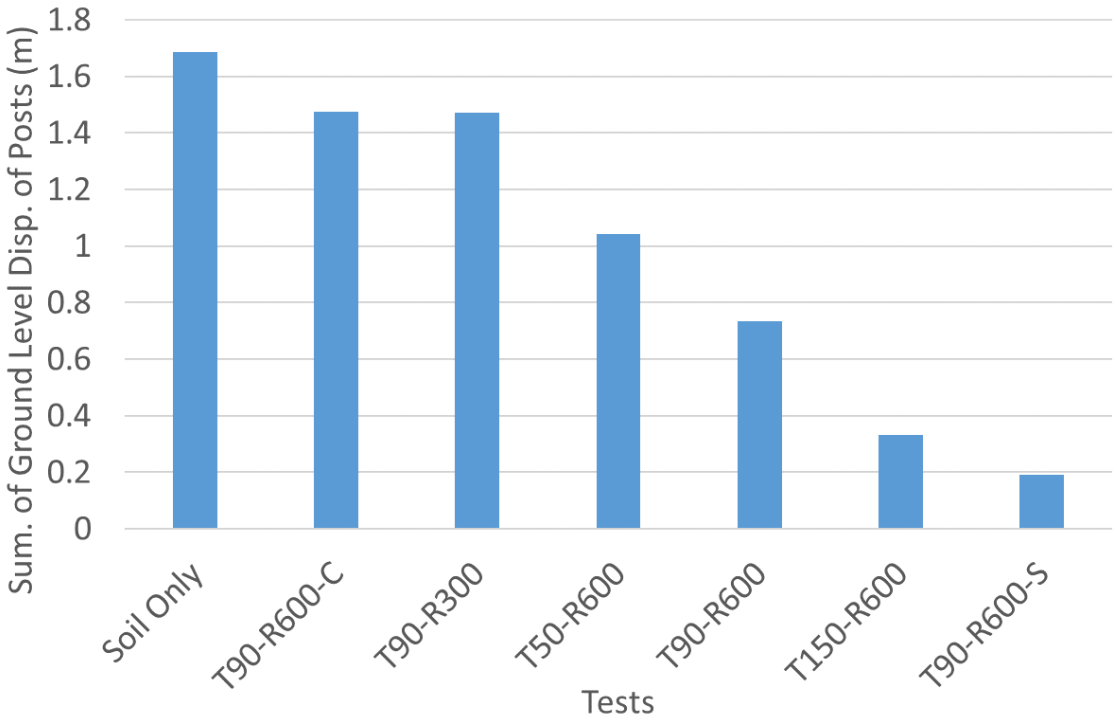

Figure 161. Summation of ground level displacement of posts compared for guardrail systems with different mow strips based on simulation results.

Table 17. Comparison between the simulation results for guardrail systems with different mow strips. Setups are sorted based on decreasing ground restraint from the left side to the right side of the table.

Test Number		Soil Only Exp. [60]	Soil Only	T90-R600-C	T90-R300	T50-R600	T90-R600	T150-R600	T90-R600-S
Exit Conditions	Speed (km/h)	64	58	58	60	57	58	57	60
	Trajectory angle, deg	14	19	13	15	13	18	18	15
ORA, g	Longitudinal	8.2	-7.3	7.4	-7.8	-9.3	-11.2	-7.4	-7.8
	Lateral	6.9	7.4	8.5	7.4	8.7	11.7	7.3	7.4
OIV, m/s	Longitudinal	4.7	5.5	4.7	4.9	5.8	5.6	5.1	4.9
	Lateral	4.8	4.8	4.5	4.9	4.6	4.7	4.8	4.9
Test article deflection, m	Dynamic	1.100	1.013	1.021	0.909	0.961	0.842	0.812	0.909
	Permanent	0.800	0.814	0.812	0.707	0.812	0.753	0.651	0.707
Impact time for the occupant t^*, sec		N/A	0.142	0.143	0.136	0.135	0.140	0.136	0.140
Sum. of ground level displacement of posts (m)		N/A	1.686	1.474	1.473	1.042	0.734	0.331	0.191
Max. yaw angle, deg		46	41	44	40	41	44	44	44
Max. roll angle, deg		-5	-3.5	-4	-2	-3	-6	-7	-4
Max. pitch angle, deg		-2	-2.9	-4	1	-1	-5	-4	-4
Posts detached from rails during impact		4 posts	3 posts	3 posts	3 posts	3 posts	3 posts	3 posts	3 posts
Posts hit by leading tire (wheel snag)		3 posts	3 posts	3 posts	3 posts	3 posts	3 posts	3 posts	3 posts
Posts pulled out of ground		None	None	None	None	None	None	None	None
Leading tire/wheel disengaged		Mostly	Mostly	Mostly	Mostly	Mostly	Mostly	Mostly	Mostly

CHAPTER 7. EFFICIENT MODELING OF GUARDRAIL POSTS EMBEDDED IN ASPHALT LAYERS VIA P-Y CURVES

7.1 Finite Element Model of Constrained Guardrail Posts Embedded in Asphalt Mow Strips

The finite element model of the guardrail post system described in Chapter 4 included the soil around the post. The load was applied to the post dynamically using an impactor. For conducting parametric studies solely on the asphalt mow strip's geometric and material properties, a simpler model was used. The soil was removed from the model to reduce the simulation time and focus on the effect of mow strip's geometric and material properties on the force applied to the post from the asphalt layer. The nodes on the free edge of the asphalt mow strip were set free, and the nodes on the other three edges of the asphalt layer were fixed, as in the model that is shown in Figure 162. All of the nodes of the steel post were translated together to apply a uniform load to the asphalt layer in order to find the asphalt bearing and rupture capacities. Moreover, all nodes of the post were rotated around the z-axis located at the center of the post cross section area in order to obtain the torsional capacity of the asphalt layer. This allowed for measurement of the force and moment coming from the asphalt layer for a given translation or rotation of the guardrail post with a specific displacement or rotation rate. The applied dynamic loads and moments per unit thickness of the asphalt layer were obtained by dividing the forces and moments from finite element simulation results by the thickness of the asphalt layer. The obtained force-

displacement and moment-rotation curves are the dynamic p-y curves for the asphalt layer with particular mow strip geometric and dynamic material properties.

The force and moment applied to the post from the asphalt layer are functions of displacement rate and rotation rate. These rates were estimated by studying full-scale crash simulations and measuring the displacement and rotation rates of the post at the ground level. The displacement rate, which is used in this dissertation for the dynamic finite element simulations to obtain p-y curves, is equal to 5 m/s and the rotation rate used is equal to 500 deg/s. The rate of displacement and rotation at the top of the post is typically much higher. However, the rates that affect the asphalt layer are the ones at the ground level.

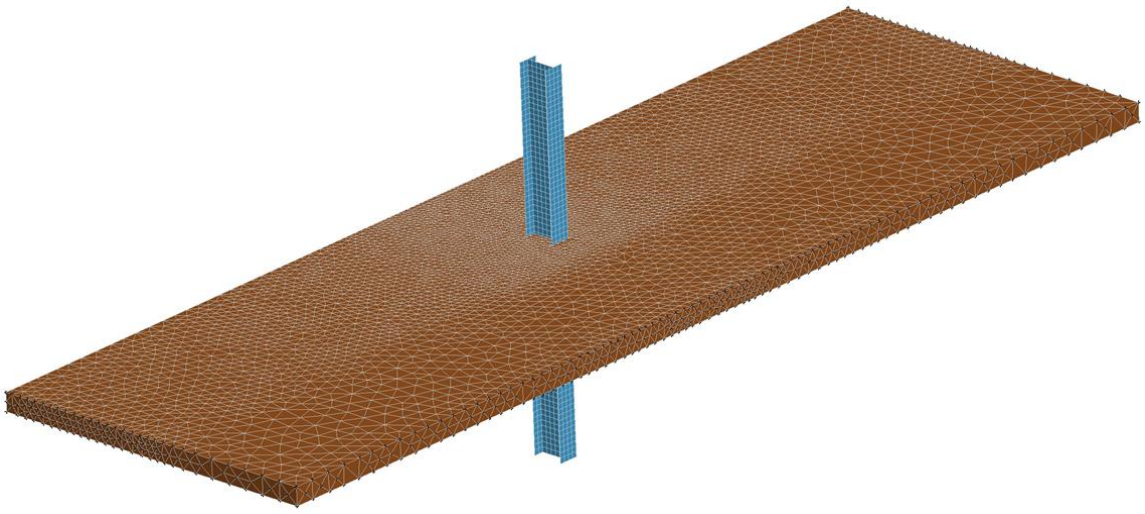

Figure 162. The Finite Element Model used for parametric studies in order to develop p-y curves.

7.2 P-Y Curves for the Lateral Strength of Guardrail Posts Embedded in Asphalt Mow Strips Using Simplified Analytical Solutions and Dynamic FE Simulations

A parametric study was performed by varying the mow strip material properties and geometry, the guardrail post flanges width, and the post's cross section depth. The asphalt friction angle ϕ, cohesion c, shear modulus G, Poisson's ratio υ, rear distance r, post cross section depth h, and post flanges width b_f were varied using discrete values equal to [10, 20, 30, 40, 50] deg., [100, 500, 1,000] kPa, [50, 100, 1,000] MPa, [0.2, 0.3, 0.4], [0, 150, 300, 450, 600, 1,200, ∞] mm, [75, 150, 300] mm, and [50, 100, 200] mm, respectively. The asphalt thickness was set equal to 100 mm; this was based on the p-y curve assumption that the thickness does not change the shape of the force-displacement curve and only scales it. (This assumption was validated and presented previously in Figure 22b in Section 3.2.2.) When the force-displacement curves were obtained after each simulation, the force and stiffness values were divided by 100 mm to obtain p-y curves for a unit thickness of asphalt. The results were used in a regression analysis to find unknown constants in the fundamental mechanics of materials equations obtained for each failure mechanism. This methodology has been used successfully in various other research areas in order to solve complex problems in civil engineering [61]–[65].

7.2.1 Rupture

7.2.1.1 Upper Bound Solution for the Shear Capacity of Asphalt Layers

The expression for the shear capacity of the asphalt layer was derived using the upper bound theorem in geotechnical engineering [53]. This theorem compares the rate of work of the external loads with the internal energy dissipation. Because the asphalt in this research is assumed to be a Mohr-Coulomb material, it was necessary to determine the internal dissipation for this idealization. The formulation presented by Davis and Selvadurai [53] is used in this paper; it assumes that internal energy dissipation would occur within shear bands. By localizing all dissipation on a single surface, the problem was simplified. By assuming an associated flow rule, the plastic strain rates must be normal to the yield surface, as shown in Figure 163.

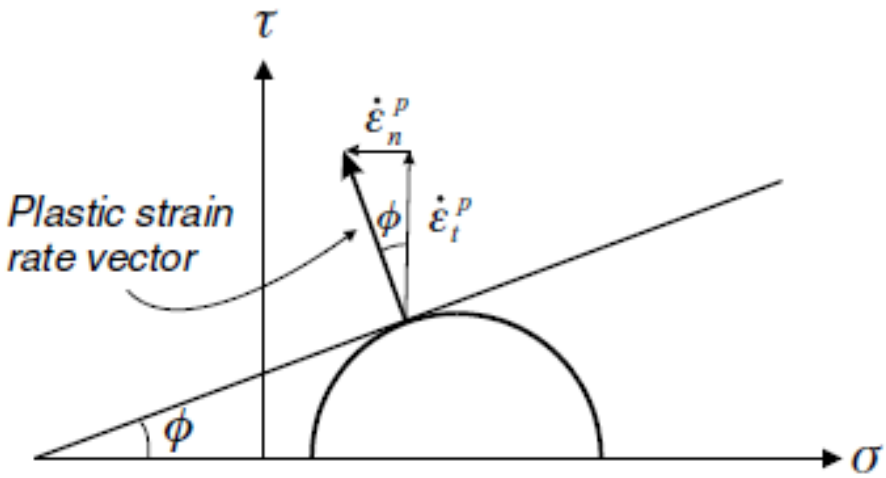

Figure 163. Mohr-Coulomb yield criterion with a normal plastic strain rate vector.

The plastic shear strain rate, $\dot{\varepsilon}_t^p$, acting tangential to the slip surface, and the plastic extensional strain rate, $\dot{\varepsilon}_n^p$, acting normal to the slip surface were two components of the plastic strain rate vector, $\dot{\varepsilon}^p$. The rate of energy dissipation per unit volume, $D_{\text{vol,}}$ within the shear band was calculated as

$$D_{vol} = \tau\dot{\varepsilon}_t^p + \sigma\dot{\varepsilon}_n^p \quad (9)$$

The velocity components of the parts of the material on the sides of the shear band relative to each other were defined as v_t and v_n. Since the shear band was thin, the plastic strain rates were approximated by:

$$\dot{\varepsilon}_t^p = v_t/h \quad (10)$$

$$\dot{\varepsilon}_n^p = v_n/h$$

where h was the thickness of the shear band. Next, D, the rate of dissipation per unit length of the shear band was obtained using Eq. 9 and 10 as

$$D = \tau v_t + \sigma v_n \quad (11)$$

Knowing that $\dot{\varepsilon}_n^p = -\dot{\varepsilon}_t^p \tan\phi$ and $v_n = -v_t \tan\phi$, Eq. 11 was further simplified to

$$D = v_t(\tau - \sigma \tan\phi) \quad (12)$$

The combination of Eq. 1 (see Section 2.2.10.2) and Eq. 12 yielded the resulting equation for the internal energy dissipation:

$$D = v_t c = cv\cos\phi \quad (13)$$

A typical failure mechanism of the asphalt layer behind the guardrail posts is presented in Figure 164, where $\beta = 90 - \phi$ and *v* is the velocity of the asphalt segment behind the post moving in the direction of the applied load. Based on this failure mechanism, shearing happened within a relatively narrow region and the rate of dissipation was equal to *D* multiplied by the length of the shear band; that is, $2(r + h)/\sin(\beta)$ as shown in Figure 164. Therefore, the equality of the rate of work of the external loads and internal energy dissipation rate was written as

$$p_s\, v = 2\, c\, v \cos(\phi) \frac{(r+h)}{sin(\beta)} \quad (14)$$

where p_s is the shear capacity per unit thickness of asphalt. Because the sum of ϕ and β was equal to 90 degrees, Eq. 14 was simplified to

$$p_s = 2\, c\, (r + h) \quad (15)$$

The equation above gives the static peak load applied to the post per unit thickness of the asphalt layer when the shear failure occurs. The shear capacity is a function of asphalt cohesion and the sum of the rear distance and post cross section depth ($r + h$).

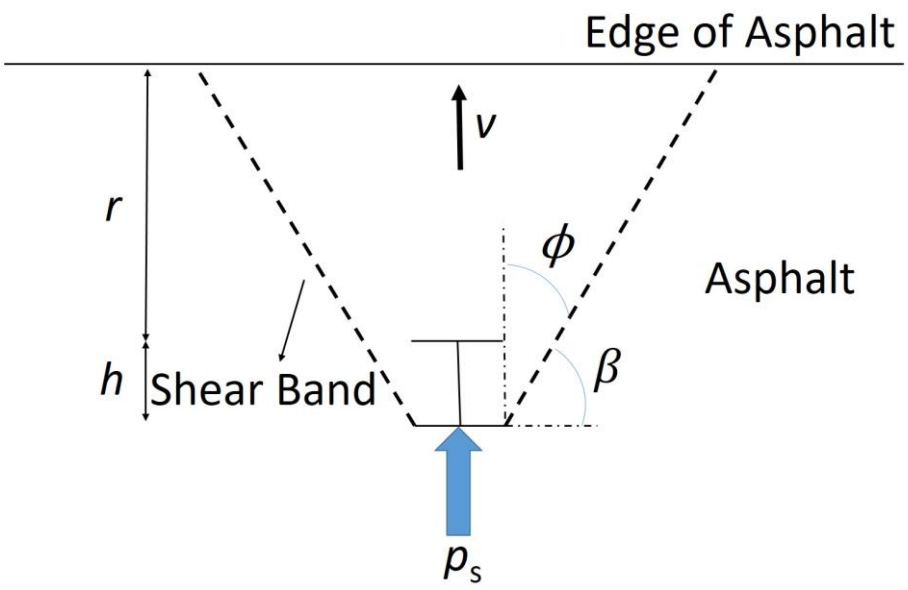

Figure 164. Assumed failure mechanism for the shear capacity.

7.2.1.2 Limit Equilibrium Solution for the Tensile Capacity of the Asphalt Layer

Because the asphalt was assumed to be a Mohr-Coulomb material, at the tip of the yield surface (cone shape), the shear stresses were equal to zero, and the value of all principal stresses became equal to the value of failure pressure, *p*, or the negative of the principal failure stress, $-\sigma_{Max}$. The components of stress at this point were written as

$$\sigma_{12} = \sigma_{13} = \sigma_{21} = \sigma_{23} = \sigma_{31} = \sigma_{32} = 0$$

$$\sigma_{11} = \sigma_{22} = \sigma_{33} = p_f = -c/\,tan(\phi) = -\sigma_{Max} \quad (16)$$

where p_f is the failure pressure. Moreover, the shear strains were zero, and the principal strains became equal to the volumetric strain divided by three, which was written as

$$\varepsilon_{12} = \varepsilon_{13} = \varepsilon_{21} = \varepsilon_{23} = \varepsilon_{31} = \varepsilon_{32} = 0$$

$$\varepsilon_{11} = \varepsilon_{22} = \varepsilon_{33} = \varepsilon_v/3 \quad (17)$$

In this dissertation, it was assumed that when the pressure reached the failure pressure, p_f, it remained constant. In addition, it was assumed that the volumetric strain increased until it reached the volumetric failure strain, and then the asphalt failed. By assuming failure planes on each side of the post at which the shear stresses are zero and the principal stresses are equal to $-\sigma_{Max}$ (Figure 165), the equilibrium of forces for the space between these two planes and unit thickness was written as

$$p_t = 2(r+h)\,\sigma_{Max}\tan\alpha = 2(r+h)\,p_f\tan\alpha = 2(r+h)\frac{c}{tan(\phi)}\tan\alpha \quad (18)$$

where p_t is the tensile capacity per unit thickness of asphalt and α is the angle between the assumed zero-shear planes and the direction of post's movement. This simplified solution demonstrated that an increase in the rear distance or maximum tensile stress at failure had a direct impact on the tensile capacity.

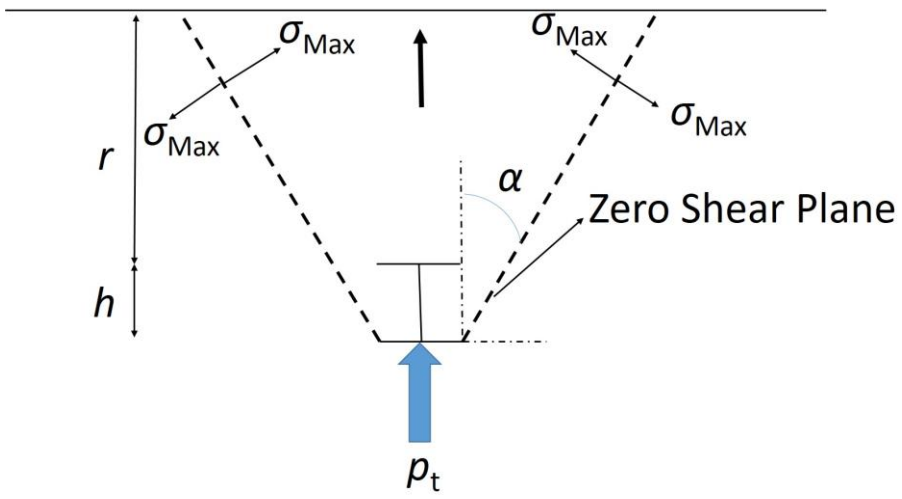

Figure 165. Assumed tensile failure mechanism with zero shear planes.

7.2.1.3 Rupture Capacity of the Asphalt Layer

Based on Eq. 15, the shear capacity is a function of the cohesion *c* and the sum of rear distance and the post's cross section depth ($r + h$). Based on Eq. 18, the tension capacity is a function of the asphalt cohesion *c*, the sum of rear distance and the post's cross section depth ($r + h$), and the asphalt friction angle ϕ. However, the real failure mechanism was more sophisticated, involving a combination of shear and tension failure. In order to simplify the solution and include both failure modes, a single equation was proposed to combine these two failure mechanisms. The combined strength is referred to as the rupture capacity. The following predictive equation was proposed for the rupture capacity per unit thickness of asphalt

$$p_r = c\,(\mathrm{r}+\mathrm{h})(a_r + f_r\phi) < p_{bf} \quad (19)$$

where a_r and f_r are dimensionless constants. The proposed rupture capacity is a function of cohesion and (r+h), which is similar to the shear capacity in Eq. 15 and the tensile capacity in Eq. 18. The rupture capacity decreased as the friction angle increased, based on the results presented in Section 3.2.4 and Figure 22d. The decrease in the rupture capacity shown in Figure 22d was approximately proportional to the angle of friction. Therefore, a linear function of the angle of friction is included in Eq. 19. This linear approximation accounts for the decrease in tensile capacity when the friction angle increased, which appeared as $\tan\alpha\,/\tan(\phi)$ in Eq. 18. The rupture capacity was limited to the bearing capacity perpendicular to flanges p_{bf} , which will be discussed in section 7.2.2. The peak force increased as the rear distance increased until it reached the bearing capacity for large rear distances. In the finite element simulations, the peak forces obtained for cases with limited rear distance were compared to cases with infinite rear distance. In each case, if the peak force for a limited rear distance was equal to the peak force with infinite rear distance, then the rear distance was large enough that the bearing capacity was reached. These cases cannot be used in a regression analysis to find the constants in Eq. 19. On the other hand, if the peak force for a limited rear distance was less than the peak force with infinite rear distance, the bearing capacity was not reached, and the rupture capacity controlled the behavior. These peak forces were used in the regression analysis to find constants a_r and f_r in Eq. 19. Based on the FEA simulation results and regression analysis, a_r and f_r were

found. The mean values for these constants, their standard deviations, and the model standard deviation for p_r are given in Table 18. The rupture capacity or peak force obtained from the FEA and predicted by Eq. 19 are compared in Figure 166. The comparison shows that Eq. 19 can predict the dynamic rupture capacities obtained from the FEA simulations.

Table 18. Variables and constants for rupture failure.

Parameter	Mean value	Standard error
p_r	N.A.	29.49 N/mm
a_{r}	2.87	0.07
f_{r}	-0.025	0.003
y_r	N.A.	1.5
l_{yr}	1362 mm	33 mm
y_u	N.A.	12 mm
u_r	15.12	2.17

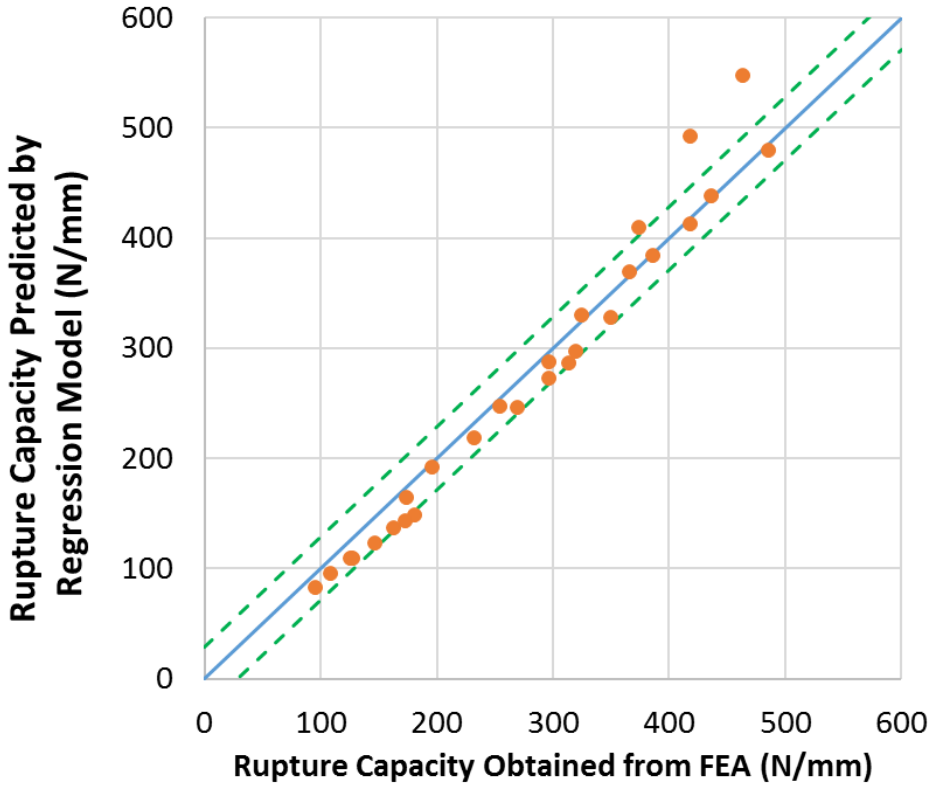

Figure 166. Rupture capacity predicted by regression model versus FEA results.

7.2.1.4 P-Y Curves for the Rupture Capacity

The resisting lateral force in the asphalt layer increased as the displacement increased. On the force-displacement curve, the force increased until it reached its peak, and then decreased in the softening phase until it became zero. The force reached zero because the rear distance was limited and one part of the asphalt layer detached from the rest of the mow strip. After this point, there was no asphalt resistance. The portion of the curve up to the peak force was approximated by a second-degree polynomial, knowing that the curve passed the origin (0 N/mm, 0 mm) and that the peak of the curve was where the

peak force occurred (p_r, y_r). The force was then assumed to decrease linearly until it reached zero. Therefore, the equation for the p-y curve could be written as

$$\mathrm{p} = \left[-\left(\frac{y}{y_r}\right)^2 + 2\frac{y}{y_r}\right] p_r \qquad y \leq y_r$$

$$\mathrm{p} = \frac{(y_u - y)p_r}{(y_u - y_r)} \qquad y_r < y < y_u$$

$$p = 0 \qquad y \geq y_u \tag{20}$$

where y_r is the lateral displacement at which the peak force p_r occurred, and y_u is the lateral displacement where one piece of the asphalt layer became detached, and the resistance of the layer reached zero. The lateral displacement, y_r, was obtained using the following proposed equation

$$y_r = l_{yr}\frac{c}{G} \tag{21}$$

where l_{yr} is a constant with a dimension of length. Using finite element parametric studies, l_{yr} was obtained. The model standard error for y_r, along with the mean value and standard error for l_{yr}, are provided in Table 18. The ultimate lateral displacement y_u was calculated as:

$$y_u = y_r + u_r\frac{c\,(r+h)}{G} \tag{22}$$

where u_r is a dimensionless constant obtained from parametric studies. The model standard error for y_u, along with the mean value and standard error for u_r, are provided in Table 18. Moreover, the unloading curve for the rupture capacity was assumed to have the same slope as the initial slope of the loading curve, which was $k_{ru} = 2p_r/y_r$. Sample rupture capacity p-y curves for various values of cohesion, friction angle, rear distance, and shear modulus are presented in Figure 167 through Figure 170. With the exception of the varied parameter in each figure, constant values of c = 500 kPa, Φ = 35 deg., G = 50 MPa, r = 300 mm, and h = 150 mm were used.

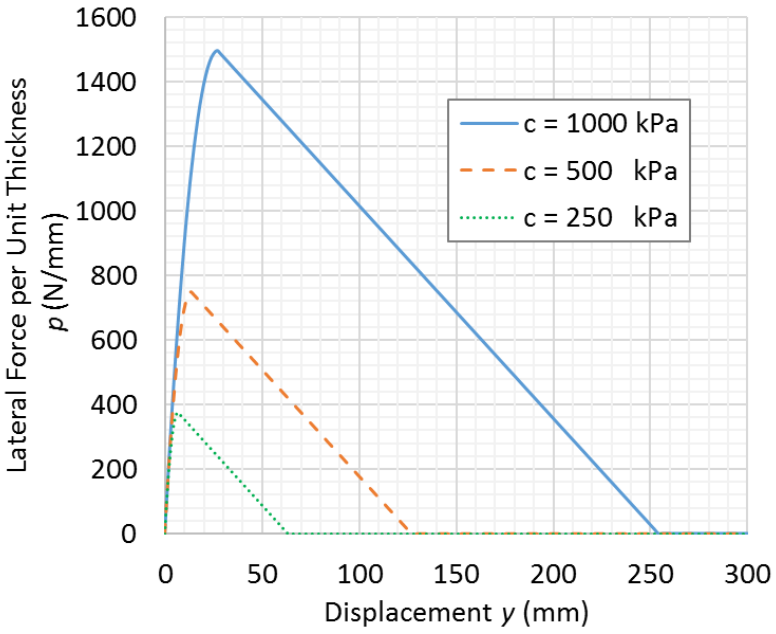

Figure 167. Rupture capacity p-y curves for various values of cohesion c.

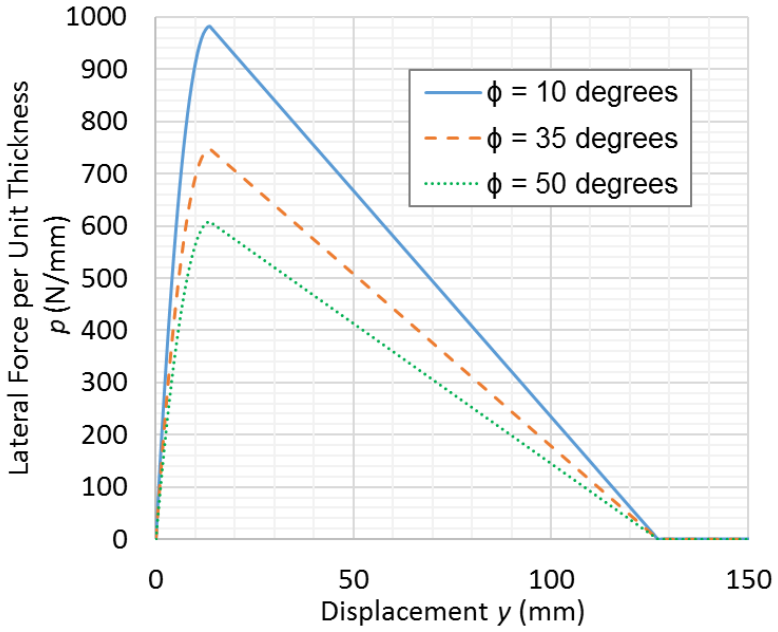

Figure 168. Rupture capacity p-y curves for various values of friction angle Φ.

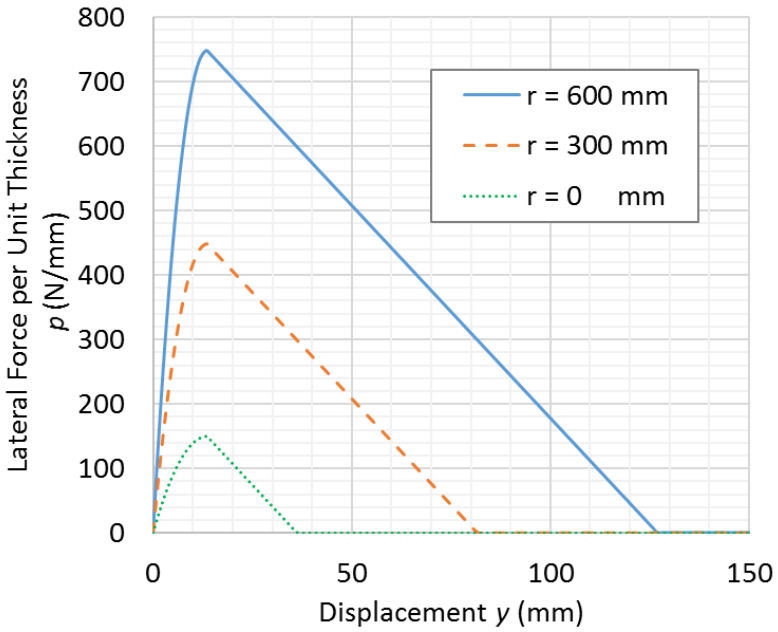

Figure 169. Rupture capacity p-y curves for various values of rear distance r.

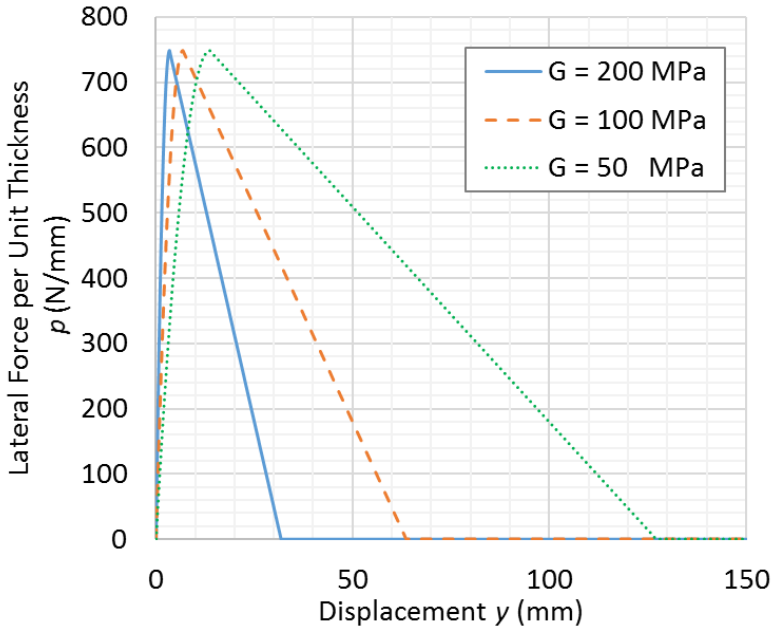

Figure 170. Rupture capacity p-y curves for various values of shear modulus G.

7.2.2 Bearing Failure of the Asphalt Perpendicular to Post Flanges

7.2.2.1 Limit Equilibrium Solution for Bearing Capacity of the Asphalt Perpendicular to Post Flanges

The post's cross-sectional depth was comparable to the flange width. Therefore, the stresses behind each flange affected the other flange, and they acted in a coupled fashion. A possible failure mechanism for this case occurred when the rear flange reached its bearing capacity and shear failure occurred on two sides of the post, as shown in Figure 171.

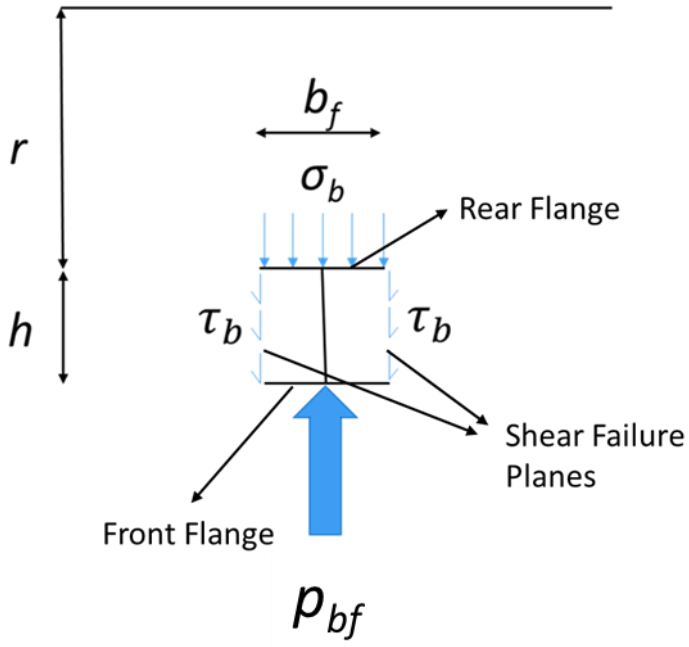

Figure 171. Bearing capacity failure mechanism perpendicular to the flanges.

The bearing capacity per unit thickness of asphalt was then obtained as

$$p_{bf} = \sigma_b b_f + 2\tau_b h \quad (23)$$

where the bearing stress σ_b and the side shear stress when the bearing capacity is reached τ_b are functions of cohesion c and friction angle ϕ.

7.2.2.2 Bearing Capacity of the Asphalt Layer Perpendicular to the Post Flanges

Based on Eq. 23, the bearing capacity perpendicular to flanges is a function of flange width, b_f, post cross-section depth, h, bearing stress, σ_b, and shear stress when the bearing stress is reached, τ_b. The bearing stress and shear stress are functions of the

cohesion and the friction angle of the asphalt. When the asphalt cohesion increased, the size of the Mohr-Coulomb yield surface increased proportionally. Therefore, the finite element simulation results show that when cohesion increased, the bearing capacity increased proportionally. Moreover, an increase in the friction angle increased the slope of the Mohr-Coulomb yield surface proportionally, which resulted in larger shear stresses at failure. When the friction angle became equal to zero, the material was not pressure-dependent anymore, and the bearing stress became a linear function of the cohesion. Therefore, the following equation was used to estimate the bearing stress σ_b:

$$\sigma_b = c\left(a_{bf}+f_{bf}\phi\right) \tag{24}$$

where a_{bf} and f_{bf} are dimensionless constants. By assuming that τ_b is proportional to σ_b it was then written as

$$\tau_b = h_{bf}\sigma_b = c\left(a_{bf}+f_{bf}\phi\right)\left(h_{bf}\right) \tag{25}$$

where h_{bf} is a dimensionless constant. By inserting σ_b and τ_b from Eqs. 24 and 25 into Eq. 23, the bearing capacity perpendicular to the post flanges was determined to be

$$p_{bf} = c\left(a_{bf} + f_{bf}\phi\right)\left(b_f + 2\,h_{bf}\mathrm{h}\right) \tag{26}$$

The peak force obtained from simulation results for the cases with infinite rear distance was used in a nonlinear regression analysis to determine these parameters. The model standard error for p_{bf}, the mean values, and standard errors for the constants a_{bf}, f_{bf}, and

h_{bf} are given in Table 19. The bearing capacities, obtained by FEA and predicted by Eq. 26, are compared in Figure 172. The comparison shows that Eq. 26 can predict the bearing capacity perpendicular to flanges obtained from FEA.

Table 19. Variables and constants for bearing failure perpendicular to flanges.

Parameter	Mean value	Standard error
p_{bf}	N.A.	89 N/mm
a_{bf}	8.55	0.48
f_{bf}	0.10	0.016
h_{bf}	0.250	0.026
k_{bf}	N.A.	14 N/mm^2
h_{kbf}	0.0198 mm^{-1}	0.0016 mm^{-1}
b_{kbf}	0.0362 mm^{-1}	0.0029 mm^{-1}

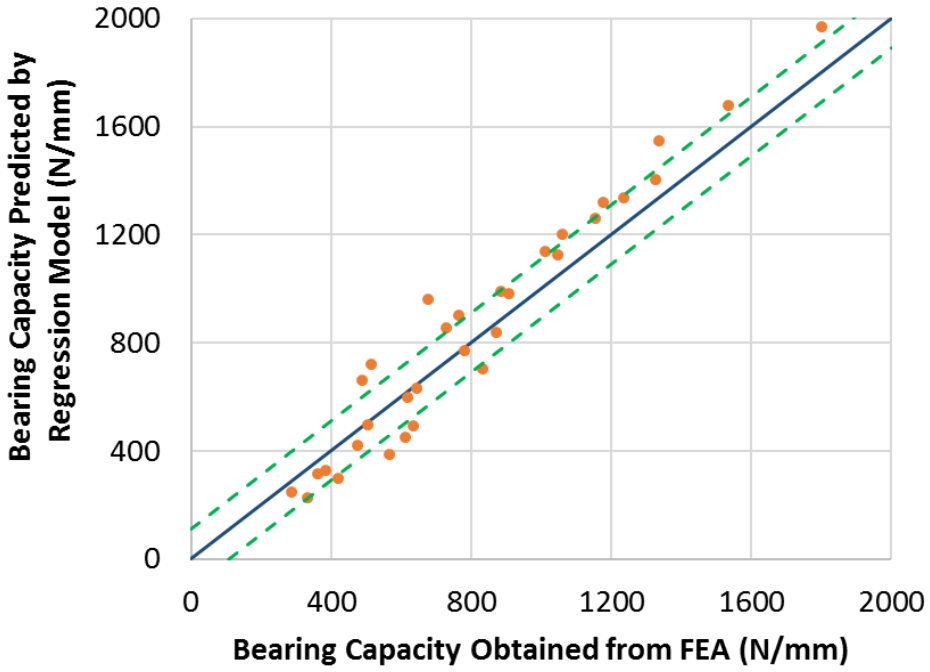

Figure 172. Bearing capacity perpendicular to flanges by Eq. 26 versus FEA results.

7.2.2.3 P-Y Curves for the Bearing Capacity of the Asphalt Layer Perpendicular to Flanges

The resisting force increased as the post moved, reached the maximum force, and stayed constant thereafter. Using the bearing capacity, p_{bf}, and the initial slope of the curve, k_{bf}, a simple hyperbolic function was used to estimate the behavior of the system. The equation for the hyperbola was written as

$$p = y/(1/k_{bf} + y/p_{bf}) \quad (27)$$

The initial slope of the curve k_{bf} with dimension of N/mm^2 were calculated using the following proposed equation

$$k_{bf} = G\left(h_{kbf}h + b_{kbf}b_f\right) \quad (28)$$

Using finite element parametric studies and linear regression, the constants h_{kbf} and b_{kbf} were obtained. The model standard error for k_{bf}, along with the mean values and standard errors for h_{kbf} and b_{kbf}, are provided in Table 19. This equation indicated that the initial slope of the curve had a direct relation with the post flange width, cross section depth, and the shear modulus of the asphalt. The unloading curve for the rupture capacity was assumed to have the same slope as the initial slope of the loading curve equal to k_{bf}. Sample bearing capacity p-y curves for various values of cohesion, friction angle, and shear modulus are shown in Figure 175 throughFigure 181. Except for the varied parameter in each case figure, constant values of c = 500 kPa, Φ = 35 deg., G = 50 MPa, b_f = 100 mm, and h = 150 mm were used.

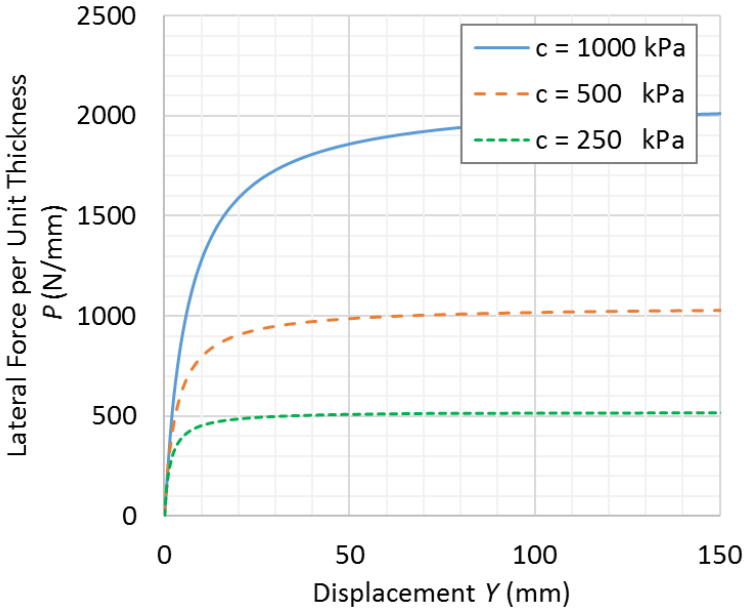

Figure 173. P-Y curves for the bearing capacity perpendicular to post flanges for various values of cohesion c.

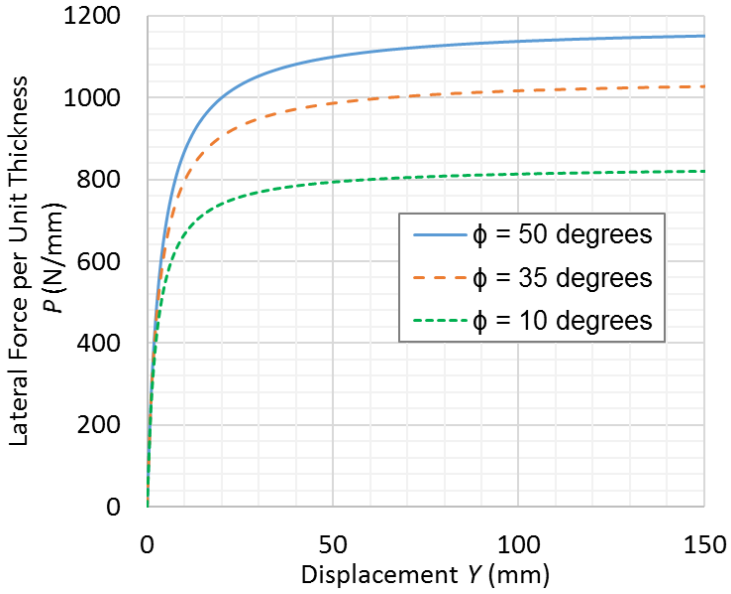

Figure 174. P-Y curves for the bearing capacity perpendicular to post flanges for various values of friction angle Φ.

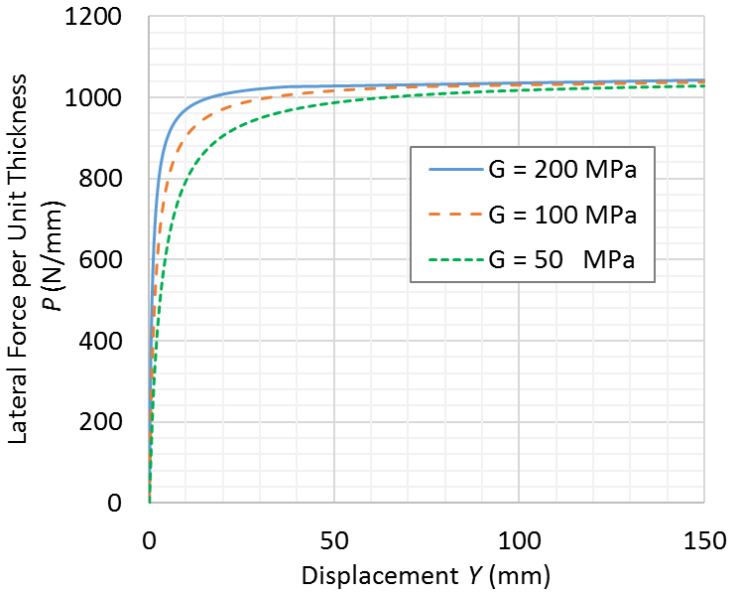

Figure 175. P-Y curves for the bearing capacity perpendicular to post flanges for various values of shear modulus G.

7.2.3 Bearing Failure of Asphalt Perpendicular to the Post Web

7.2.3.1 Limit Equilibrium Solution for Bearing Capacity of Asphalt Perpendicular to the Web

When the load was applied perpendicular to the web, the post reached its bearing capacity when the asphalt in front of the web reached its bearing capacity, as shown in Figure 176. The bearing capacity per unit thickness of asphalt was calculated as

$$p_{bw} = \sigma_b h \tag{29}$$

where σ_b is the bearing stress, which is a function of cohesion c and friction angle ϕ. Therefore, the bearing capacity was directly related to the web depth and bearing stress.

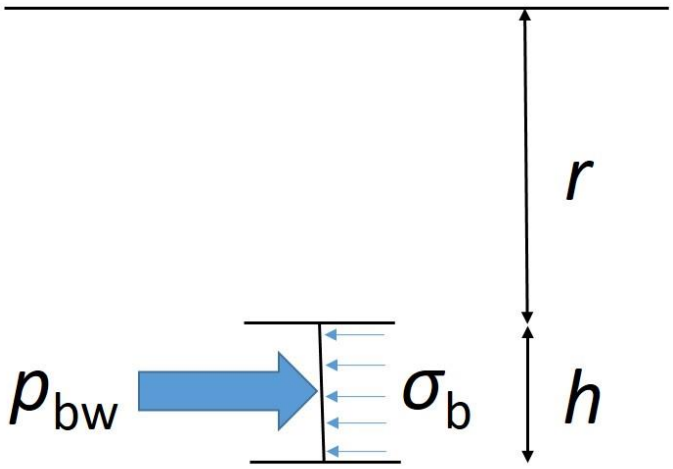

Figure 176. Bearing capacity failure mechanism when the load is applied perpendicular to the web.

7.2.3.2 Bearing Capacity of the Asphalt Layer Perpendicular to the Web

Based on Eq. 29, the bearing capacity perpendicular to the web was a function of cross-section depth, h, and the bearing stress, σ_b. The bearing stress was a function of cohesion and friction angle. Therefore, the following predictive equation was utilized for the bearing capacity perpendicular to the web per unit thickness

$$p_{bw} = c\,(a_{bw}+f_{bw}\phi)h \tag{30}$$

where $a_{bw}, and\ f_{bw}$ are dimensionless constants. The model standard error for p_{bw} along with the mean values and standard errors for a_{bw}, and f_{bw} are given in Table 20. The bearing capacities obtained by FEA for cases with various friction angles are presented in Figure 177. As can be seen from this figure, the bearing capacity had a linear relation with friction angle.

Table 20. Variables and constants for bearing failure perpendicular to the web.

Parameter	Mean value	Standard error
p_{bw}	N.A.	8.76 N/mm
a_{bw}	5.50	0.18
f_{bw}	0.142	0.011
k_{bw}	N.A.	11 N/mm^2
l_{kbw}	0.021 mm^{-1}	0.002 mm^{-1}

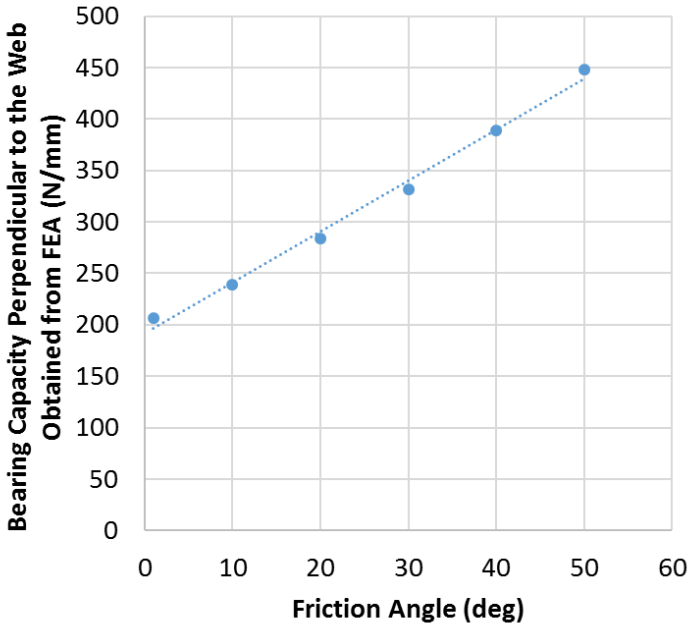

Figure 177. Bearing capacity perpendicular to the web obtained from FEA versus friction angle of asphalt.

7.2.3.3 P-Y Curves for the Bearing Capacity of the Asphalt Layer Perpendicular to the Web

The resisting lateral force in the asphalt layer increased as the displacement increased. It was assumed that the rear distance had no effect on the bearing resistance perpendicular to the web. Using the bearing capacity, p_b, and the initial slope of the curve, k_b, a simple hyperbolic function was used to estimate the behavior of the system. The equation of the hyperbola was written as

$$p = \ y/(1/k_{bw} + y/p_{bw}\ ) \tag{31}$$

The initial slope of the curve k_{bw} was found using the following proposed equation

$$k_{bw} = l_{kbw}Gh \tag{32}$$

Using finite element parametric studies and linear regression, the constant l_{kbw} was obtained; it is presented in Table 20. The unloading curve for the bearing capacity was assumed to have the same slope as the initial slope of the loading curve equal to k_{bw}. Sample bearing capacity p-y curves for various values of cohesion, friction angle, and shear modulus are shown in Figure 178 through Figure 180. Except for the varied parameter in each figure, constant values of c = 500 kPa, Φ = 35 deg., G = 50 MPa, b_f = 100 mm, and h = 150 mm were used.

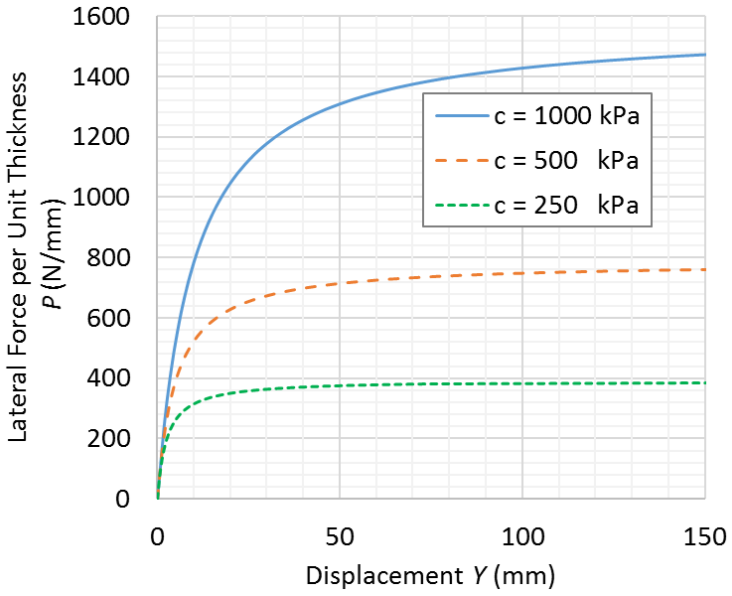

Figure 178. P-Y curves for the bearing capacity perpendicular to the post's web for various values of cohesion c.

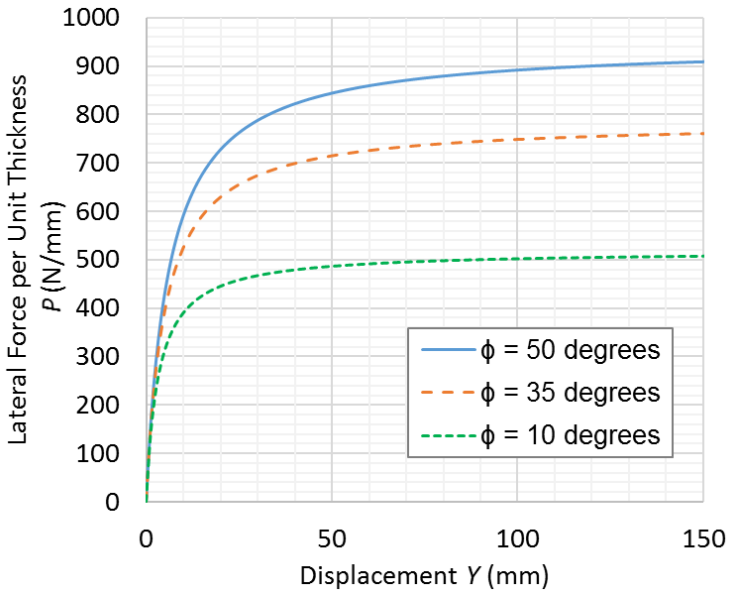

Figure 179. P-Y curves for the bearing capacity perpendicular to the post web for various values of friction angle *Φ*.

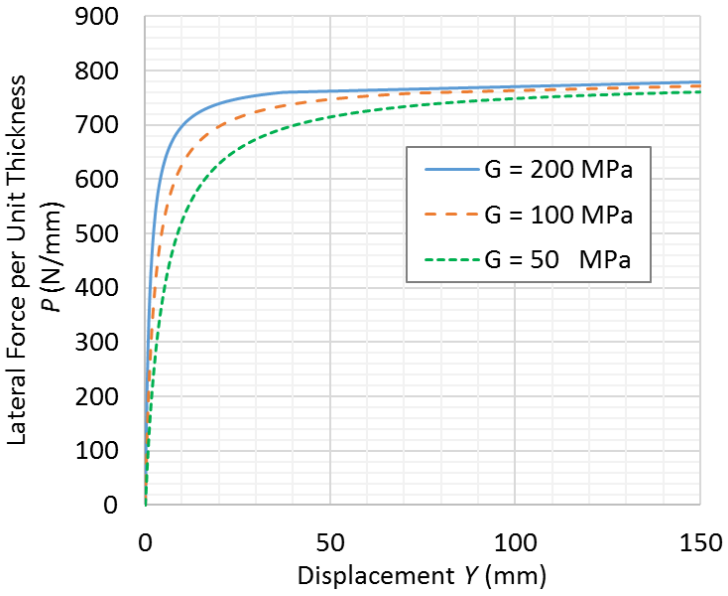

Figure 180. P-Y curves for the bearing capacity perpendicular to the post web for various values of shear modulus G.

7.2.4 Torsional Failure

7.2.4.1 Limit Equilibrium Solution for the Torsional Capacity of Asphalt

Vehicles impact guardrail systems at an angle and the guardrail posts are twisted during the vehicle crash. By simplifying assumptions, the torsional capacity of the asphalt can be found. If the post rotates around its center point, then, for small rotations, the applied stresses will be perpendicular to the web as shown in Figure 181.

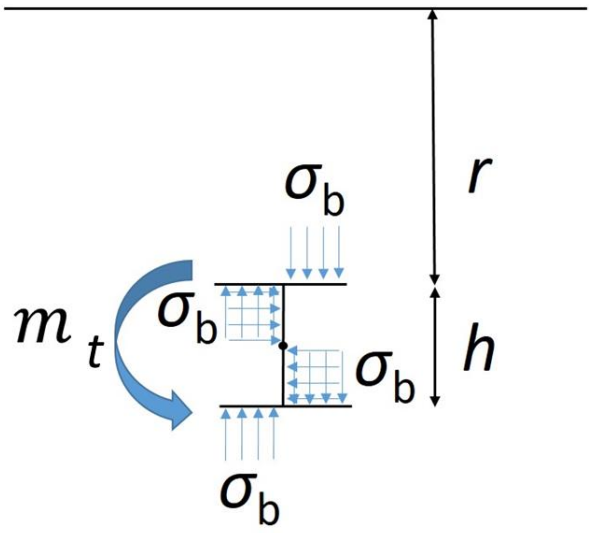

Figure 181. Torsional capacity when a torsional moment is applied to the post.

If it is assumed that the asphalt reaches its bearing capacity uniformly along the web and flanges, then the torsional capacity is obtained as

$$m_t = \sigma_b\left(h^2/4 + b_f^2/2\right) \quad (33)$$

where m_t is the torsional capacity per unit thickness of asphalt.

7.2.4.2 Torsional Capacity of Asphalt

Based on Eq. 33, the torsional capacity is a function of cross section depth, *h*, flanges width, b_f, and the bearing stress, σ_b. The bearing stress is a function of cohesion and friction angle. Therefore, the following predictive equation was used for the torsional capacity of asphalt:

$$m_t = c(a_{mt} + f_{mt}\phi)\left(h_{mt}h^2 + b_{mt}b_f^2\right) \quad (34)$$

where a_{mt}, f_{mt}, h_{mt} and b_{mt} are dimensionless constants and m_t is the asphalt torsional capacity per unit thickness. The post in the finite element model was rotated around the z axis with rotation rate of 500 deg/s, and the torsional moment applied to it was measured. The peak moment obtained from simulation results for the cases with infinite rear distance was used in nonlinear regression analysis, and it was assumed that rear distance did not affect the torsional capacity. The unknown constants in Eq. 34 were obtained via nonlinear regression analysis using the finite element simulation results. The model standard error for m_t, the mean values, and standard errors for constants a_{mt}, f_{mt}, h_{mt} and b_{mt} are given in Table 21. The torsional capacities obtained by FEA and predicted by Eq. 34 are compared in Figure 172. The comparison shows that Eq. 34 can predict the torsional capacity.

Table 21. Variables and constants for torsional failure.

Parameter	Mean value	Standard error
m_t	N.A.	3450 N.mm/mm
a_{mt}	7.51	0.12
f_{mt}	0.199	0.030
h_{mt}	0.181	0.012
b_{mt}	0.208	0.019
k_{mt}	N.A.	2265 (N.mm)/(mm.deg)
h_{kmt}	0.0052	0.0006
b_{kmt}	0.0138	0.0011

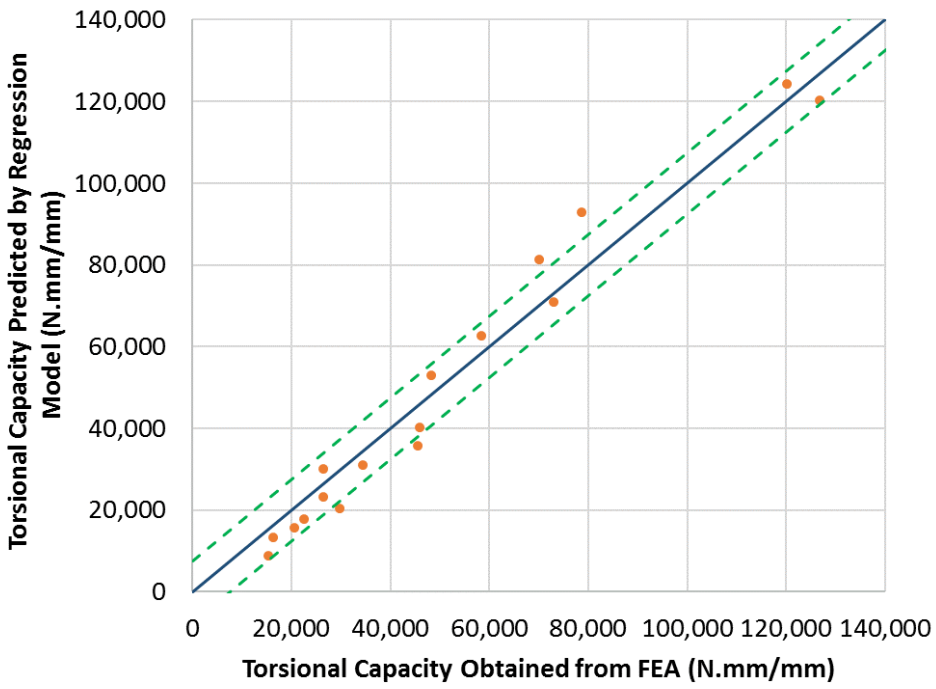

Figure 182. Asphalt torsional capacity predicted by Eq. 34 versus FEA results.

7.2.4.3 P-Y Curves for the Torsional Capacity of the Asphalt Layer

The resisting torsional moment increased as the post rotated. It was assumed that the rear distance did not affect the torsional resistance. Using the torsional capacity, m_t, and the initial slope of the curve, k_{mt}, a simple hyperbolic function can be used to estimate the behavior of the system. The equation of the hyperbola was written as

$$p = \mathrm{y}/(1/\mathrm{k_{mt}} + \mathrm{y}/\mathrm{m_t}) \quad (35)$$

The initial slope of the curve k_{mt} was found using the following equation:

$$k_{mt} = G\left(h_{kmt}\mathrm{h}^2 + b_{kmt}b_f^2\right) \quad (36)$$

Using finite element parametric studies and linear regression, the constants h_{kmt} and b_{kmt} were obtained as shown in Table 21. This equation indicated that the initial slope of the curve had a direct relation with shear modulus and square of the cross-section depth and the flanges width. A comparison between predictions using Eq. 36 and FEA results is presented in Figure 183. The unloading curve for the rupture capacity was assumed to have the same slope as the initial slope of the loading curve equal to k_{mt}. Sample torsional capacity p-y curves for various values of cohesion, friction angle, and shear modulus are shown in Figure 184 throughFigure 186. Except for the varied parameter in each figure, constant values of c = 500 kPa, Φ = 35 deg., G = 50 MPa, b_f = 100 mm, and h = 150 mm were used.

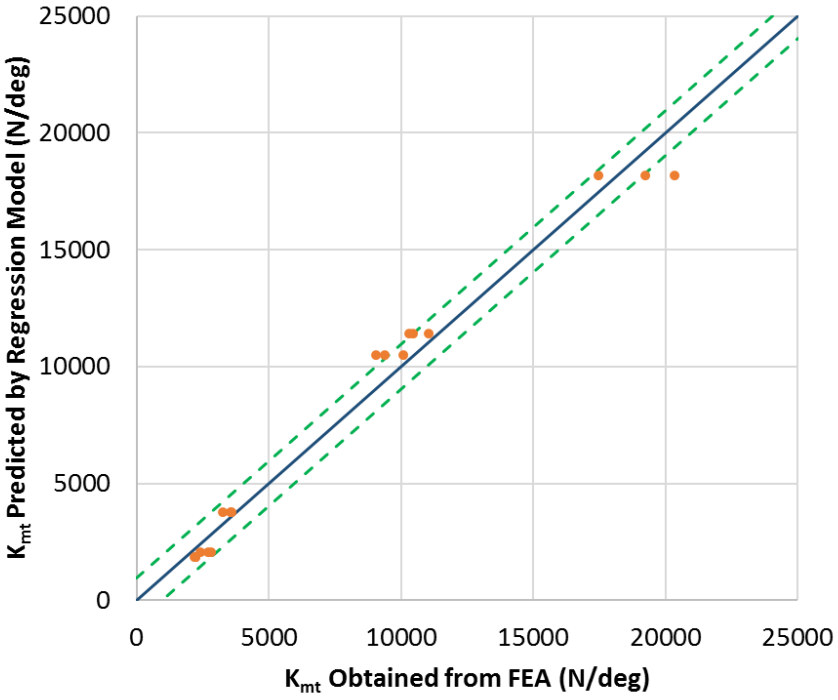

Figure 183. Comparison between predictions using Eq. 36 and FEA results for k_{mt}.

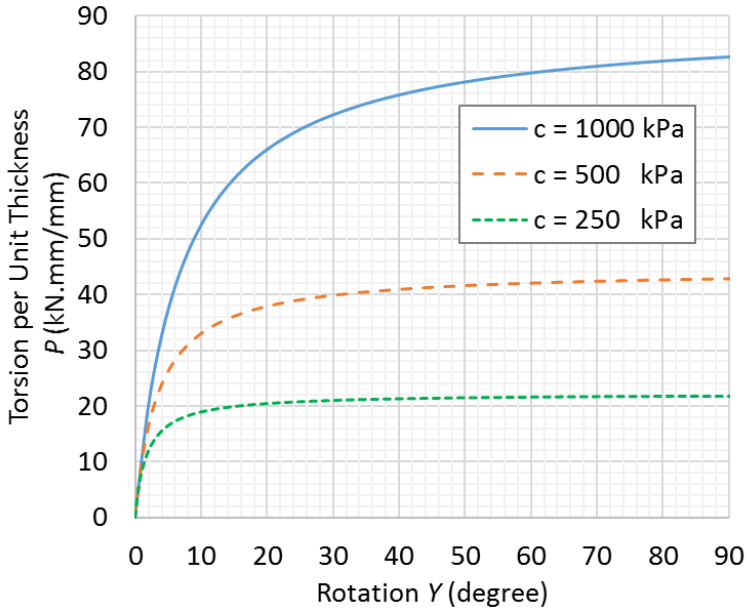

Figure 184. P-Y curves for the torsional capacity for various values of cohesion c.

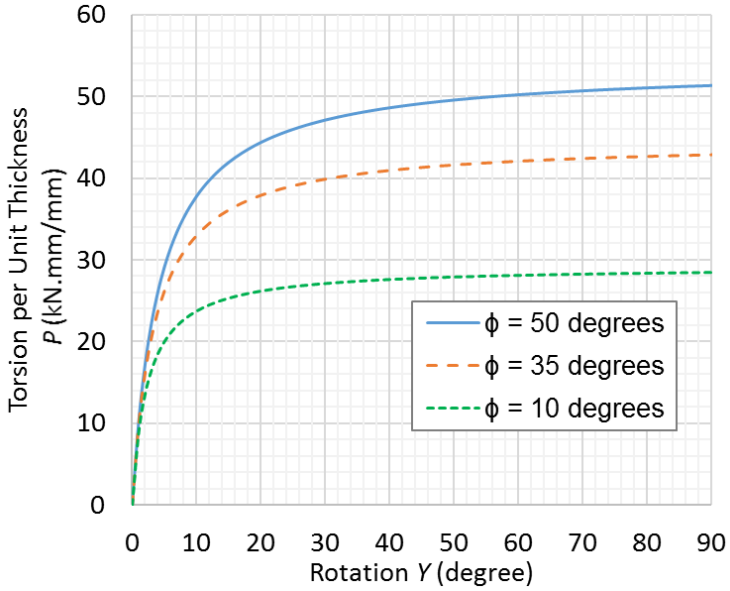

Figure 185. P-Y curves for the torsional capacity for various values of friction angle.

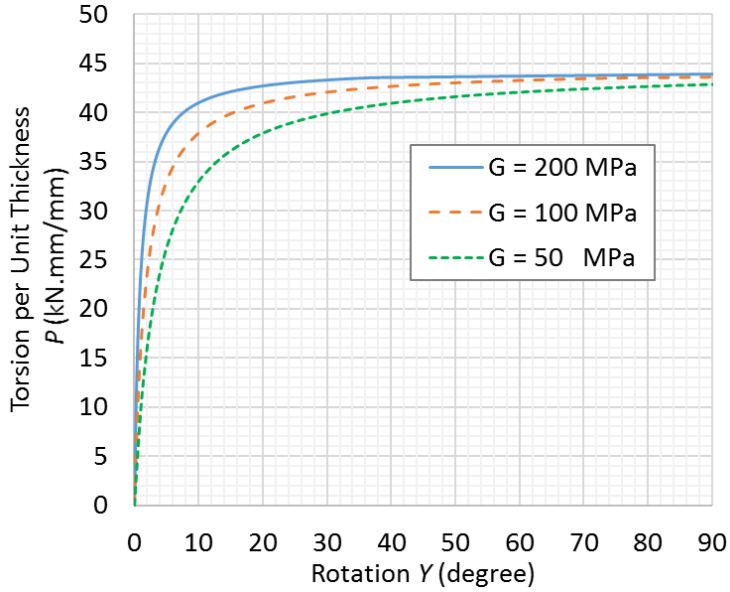

Figure 186. P-Y curves for the torsional capacity for various values of shear modulus G.

7.3 Dynamic Simulation of Guardrail Posts Embedded in Asphalt Mow Strips Using P-Y Curves

The finite element model discussed in Chapter 4 with 90 mm thick asphalt mow strip and 600 mm rear distance was updated by removing the continuum mesh for the asphalt layer. Instead, the asphalt was modeled using inelastic nonlinear springs in LS-DYNA (material #S08) for translational springs and a general nonlinear spring (material #S06) for the rotational spring. Two springs on the sides of the post, two springs on the back and front of the post, and one rotational spring were used. All springs were connected to the center node of the post at the middle of the web and at a depth of 45 mm, which was half of the asphalt depth. The model is shown in Figure 187 with all parts and in Figure 188 with only the steel post and the springs to better illustrate the arrangement of the springs. One spring was used on each side of the post because the translational springs are only active in compression, and their tensile force was always zero. The rotational spring acts the same way in both clockwise and counter-clockwise rotations because of the model symmetry. Cohesion c = 500 kPa, friction angle Φ = 35 deg, shear modulus G = 50 MPa, flange width b_f = 100 mm, cross section depth h = 150 mm, rear distance r = 600, and thickness t = 90 mm were used. The rupture capacity, p_r, was calculated using Eq. 19 equal to 748 N/mm. The displacement at peak load, y_r, and the ultimate displacement, y_u, were obtained using Eq. 21 and Eq. 22 and were equal to 14 mm and 147 mm, respectively. The p-y curve was obtained using Eq. 35 and then scaled by the thickness of the asphalt layer

(90mm) to obtain the force-displacement curve for the inelastic spring behind the post (spring #1) as shown in Figure 189.

The bearing capacity perpendicular to the flanges, $p_{bf,}$ and the initial slope of the p-y curve, $k_{bf,}$ were calculated using Eq. 26 and Eq. 28 equal to 1,049 N/mm and 330 N/mm^2, respectively. The p-y curve was obtained using Eq. 27 and then scaled by the thickness of the asphalt layer (90mm) to obtain the force-displacement curve for the compressive inelastic spring in front of the post (spring #2) as shown in Figure 190.

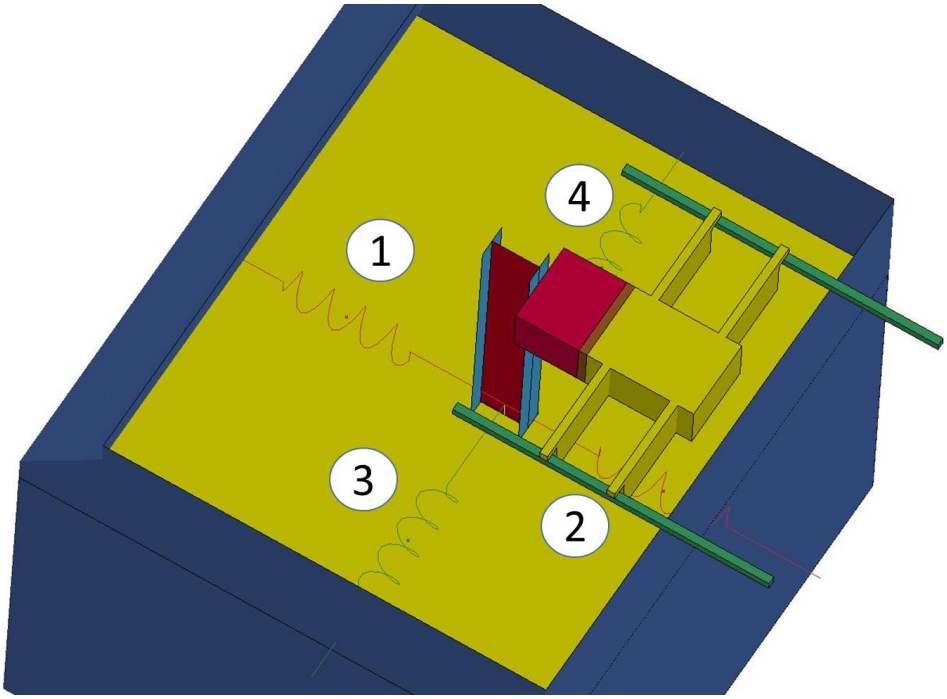

Figure 187. The model of the guardrail post embedded in soil and asphalt. Asphalt was modeled using one rotational and four translational springs.

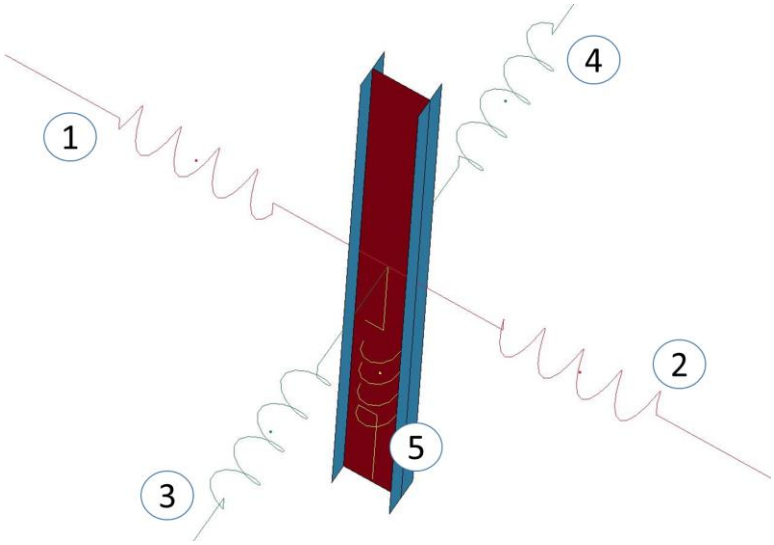

Figure 188. The model of the guardrail post embedded in soil and asphalt. Asphalt was modeled using one rotational and four translational springs.

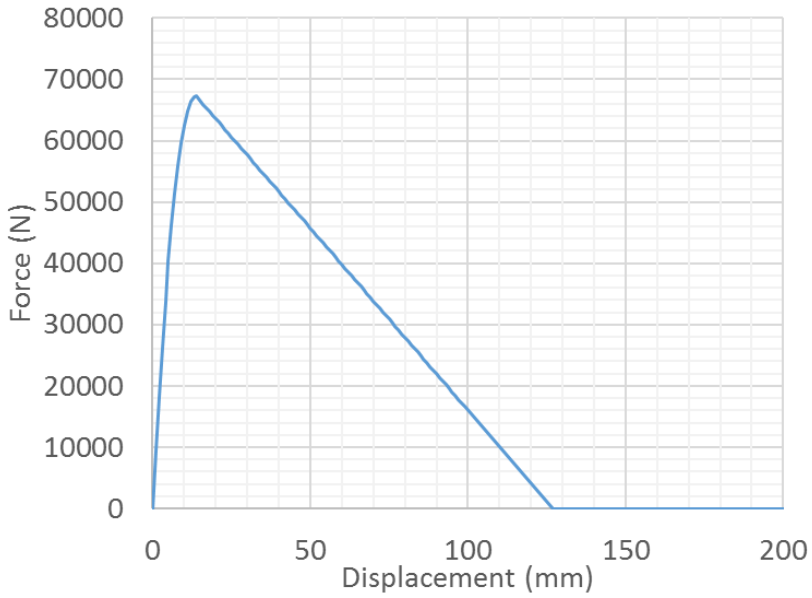

Figure 189. Force-displacement curve for the inelastic spring (Spring #1) behind the post to model asphalt rupture.

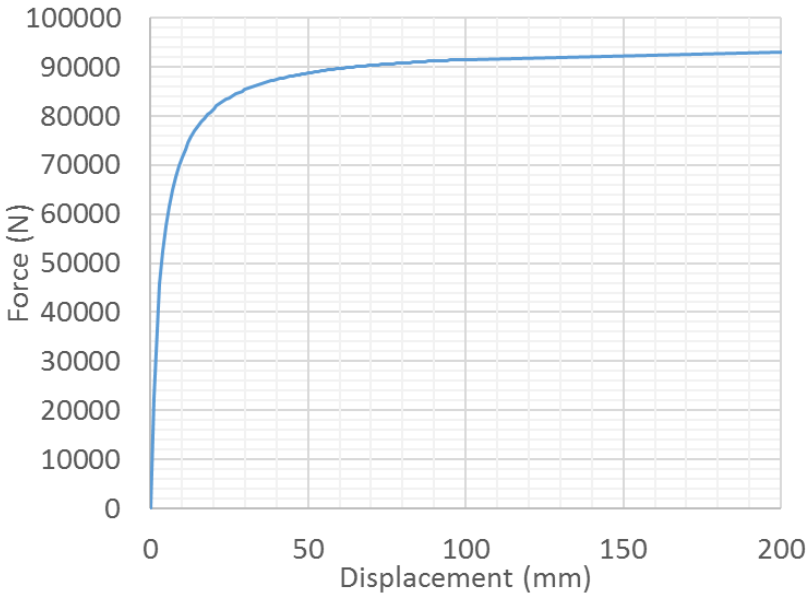

Figure 190. Force-displacement curve for the inelastic spring (spring #2) in front of the post to model asphalt bearing capacity when pulled toward the front of the post.

The bearing capacity perpendicular to the web, p_{bw}, and the initial slope of the p-y curve, k_{bw}, were calculated using Eq. 29 and Eq. 32 equal to 785 N/mm and 158 N/mm^2, respectively. The p-y curve was obtained using Eq. 31 and then scaled by the thickness of the asphalt layer (90mm) to obtain the force-displacement curve for the compressive inelastic spring on the right and left-hand sides of the post (spring #3 and #5) as shown in Figure 191.

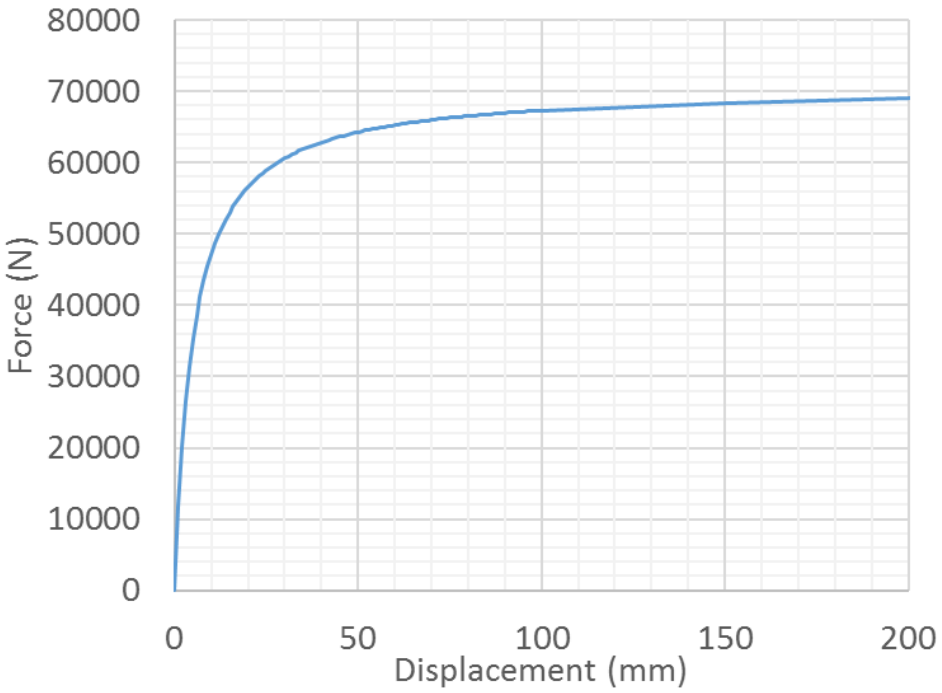

Figure 191. Force-displacement curve for the inelastic springs (spring #1 and #2) on the right and left-hand sides of the post to model asphalt lateral strength.

The torsional bearing capacity m_t and the initial slope of the p-y curve k_{mt} were calculated using Eq. 34 and 36 Eq. equal to 44,529 N.mm/mm and 12,750 N.mm/mm^2, respectively. The p-y curve was obtained using Eq. 35 and then scaled by the thickness of the asphalt layer (90mm) to obtain the moment-rotation curve for the nonlinear spring on the center of the post, as shown in Figure 192.

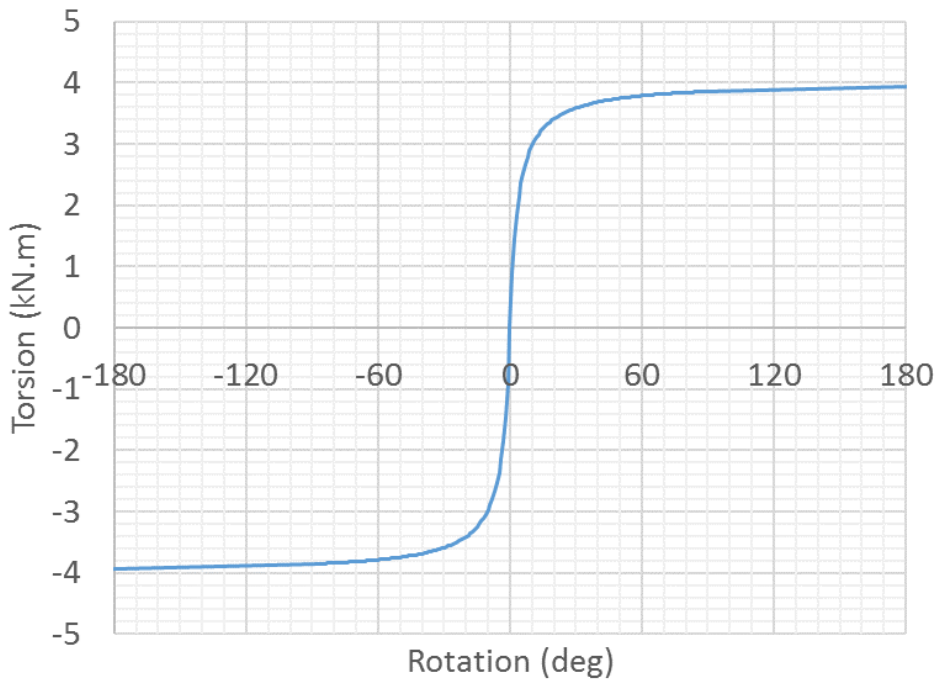

Figure 192. Torsion-rotation curve for the inelastic spring in the center of the web to model the torsional capacity.

The acceleration-time history, the displacement of the post at the impact point, the residual ground level displacement of the post, the peak force applied to the post and the ground level velocity of the post were obtained from the simulation outputs. The results were compared with the results obtained from experimental tests and finite element simulations using the continuum asphalt model. The acceleration-time history is compared in **Figure 193**, and the other parameters are compared in Table 22. The results of the simulations using springs were different from the results using continuum asphalt. This difference occurred because of several factors, including:

- The interaction between the asphalt layer and the soil, including the friction between them, is ignored when springs are used.
- The springs do not account for the limited boundary because of using the steel container.
- It is assumed that the stresses in the asphalt layer are uniform throughout the thickness of the layer.
- All the springs are connected to the center of the web in the post. However, when a continuum model of asphalt is used, stresses are applied to all parts of the posts.

Table 22. Comparison between measurements for different modeling of the asphalt versus experimental results.

Parameter	Experiment	FEA Continuum Asphalt	FEA Springs
Residual Ground Level Disp. (mm)	130	155	173
Peak Disp. at Impact Point (mm)	348	317	341
Peak Force (kN)	61	65	68
Peak Ground Level Vel. (m/s)	-	4.54	5.33

Although there is a difference between the results obtained using continuum asphalt and springs, the model using springs predicted a peak acceleration with less than 5%

difference from the peak predicted by the finite element model with a continuum asphalt. Even when continuum asphalt was used, the results still differed from the results of the experiments. This difference was due to the limitations of the finite element model. The foam programmer in the experimental tests was crushed into several pieces. However, the foam part in the FE model remained as one piece throughout the simulation time. This caused higher forces to be applied to the impactor, and therefore higher accelerations occurred.

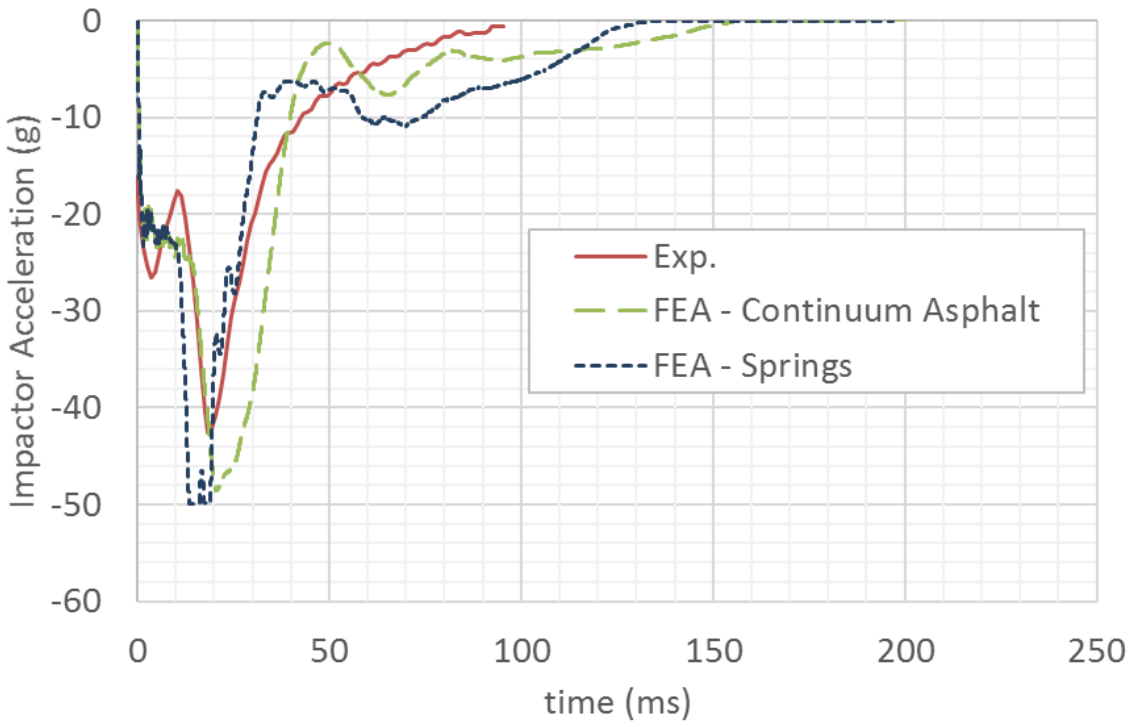

Figure 193. Acceleration-time history for different methods of modeling of the asphalt versus experimental results.

7.4 Full-Scale Crash Simulation of Guardrail Systems with Asphalt Mow Strips Using P-Y Curves (Test T90-R600-Springs)

The model used in Chapter 6 for full-scale crash simulation of a guardrail setup with 90 mm asphalt thickness and 600 mm rear distance was used to compare the finite element results with continuum asphalt with the model utilizing springs to model asphalt. The asphalt portion was removed from the model and replaced with springs. Identical springs with identical arrangement and formulation to those that are shown in Figure 187 for one guardrail post were used for all guardrail posts in this model. A schematic of the model showing a few of the posts is presented in Figure 194 and Figure 195. Figure 196 shows the guardrail posts with the springs attached. The other parts of the model are hidden to better illustrate the arrangement of the springs in the model.

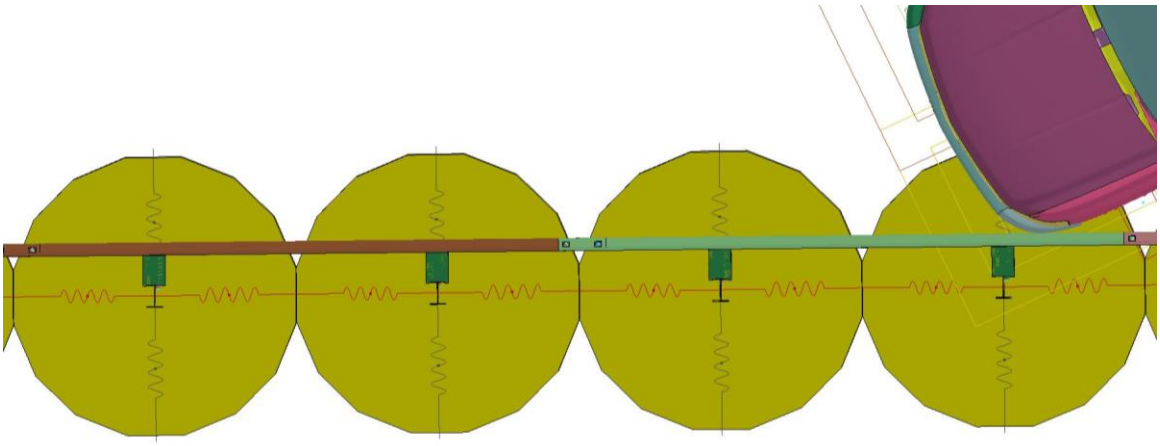

Figure 194. FE model used for the full-scale crash simulation with asphalt modeled using springs – top view.

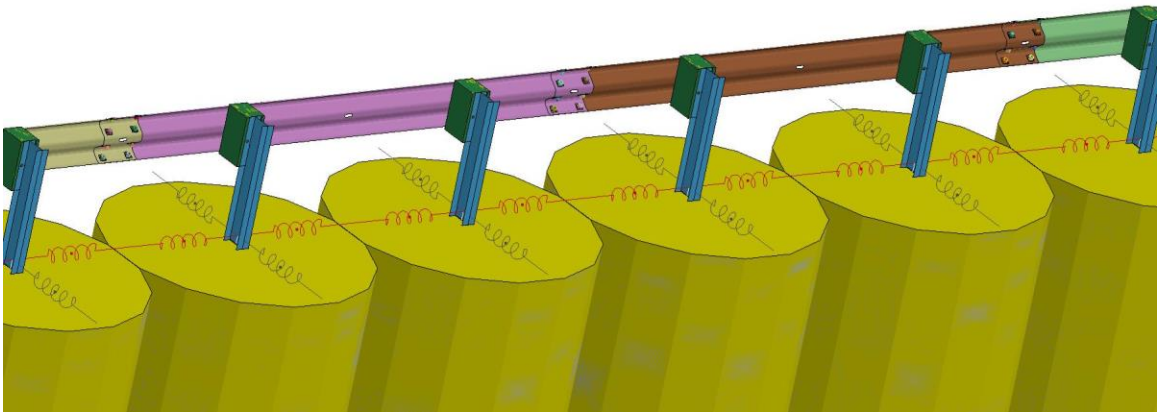

Figure 195. FE model used for the full-scale crash simulation with asphalt modeled using springs.

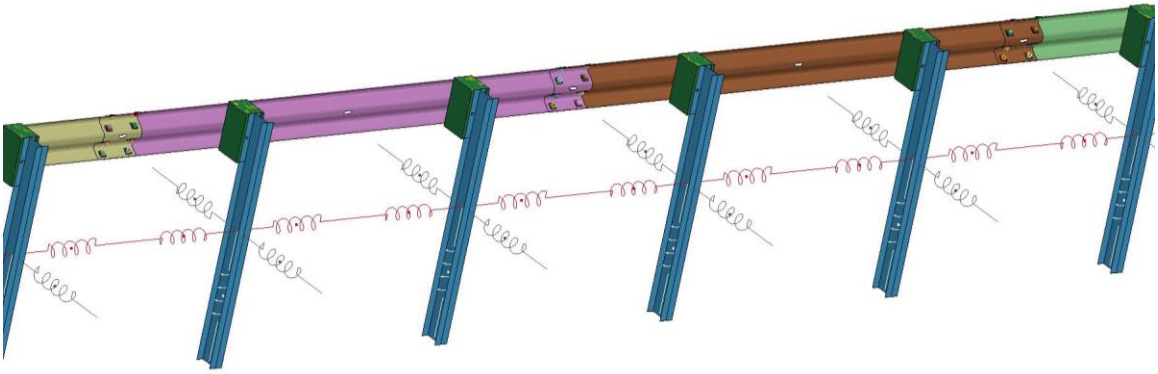

Figure 196. Illustration of the arrangement of springs in the model.

The simulation results are illustrated in Figure 197 through Figure 201 for every 0.1 sec of the simulation from the side and top views. The acceleration-time history of the vehicle is compared with the results of the simulation with continuum asphalt in Figure 202. The shape of the acceleration-time history was similar for both cases. However, the model with springs failed to capture one large acceleration peak at 0.16 sec. The longitudinal relative velocity of the occupant is shown in Figure 203. The velocity predicted by the two models

deviated considerably after 0.15 sec mostly because the peak acceleration was not captured in the model with springs. The time when the occupant impacted inside of the vehicle was calculated as equal to 0.155, and it was assumed that the occupant moved with the vehicle after this time. Therefore, the relative velocity of the occupant became zero after this time, and the relative velocity curve is only valid up to 0.155. The considerable difference between the relative velocities predicted by the two models occurred after this time, and therefore it did not affect the results.

The same argument is valid for the relative displacement curve shown in Figure 204. The lateral acceleration, velocity, and displacement curves are presented in Figure 205 to Figure 207. As shown in these figures, both model's predictions are similar. However, the model with springs underestimated the results. The pitch and roll of the vehicle were compared for the models in Figure 208 and Figure 209. The values for the pitch and roll angles were relatively low, and they were up to 5 degrees. The upper bound value for these angles in the MASH guidelines is 75 degrees. Therefore, although the models' predictions for the pitch and roll angles had a considerable difference, this difference did not affect the system response significantly. Figure 210 shows the comparison for the vehicle yaw angle, which was very similar for both models. The structural adequacy and occupant risk parameters were compared and presented in Table 23. The spring model produced similar predictions for the parameters as the continuum asphalt model did, except for the value of the peak longitudinal ride down acceleration. The differences in the models' predictions were due to multiple factors, including:

- The springs do not account for the friction and bond between the asphalt and soil.
- When asphalt is modeled as a continuum, it covers the top of the soil and prevents soil dilation and plowing. The soil pushes the asphalt upward, while asphalt adds additional compressive stresses to the soil, which increases the soil strength. However, springs are not in contact with soil and cannot help to provide the same additional soil strength. This causes lower strength predictions.
- Each spring acts separately from the other springs. However, in a full-scale crash test, the asphalt layer is shared between two posts, and there is an interaction between posts.
- Springs are assumed to remain perpendicular to the post. However, for large deformations, this assumption becomes less accurate.

Although there are differences between the predictions made by the spring model and the continuum asphalt model, the spring model provides a good prediction of the response and can be used with proper model calibration and validation.

It is important to note that if the asphalt layer is very thick, more than one layer of springs should be used through the thickness of asphalt. Using only one layer of springs assumes that the post displacement in the asphalt layer is uniform through the thickness and is equal to the displacement at the center of the asphalt layer. When the asphalt layer is very thick, this approximation becomes less accurate. Specifically, if it is expected that the asphalt layer is thick enough that it can apply a significant moment to

the post, then at least two layers of springs through the asphalt thickness are required to be able to model the moment applied to the post by the asphalt layer. In the cases simulated in this dissertation, asphalt thickness of 90 mm was used. For this asphalt thickness with the cohesion of 500 kPa and friction angle of 35 degrees, the guardrail post is able to translate through the asphalt layer and the center of rotation of the post is below the asphalt layer. Because the center of rotation is below the layer, the asphalt layer is in compression through its thickness. Therefore, a moment is not applied to the post from the asphalt layer and using one layer of springs is enough.

The other important assumption used to develop the p-y curves is that the asphalt cohesion is large enough and the asphalt is thin enough that the effect of gravity on the asphalt strength can be ignored. This assumption is valid for the practical asphalt thicknesses, which are typically less than 250 mm.

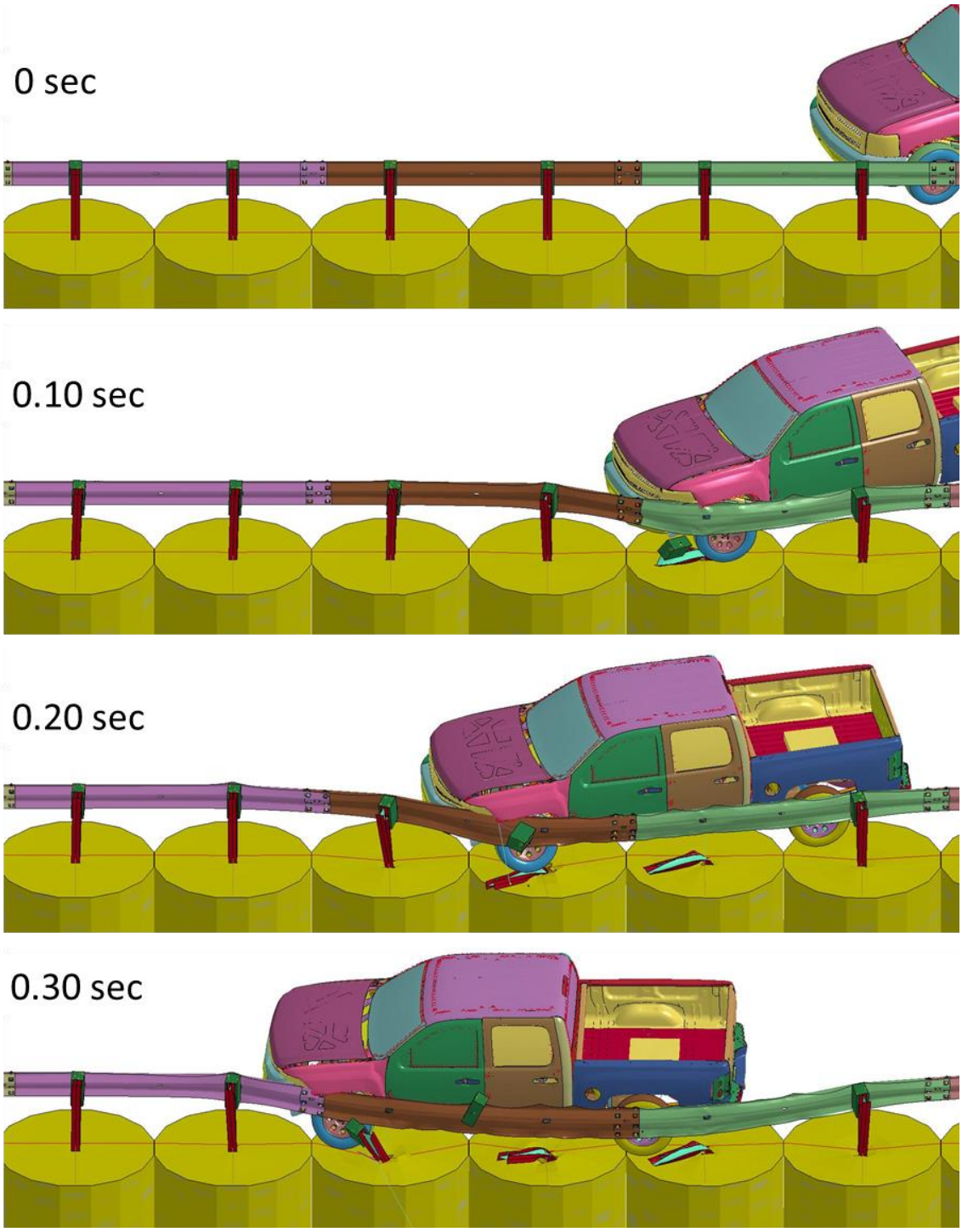

Figure 197. Simulation for the guardrail system with asphalt modeled via springs.

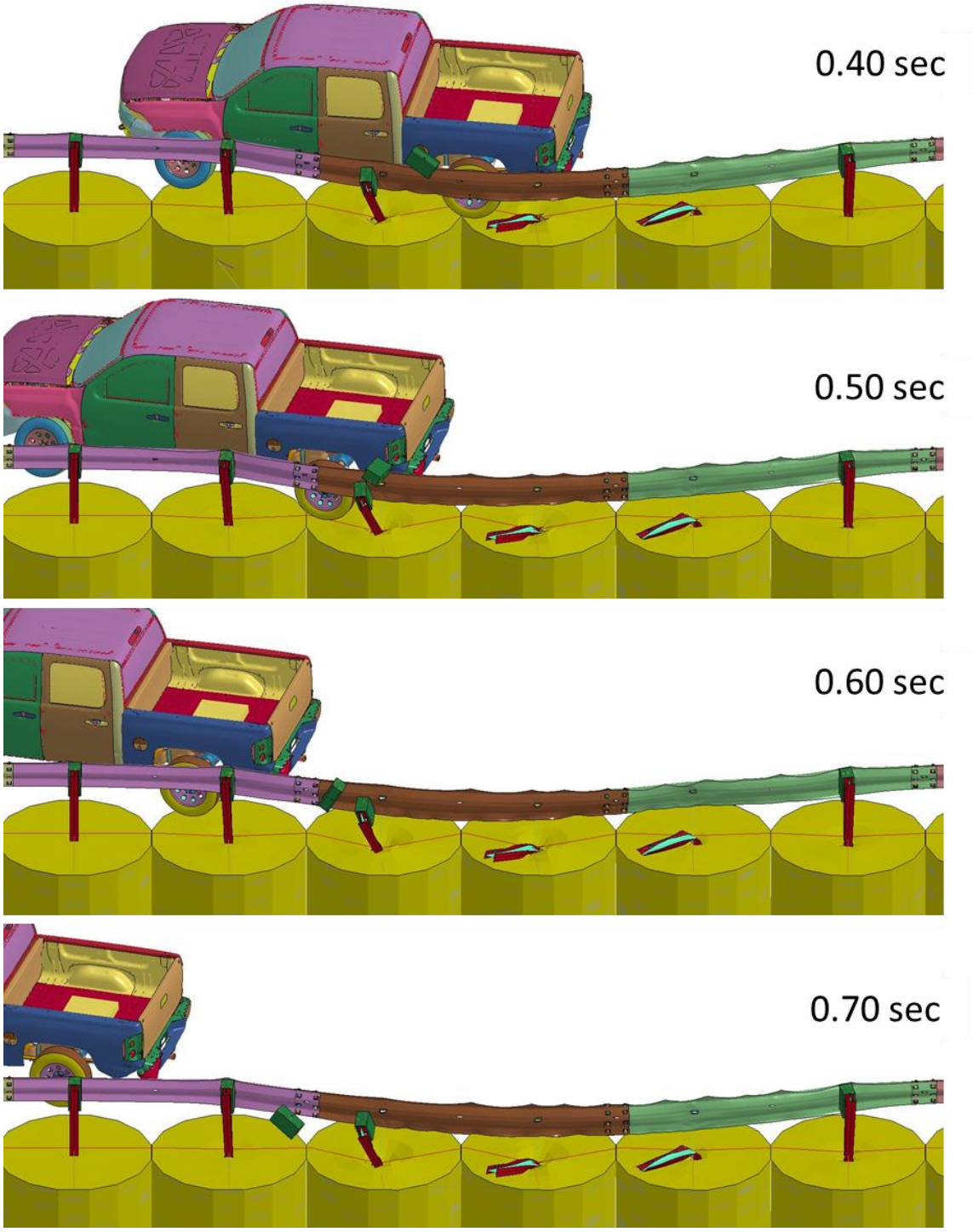

Figure 198. Simulation for the guardrail system with asphalt modeled via springs.

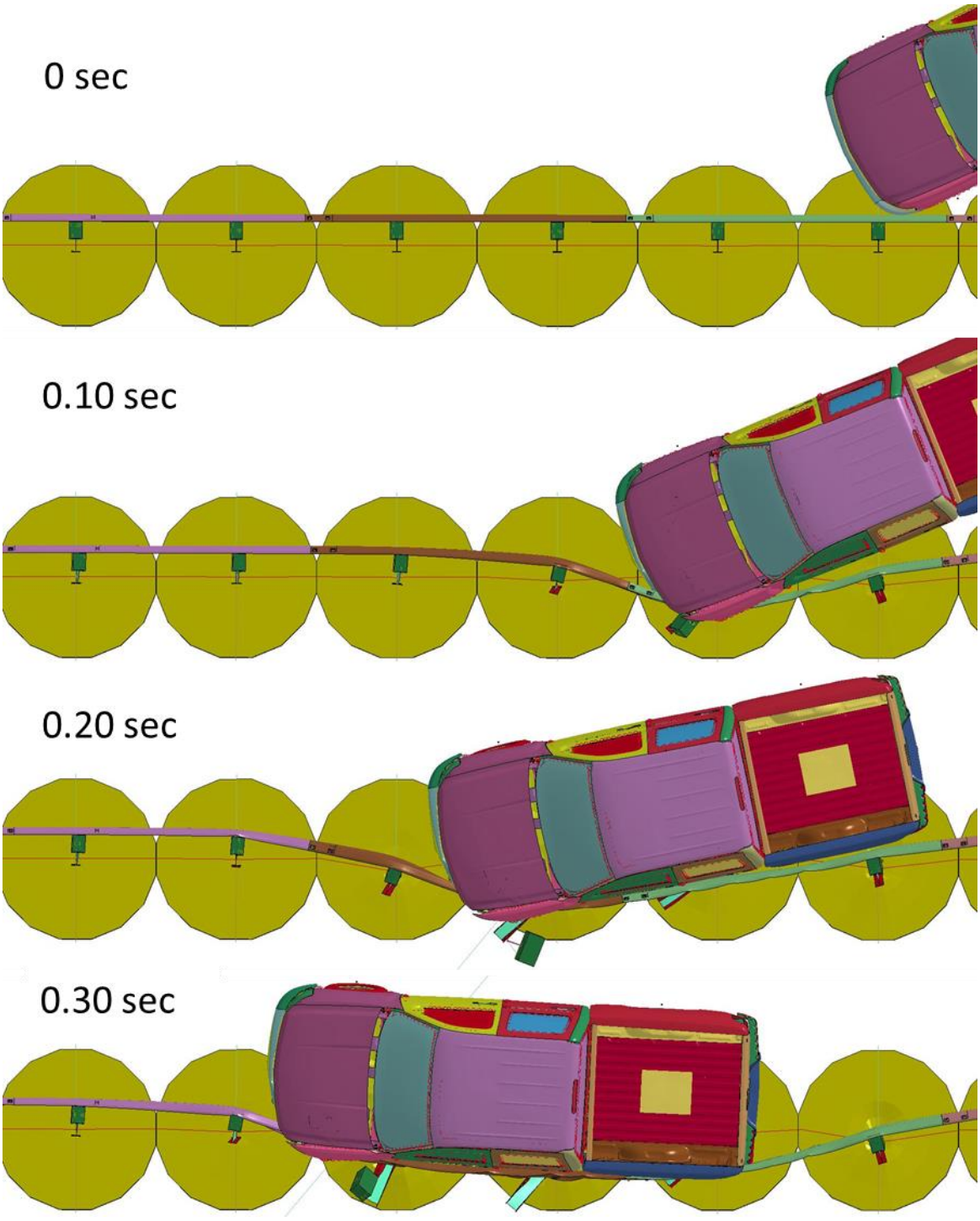

Figure 199. Simulation for the guardrail system with asphalt modeled via springs.

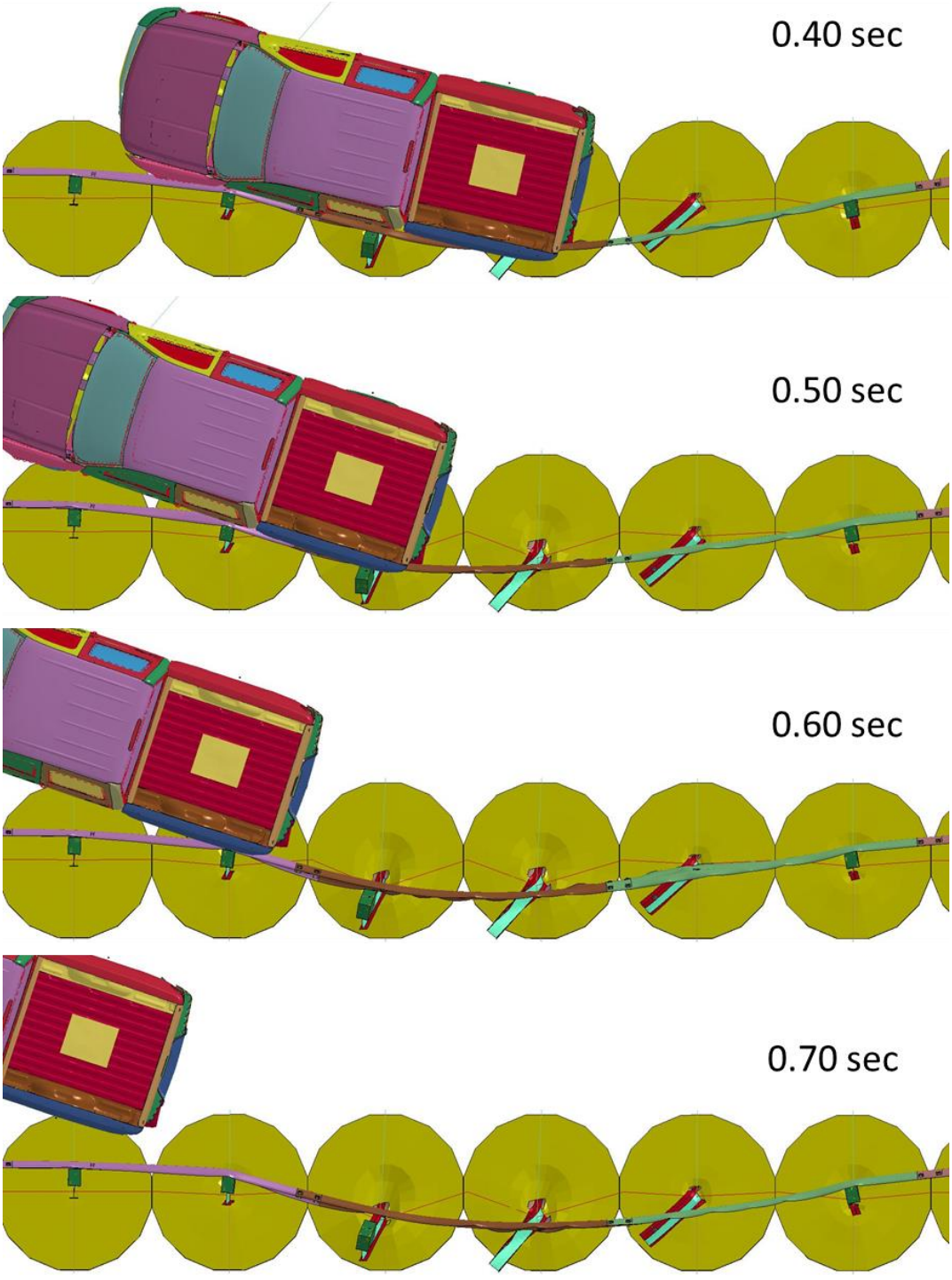

Figure 200. Simulation for the guardrail system with asphalt modeled via springs.

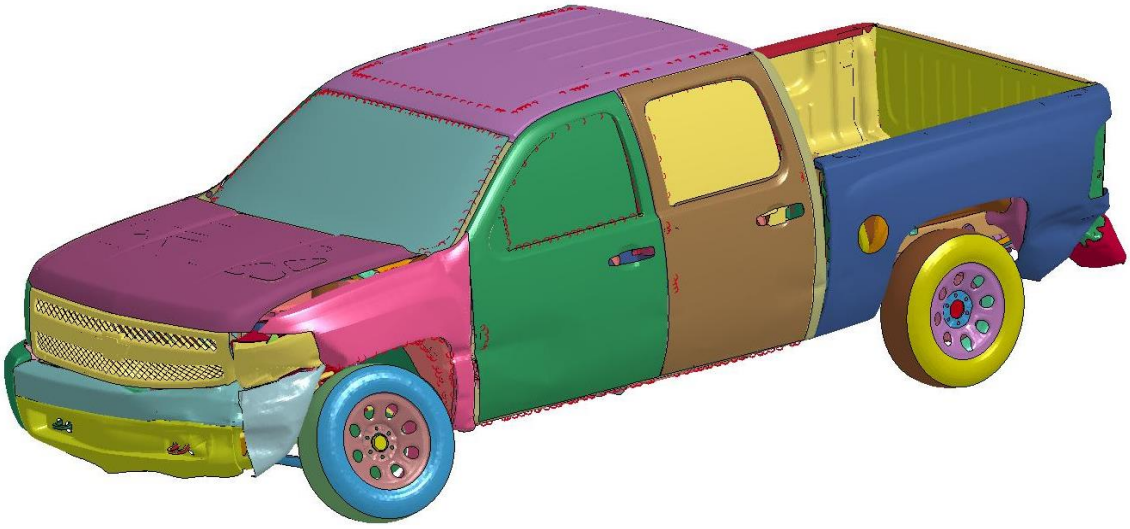

Figure 201. Vehicle deformation for the system with asphalt modeled via springs.

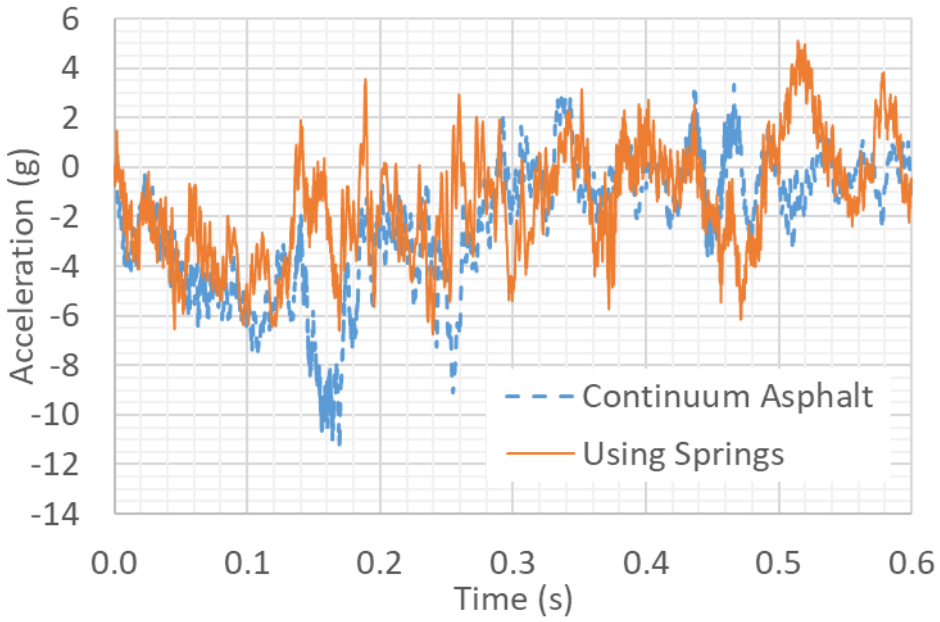

Figure 202. 10 m/s average vehicle longitudinal acceleration (g) - asphalt modeled via springs versus continuum asphalt.

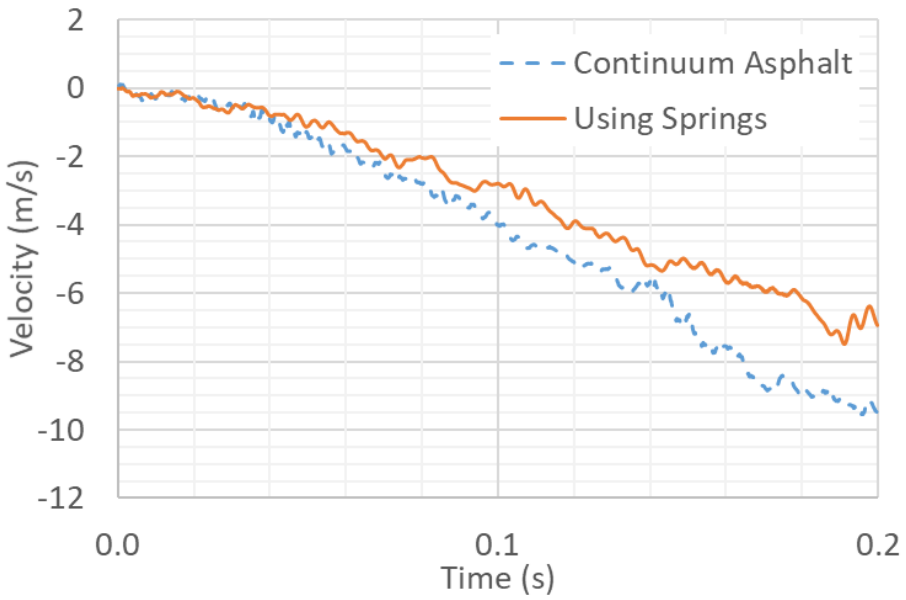

Figure 203. Relative longitudinal velocity of the occupant (m/s) - asphalt modeled via springs versus continuum asphalt.

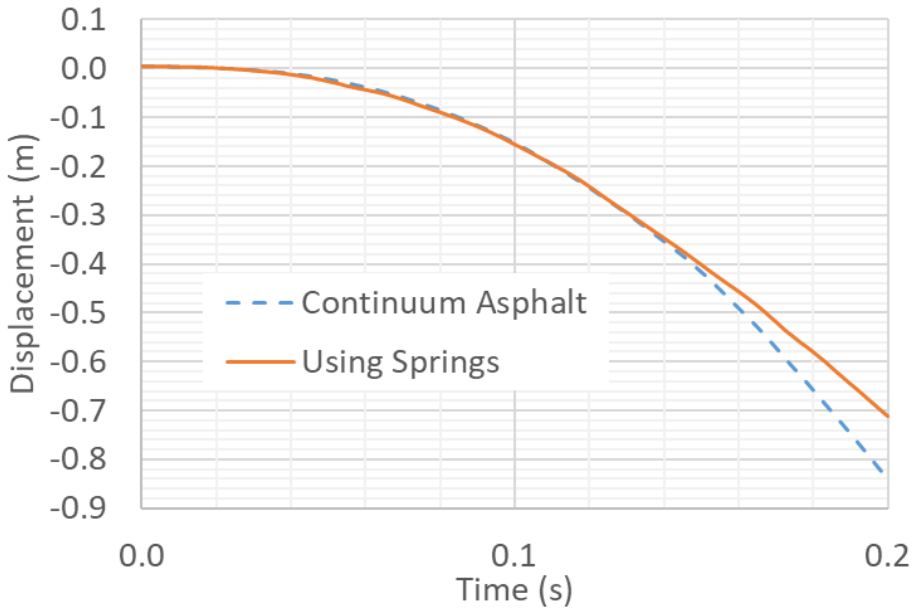

Figure 204. Relative longitudinal displacement of the occupant (m) – asphalt modeled via springs versus continuum asphalt.

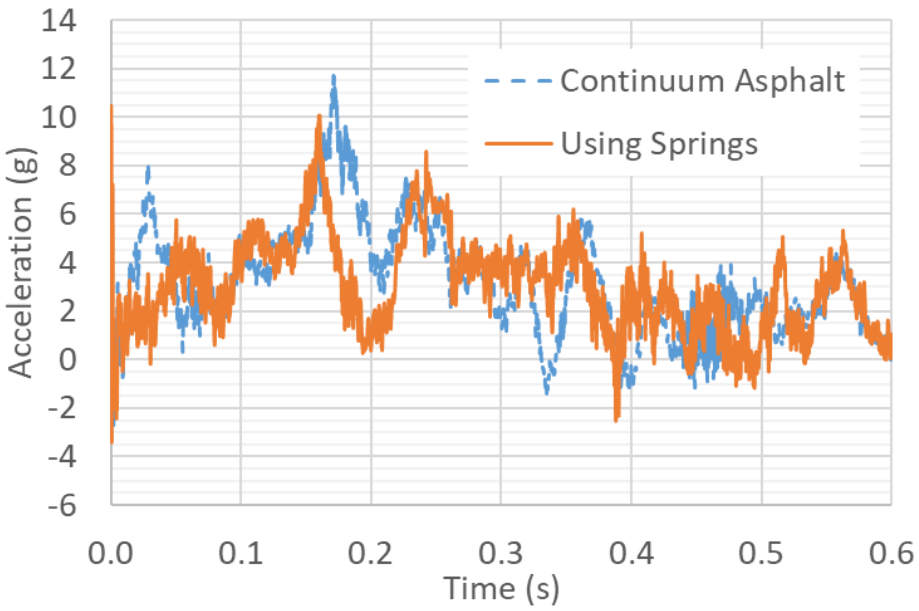

Figure 205. 10 m/s average vehicle lateral acceleration (g) – asphalt modeled via springs versus continuum asphalt.

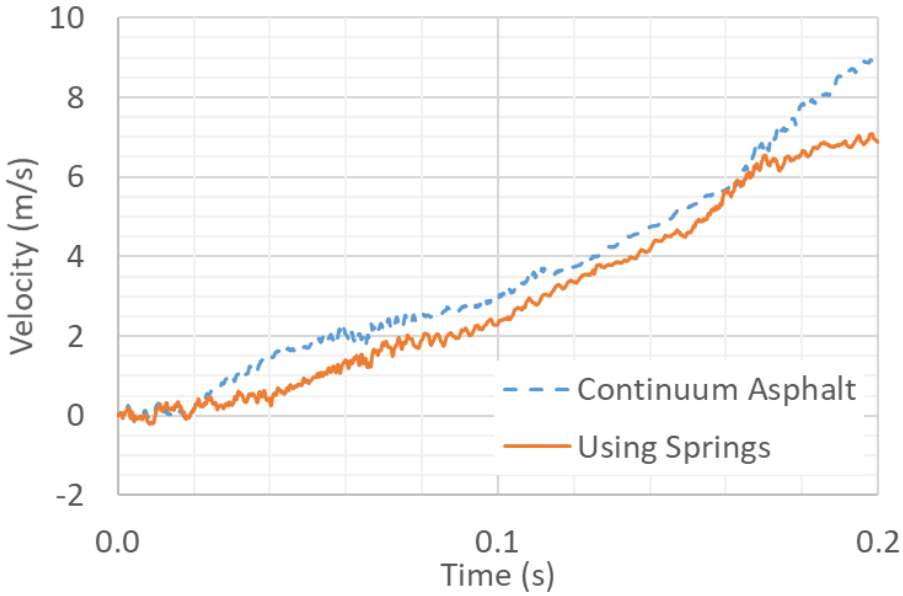

Figure 206. Relative lateral velocity of the occupant (m/s) - asphalt modeled via springs versus continuum asphalt.

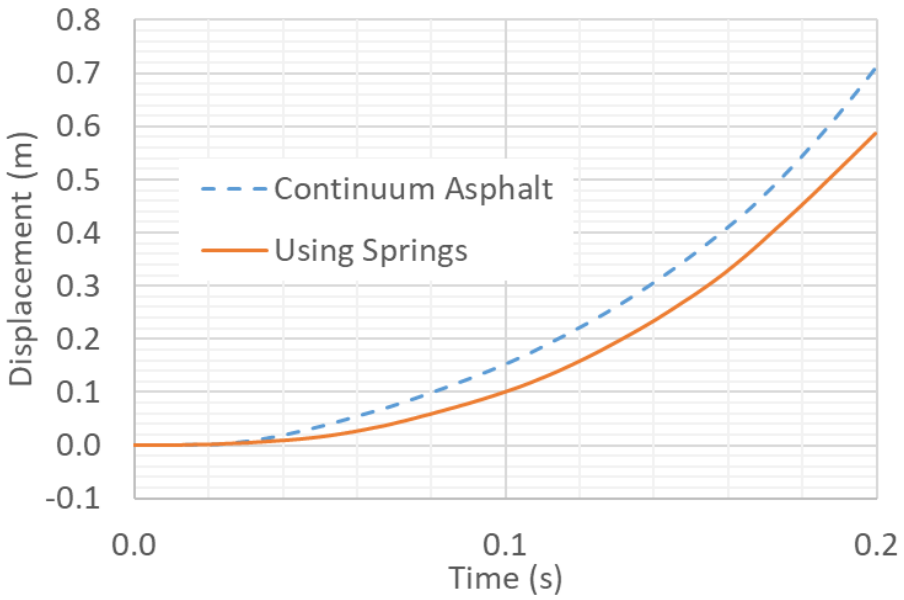

Figure 207. Relative lateral displacement of the occupant (m) - asphalt modeled via springs versus continuum asphalt.

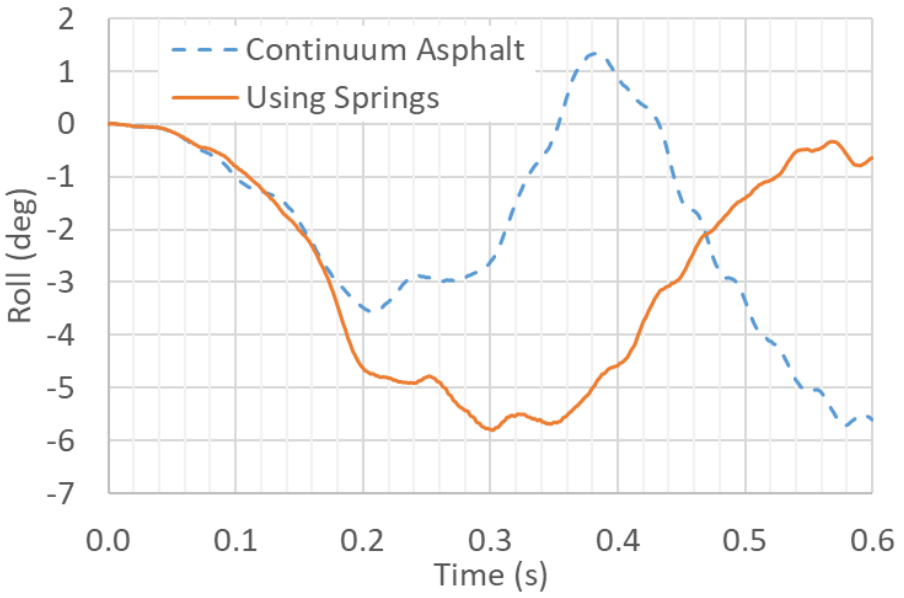

Figure 208. Vehicle roll (deg) - asphalt modeled via springs versus continuum asphalt.

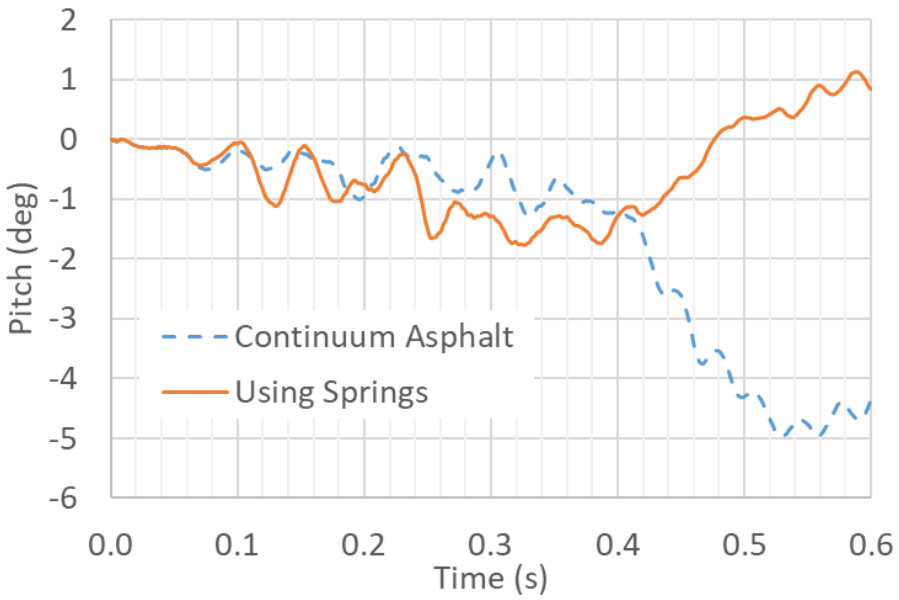

Figure 209. Vehicle pitch (deg) - asphalt modeled via springs versus continuum asphalt.

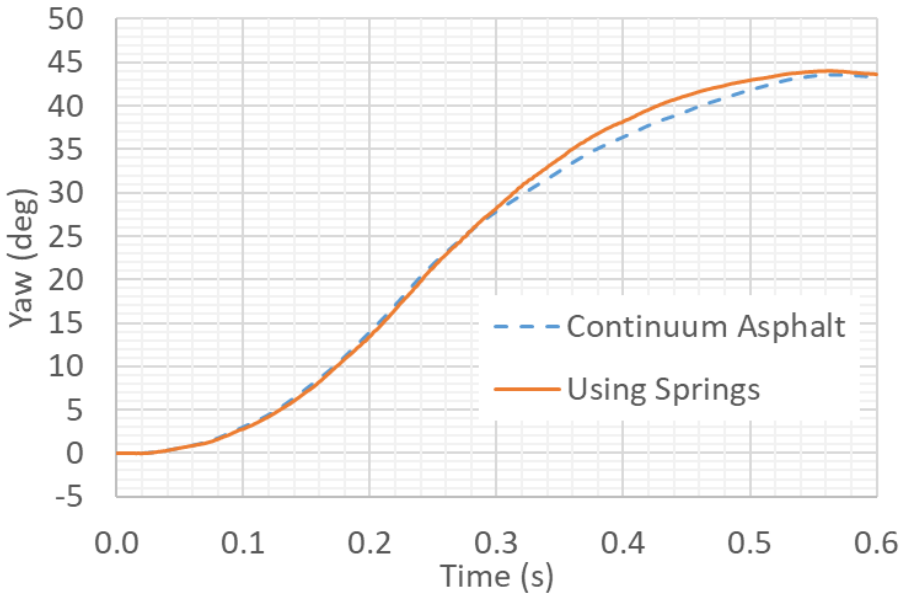

Figure 210. Vehicle yaw (deg) - asphalt modeled via springs versus continuum asphalt.

Table 23. Comparison between the simulation with continuum asphalt and with asphalt modelled using springs.

Test Number		T90-R600	T90-R600-Springs
Vehicle	Designation	2270P	2270P
	Test Inertial, kg	2,270	2,270
Impact Conditions	Speed, km/h	100	100
	Angle, deg	25.0	25.0
Exit Conditions	Speed (km/h)	58	61
	Trajectory Angle, deg	18	18
ORA, g's < 20.49 g	Longitudinal	-11.2	-6.7
	Lateral	11.7	10.1
OIV, m/s < 12.2 m/s	Longitudinal	5.6	4.3
	Lateral	4.7	4.9
Test Article Deflections, m	Dynamic	0.842	0.947
	Permanent	0.753	0.727
Impact time for the occupant, sec		0.140	0.155
Sum of all posts ground level displacement (m)		0.734	0.937
Max. Yaw Angle, deg		44	44
Max. Roll Angle, deg < 75 deg		-6	-6
Max. Pitch Angle, deg < 75 deg		-5	1
Posts detached from rail during impact		3 posts	3 posts
Posts hit by leading tire (wheel snag)		3 posts	3 posts
Posts pulled out of ground		none	none
Leading tire/wheel disengaged		mostly	mostly

CHAPTER 8. CONCLUDING REMARKS

8.1 Conclusions

Given improvements in computational methods and speed that have occurred since the development of early models for guardrail systems, it is now feasible to perform detailed finite element simulations to characterize the responses at a fundamental material level. Prior FEA of the performance of guardrail posts in which the asphalt layer was assumed to be rigid represents the response of cases where the asphalt layer provides excessive levels of restraint. This occurrs in cases with thicknesses more than 150 mm combined with rear distances larger than 600 mm for regular asphalt in this research. If asphalt is approximately twice as strong as regular asphalt, even setups with mow strip thicknesses more than 150 mm combined with rear distances larger than 600 mm show behavior similar to having a rigid mow strip layer. In other cases below these ranges, such models with rigid mow strips are not capable of accounting for the influence of the deformability and finite strength of many typical mow strip geometries. Therefore, as shown in this study, the finite stiffness and strength of the asphalt layer should be modeled to capture the general non-rigid response of this layer.

The use of a Mohr-Coulomb material model for the soil and asphalt provides an effective representation of the load-deflection response of the guardrail post, soil, and asphalt layer system over a broad range of material and geometric parameters. Moreover, erosion based on the stress and volumetric strain to capture the rupture of the asphalt layer

and the modeling of the contact conditions between the post and the soil are also key attributes of the FE simulation models.

To ensure proper performance of the Mohr-Coulomb material model and the contact definitions, gravity loading must be applied. Dynamic relaxation should be employed in applying the gravity load to avoid waves caused by the sudden application of the gravity loading to the model.

The relationships between asphalt material properties, geometric properties, and guardrail post resistance were investigated using simplified analytical solutions and FE simulations. Mow strip thickness, rear distance, cohesion, friction angle, and shear modulus showed significant impacts on the amount of restraint that the asphalt layer provides. Equations for rupture, bearing, and torsional capacities of mow strips were obtained as functions of these parameters. These predictive equations clearly show the dependence of each failure mode on material and geometric properties, and they were utilized to construct p-y curves. The p-y curves provide an efficient way to model asphalt layers using nonlinear inelastic springs, which eliminates the need to use hundreds of thousands of elements to model asphalt rupture. Using fewer elements and simpler FE models decreases the run time for full-scale crash simulations. The p-y curves developed in this research can only be used directly for I-shaped guardrail posts embedded in asphalt mow strips. However, the approach, which was used to find the p-y curves for mow strips with limited rear distance, can be used for other post shapes and other pressure dependent

materials used as a mow strip. This methodology can also be expanded to include uses for short piles embedded in concrete or rock with limited rear distance behind the piles.

A workshop with Georgia Department of Transportation personnel was held to discuss the alternative design and installation strategies. Five alternative design strategies were identified and prioritized to decrease the ground level stiffness of guardrail posts installed in asphalt mow strips.

1. Limit the maximum rear distance and thickness of the asphalt layer
2. Pre-cut the asphalt mow strip behind the post
3. Use a tapered mow strip
4. Make a cutout portion in the mow strip behind the post
5. Replace the asphalt with gravel to prevent vegetation growth

After consideration of constructability and potential maintenance issues, options (1) and (2) were selected for further investigation.

The ground-level restraint of guardrail posts by various asphalt mow strip designs was investigated using static finite element analysis, dynamic finite element simulations, and full-scale crash simulations. Measured data were utilized for a quantitative assessment of the relative performance of various post-mow strip designs compared to a common leave-out incorporated design. First, static simple finite element simulations were used to study the performance of guardrail post encased in asphalt mow strips on a wide range of material and geometric properties. The results were used to plan targeted simulations for dynamic

subcomponent simulation of guardrail posts embedded in soil and asphalt. The results obtained from the first two levels of simulation were used to build models for full-scale crash simulations and select particular mow strip geometries and material properties for evaluation.

In the static FEA simulation, the Mohr–Coulomb material models for the soil and the asphalt were calibrated using experimental data. Various modeling attributes, including mesh refinement, nonreflecting boundary condition, hourglass control, contact definition, and element erosion were scrutinized and implemented to represent the responses of the guardrail post, soil, and asphalt layer system over a large deformation of the post. Parametric studies on targeted geometric parameters were performed and provided the information on expected performance of post-mow strip system.

The FEA results were evaluated using three quantitative performance criteria (peak applied force, ground-level displacement, and maximum post strain) to evaluate the restraint of guardrail posts affected by asphalt mow strips. Decreasing the mow strip thickness and/or rear distance behind the post appears to be an effective way to reduce the restraint imparted by a mow strip on a guardrail system. A range of geometric parameters of desirable performance (less ground-level restraint) was presented with contour plots that included the target performance curve of the typical leave-out-incorporated design of the AASHTO Roadside Design Guide. Based on the contour plots, mow strips with 90 mm thickness and 300 mm rear distance, or 50 mm thickness and 300 mm rear distance, or 50

mm thickness and 600 mm rear distance all show ground level restraint less than or equivalent to mow strips with incorporating leave-out.

A computational investigation was conducted to study the effectiveness of installing pre-cut fracture planes on asphalt performance. Specifically, the performance was evaluated in terms of ground restraint to develop configurations to be used in lieu of leave-outs. The results of the analysis showed that four of the proposed designs involving parallel and diagonal cuts successfully reduced ground level restraint.

In the second part of the research, dynamic subcomponent tests and simulations were conducted to assess the performance of guardrail posts embedded in soil and asphalt. The simulations were much less computationally intensive than full-scale crash tests and simulations. Therefore, these simulations were used to evaluate more alternative designs for asphalt mow strips. The material models were updated for use in the dynamic loading simulations. The dynamic FEA results were evaluated using four quantitative performance criteria (peak dynamic applied force, permanent ground-level displacement, peak displacement of the post at the impact point, and effective applied load) to evaluate the restraint of guardrail posts affected by asphalt mow strips. Decreasing the mow strip thickness and/or rear distance behind the post appears to be an effective way to reduce the restraint imparted by a mow strip on a guardrail system.

A range of geometric parameters of desirable performance (i.e., less ground-level restraint) was presented with contour plots that include the target performance curve of the

typical leave-out-incorporated design of the AASHTO Roadside Design Guide. Based on the contour plots, mow strips with 90 mm thickness and 300 mm rear distance, or 50 mm thickness and 300 mm rear distance, or 50 mm thickness and 600 mm rear distance show ground level restraint less than or equivalent to mow strips with incorporating leave-out. The analyses also indicate that fabricating targeted full-depth cuts in the mow strip significantly reduces the amount of restraint the mow strip provides to a guardrail post.

In the third part of the research, full-scale crash simulations were conducted to assess the performance of guardrail posts embedded in soil and asphalt mow strips. The baseline model without mow strip was first validated using available crash test results in the literature. Then the model was updated to include an asphalt mow strip. Five different mow strip setups with various rear distances and thicknesses were studied. Two additional setups, one with stiffer asphalt than normal and one with diagonal mow strips pre-cuts, were studied. Numerous parameters based on MASH guidelines were used to evaluate the results. Moreover, additional parameters were defined and used to evaluate the relative ground level restraint caused by different mow strips. The summation of ground level displacement of posts in simulations was used as the primary parameter. By comparing the results of the simulations visually and quantitatively, it was observed that mow strips with 90 mm thickness and 300 mm rear distance, or mow strips with full depth diagonal pre-cuts behind the post have a ground level displacement of posts that is similar to the setup without any mow strips.

The static simulation, dynamic subcomponent simulations, and full-scale crash simulations give very similar conclusions. If the same asphalt that was used in this research is utilized, mow strips with 90 mm thickness and 300 mm rear distance and mow strips with full depth diagonal pre-cuts behind the post show similar ground level restraint to setups with leave-outs.

8.2 Future Work

The finite element model used in this research for crash simulations can be improved in future using the following recommendations:

- Steel rupture can be included in the model to capture the rupture in guardrails and posts. This will provide more accurate capturing of the guardrail system failure modes.
- The model of the vehicle wheels can be enhanced so that they can fail and get detached from the vehicle as easily as they typically fail in experimental tests.
- Steel rupture should be captured for bolted connections of the guardrails.
- The friction coefficient between the vehicle and the guardrail system is an important parameter in crash simulations. In this research, the friction coefficient was assumed to be the same between all surfaces of the vehicle

and all parts of the guardrail system. However, the friction coefficient is different between different parts of the vehicle and the guardrail system. This important parameter can be investigated more thoroughly in a future study.

The p-y curves developed in this research are calibrated to be used for springs with a displacement rate of 5 m/s and rotational rate of 500 deg/s. However, the approach utilized to develop these curves can be used in future to obtain p-y curves for different displacement and rotation rates. Although, these curves can only be directly used for typical steel guardrail posts with an "I" shape, the formulations for the p-y curves can be updated to utilize these curves for modeling of wooden circular posts embedded in asphalt or concrete mow strips or short piles embedded in rock or concrete.

REFERENCES

[1] M. Budhu, *soil mechanics and foundations*, 3rd ed. Hoboken, NJ: John Wiley & Sons Inc., 2010.

[2] D. W. Scott, D. W. White, L. K. Stewart, C. F. Arson, E. Bakhtiary, and S.-H. Lee, "Evaluating the Performance of Guardrail Systems for Installation in Georgia by Driving Through Asphalt Layers, Project FHWA-GA-15-1321-13-21," Atlanta, Ga, 2015.

[3] R. P. Bligh, N. R. Seckinger, A. Y. Abu-Odeh, P. N. Roschke, W. L. Menges, and R. R. Haug, "dynamic response of guardrail systems encased in pavement mow strips," College Station, TX, 2004.

[4] T. F. Fwa, S. A. Tan, and L. Y. Zhu., "Rutting Prediction of Asphalt Pavement Layer Using C-ϕ Model," *J. Transp. Eng.*, vol. 130, no. 5, pp. 675–683, 2004.

[5] Y. Zhang, R. Luo, and R. L. Lytton, "Characterization of viscoplastic yielding of asphalt concrete," *Constr. Build. Mater.*, vol. 47, pp. 671–679, 2013.

[6] a. Bell, "Summary report on the aging of asphalt-aggregate systems," *Transp. Res. board*, vol. 10, p. 10PM, 1989.

[7] M. J. Farrar, T. F. Turner, J.-P. Planche, J. F. Schabron, and P. M. Harnsberger, "Evolution of the Crossover Modulus with Oxidative Aging," *Transp. Res. Rec. J.*

Transp. Res. Board, vol. 2370, no. 1, pp. 76–83, 2013.

[8] D. W. Scott, S.-H. Lee, E. Bakhtiary, C. F. Arson, and D. W. White, "static response of steel guardrail posts driven through asphalt vegetation barriers," in *Transportation Research Board 94th Annual Meeting*, 2015.

[9] S.-H. Lee, "Experimental Testing and assessment of guardrail systems in asphalt ground layers," Ph.D. Dissertation, Georgia Institute of Technology, 2017 (in press).

[10] "LS-DYNA Version R7.1." Livermore Software Technology Corporation (LSTC), Livermore, CA, 2014.

[11] A. Tabiei and J. Wu, "roadmap for crashworthiness finite element simulation of roadside safety structures," *Finite Elem. Anal. Des.*, vol. 34, no. 2, pp. 145–157, 2000.

[12] M. Borovinšek, M. Vesenjak, M. Ulbin, and Z. Ren, "simulation of crash tests for high containment levels of road safety barriers," *Eng. Fail. Anal.*, vol. 14, no. 8 SPEC. ISS., pp. 1711–1718, 2007.

[13] A. O. Atahan, "finite element simulation of a strong-post w-beam guardrail system," *Simul. Trans. Soc. Model. Simul.*, vol. 78, no. 10, pp. 587–599, 2002.

[14] C. a. Plaxico, G. S. Patzner, and M. H. Ray, "finite element modeling of guardrail timber posts and the post-soil interaction," *Transp. Res. Rec. J. Transp. Res. Board*,

vol. 1647, no. 1, pp. 139–146, 2007.

[15] M. H. Ray and R. G. McGinnis, “guardrail and median barrier crashworthiness. No. project 20-5, NCHRP synthesis 244,” Washington, D.C., 1997.

[16] J. Reid, “LS-DYNA simulation influence on roadside hardware,” *Transp. Res. Rec. J. Transp. Res. Board*, vol. 1890, no. 1, pp. 34–41, 2004.

[17] A. O. Atahan, “vehicle crash test simulation of roadside hardware using LS-DYNA: a literature review,” *Int. J. Heavy Veh. Syst.*, vol. 17, no. 1, pp. 52–75, 2010.

[18] Z. Ren and M. Vesenjak, “computational and experimental crash analysis of the road safety barrier,” *Eng. Fail. Anal.*, vol. 12, no. 6 SPEC. ISS., pp. 963–973, 2005.

[19] C. E. Hampton and H. C. Gabler, “crash performance of strong-post W-beam guardrail with missing blockouts,” *Int. J. Crashworthiness*, vol. 17, no. 1, pp. 93–103, 2012.

[20] P. Mohan, M. Dhafer, L. Meczkowski, and N. Bedewi, “finite element modeling and validation of a 3-strand cable guardrail system,” *Int. J. Crashworthiness*, vol. 10, no. 3, pp. 267–273, 2005.

[21] D. Sicking, J. Reid, and J. Rohde, “development of the midwest guardrail system,” *Transp. Res. Rec.*, vol. 1797, no. 1, pp. 44–52, 2002.

[22] K. K. Mak, R. P. Bligh, and W. L. Menges, “testing of state roadside safety

systems—volume XI: appendix J—crash testing and evaluation of existing guardrail systems, report FHWA-RD-98-046," Washington, D.C., 1998.

[23] J. Ross, E. H., D. L. Sicking, R. A. Zimmer, and J. D. Michie, "recommended procedures for the safety performance evaluation of highway features. NCHRP report 350." National Cooperative Highway Research Program, 1993.

[24] C. Plaxico, M. Ray, and K. Hiranmayee, "impact performance of the G4(1W) and G4(2W) guardrail systems: comparison under NCHRP report 350 test 3-11 conditions," *Transp. Res. Rec.*, vol. 1720, no. 1, pp. 7–18, 2000.

[25] D. J. Gabauer, K. D. Kusano, D. Marzougui, K. Opiela, M. Hargrave, and H. C. Gabler, "pendulum testing as a means of assessing the crash performance of longitudinal barrier with minor damage," *Int. J. Impact Eng.*, vol. 37, no. 11, pp. 1121–1137, 2010.

[26] R. P. Bligh, A. Y. Abu-Odeh, and W. L. Menges, "MASH test 3-10 on 31-inch w-beam guardrail with standard offset blocks, report FHWA/TX-11/9-1002-4," College Station, TX, 2011.

[27] D. L. Sicking, K. K. Mak, J. R. Rohde, and J. D. Reid, *manual for assessing safety hardware*. Washington, D.C.: AASHTO, 2009.

[28] A. Y. Abu-Odeh, K.-M. Kim, and R. P. Bligh, "guardrail deflection analysis, phase

I: (2010-11), report 405160-24," College Station, TX, 2011.

[29] K. D. Schrum *et al.*, "safety performance evaluation of the non-blocked midwest guardrail system (MGS) Report TRP-03-262-12/ RPFP-11-MGS-3," Lincoln, NE, 2013.

[30] J. F. Dewey, J. K. Jeyapalan, T. J. Hirsch, and H. E. Ross, "A study of the soil-structure interaction behavior of highway guardrail posts, research report 3431," College Station, TX, 1983.

[31] M. R. Ferdous, A. Abu-Odeh, R. P. Bligh, H. L. Jones, and N. M. Sheikh, "performance limit analysis for common roadside and median barriers using LS-DYNA," *Int. J. Crashworthiness*, vol. 16, no. 6, pp. 691–706, 2011.

[32] LSTC, "LS-DYNA® keyword user's manual–vol. 2–v971 build R9.1.0." Livermore Software Technology Corporation, Livermore, CA, 2017.

[33] J. Rohde, B. Rosson, and R. Smith, "instrumentation for determination of guardrail-soil interaction," *Transp. Res. Rec.*, vol. 1528, no. 1, pp. 109–115, 1996.

[34] W. Wu and R. Thomson, "a study of the interaction between a guardrail post and soil during quasi-static and dynamic loading," *Int. J. Impact Eng.*, vol. 34, no. 5, pp. 883–898, 2007.

[35] M. Souli and I. Shahrour, "arbitrary lagrangian eulerian formulation for soil

structure interaction problems," *Soil Dyn. Earthq. Eng.*, vol. 35, pp. 72–79, 2012.

[36] A. R. Dusty, R. P. Bligh, and W. L. Menges, "alternative design of guardrail posts in asphalt or concrete mowing pads," College Station, TX, 2009.

[37] S.-H. Lee, E. Bakhtiary, D. W. Scott, L. K. Stewart, and D. W. White, "Influence of geometric parameters on the restraint of guardrail posts by asphalt mow strips," *Sustain. Resilient Infrastruct.*, vol. 2, no. 1, pp. 22–36, 2016.

[38] E. Bakhtiary and C. Arson, "Relationship between Branch Length Distribution and Free Energy of a Granular Assembly Subject to Crushing," in *Geo-Congress 2014 Technical Papers*, 2014, pp. 2867–2876.

[39] E. Bakhtiary and C. Arson, "Towards a thermodynamic framework to model particle crushing and sieving," in *47th US Rock Mechanics / Geomechanics Symposium 2013*, 2013, vol. 1, pp. 582–589.

[40] P. Wang, E. Bakhtiary, S. Ecker, C. Arson, T. Cristopher, and K. Francis, "Discrete Element modeling and analysis of shielding effects during the crushing of a grain," in *49th US Rock Mechanics/Geomechanics Symposium of the American Rock Mechanics Association*, 2015.

[41] LSTC, "LS-DYNA® keyword user's manual–vol. 1–v971 build R9.1.0." Livermore Software Technology Corporation, 2017.

[42] AASHTO, *roadside design guide*, 4th ed. Washington, D.C.: AASHTO, 2011.

[43] LSTC, "LS-DYNA Support," 2017. [Online]. Available: http://www.dynasupport.com/howtos/element/hourglass. [Accessed: 01-Jan-2017].

[44] F. H. Kulhawy, C. H. Trautmann, J. F. Beech, and T. D. O'Rourke, "Transmission line structure foundations for uplift-compression loading. Report EPRI EL-6800," 1983.

[45] E. Bakhtiary, S.-H. Lee, D. W. Scott, L. K. Stewart, and D. W. White, "Evaluation of Guardrail Posts Installed in Asphalt Mow Strips by Static Finite Element Simulation," *Open J. Civ. Eng.*, vol. 7, no. 1, pp. 141–164, 2017.

[46] ASTM, "standard test methods for tension testing of metallic materials (ASTM E8/E8M)." 2001.

[47] USACE, *Bearing capacity of soils: Engineering Manual*. United States Army Corps of Engineers, 1982.

[48] J. E. Bowles, *foundation analysis and design*, 5th ed. New York: McGraw-Hill, 2001.

[49] R. F. Christensen, Donald W. Bonaquist, "Evaluation of indirect tensile test (IDT) procedures for low-temperature performance of hot mix asphalt. No. 530," 2004.

[50] T. K. Pellinen, J. Song, and S. Xiao, "Characterization of Hot Mix Asphalt With

Varying Air Voids Content Using Triaxial Shear Strength Test," in *8th Conference on Asphalt Pavements for Southern Africa*, 2004.

[51] B. A. Lewis, "manual for LS-DYNA soil material model 147. NO. FHWA-HRT-04-095," Washington, D.C., 2004.

[52] Y. D. Reid, J. D., Coon, B. A., Lewis, B. A., Sutherland, S. H., & Murray, "evaluation of LS-DYNA soil material model 147 No. FHWA-HRT-04-094," Washington, D.C., 2004.

[53] R. O. Davis and A. P. Selvadurai, *plasticity and geomechanics*. Cambridge University Press, 2005.

[54] ASTM, *standard method of test for direct shear test of soils under consolidated drained conditions ASTM D3080*. ASTM, 2000.

[55] D. A. Lekarp F, Richardson IR, "Influences on permanent deformation behavior of unbound granular materials," *Transp. Res. Rec.*, vol. 1547, pp. 68–75, 1996.

[56] S. H. Lee, E. Bakhtiary, L. K. Stewart, D. Scott, and D. White, "Effect of pre-cut asphalt fracture planes on highway guardrail performance," *Int. J. Comput. Methods Exp. Meas.*, vol. 4, no. 3, pp. 353–363, 2016.

[57] L. J. Malvar, "Review of Static and Dynamic Properties of Steel Reinforcing Bars," *Am. Concr. Inst. Mater. J.*, vol. 95, no. 5, pp. 609–616, 1997.

[58] D. Allen, “Stiffness Evaluation of Neoprene Bearing Pads under Long-Term Loads,” University of Florida, 2008.

[59] National Crash Analysis Center (NCAC), “Development and Validation of a Finite Element Model for a 2007 Chevy Silverado, NCAC 2009-T-005, 5, prepared for FHWA,” 2009.

[60] K. A. Polivka, R. K. Faller, D. L. Sicking, J. R. Rohde, B. W. Bielenberg, and J. D. Reid., “PERFORMANCE EVALUATION OF THE MIDWEST GUARDRAIL SYSTEM – UPDATE TO NCHRP 350 TEST NO . 3-11 WITH 28 " C . G . HEIGHT (2214MG-2), Final Report to the National Cooperative Highway Research Program, MwRSF Research Report No. TRP-03-171-06,” Lincoln, NE, 2006.

[61] E. Bakhtiary, H. Xu, and C. Arson, “probabilistic optimization of a continuum mechanics model to predict differential stress-induced damage in claystone,” *Int. J. Rock Mech. Min. Sci.*, vol. 68, pp. 136–149, 2014.

[62] E. Bakhtiary and P. Gardoni, “Probabilistic seismic demand model and fragility estimates for rocking symmetric blocks,” *Eng. Struct.*, vol. 114, pp. 25–34, 2016.

[63] E. Bakhtiary, “Probabilistic Seismic Demand Model and Fragility Estimates for Symmetric Rigid Blocks Subject to Rocking Motions,” Texas A&M University, 2013.

[64] A. Tabandeh and P. Gardoni, “Probabilistic capacity models and fragility estimates for RC columns retrofitted with FRP composites,” *Eng. Struct.*, vol. 74, pp. 13–22, 2014.

[65] A. Tabandeh and P. Gardoni, “Empirical Bayes Approach for Developing Hierarchical Probabilistic Predictive Models and Its Application to the Seismic Reliability Analysis of FRP-Retrofitted RC Bridges,” *ASCE-ASME J. Risk Uncertain. Eng. Syst. Part A Civ. Eng.*, vol. 1, no. 2, 2015.